Doctoral Dissertations   Graduate School

8-2019

Improving the Isotropy of Additively Manufactured Parts by Fused Deposition Modeling: From Polymeric Self-Assembly to Reactive Processing

Neiko Levenhagen
University of Tennessee, nlevenha@vols.utk.edu

To the Graduate Council:

I am submitting herewith a dissertation written by Neiko Levenhagen entitled "Improving the Isotropy of Additively Manufactured Parts by Fused Deposition Modeling: From Polymeric Self-Assembly to Reactive Processing." I have examined the final electronic copy of this dissertation for form and content and recommend that it be accepted in partial fulfillment of the requirements for the degree of Doctor of Philosophy, with a major in Chemistry.

Mark Dadmun, Major Professor

We have read this dissertation and recommend its acceptance:

Mike Kilbey, Sheng Dai, Chad Duty

Accepted for the Council:

Dixie L. Thompson

Vice Provost and Dean of the Graduate School

(Original signatures are on file with official student records.)

Improving the Isotropy of Additively Manufactured Parts by Fused Deposition Modeling: From Polymeric Self-Assembly to Reactive Processing

A Dissertation Presented for the

Doctor of Philosophy

Degree

The University of Tennessee, Knoxville

Neiko Phillip Levenhagen

August2019

ACKNOWLEDGEMENTS

ABSTRACT

This dissertation focuses on understanding how the interfacial segregation of low molecular weight polymeric species in a polymer blend impacts the interlayer adhesion and mechanical isotropy of objects prepared by fused deposition modeling (FDM), a widely used additive manufacturing technique. The molecular weight, architecture, and chemical identity of the low molecular weight polymer in the blend dramatically impacts the formation of a robust interlayer interface. An additional modification of the low molecular weight component presents opportunities for reactive processing. The impact of covalent bonds between interfacial layers on the interlayer adhesion and overall isotropy of an FDM printed object is examined.

TABLE OF CONTENTS

LIST OF TABLES

LIST OF FIGURES

Chapter 1 - INTRODUCTION

Additive manufacturing: an overview

Additive manufacturing, colloquially known as 3D printing, has experienced an exponential rise in research dedicated to solving and understanding the technical and material challenges for its broad implementation and adoption in industry.[1] Compared to traditional subtractive techniques such as milling, casting, and forming, additive manufacturing utilizes a bottom-up approach where the desired part is formed in a layer-by-layer fashion.[1] This holds a distinct advantage to subtractive techniques in that there is no requirement for expensive molds and forms, minimal waste of material, and very complex geometries can be achieved.[2] Additionally, additive manufacturing can be utilized for a number of materials including both metals and polymers.[3] In additive manufacturing, a computer aided design program (CAD) is utilized to model an object. This designed part is then sliced into 2D stereolithographic layers by a program such as Slic3r™. The sliced file is then exported as a generated .gcode file which inputs all the commands into the 3D printer. This process is extremely streamlined and makes additive manufacturing optimal for rapid prototyping and for visualizing designs in three dimensions. As such, additive manufacturing has gained a significant foothold in many industries, such as automotive and aerospace, as a prototyping tool.[4] Because of the high precision of additive manufacturing technologies, it has also become a useful tool in the medical industry. Additive manufacturing technologies allow doctors to design and develop prosthetics, implants, and cell scaffolds that can be tailored precisely for each patient.[5–9]

The term additive manufacturing is a broad term that covers a plethora of different techniques that are often split into several categories such as vat

photopolymerization, powder bed fusion, material extrusion, material jetting, binder jetting, and direct energy deposition.[10] These broad categories include selective laser sintering (SLS), stereolithography (SLA), direct light processing (DLP), and fused deposition modeling (FDM). Of the many additive manufacturing techniques, these technologies are the most common in the 3D printing of polymer materials.[2] In SLS, a powder bed fusion type technology, a laser rasters over a bed filled with polymer or metal powder. The areas irradiated by the laser are then selectively sintered to form a cohesive part. The bed is lowered, and the powder recoated for each subsequent layer until the final part is achieved. Another additive technology, SLA, is a vat photopolymerization type technique. In SLA, a light source, often UV or visible, rasters over a pool of polymer resin. In areas illuminated by the laser, a crosslinking reaction occurs solidifying the layer in the desired shape.[3] Depending on printer design, the shape may be lowered into the resin to build subsequent layers or pulled from the resin.[11,12] Similarly, DLP interacts with a pool of resin; however, an entire image representing a layer is flashed on the resin.[13] While these techniques are extremely powerful in producing high fidelity parts, the optics, limited material options and equipment requirements for these machines make them expensive and difficult to scale.[2]

The FDM additive technique overcomes these limitations by utilizing a simple extrusion-based nozzle affixed to a gantry. More specifically, a polymer filament is passed through a heated nozzle to melt or soften the polymer. This molten filament is then laid onto a build platform in a layer-by-layer format (Figure 1.1). The relative simplicity of the extrusion nozzle and gantry system makes it easy to scale and the most versatile in terms of available print materials.[14] Common print materials incorporate a

variety of commercial engineering plastics such as acrylonitrile-butadiene-styrene (ABS), poly(lactide) (PLA), polycarbonate (PC), and nylon.[3] For these reasons, it is the most widely adaptable and economical additive technique.[2] While extremely versatile and adaptable, there exists a number of challenges for its broad use and implementation in industrial applications. The most pronounced of these challenges is the observed mechanical anisotropy of printed parts.[15–20]
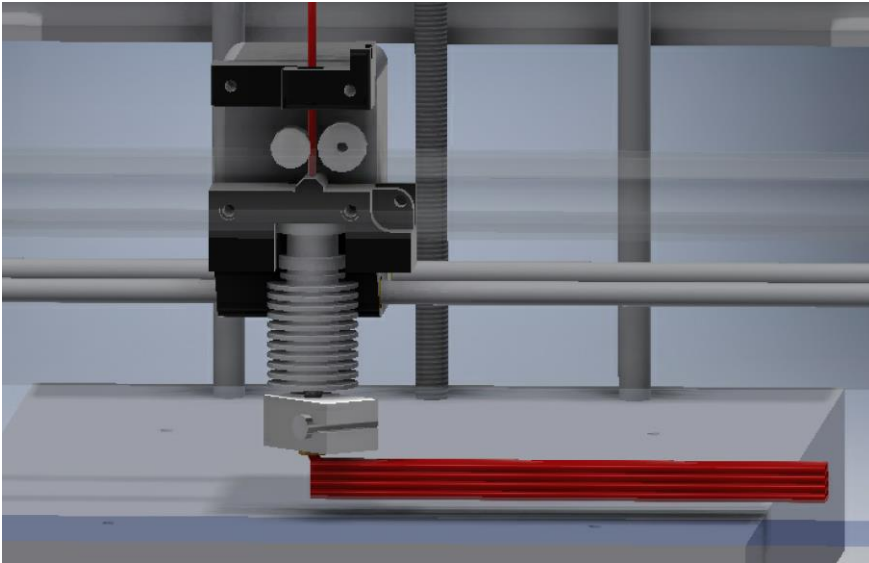
Figure 1.1 Fused deposition modeling (FDM) extruder design

Anisotropy in fused deposition modeling (FDM)

Anisotropy is defined as having directional dependent properties and often occurs in metals, minerals, and polymers. Anisotropic properties may be mechanical, thermal, electrical etc., and is the opposite of isotropy where properties are independent of direction.[21] For FDM, the directional dependence of the observed mechanical properties arises from the poor interlayer adhesion of adjacent layers during the deposition process.[22–24] A necessary requirement of the deposition process in FDM is the formation of interlayer welds between adjacent filaments. These interlayer welds directly impact the mechanical properties of the final printed object.[25–29] As highlighted by Q. Sun et al. in Figure 1.2, bond formation in FDM occurs in essentially three steps. First two filaments make surface contact. Second is the coalescence of the two filaments leading to neck growth. Finally, the molecular diffusion of chains in adjacent layers and entanglement leads to a welded interface. For FDM, the polymer is extruded at the print nozzle temperature and then rapidly cooled, on the order of seconds.[30] Subsequent passes of the nozzle can then reheat the previous layers above the glass transition temperature, T_g.[31] As a result of this complex heating profile, polymer chains in adjacent layers may continue to diffuse and entangle across the interface even after the initial deposition.[16] Despite this, the diffusion and entanglement between adjacent layers is incomplete and poor interlayer adhesion results. Ultimately, the complex thermal profile of the deposition process coupled with the poor diffusion of chains between layers results in mechanical properties that are dependent on printed part orientation, and thus anisotropic mechanical properties are observed (Figure 1.3).[2]
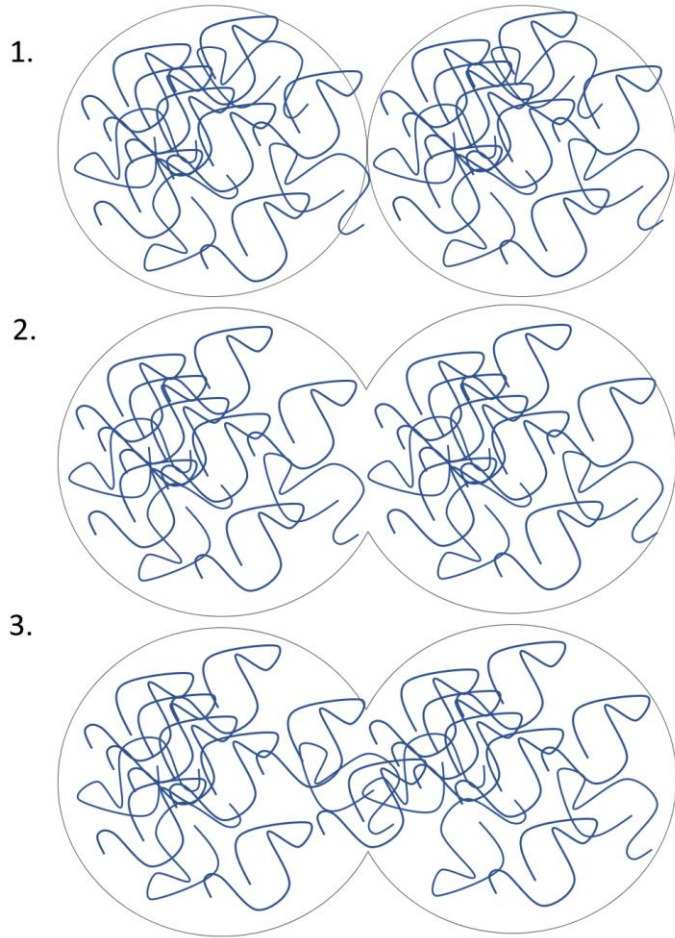
Figure 1.2 Bond formation in FDM printed parts (1) adjacent filaments contact (2) necking of adjacent filaments (3) interdiffusion and entanglement of adjacent filaments.

Different mechanical
properties observed

Adhesion at the interface
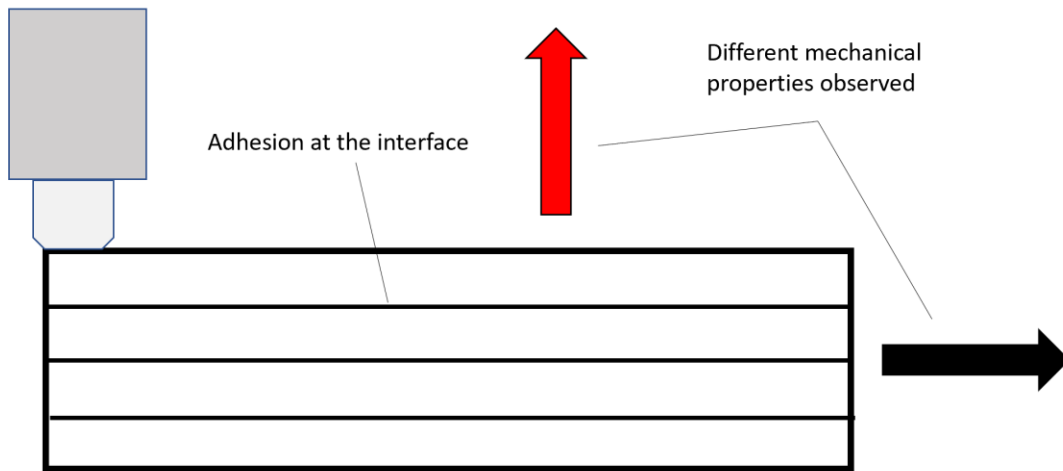
Figure 1.3 Anisotropy in FDM

For these chapters and much of the available research, two print orientations are often utilized to probe this anisotropic character. The first is the longitudinal print orientation. This orientation describes the properties along the print axis. Moreover, it describes the properties of entangled chains within a single filament. The second print orientation is the transverse orientation, which is orthogonal to the longitudinal orientation and is highly dependent on the interlayer adhesion of neighboring layers (Figure 1.4). Much research has elucidated the different mechanical properties observed between these print orientations.[15,16,19,32] For example, Sung-Hoon Ahn et al. studied the directional dependence on the tensile strength of FDM printed ABS,[16] where tensile strength is the measure of how much force per unit area is required for part failure.[33] These studies found that samples printed in the transverse orientation, across the filament, exhibited tensile strengths nearly 85% weaker than the longitudinal orientation.[16] The work presented in the next Chapters will expand on these findings and attempt to provide molecular-level insight into the design of materials that can mitigate the anisotropy in FDM printed parts.

In order to address and minimize anisotropy in parts prepared by FDM, a number of methods have been utilized.[26,34–37] Of these, the most common is to modify the print parameters.[38–42] In this way parameters such as print temperature, filament overlap, infill direction, and print speed are modified to optimize filament to filament interaction and promote adhesion.[17,43] Print temperature is a vital component to consider and is one of the easiest parameters to modify to improve the flow and diffusion of polymers between layers. Unfortunately, the rheology or complex material flow properties of polymers are non-trivial. Increasing the temperature does not necessarily lead to a reduction in
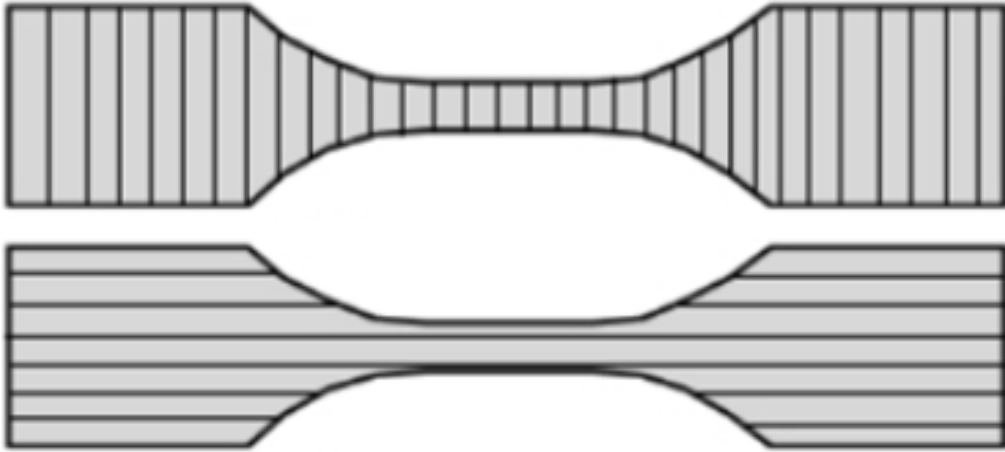
Figure 1.4 Raster orientations for D638-V tensile specimens (top: transverse, bottom: longitudinal)

viscosity and therefore does not necessarily translate to better flow.[44] Likewise print speed is tuned to allow more time for the polymers to extrude from the nozzle and entangle with adjacent layers, yet the rapid cooling of layers prevents sufficient entanglement to eliminate anisotropy. Additionally, parameters like filament overlap serve as a physical means to increase the amount of filament to filament interaction during a print but again does not address the rapid cooling of layers and the necessity for polymers to diffuse and entangle between layers. Lastly, the infill pattern, or the way the printer fills in the printed object, is utilized as a physical means to minimize anisotropy. By alternating the directional orientation of a printed filament, visualize a cross-hatched pattern, the isotropy of the print can be improved. However, this methodology still ignores the necessity of chain entanglements between layers and therefore the observed mechanical properties of the layer adhesion only modestly improved.[45]

Recent research in this area has utilized computer modeling to generate optimum printing parameters, including printing temperatures and infill patterns, to maximize the structural integrity of printed parts.[14,26,29,46–48] The research provides invaluable data in reducing anisotropy by mechanical means, but a closer investigation of the molecular level interactions of chains in adjacent layers is necessary. As described earlier the entanglement of polymer chains in adjacent layers is a vital step to producing robust welds between layers. It is, therefore, beneficial to address the problem of anisotropy from a molecular level. Furthermore, it is necessary to optimize chain interaction in adjacent layers under typical print conditions and temperatures. To do this, the following chapters exploit the thermodynamic differences of short polymer chains relative to their large and bulky counterparts.

Surface segregation of low molecular weight polymers in polydisperse melts

The research presented in the following chapters is founded on the idea that lower molecular weight (LMW) polymer chains diffuse more readily than their high molecular weight (HMW) counterparts. Additionally, the low molecular weight chains entropically favor the interface. By utilizing this behavior, an increase in the interfacial strength of adjacent filament beads, and thus a more substantial bond may be achieved. It is of great benefit then, to delve into the thermodynamic principles and current literature that elucidates these phenomena and guides the ideas presented.

First, when discussing an entropic driving force for low molecular weight polymer chains to the interface, it is important to understand what affects entropy. Entropy is a thermodynamic measure of the number of microstates a system can achieve and changes in entropy define the energy not available for work during a thermodynamic process. In other words, it is a measure of the randomness of constituents or the molecular disorder. When describing the entropy of a polymer, it is the number of conformational arrangements the chain can achieve in a given system that dominates its entropy. Inherently, the number of these arrangements is based on the number of segments of the chain. Therefore, the more segments in a polymer chain, the more conformational arrangements that can be obtained. This ultimately increases the entropy of the system.[50] In the polymer matrix proposed in subsequent Chapters, we are describing two regions of the filament; the bulk and the interface of the filament bead. In the bulk, a polymer chain is free to move in any direction and therefore is free to obtain all its conformational states. At the interface, the chain is now limited in the number of conformations it can take, leading to a reduction in the entropy. This penalty to the

entropy is minimized when the chain is shorter, as there are fewer segments. At the

surface, the system will minimize the surface free energy which is thermodynamically

favorable. Utilizing the fundamental relationship

$$\Delta G = \Delta H - T\Delta S$$

Equation 1.1

where ΔG is the free energy of the interface, ΔH the enthalpic contribution to the

free energy, T absolute temperature and ΔS the entropic contribution, it can be shown

that when the entropy decreases the free energy increases. Since, LMW polymer chains

minimize the surface free energy, as there is a smaller entropic penalty, low molecular

weight chains are entropically driven to the interface of the filament. There exists a

number of experimental studies that are in good agreement with this result..[51–59]

Additionally, Demarquette et al studied the effect of MW on surface energy and found

that with increasing MW, surface energy increased.[60] Thus, entropy and a reduction in

surface free energy drove diffusion of the LMW chains to the interface, but we can also

look to more thoroughly understand the diffusion of chains across the interface of

adjacent filaments.

Diffusion of polymers in a melt

In a polymer melt, chains are entangled creating constraints to movement. As

described by De Gennes and expanded upon by Doi and Edwards, the movement of

polymers in an entangled melt can be described by reptation.[61,62] This movement can be

envisioned as a polymer chain being confined to a theoretical tube of some diameter.[63] As

12

illustrated in Figure 1.5, this tube is a result of constraints imposed by adjacent chains in the melt. As a consequence of these constraints, for chains to move, they must move along the tube length, which may be envisioned occurring in a worm-like manner. Directly correlated to the length of the polymer are the molecular weight and the number of entanglements/constraints it has with other chains within the melt.[64] For polymers, a higher molecular weight equals more entanglements and constraints present on the chain. Therefore, chains of low molecular weight have fewer entanglements/constraints than those of high molecular weight. For this reason, under the same conditions, low molecular weight chains move more readily within a melt. Diffusion describes the movement of a polymer chain through a polymer matrix and is inversely proportional to the square of the polymer molecular weight as illustrated in the following equation.[61] In this equation, D is the diffusion coefficient and M is the molecular weight of the polymer.[65]

$$\boldsymbol{D \sim M^{-2}}$$

Equation 1.2

From the equation, diffusion for small polymer chains is much faster than for chains of high molecular weight. Molecular weight is thus a vital factor in the diffusion of polymers between filaments and thus the ability of a chain to form entanglements between filament in FDM.
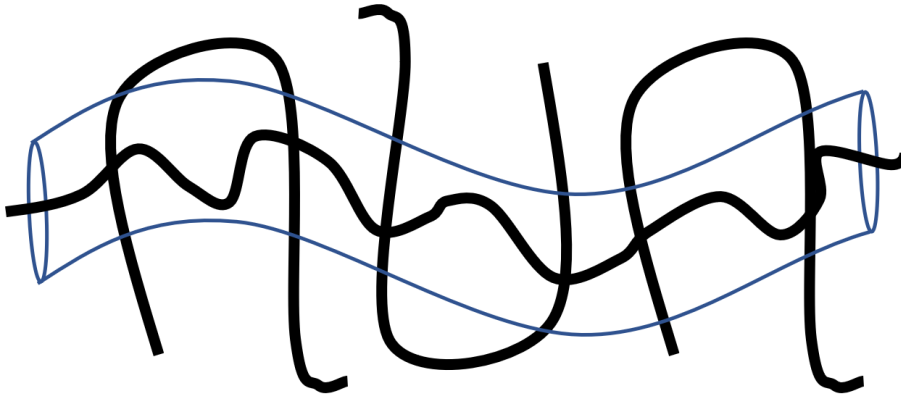
Figure 1.5 Tube model for polymers in a melt

Diffusion of chains across an interface

       Diffusion of the chains within the filament is an important factor to consider, but we also must consider when the next layer is added. For a robust interface to form, the chains need to diffuse into the adjacent layer and become entangled. The diffusion can be described by a modified Fick's first law.[66,67]

$$J_i = - \frac{Dc_i}{RT} \frac{\partial_{\mu_i}}{\partial_x}$$

Equation 1.3

       Here J_i is the diffusional flux ($m^{-2}s^{-1}$), D the diffusion coefficient (m^2/s), c the concentration (mol/m^3), R the universal gas constant ($J/K*mol$), T the absolute temperature (K), and μ the chemical potential (J/mol). The chemical potential gradient arises from the concentration of LMW species at the interface, where the thermal energy provides the mobility to allow diffusion. This fundamentally describes what drives the diffusion, but it is important to also present potential models that may predict the behavior of the system.

       Polymer dynamics, including polymer diffusion, is an active area of research.[67–69] In understanding polymer diffusion, the difference between mutual diffusion and tracer or self-diffusion must be clarified. Mutual diffusion describes how two components diffuse among each other. An example would be the diffusion of sodium ions in water. Tracer diffusion or self-diffusion describes a spontaneous mixing of molecules in the absence of a chemical potential gradient.[70] An example being a polymer melt of polystyrene where

all chains are the same. Our system can initially be described by mutual diffusion because we have two different species i.e. the LMW and HMW components. If we describe the mutual diffusion coefficient as shown in Equation 1.4, we can relate the mutual diffusion coefficient, D_m, to the tracer diffusion coefficient, ultimately simplifying the system.

$$D_M = 2(\chi_s - \chi)\phi_1\phi_2 D_T$$

Equation 1.4

Here χ is the Flory-Huggins interaction parameter, D_T the Onsager coefficient, and φ_i the volume fractions of the *i*th component. Since the polymers are the same in chemical makeup, the interaction parameter $\chi=0$ and the interaction parameter at the spinodal χ_s can be estimated by Equation 1.5.

$$\chi_s = \frac{1}{2}\left(\frac{1}{\phi_1 N_1} + \frac{1}{\phi_2 N_2}\right)$$

Equation 1.5

N is the degree of polymerization of the components. Lastly, we can relate the Onsager coefficient to the tracer diffusion coefficient by Equation 1.6.

$$D_T = \phi_{LMW}D_{HMW}N_{HMW} + \phi_{HMW}D_{LMW}N_{LMW}$$

Equation 1.6

Substituting Equation 1.5 and Equation 1.6 into Equation 1.4 gives us the

relationship between the mutual diffusion coefficient and the tracer diffusion coefficient.

When the volume fraction of the LMW component is low, it is shown that D_m becomes

approximately equal to D_{LMW}.[70] Essentially, the mutual diffusion is dictated by the faster

LMW component. This allows us to follow self-diffusion dynamics and utilize equations

like the center-of-mass diffusion distance (Equation 1.7) to estimate the distance a test

chain would travel under conditions given an experimentally determined diffusion

coefficient.[71]

$$< X^2 cm > = 2Dt$$

Equation 1.7

Here $<X^2cm>$ is the center of mass diffusion distance and t is time. Given the

same conditions, a LMW chain will have a higher diffusion coefficient and travel a

further distance, such as across the interface.

If the interfacial strength is to increase, the interpenetration of polymer chains

from adjacent filaments must be sufficiently large to allow for entanglement to occur.

Thus, it should be expected that if this occurs, the interfacial width should increase.

Previous work by Eastwood et al. has shown that interfacial strength directly correlates to

interfacial width. In other words, as interfacial width increases, interfacial strength

increases. In the study, neutron reflectivity was utilized to analyze the interfacial width of

films compatibilized with a number of blocky copolymers. It was shown that when the

blocks were sufficiently long, they were able to form loops in the adjacent layers and

17

become more readily entangled. This resulted in an increase in the interfacial width and the interfacial strength.[72] Following these guidelines, the LMW chain compatibilized system presented in the following Chapters behave in much the same way. In conjunction with the optimum compatibilization loadings (0.5-10 wt.%) as reported in the literature, optimum improvement in the interfacial strength may be achieved.[73,74]

Thus, at low loadings, diffusion is dictated by the LMW chains. LMW chains diffuse faster than the HMW chains which allows greater interpenetration to entangle. More entanglement and greater interpenetration of chains leads to a broadening of the interfacial width and ultimately an increase in the interfacial strength. Thus, utilizing a bimodal system with a LMW chain, as a compatibilizer, allows the formation of a stronger interface and a more isotropic printed part. It is important to note that the above systems deal with isothermal conditions. In the FDM deposition procedure, there exists a temperature gradient which will not follow precisely the dynamics shown above; however, the above principles provide a guideline to follow and utilize to semi-empirically predict the improvements that are seen with the bimodal system.

The diffusion of star-shaped polymers in a melt

In the previous sections, the dependence of surface segregation and diffusion on molecular weight was described in detail. As will be introduced in Chapter 3, another factor to consider is the architecture of the polymer chain. Polymer chains consist of many repeating segments, but the way these segments are connected can vary. Figure 1.6 illustrates a number of different architectures for polymers, ranging from linear architectures to more exotic architectures including graft and star-shaped polymers. As can be imagined, the architecture has a significant impact on the observed properties and

Linear polymer

Star polymer

Cyclic polymer

Graft polymer
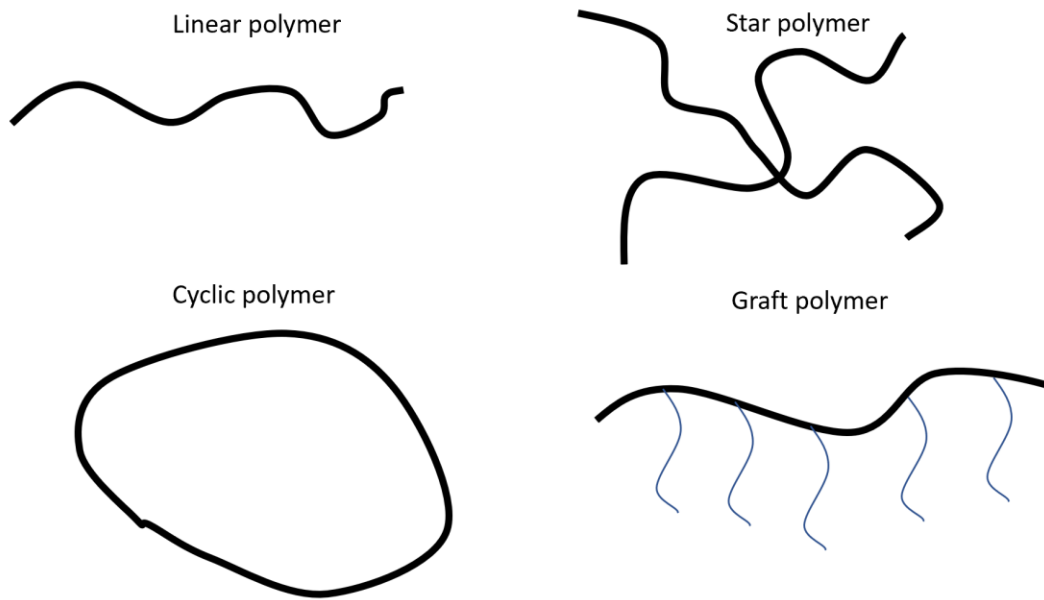
Figure 1.6 Various polymer architectures

dynamics of the polymer including number of entanglements, entropic considerations, and diffusion. In Chapter 3, low molecular weight star type architectures are introduced and their behavior is compared to that of linear polymers as a means to further understand and improve the interlayer properties of FDM printed objects.

Star-shaped polymers are distinct from linear polymers in that they contain a central branch point. This central branch point imposes additional constraints to the polymer motion. A major consequence of this additional constraint is that stars do not follow traditional reptation diffusion dynamics.[75] Instead, we can envision a polymer star where each branching arm has its own tube. Since they are intimately tied by the central branch point, movement by reptation would require retraction of its arms back along the tube. For many armed stars (>4) this process is prohibitive because of the number of arms that need to retract. For high ordered stars diffusing in a star matrix, the movement is therefore only possible when other constraints are released or tube dilation occurs as a result of dynamic dilution of the retracting free arm.[76,77] Diffusion of entangled stars is, therefore, slower than linear polymers of similar MW. For entangled stars in a linear matrix, the constraint release mechanism is the primary mode of diffusion as the linear chains will relax at faster times than the stars.[76,78–80] For most cases then, entangled star polymers diffusing in themselves or in a linear matrix is slower than a comparable linear chain diffusing in a linear matrix. However, in between linear and many arm stars exists a unique transitional point, 3-arm stars, where traditional reptation is possible in stars.[80] For 3 arm stars, only one arm needs to retract to obtain a pseudo-linear conformation. At this point, the star may follow traditional reptation dynamics similar to a linear polymer of the same molecular weight.[78]

The central branch point not only affects the diffusion of polymer stars but also impacts the number of conformational states the chain may obtain. As described earlier this is directly correlated to the entropy of the system. Since the central branch point is an added constraint, a star polymer cannot obtain as many conformational arrangements as a linear polymer of the same molecular weight. Therefore, star polymers experience a preferential entropic driven segregation to the interface. This phenomena is observed in many self-healing materials where exotic architectures like cyclic, star and graft type polymers are shown to preferentially migrate to the interface to repair the damage.[81–84]

UV initiated crosslinks in polymers and reactive processing

Chapter 5 introduces ultraviolet (UV) light reactive processing as a means to introduce covalent crosslinks between layers during the print. Covalent crosslinks in polymers are well-known to increase the strength and toughness of materials.[85–88] Crosslinks formed between filaments will, therefore, lead to substantially more robust interfaces with nearly isotropic properties observed for the printed objects.

The use of UV to induce crosslinks in polymers has been readily utilized in industry to cure everything from high molecular weight polymer epoxies to hydrogels.[89–94] In many of the hydrogel systems, polyethylene glycol (PEG) or similar polymers are terminated with acrylate or methacrylate functional groups.[91] The addition of a radical generating photoinitiator in the presence of UV light creates a radical-radical coupling reaction between two acrylate moieties which crosslinks the polymer.[90] These crosslinks increase the polymer's toughness and strength.[95] The coupling reaction in these UV systems is known to occur quickly and completely but studying the factors that influence the reaction is important to understanding its use within printing applications like FDM.[96]

As mentioned above, the reaction proceeds via the generation of a radical provided by a photoinitiator excited by UV light. Subsequently, the radical attacks the carbon-carbon double bond of a nearby acrylate group. The crosslinking event that occurs may happen by two pathways. One path is the coupling of two radicalized acrylate functional groups to terminate the reaction. In another case, the radical bearing acrylate group may attack another acrylate and polymerize before termination.[97] By either termination mechanism, a crosslinked network may form. Due to its high reactivity, the acrylate group is shown to react very quickly. Research into the photocuring of acrylates report full cures achieved in approximately 60s with a conversion of about 98%.[96] This high rate of reaction and high conversion makes the photocuring of acrylates and their derivatives a prime candidate for FDM applications. A common issue with acrylate systems are their sensitivity to oxygen. In these systems oxygen acts as a radical scavenger.[98] With ambient oxygen present, it has been shown that acrylates will polymerize slower, reaching about 87% conversion after 1 min of exposure to UV.[96] Thus, when translating this type of system to an FDM print application, it must be considered that oxygen present during the build may inhibit the reaction. As discussed earlier, the interface that forms between filaments requires sufficient mobility of chains to allow diffusion and entanglement between adjacent layers. If we consider that crosslinks inhibit diffusion between layers as chain mobility is hindered when crosslinks form, then a high conversion of the acrylate is not necessarily desirable in FDM applications. Therefore, the inhibition by oxygen may be beneficial by allowing chains adequate time to diffuse across the interfilament interface and entangle before the crosslinking of the acrylate functional groups occurs. This ultimately highlights the necessity to balance

chain mobility and the immobilization of chains during crosslinking to optimize the interlayer strength.

For UV cured systems, the reaction proceeds by radical formation and subsequent reaction. Under a typical free radical polymerization or reaction, the concentration of the radical generated dictates the probability a reaction will occur. A reaction can occur only when a radical is generated and a radical and a nearby acrylate interact. Therefore, we must consider over the time of the print that a layer may go above and below T_g multiple times, that there must be a sufficient number of radicals produced and sufficient mobility of acrylate end groups to interact with the initiating radical, and an adjacent acrylate for a crosslink to form. From the previous discussion, the addition of low molecular species to a blend should result in improvements to the interlayer adhesion by improving the diffusion between adjacent filament layers. By attaching an acrylate functional group to this additive, we may introduce the crosslinking reaction; however, the high rate of reaction of the acrylate functional group may prove problematic by reacting too quickly and immobilizing the polymer chains before diffusion and a robust interlayer interface form. Therefore, we will utilize a slower rate of reaction by attaching the methacrylate moiety. Utilizing the slower reaction rate should allow adequate diffusion and entanglement of chains before the polymer flow is inhibited by crosslink formation.[96]

Additional control of this reaction to promote the diffusion of chains between layers followed by crosslinking, is possible with control of the concentration of radicals being generated. This can be realized by adjusting the intensity of the UV source. The rate of radical generation is directly dependent on spectral photon flux (I_0) which is a

function of the intensity of incident light.[99] Therefore, by adjusting the incident UV intensity, the rate of radical generation can be controlled to optimize the mobility of chains in adjacent layers and the crosslinking reaction that greatly inhibits mobility.

Thus, in the reactive LMW-SuSA systems presented in Chapter 5, the polymers are modified such that the end groups of the poly(lactide) chains are replaced with reactive methacrylate groups. In a similar fashion to the hydrogel systems, the UV irradiation of the polymers during the print process in the presence of a radical generating photoinitiator should provide conditions that promote a crosslinking reaction between chains in adjacent layers. Additional control of the UV intensity should allow the optimization of both interlayer diffusion and entanglement with crosslinking occurring simultaneously. As a result, substantially increased interlayer adhesion may be realized with FDM printed parts. Thus, the application and introduction of UV crosslinkable blends provides a platform to further optimize and improve the layer adhesion and reduce the anisotropy in FDM.

Low molecular weight surface segregating additives to reduce anisotropy

In summary, additive manufacturing presents many unique and exciting opportunities to improve the production and development of parts on an industrially relevant scale. Specifically, extrusion-based techniques like FDM are easy to scale and modify to fit the specific needs of an application. Furthermore, the numerous printable polymers available and complex geometries that are attainable by FDM make it a prime candidate to be implemented and integrated into the industrial space. However, the mechanical inferiority of parts printed by FDM and the anisotropic properties observed are detrimental to broadening the use of FDM as an industrial tool. Thus, there is a need

for a concerted research effort to address and minimize anisotropy in FDM printed parts. As discussed, the anisotropic mechanical properties observed in parts printed by FDM result from the slow diffusion and limited entanglement of chains in adjacent layers. It is therefore conducive to probe and understand how modifying the structure of the polymer chains may influence and promote improved diffusion and entanglement. Given the relative simplicity of altering the molecular weight of a polymer or changing its architecture, the introduction and utilization of low molecular weight polymers and their bimodal blends presents an promising area of study to develop scalable methods to improve interlayer adhesion in FDM. Under the same printing conditions of the neat material, LMW-SuSAs will be entropically driven to the interface where they may more readily diffuse between adjacent filaments over that of longer and bulkier polymer chains. Additionally, when of sufficient length, they should readily entangle with chains in adjacent layers and thus form a more robust interlayer interface.

There is therefore a need to understand the important parameters that dictate the ability of LMW-SuSAs to improve inter-filament adhesion in FDM and decrease anisotropy in printed parts. Parameters that must be optimized include the LMW-SuSA molecular weight, concentration, and architecture to provides fundamental insight into how and when these low molecular weight species may beneficially improve the interface. Further, this parameter space provides insight into how these additives may lead to the formation of strong interlayer interfaces and provide FDM printed objects that are mechanical robust and isotropic. Further modification of the additive end-groups presents the opportunity to develop methods to incorporate reactive processing in extrusion-based 3D printing, where the introduction of covalently linked chains between

layers can open new pathways to more robust and isotropic 3D printed samples. Crosslinks between layers should lead to superior interlayer properties over that of the neat material and further optimize the utilization of LMW-SuSAs within the FDM space. The following chapters describe our research in this area and provide guidelines needed to develop more robust and mechanically isotropic parts by extrusion based 3D printing.

Chapter 2 - BIMODAL MOLECULAR WEIGHT SAMPLES IMPROVE THE ISOTROPY OF 3D PRINTED POLYMERIC SAMPLES

ABSTRACT

Parts prepared by the fused deposition modeling (FDM) 3D printing process suffer from poor interfacial adhesion between layers. This is due to poor diffusion of the very large and slow polymer chains across the inter-filament interface. To address this issue, we have developed the use of a bimodal blend of poly(lactide) (PLA) comprised of a series of synthesized low molecular weight PLA components (8.5k, 50k, and 100k) added to a commercially available PLA (220K). Tensile testing results indicate that when the LMW additive is of a sufficient length, the maximum stress and modulus in the part printed orthogonal to the print head (transverse) is significantly improved. More specifically, this behavior is observed where increased diffusion and increased entanglement of chains across adjacent layers occurs. The extent of crystallization at various stages of processing is also analyzed and indicates no correlation between the mechanical properties obtained and the extent of crystallinity.

INTRODUCTION

Fused deposition modeling (FDM) has been used as a rapid prototyping technique for many years and has achieved large commercial success. It has often been used to model prototype designs for cars[100], medical prostheses[101], buildings[102] and many other design processes.[19] While it has been a great tool for prototype modeling, a desire to expand the technique to build structural and functional parts has come with a number of problems.

In FDM, a hot extruding end melts polymer onto a build platform in an XYZ coordinate system. The model is created via a computer-assisted design program (CAD) and then sliced into layers which the printer reads.[16] In a common set up, the printer

28

controls the motors which move the head (XY) or the bed (Z) to build a 3D model layer by layer.[41]

Due to the stratified nature of the printing process, it has been shown that the mechanical properties of the print are dependent on the print orientation (Figure 2.1).[72,103,104] Depending on the print orientation, different mechanical properties are observed. As shown by Ziemian and coworkers, tensile measurements performed on specimens printed in various orientations show that when stress is applied along the filament (longitudinal), the modulus is significantly higher than when stress is applied perpendicular to the filament (transverse).[15] These experiments highlight the fact that parts prepared by the FDM method suffer from poor interfacial adhesion between layers which introduces anisotropic mechanical properties.[16,19,105] More precisely, significantly different mechanical properties are observed with respect to the orientation of the printed part to the print head.[48] To address these problems and to create more robust 3D printed objects, extensive research into FDM printed objects has studied the effect of printing parameters on the mechanical properties. Some of these parameters include raster orientation, filament to filament air gap, and layer height. Other parameters such as print and bed temperature have additionally been studied.[16,45] The focus of such studies has relied primarily on optimizing the properties of an FDM print through the adjustment of the printing parameters; however, little research has been presented that examines the entanglement of polymer chains at the interface or how controlling the level of
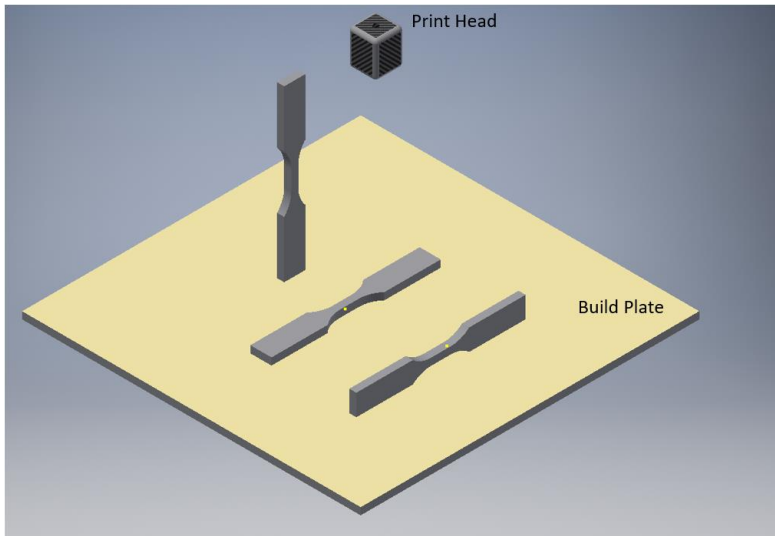
Figure 2.1 Illustration of the different build orientations possible for the same tensile specim

entanglement can impact material properties. In the standard printed part, diffusion of polymer chains across the inter-filament interface is slow.[67,71] Poor diffusion across the interface leads to less entanglement of chains between layers and poor interlayer adhesion.

It is well known that small polymer chains diffuse more readily than their large counterparts.[106] Additionally, it is entropically favorable for these small chains to preferentially migrate to an interface, such as the outer surface of a filament.[51,60,70,107,108] Utilizing this chemistry and these thermodynamic principles, bimodal blends can be prepared that incorporate a smaller, but identical polymer chain to that of the starting filament. Under the same printing conditions of the neat printed samples, the presence of the low molecular weight (LMW) chains improves entanglement across layers as they more readily diffuse across the filament interface. If the LMW chains are of a sufficient length, chain entanglement between layers increases. Thus, an improvement in interfilament adhesion and a more isotropic printed part should result. In the research presented, a model study of these principles is tested by 3D printing bimodal blends created by the addition of a synthesized poly(lactide) (PLA) at various low molecular weights and loadings to a higher molecular weight commercially available PLA. Tensile specimens were printed and used to quantify the improvement of the interfacial adhesion and the structural isotropy of the sample. Moreover, these experiments show that, with the proper molecular weight and loading of the additive, a significant improvement in the interfacial adhesion is obtained. The role of the change in the crystallinity of the samples with the addition of the low molecular weight material, and its role on the properties of the printed sample will also be discussed.

EXPERIMENTAL SECTION

Materials

NatureWorks Poly(lactide) 4043D pellets (4043D, Filabot, Barre, VT), DL-Lactide (DL-LA, Fisher Scientific), Isopropanol (iPrOH, Fisher Scientific), Stannous Octoate (Sn(Oct)$_2$, Sigma Aldrich) and Toluene (Fisher Scientific) were used as received. All glassware and magnetic stirrers were stored in an oven at 110 °C and cooled before reaction.

Synthesis of 50k low molecular weight poly(lactide) (PLA)

To a 2-neck round bottom flask was added 12.6330g of DL-LA, 30μL iPrOH, 141μL Sn(Oct)$_2$, and 30mL of Toluene. The reaction vessel was equipped with a condenser and purged under nitrogen for 5 minutes and the reaction was refluxed under N$_2$ atmosphere for 4 hours. The resulting PLA was precipitated into cold, stirring hexanes and redissolved into methylene chloride. Methylene chloride was evaporated and PLA dried at 90 °C under vacuum for 24hrs prior to use. 8.5k and 100k PLA molecular weights were prepared analogously. Molecular weight characterization was performed by gel permeation chromatography (GPC) on a Tosoh EcoSEC equipped with a refractive index (RI) detector. All molecular weights are presented relative to a calibrated polystyrene standard. (GPC chromatograms may be found in the Appendix Figure S2.1-S2.4.)

Preparation of bimodal PLA blends

4043D pellets and low molecular weight (LMW) synthesized PLA were dried under vacuum prior to use. Bimodal blends that consisted of the parent NatureWorks 4043D PLA (M$_w$- 220k) and one of three molecular weights (M$_w$- 8.5k, 50k, and 100k) of

the LMW additive were prepared at loadings of 3, 10, and 15 mol%. Blends were prepared by mechanical mixing in a Filabot Original™ single screw extruder. The filament was extruded at 160-165 °C, depending upon LMW added, to a diameter of 2.85+/- 0.1mm.

ASTM D638-V tensile and T-peel specimen fabrication

All tensile specimens were cut, using a desktop scroll saw, from a cube that was printed by FDM on an unenclosed LulzBot TAZ 5 3D printer with a 0.5mm nozzle. All cubes were printed with 233 layers at a layer height of 0.3 mm and the same print speed of 60 mm/s. The cube was sliced using Slic3r™ and the .gcode was compiled using Repetier-Host. Specimens were cut from a printed cube to ensure that each sample was exposed to the same thermal history and to ensure every filament fiber was oriented in the desired direction. The extruder nozzle was heated to 190 °C and the build platform heated to 70 °C. Tensile bars that follow the ASTM D638-V standard were prepared from the printed cube by cutting the dogbones such that the direction of applied stress is in the longitudinal and transverse orientation relative to the filament (Figure 1.4). To maintain a statistical average, six specimens were prepared for each molecular weight and loading. T-peel specimens were printed such that the layers were parallel to the print bed. The T-peel specimens were printed with 133 layers utilizing the same print conditions as the tensile measurements. Upon cutting the samples into dogbones or printing into T-peel geometries, the tensile properties were determined on an Instron™ universal testing machine equipped with a 100kN load cell and wedge action grips. Tensile measurements were carried out at an extension rate of 1.00 mm/min with 20% sensitivity.

Scanning electron microscopy image analysis

The void space between filaments of neat PLA printed samples were imaged using a Zeiss Auriga Scanning Electron Microscope equipped with an Everhardt-Thornley SE2 detector. Due to charge build-up issues with the Neat PLA samples, the remaining were imaged using a Zeiss EVO MA15 SEM with variable pressure and a Bruker eFlash Electron Backscattered Detector.

Crystallization studies of prepared PLA bimodal blends

Samples were obtained before single screw extrusion, after single screw extrusion, and after printing. Melt temperature (T_m) and crystallization temperature (T_c) were determined from the heat flow measured on a TA Instruments Q-2000 differential scanning calorimeter. Thermal control of the samples was implemented using a cyclic program in which the sample was heated from 10 °C-180 °C with a ramp rate of 10 °C/min and then cooled at a rate of 20 °C/min.

RESULTS AND DISCUSSION

Quantifying inter-layer adhesion

To directly monitor inter-layer adhesion between filaments, and quantify the extent to which the addition of the low molecular weight additive improves the strength of these interfaces, we initially developed and utilized a protocol to monitor inter-layer adhesion in 3D printed samples. This protocol is based on the ASTM T-Peel standard and involves 3D printing the T-Peel specimens and determining the interfacial adhesion between layers using an Instron™ as shown in Figure 2.2. An intentional notch is placed at the interface of two layers to begin crack formation. Tensile

Figure 2.2 T-peel sample during the experiment

stress is measured as a function of extension where the layer strength is determined as the average stress once the stress curve reaches a minimum (Figure 2.3). Furthermore, a value for interfacial adhesion (G_a) is calculated using the following equation:

$$G_a = \frac{F}{W}$$

Equation 2.1

Where F is the force required to separate the layers and W is the width of the layer in meters. In this way, we can monitor the layer adhesion from the peel test of the interlayer interface.

We completed these initial experiments for a neat filament consisting of NatureWorks 4043D PLA as well as two bimodal filaments consisting of the parent NatureWorks 4043D PLA (M_w- 220k) and a 50k molecular weight PLA at loadings of 10 and 15 mol%. It was found that in the neat samples the failure propagated along the interface (Figure 2.4a) resulting in an interfacial strength of ~15MPa. This appears to indicate a weak interface where diffusion and entanglement of polymer chains across the inter-layer interface are poor. Upon testing of the 10 mol% samples, the crack formation did not propagate along the interface and instead was redirected into adjacent layers as seen in Figure 2.4b. Furthermore, this is indicated in Figure 4 where the samples with 10 mol% and 15 mol% LMW additive do not reach a plateau. These samples instead failed at the arms. While this behavior prevents assigning a quantitative value to the interfacial strength in these samples, this is a clear indication of a dramatic improvement in the interfacial adhesion. It would appear that upon addition of the LMW additive, layer

36

adhesion becomes significantly enhanced such that the path of least resistance is not along the interface, as in the neat samples, and therefore crack propagation transfers into adjacent layers. To explain this improvement, it would seem that the low molecular weight additive enhances layer adhesion through an *increase* in diffusion and entanglement of chains across the inter-layer interface. The 15 mol% samples behaved in the same manner as the 10 mol% samples and crack propagation transferred into adjacent layers. Additionally, as shown in Figure 2.3 the maximum stress for the 10 and 15 mol% samples is significantly higher than the neat sample indicating more force was required to initiate the crack at the beginning of the experiment even with the intentional starting notch. Ultimately, these experiments provide strong qualitative evidence that the LMW additive substantially improves the interfacial adhesion of a 3D printed sample, but a more quantified understanding of this behavior was desired.
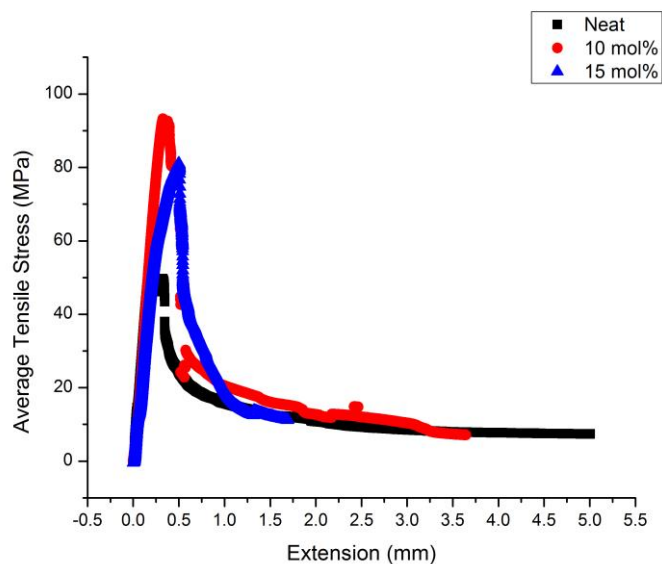
Figure 2.3 Average tensile stress as a function of extension for the Neat, 10 mol%, and 15 mol% 50k LMW blends during the T-peel experiment
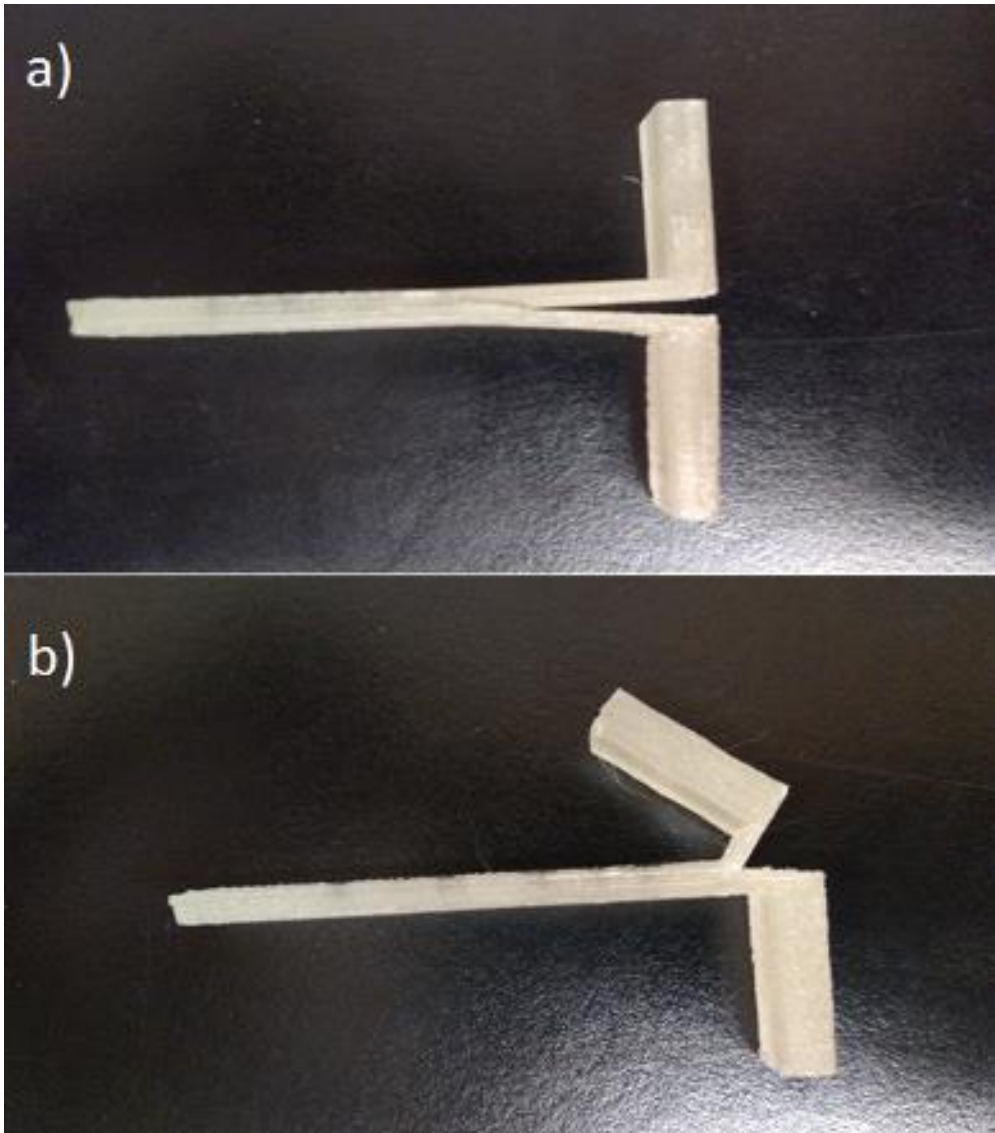
Figure 2.4 (a) Fractured neat T-peel specimen and (b) Fractured 10 mol% 50k LMW PLA T-peel sample

Mechanical testing of printed ASTM D638-V specimens

To better quantify the behavior shown above, mechanical tensile testing of the bimodal blends was performed. Given that 50k is approximately five times the 8.5k entanglement weight, M_e, of PLA the experiment was expanded to include two other molecular weights.[109] The 8.5k MW sample was selected because it is close to the entanglement molecular weight. At this molecular weight, the diffusion of the polymer is fastest, yet chain entanglement may begin to decrease. 100k was selected as it is approximately 10 times M_e and exhibits a large polydispersity (PDI) of 4.3 as shown in Table 2.1. This sample set gives insight into the effect of PDI on the blend's mechanical properties as well. Table 2.2 illustrates the shift in the GPC traces for the 50k blend series with increased loading of the LMW component. The shift to a lower molecular weight, as well as a broadening of the PDI, is consistent with good incorporation of the LMW additive into the bulk material.

Mechanical testing of the tensile specimens provides a quantification of the improvement of interfacial adhesion with the addition of a LMW additive. For all tensile specimens, regardless of blend percentage or molecular weight, the samples failed in a brittle fashion. First, it is useful to compare the tensile properties of an injection molded PLA specimen to those that are 3D printed. As provided by the PLA supplier, NatureWorks™, the technical specifications list a maximum stress value, for the 4043D PLA specimen, of 60 MPa with a modulus of 3.6 GPa using the testing method ASTM D882.[110] According to Prospector™, PLA maximum stress values range from approximately 50-60 MPa and modulus ranges from 2.0-3.6 GPa utilizing the ASTM D638 standard. The samples tested for these experiments reach a maximum stress of 45

MPa and 0.640 GPa for the modulus. While there is a difference in the maximum stress compared to that of an injection molded part, the results presented here match closely to the mechanical properties expected from 3D printed specimens with an average of ~41 MPa for the maximum stress and a reported modulus of 3.2 GPa of a 3D printed PLA specimen.[111] It is important to note that the modulus we report is obtained without a strain gauge, which may explain the large difference in the reported modulus between the literature values for PLA and our specimens. Furthermore, the results presented illustrate that the addition of a low molecular weight additive improves the mechanical properties relative to those of neat 3D printed specimens under the same conditions, towards those of injected molded parts.

Figure 2.5a plots the maximum stress as a function of the percent loading of the 8.5k LMW component. At this molecular weight, regardless of loading and printing orientation, there is a significant decrease in the maximum stress relative to that of the neat samples. At this chain size, the LMW component appears to lack the ability to significantly entangle across the interlayer interface. Ultimately, this hinders the stress transfer, which requires the formation of a highly entangled network and results in failure at low levels of stress. Moreover, Figure 2.5b highlights that with the addition of the 8.5k LMW additive, the moduli in the longitudinal and transverse print orientations become nearly equivalent, demonstrating that the printed parts are now more isotropic. We interpret this to indicate that the diffusion of the 8.5k additive occurs readily during the printing process for all loadings. It is worth noting that the 15 mol% 8.5k sample could not be extruded into a useable filament, presumably because of the lower viscosity of this sample.

40

Table 2.1 Molecular weight distributions for the LMW PLA additives

LMW sample	M_n (x10^3)	M_w (x10^3)	PDI
8.5k	5.9	8.5	1.4
50k	35.6	54.3	1.5
100k	24.2	104.5	4.3

Table 2.2 Blend incorporation of 50k LMW series

Sample	M_n (x10^3)	M_w (x10^3)	PDI
HMW (Natureworks 4043D)	109	220	2.0
3 mol%	87	213	2.4
10 mol%	83	206	2.5
15 mol%	71	194	2.8
LMW	36	54	1.5

Figure 2.5 (a) Maximum stress and (b) Modulus as a function of percent LMW loading and print orientation for 8.5k bimodal PLA blend

In the longitudinal direction, a large drop in the maximum stress is reported with the addition of the lower molecular weight polymer. This again is a consequence of the fact that the LMW chains are of insufficient length to readily entangle. Moreover, the presence of the smaller chains inhibits the entanglement of the large chains throughout the filament. Alternatively, the stress-strain properties of the bimodal filaments fabricated using the 50k PLA are shown in Figure 2.6, which shows that at 10 mol% loadings of the 50k LMW component, the maximum stress in the transverse orientation *increases by 66%* over that of the neat sample. This indicates a substantial increase in inter-layer adhesion. Additionally, at 15 mol% an improvement of approximately 15% is observed (note: Failure occurred consistently within the grips of the Instron for the 3 mol% samples and therefore those results are not reported). The improvement in the maximum stress is interpreted to indicate enhanced entanglement across layers due to the presence of the faster moving, lower molecular weight polymer. At 50k, the LMW chains are sufficiently above the entanglement molecular weight (M_e) such that they readily entangle, but the MW is not so high as to hinder the diffusion of the LMW chains across the interface during the printing process. Inspection of the moduli of the samples with 50k PLA in Figure 2.6b shows that these samples behave similarly to the 8.5k LMW samples, where the addition of the lower molecular weight chains produces a more isotropic sample. Additionally, a ~10% improvement in the modulus is observed for the 10 mol% 50k sample and a ~1% improvement for the 15 mol% 50k sample, further indicating an improvement in the interfacial adhesion. More importantly, the samples with 50k additive dramatically improve the interdiffusion of the polymer chain across the layer, indicating a beneficial plasticizing effect, which results in an improvement in the

43

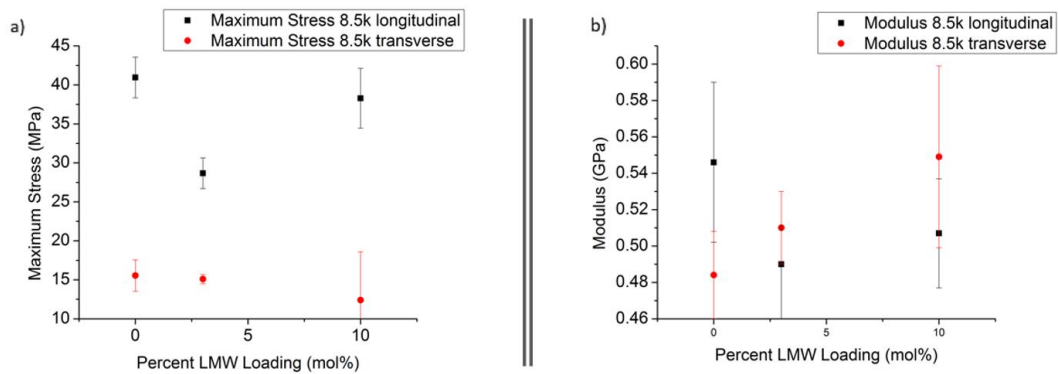**Figure 2.6 (a) Maximum stress and (b) Modulus as a function of percent LMW loading and print orientation for 50k bimodal PLA blend**

layer adhesion. It is interesting to note that the 15 mol% sample exhibited a lower maximum stress and modulus than the 10 mol% sample. This could be because at high concentrations of the LMW additive, the properties are diminished due to excess LMW species at the interface. The lower molecular weight material results in fewer entanglements, which manifest as a lower maximum stress and modulus for both orientations of the 15 mol% sample relative to those of the 10 mol% sample. It appears that it is vitally important that selection of molecular weight and loading balance the plasticizing effect afforded by lower molecular weight chains with the enhancement in layer adhesion afforded by interdiffusion and entanglement of higher molecular weight chains.

To further illustrate the need for this control, the tensile properties of the 100k LMW series were studied and are plotted in Figure 2.7a shows that the maximum stress in the transverse orientation decreases with the addition of the 100k polymer, indicating that interfacial adhesion is actually hindered by its presence. The large polydispersity of the 100k sample leads to a sample in which a large portion of chains are very long (> 430k, which is nearly double that of the neat material) (Figure 2.8). Thus, the presence of these longer chains severely limits the diffusion and entanglement of the polymers across the interlayer interface. Inspection of Figure 2.7b shows the moduli of the sample in the transverse and longitudinal directions are more isotropic and higher than the neat sample. While this would seem to indicate an improvement in the material, this behavior appears to be dictated by the LMW components that are present in the sample. More specifically, diffusion of the polymer across the interlayer interface still occurs via the LMW component yielding a part that is more isotropic and, in this case, larger than the neat

45

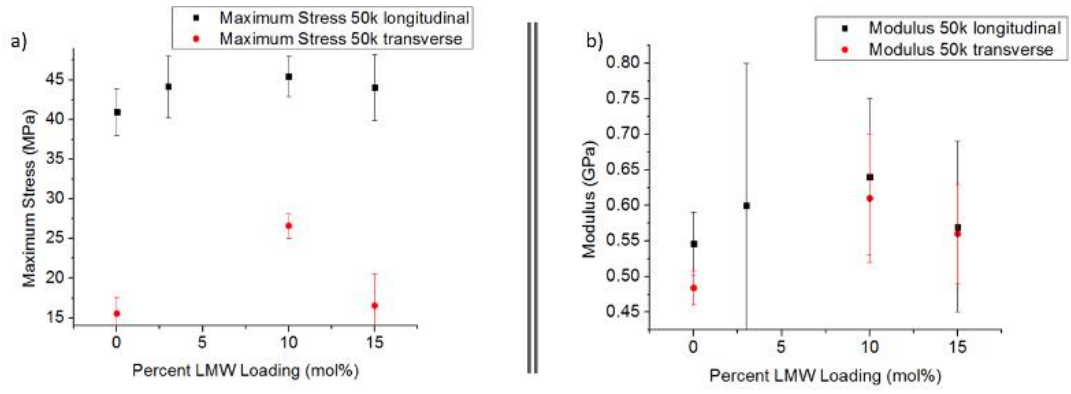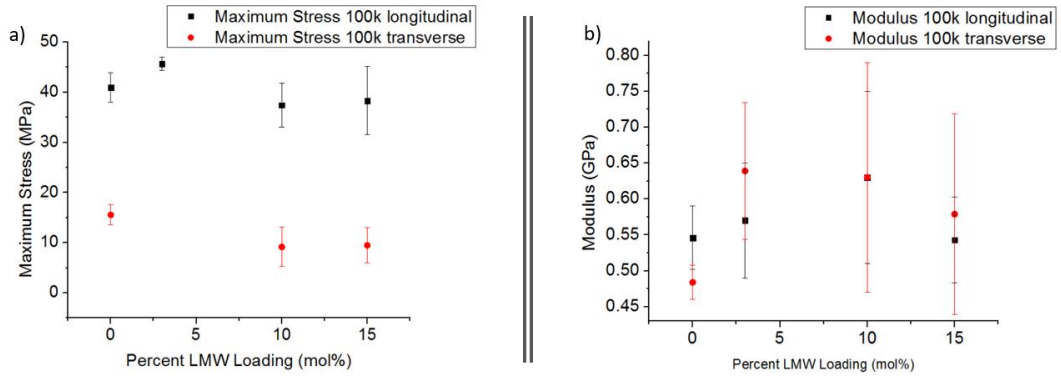**Figure 2.7 (a) Maximum stress and (b) Modulus as a function of percent LMW loading and print orientation for 100k bimodal PLA blend**
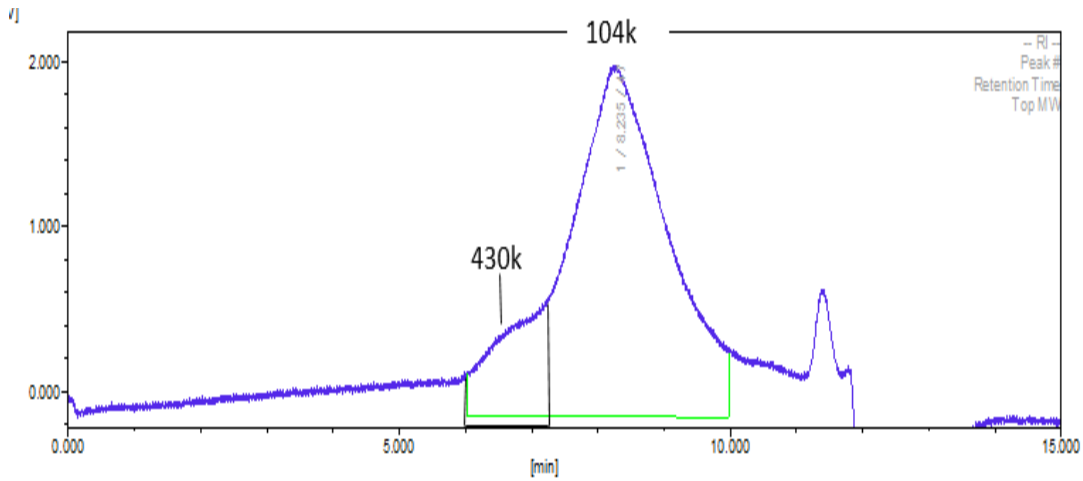
Figure 2.8 GPC chromatogram of 100k LMW component

sample; however, the mechanical behavior is dominated by the high molecular weight fraction, resulting in poor interlayer adhesion. The experiment further indicates the necessity of balancing the plasticizing effect of the LMW chains with the enhancement in layer adhesion afforded by the diffusion and entanglement of the higher molecular weight chains.

The results obtained indicate that optimum conditions that augment both the maximum stress and the modulus are accessible simply by tuning the molecular weights and loadings of the LMW component. As discussed above, the 8.5k series exhibits a decrease in the maximum stress in both print orientations due to the presence of the low molecular weight, which translates to poor entanglement at the inter-filament interfaces. Additionally, the modulus decreases to 0.5 GPa but becomes more isotropic. This behavior indicates that the 8.5k LMW additive readily plasticizes the filament which translates to isotropic properties but is not large enough to increase the entanglements at the inter-layer interface. On the other extreme, the addition of the 100k LMW material to the filament results in less desirable properties. The maximum stress in the transverse direction decreases with added 100k PLA, due to the slow diffusion of the higher molecular weight chains in this broadly distributed sample, maintaining a weak interface. As with the samples with 8.5k additive, the samples with 100k LMW chains create an isotropic modulus that fluctuates around 0.6 GPa. The ability of the lower molecular weight fraction of the 100k additive to plasticize the sample is exacerbated by the presence of the HMW components in the blend, which hinder diffusion of chains that could potentially entangle across the interface. Lastly, the samples with the 50k additive series exhibit an *increase* in the maximum stress indicating a significant increase in the

interfacial adhesion, unlike the other tested samples. Furthermore, an isotropic modulus of ~ 0.6 GPa is observed above 10 mol% of the 50k LMW polymer. Thus, it appears that the 50k LMW additive is optimal for the systems studied, as it offers both an improvement in interfacial adhesion and an isotropic modulus. These results, therefore, verify that the addition of a low molecular fraction to FDM filament is a straightforward and cost-effective method to improve interlayer adhesion. Additionally, the selection of a LMW additive that balances the plasticizing effect of the additive with the ability to entangle and improve the interfacial adhesion provides an optimal improvement in tensile properties. For the limited molecular weights examined here, the 50k LMW samples fit this criterion and offer the best opportunity to enhance the interlayer adhesion of an FDM printed part.

The finished print quality is also indicative of the ability of the low molecular weight additive to improve the mechanical isotropy of these 3D printed samples. Figure 2.9 provides an image of the print quality of the samples for each molecular weight of the LMW additive. Since the printing parameters were held constant, any changes in the part quality are purely a result of the behavior of the blended filament. In comparison to the neat sample, the 8.5k sample exhibits a heavily over extruded and rough appearance. This indicates that the 8.5k component flows readily under the printing conditions and appears to be more isotropic as the distinction between layers is more difficult. Unfortunately, the LMW chains cannot entangle and thus interlayer adhesion does not increase as discussed above. Compared to the neat sample, the print quality and layer appearance of the 50k LMW sample is smoother with less definition between layers. This is consistent with the enhancement of the layer adhesion in the 50k LMW blended samples as shown by tensile
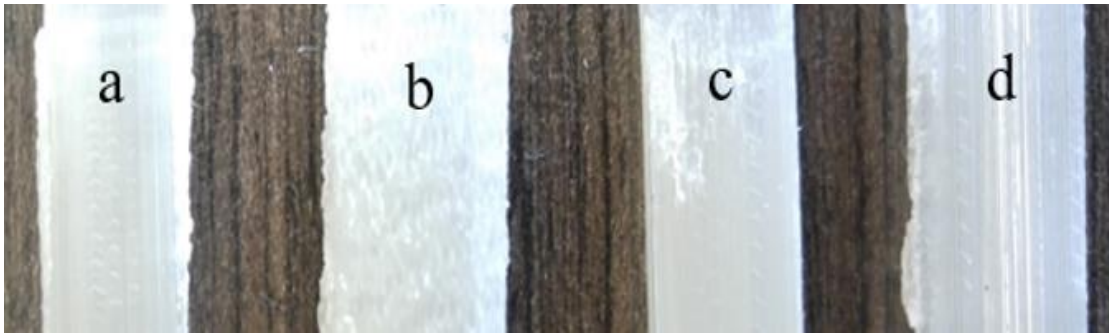
Figure 2.9 Print quality as a function of MW at 10 mol% loading (a) neat, (b) 8.5k, (c) 50k, and (d) 100k

testing. The 100k sample has well-defined filament layers, a structure that can be expected where poor interlayer adhesion occurs, which is consistent with the tensile measurements. Thus, the macroscopic finished part quality agrees completely with the mechanical testing experiments and indicates that the 50k 10mol% sample provides desirable printing conditions for samples with improved mechanical and isotropic properties.

Change in void space with LMW additive

Tensile measurements of the bimodal blends show that a drastic improvement in tensile properties of printed samples is possible with the appropriate loading and molecular weight of the LMW species. While this proves that the isotropy can be reduced by adding a LMW species to the bulk material, it does not provide an understanding of the mechanisms that drive these improvements. To develop this understanding of the underlying mechanism, the change in the amount of void space between filaments has been investigated as a function of LMW additive. The amount of void space is quantified using image analysis. Figure 2.10 illustrates how the void spaces in the longitudinal orientation decrease with the addition of the LMW species. Additionally, Figure 2.11 illustrates this same trend in the transverse orientation. The decrease in the amount of void space by itself indicates an increase in entanglement due to the increase of layer-to-layer interface. This change in void space also means that the cross-sectional area that is utilized in interpreting the stress-strain curve must be corrected. For instance, in the neat sample, there is substantial empty space that is not accounted for. To correct for the presence of the void space, image analysis was performed to quantify the percent void

space in the sample and the stress and modulus were corrected using the following

equations:

$$Void\ fraction = \frac{pixels\ of\ void\ space}{total\ pixels\ of\ image}$$

<div align="right">**Equation 2.2**</div>

$$Corrected\ Value = \frac{Original\ Value}{1 - Void\ Fraction}$$

<div align="right">**Equation 2.3**</div>

Figure 2.10 demonstrates that the addition of the 8.5k LMW PLA at 10 mol% completely

eliminate the voids. However, at the same time, the mechanical properties of this sample

are poorer than the neat sample, as shown in Table 2.3. The fact that the 8.5k LMW PLA

does not entangle confirms that the LMW species must be sufficiently long to entangle

with chains in adjacent filaments to improve the properties of the material. This also

demonstrates that the improved inter-filament contact area is not sufficient to realize

improved interlayer adhesion; entanglements between the filaments are also required. In

the sample with 10 mol%, 50k LMW added, Figure 2.10c) the void space decreases

substantially, signifying enhanced inter-filament surface area contact. shows that the

corrected maximum stress and modulus exhibit significant improvement over that of the

neat samples. This further corroborates the interpretation that the decrease in the void

space does not fully account for the increase in mechanical properties and is consistent

with an increase in entanglements between filaments. Lastly, Figure 2.10d illustrates the

large inter-filament voids that are present in the 100k LMW sample relative to the neat
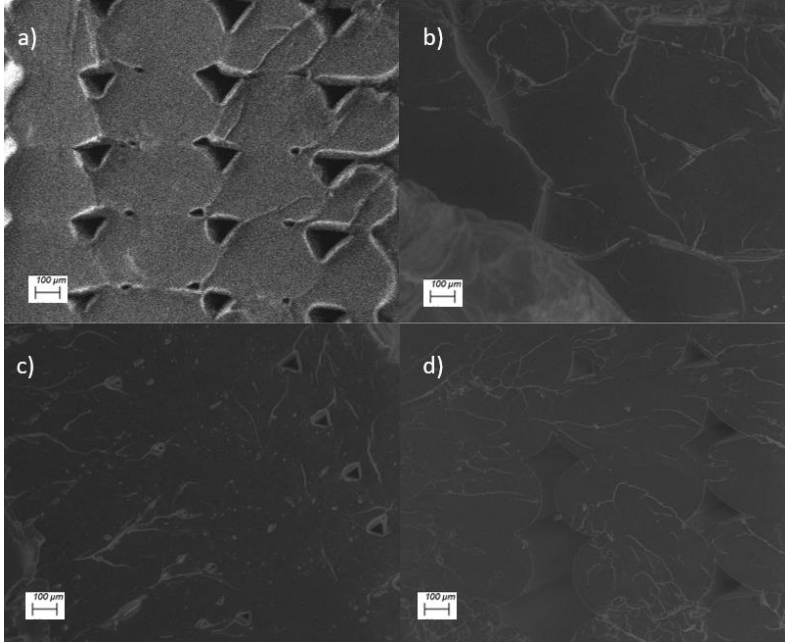
Figure 2.10 SEM image of PLA tensile specimens fracture surface in the longitudinal orientation (a) neat (b) 8.5k at 10 mol% (c) 50k at 10 mol% and (d) 100k at 10 mol%
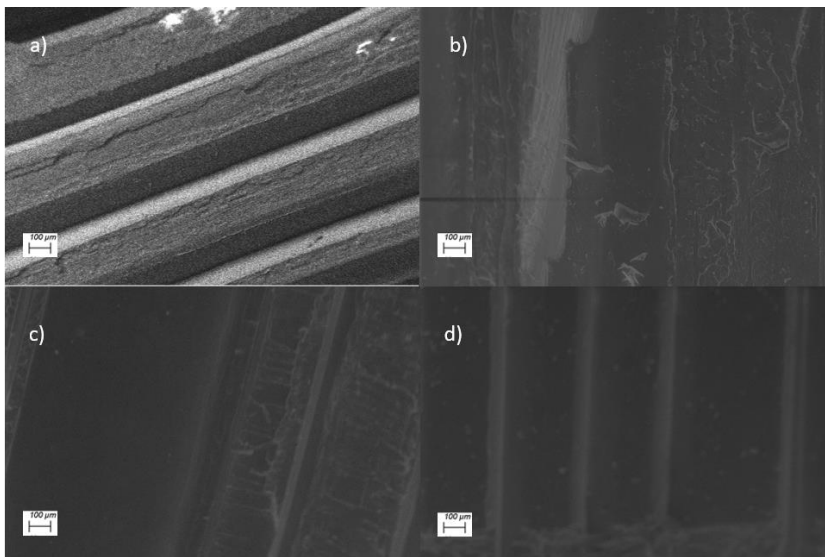
Figure 2.11 SEM image of PLA tensile specimens fracture surface in the transverse orientation (a) neat (b) 8.5k at 10 mol% (c) 50k at 10 mol% and (d) 100k at 10 mol%

Table 2.3 Corrected values for maximum tensile stress and modulus accounting for void space

Sample (10 mol% loading for blends)	Void Fraction	Maximum Tensile Stress (MPa)	Corrected Maximum Tensile Stress (MPa)	Modulus (GPa)	Corrected Modulus (GPa)
Neat long	0.103	40.96	45.19	0.546	0.608
Neat trans	0.373	15.54	24.78	0.484	0.771
8.5k long	0	28.68	28.68	0.507	0.507
8.5k trans	0	12.39	12.39	0.549	0.549
50k long	0.072	45.44	48.97	0.640	0.690
50k trans	0.033	26.60	27.51	0.610	0.631
100k long	0.119	37.43	42.47	0.630	0.715
100k trans	0.119	9.15	10.38	0.630	0.715

sample. These large voids lead to failure at lower stress even when corrected for the change in void fraction. This indicates that while the 100k LMW species is of sufficient length to entangle, the broad PDI introduces large chains that cannot readily diffuse leading to large interfilament voids and poor interlayer properties. These analyses were also performed on SEM images of the other LMW concentrations in the longitudinal orientation. The analysis of these images yields the same conclusion that improved interlayer adhesion can only occur when the LMW species is of a sufficient length to entangle. SEM of these images can be found in the Appendix. Thus, the decrease in void space does not fully account for the changes in mechanical properties, and the increase in mechanical properties is consistent with the realization of increased entanglement between filaments.

Role of crystallinity on change in mechanical properties

PLA is a semicrystalline polymer that under certain conditions can exhibit 40% crystallinity.[112] The discussion above interprets the change in the mechanical properties, and its anisotropy, in terms of the inter-diffusion of the polymer chains across the inter-filament interface during the 3D printing process. However, it might also be that the addition of the lower molecular weight materials can alter the crystallization processes that occur during the thermal treatment that is associated with the 3D printing process, and therefore, it is important to document how the addition of the LMW material affects the crystallization of PLA under the 3D printing conditions. The crystallinity of the PLA is monitored using differential scanning calorimetry (DSC) experiments. DSC thermograms for the PLA tested is provided in the appendix. To monitor the impact of the addition of the LMW PLA to the crystallinity that exists in the final 3D printed

structure, the percent crystallinity of the blends is determined in the bimodal filament after it exits the extruder, but before it is used in the 3D printing process and after it has been printed to account for shear-induced crystallization.[113] In the experiments presented, the crystallinity of all samples is determined from the equation:

$$\% Crystallinity = \frac{\Delta H_m - \Delta H_c}{\Delta H_m^o} * 100$$

Equation 2.4

Where ΔH_m and ΔH_c represent the enthalpy of melting and crystallization (J/g) respectively and $\Delta H_m^o = 75.57$ J/g is the theoretical enthalpy of melting for a 100% crystalline PLA sample as determined by Tábis and co-workers.[112] Figure 2.12 plots the percent crystallinity of each sample studied for both after the filament is extruded from the single screw extruder and after the filament is used to 3D print the cubes from which the tensile dogbones are fabricated. The percent crystallinity in all the samples is small ($<$ 10%), and in particular, the amount of crystallinity in the extruded filament appears to be fairly random. This can be explained by the relatively long cooling times required after extrusion from the die, where the exact cooling time is not well controlled. In many cases, this leads to a purely amorphous extrudate, as in the 50k samples. However, in almost all instances an increase in crystallinity is observed after printing. This may be the result of shear induced crystallization arising from the high shear applied to the PLA chains as they are extruded through the small printer nozzle and the complex thermal history of the extrudate.[114]
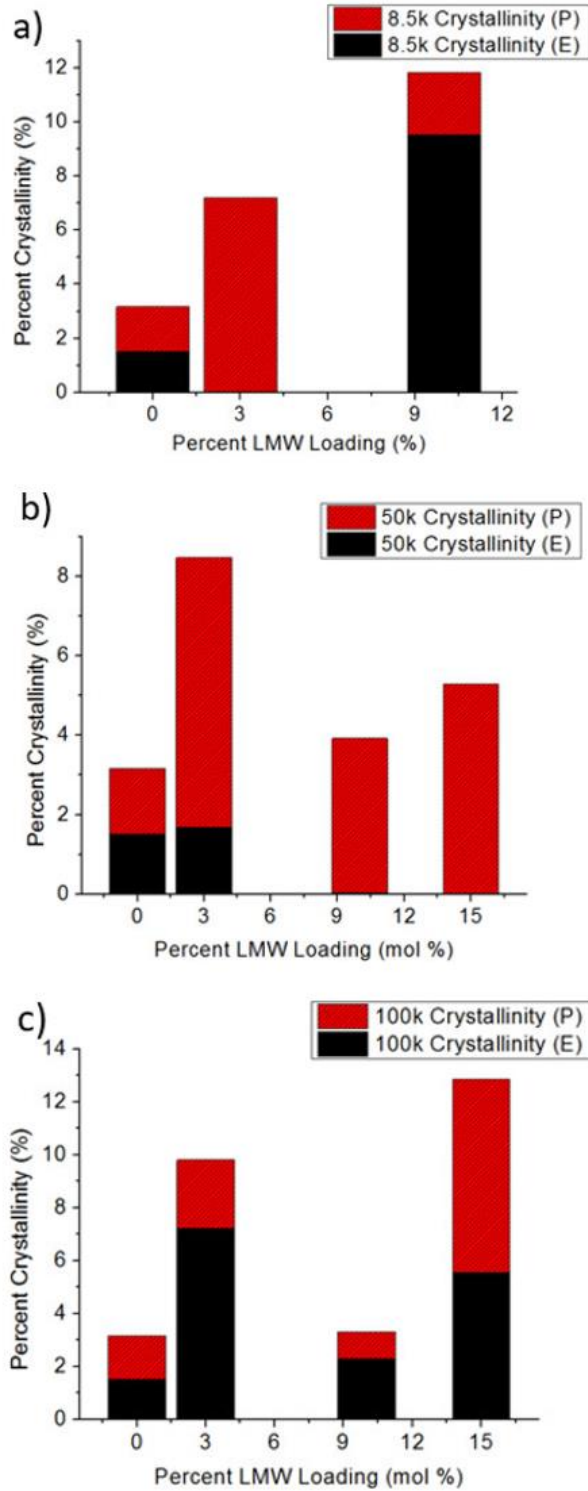
Figure 2.12 Stacked bar chart for (a) crystallinity of 8.5k (PDI- 1.4) (b) 50k (PDI 1.5) and (c) 100k (PDI 4.3) blends as a function of percent LMW loading after extrusion (E) and after printing (P)

More precisely, Figure 2.12a documents the crystallization behavior of the samples with 8.5k LMW PLA. The data suggests that at low concentrations of LMW additive, the 8.5k acts as a plasticizing agent providing the mobility needed to allow the longer polymer chains to orient into crystalline morphologies; however, at high loadings, the LMW additive appears to acts as a solvating agent which inhibits orientation of the large chains and prevents crystallization. This can further be observed in the 50k series (Figure 2.12b) where at low loadings, an increase in crystallinity after printing is observed. In this case, however, it appears that the loading of the 50k LMW PLA is not high enough to impede the crystallization of the PLA. Lastly, due to the large PDI of the 100k series (Figure 2.12c) results in no discernable trend of the crystallinity of the extruded or printed samples.

Taken as a whole, these studies indicate that crystallization under printing conditions does occur, though relatively low (<10%). Moreover, there is no recognizable correlation between the mechanical properties and the extent of crystallinity, and therefore, the change in crystallinity of the PLA with the addition of the LMW additive does not appear to be a major factor influencing the formation and properties of the interlayer interface, but further studies are needed.

CONCLUSION

In the reported studies, it is shown that the addition of a LMW component to a commercial PLA filament, at the correct molecular weight and loading, can significantly improve the inter-layer adhesion of parts prepared by FDM. This effect is attributed to the fact that the lower molecular weight polymer diffuses more quickly across the inter-filament interface during the 3D printing process, creating stronger interfaces. The choice

of the correct molecular weight and loading is governed by the need to balance the plasticizing effect of the LMW PLA with the requirement that it be long enough to entangle across the interface. The addition of the LMW PLA also alters the shear-induced crystallization of the PLA during the printing process. While this effect is small, it may also impact some of the mechanical properties observed with the LMW blends, but further studies on this matter are needed. Ultimately, the principles described by this study can easily be applied to many other polymeric materials used within the FDM industry. Additionally, the low cost and low complexity afforded by the system offers a method that is both scalable and economical.

Chapter 3 - INTERLAYER DIFFUSION OF SURFACE SEGREGATING ADDITIVES TO IMPROVE THE ISOTROPY OF FUSED DEPOSITION MODELING PRODUCTS

ABSTRACT

It is well known that 3D printed parts prepared by fused deposition modeling (FDM) exhibit large anisotropy of mechanical properties. For instance, the mechanical properties observed of samples printed orthogonal to the print bed (transverse) are significantly weaker than those printed parallel to the bed (longitudinal). This behavior is a result of poor interlayer adhesion from *limited* diffusion and entanglement of chains across the interlayer interface. To improve the diffusion and entanglement of adjacent layers, our group has implemented a process in which bimodal blends comprised of a parent, high molecular weight polymer blended with an identical but low molecular weight (LMW) polymer is utilized. These bimodal blends lead to significant enhancements in the mechanical properties of samples printed in the transverse orientation. Additionally, the moduli, regardless of print orientation, become nearly identical, indicating a more isotropic part. To more fully understand this behavior, we report the impact of LMW architectures on the improvement of structural properties of 3D printed parts. The decrease in anisotropy of mechanical properties of PLA bimodal blends containing 2-arm (linear), 3-arm and 4-arm PLA stars (M_w of arm- ~11k) at loadings of 3, 10, and 15 mol% are tested under the same protocol as previous linear specimens. With the addition of just 3 mol% of each LMW additive, i*ncreases* in the maximum stress from 15% to 100% are observed for samples printed in the transverse orientation. A significant improvement in layer adhesion and a significantly more isotropic part is thus realized, where the 3-arm star exhibits optimal performance. Interpretation of the data presented leads to the conclusion that this is true because the 3-

arm star most efficiently diffuses to the inter-filament interface and entangles with the linear polymer.

INTRODUCTION

        Mechanical anisotropy is a significant problem in parts prepared by fused deposition modeling (FDM). Poor interlayer adhesion leads to weak interfaces and parts that are, for the most part, not mechanically useful.[115] This anisotropy arises due to the deposition method in which a filament bead is deposited in a layer by layer fashion. The deposition minimizes interaction of polymer chains between adjacent layers, which limits entanglement across this interface. Ultimately, less entanglement between layers leads to a poor weld and weak interfaces.[67,70,71] As has been shown in previous experiments, the mechanical properties of an FDM printed part are heavily dependent on the raster orientation.[72,103,104] In a typical tensile test of FDM printed samples, a tensile bar is prepared such that filament orientation lies parallel to the applied stress (longitudinal), then a tensile bar is prepared such that the filament orientation is perpendicular to the applied stress (transverse). The maximum tensile stress and modulus, of the longitudinally oriented part, are significantly higher than those of the sample printed in the transverse orientation.[115] These experiments quantify the extent to which parts prepared by the FDM method suffer from poor interfacial adhesion between layers.[16,19,105,48] The molecular level reason for this macroscopic response is that the diffusion of polymer chains across the inter-filament interface is slow for the large, bulky polymer chains, where the amount of thermal energy provided by the standard FDM printing process is insufficient to allow the formation of strong interfaces.[67,71] However, if the diffusion of the polymers across the interface can be improved, more entanglement

of chains between layers and improved interlayer adhesion can be realized during a standard deposition process.

In Chapter 2 it was shown that under the same printing conditions of printed samples from a bulk polymer, the presence of low molecular weight (LMW) additive added to the bulk material to create a bimodal blend drastically improves the interlayer adhesion of parts prepared by FDM.[115] This arises from the fact that the LMW species more readily diffuses across the filament interface.[106,116] Moreover, when the LMW chains are of a sufficient length, chain entanglement between layers increases. The driving force behind this methodology arises from the entropically favorable migration of these LMW species to an interface, such as the outer surface of a filament.[51,60,70,107,108] Under this protocol, bimodal blends are prepared that incorporate a smaller, but identical polymer chain to that of the starting filament. In these experiments, utilizing a LMW poly(lactic acid) of M_w- 50,000 at 10 mol% loading led to an *increase* of up to 66% in the maximum tensile stress and an *increase* of 10% in the tensile modulus over that of the starting filament for a transversely oriented part. Thus, a drastic improvement in interfilament adhesion and a more isotropic printed part results.

These results are promising for the development of more robust FDM printed parts; however, a better understanding of how these LMW additives improve the interfacial adhesion may provide additional insight to further optimize this process. To address this, we compare the ability of LMW additives of different architectures to decrease the anisotropy of the 3D printed parts and improve their mechanical properties. More specifically, we introduce LMW additives with star type architectures (3-arm and 4-arm) to the bulk material and compare the mechanical properties and structural

anisotropy to neat samples as well as samples with linear LMW additives. The introduction of additional arms to a central branch point inhibits traditional reptation of chains, and as a result, star type polymers entanglement dynamics differ from that of linear polymers.[79,117] Furthermore, star type polymers typically do not entangle unless their branches are of sufficient length.[79] If the chains do entangle, then the diffusion of these star type additives may *decrease*.[118] While this is a simplification of the trade-off between chain diffusion and entanglements and reality is probably more complex, this discussion offers a foundation to use rheology to provide a more complete understanding of the role of LMW architecture on the response of the system. Rheological measurements comparing the viscosity of these blends relative to blends containing linear additives is presented as a way to ascertain whether the star type architectures tested readily entangle and diffuse to the interface. If entangled, viscosities of the star type LMW blends will increase and layer adhesion will decrease due to poor diffusion across the interlayer interface compared to the linear LMW additives.[119,120] If unentangled, the star type architectures should plasticize the filament, but not lead to improvements in the interlayer adhesion. By comparing the effect of these star type architectures on the layer adhesion of FDM printed parts and their rheology, we provide crucial insight into the mechanism by which the LMW additives with linear and star architectures improve the interlayer adhesion.

EXPERIMENTAL

Materials

NatureWorks Poly(lactide) 4043D pellets (4043D, Filabot, Barre, VT), DL-Lactide (DL-LA, Fisher Scientific), Isopropanol (iPrOH, Fisher Scientific),

Trimethylolpropane (TMP, Sigma Aldrich), Pentaerythritol (PENTA, Sigma Aldrich), Stannous Octoate (Sn(Oct)$_2$, Sigma Aldrich) and Toluene (Fisher Scientific) were used as received. All glassware and magnetic stirrers were stored in an oven at 110 °C and cooled before reaction.

Synthesis of 26k low molecular weight linear poly(lactide) (PLA)

Addition of the reagents was carried out under an inert nitrogen atmosphere. To a 2-neck round bottom flask, 20.0g of DL-LA, 51μL iPrOH, and 70mL of Toluene was added. The reaction vessel was stoppered and immediately transferred to an oil bath. A temperature probe was added to the vessel and the temperature set to 90˚C. The vessel was kept under an N$_2$ purge throughout the reaction. Once the vessel reached the set temperature and stabilized, 216μL Sn(Oct)$_2$ was added to the flask. The reaction was carried out for approximately 4 hrs. The resulting PLA was precipitated into cold, stirring methanol and redissolved into methylene chloride. Methylene chloride was evaporated and the PLA dried at 90 °C under vacuum for 24 hrs. prior to use. 3-arm star and 4-arm star PLA samples were prepared analogously substituting the isopropanol for trimethylolpropane (TMP) to create the 3 arm stars and pentaerythritol (PENTA) to create the 4 arm stars. Molecular weight characterization was performed by gel permeation chromatography (GPC) on a Polymer Labs GPC 220 equipped with a refractometer, differential viscometer, and static light scattering. (molecular weight distributions may be found in the Appendicx S3.1 and GPC chromatograms may be found in the Appendix Figure S3.4- Figure S3.6).

Preparation of bimodal PLA blends

4043D pellets and low molecular weight (LMW) synthesized PLA were dried under vacuum prior to use. Blends were prepared by mechanical mixing in a Filabot Original™ single screw extruder. The filament was extruded at 160-165 °C, depending upon LMW added, to a diameter of 2.85+/- 0.1mm.

ASTM D638-V tensile specimens

All tensile specimens were cut from a cube that was printed by FDM on a LulzBot TAZ 5 3D printer with a 0.4mm nozzle. The extruder nozzle was heated to 190 °C and the build platform heated to 70 °C. The specimens were prepared by laser cutting from the cube where the filament orientation is denoted as transverse and longitudinal as seen in Figure 1.4.

Scanning electron microscopy image analysis

The void space between filaments of neat PLA printed samples and 3-arm 3 mol% PLA printed samples were imaged using a Zeiss Auriga Scanning Electron Microscope equipped with an Everhardt-Thornley SE2 detector. The remaining were imaged using a Zeiss EVO MA15 SEM with variable pressure and a Bruker eFlash Electron Backscattered Detector.

Rheology studies of PLA blends

Parallel plate rheology experiments were carried out on a TA instruments AR2000ex rheometer. Viscosity experiments were carried out at 190 °C, in air, at a constant, steady shear rate of 0.01s-1. A value of 190°C was chosen for the temperature as this is the print temperature of the polymer. Additionally, a shear rate of 0.01 s-1 was

selected to obtain low shear viscosity to minimize any shear-induced effect on the polymer blend.

RESULTS

Mechanical properties of FDM printed samples containing LMW additives with linear and star architectures

Bimodal filament containing low molecular weight 2-arm (linear), 3-arm, and 4-arm poly(lactide) with M_w- ~11k/arm were prepared at concentrations of 3, 10, and 15 mol%. Actual molecular weights and their distributions of the base material and LMW additives are presented in Table S3.1 of the appendix. In all cases where the filament was printable, the addition of the LMW species did not decrease the tensile properties of the printed part in the longitudinal orientation. Moreover, in most cases, the addition of the LMW additive improved the mechanical properties of the printed part in the longitudinal orientation.

Figure 3.1a further confirms previous studies that show that the addition of a linear LMW species (26,000), of sufficient length to entangle, to high molecular weight (HMW) commercial material improves the interlayer adhesion.[115] Furthermore, at a concentration of 3 mol% an *increase* in the transverse maximum tensile stress of 33% is observed. The transverse tensile modulus for the 3 mol% samples additionally *increases* by 16% (Figure 3.1b). When an additional arm is added to the LMW additive, the bimodal sample with a low concentration of 3 mol% exhibits a drastic increase in the transversely oriented sample's mechanical properties (Figure 3.2a and Figure 3.2b). More precisely, at 3 mol% loading of the 3-arm star, a drastic *increase* in the maximum tensile stress of 100% and an *increase* of 36% in the tensile modulus for the transversely
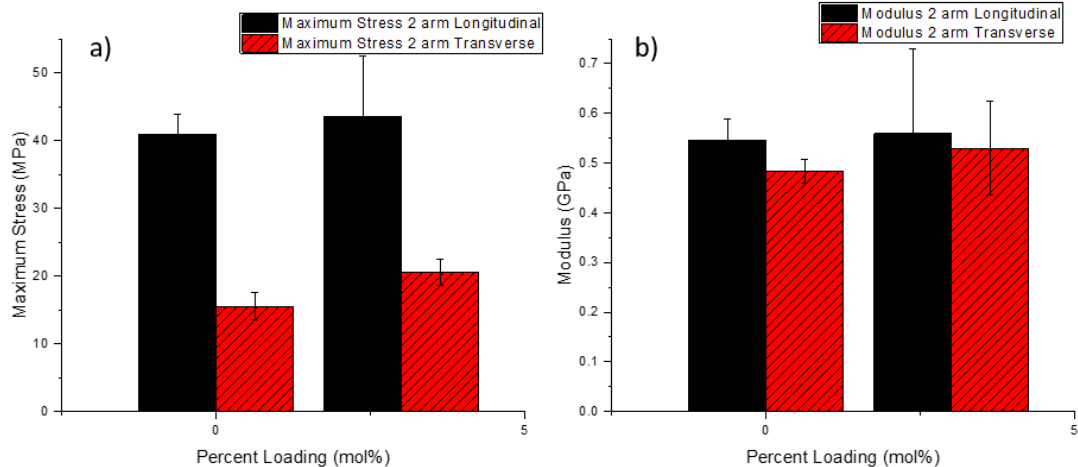
66

Figure 3.1 (a) Maximum stress and (b) modulus as a function of percent loading of the 26K linear LMW bimodal blends
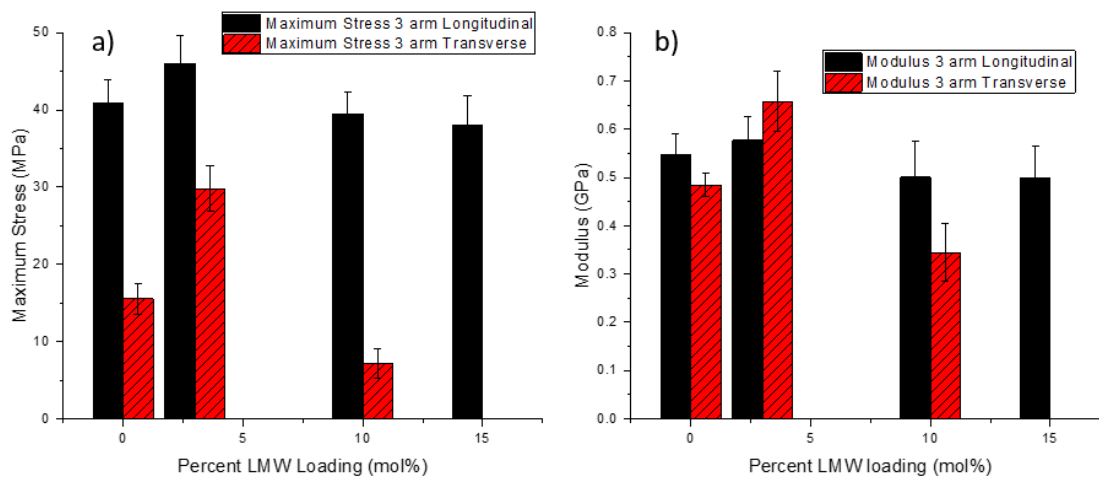

Figure 3.2 (a) Maximum stress and (b) modulus as a function of percent loading of the 3 arm LMW bimodal blends

oriented part results. Upon increasing the concentration to 10 mol%, a drastic decrease in the mechanical properties of the transversely oriented part occurs. In a similar fashion, the addition of the 4-arm star LMW additive at 3 mol% loading improves the tensile properties, and thus the interlayer interface, albeit to a much smaller extent than that of the 3-arm star (Figure 3.3a and Figure 3.3b). It should be noted that at 15 mol% for the 3-arm species, mechanical failure in the transverse direction occurred before tensile measurements of the sample. This also occurred for the 10 and 15 mol% loadings of the 4-arm species indicating extremely poor interfacial welds for these samples. For the samples tested, it would appear that 3 mol% loadings offer the greatest possible increase in transverse mechanical properties, but further studies are needed to verify this claim. Furthermore, it is interesting that such a drastic drop in interlayer adhesion is observed when the architecture of the LMW additive changes from 3-arms to 4-arms.

Figure 3.4a and Figure 3.4b compare the mechanical properties of the samples with 3 mol% of the LMW additives as a function of number of arms. The maximum tensile stress and modulus in the transverse orientation increased for all the samples tested, but the relationship between the observed mechanical properties and the LMW additive architecture is non-trivial. Furthermore, the linear species responded in a manner consistent with previous experiments where the addition of a LMW additive leads to *increased* interlayer adhesion. The 3-arm star LMW additive at 3 mol% offers the greatest *increase* in the mechanical properties of the samples tested. Finally, the 4-arm LMW species at 3 mol% offers minimal improvements. It is interesting that the modulus of the sample with the 3-arm star is larger in the transverse direction than in the
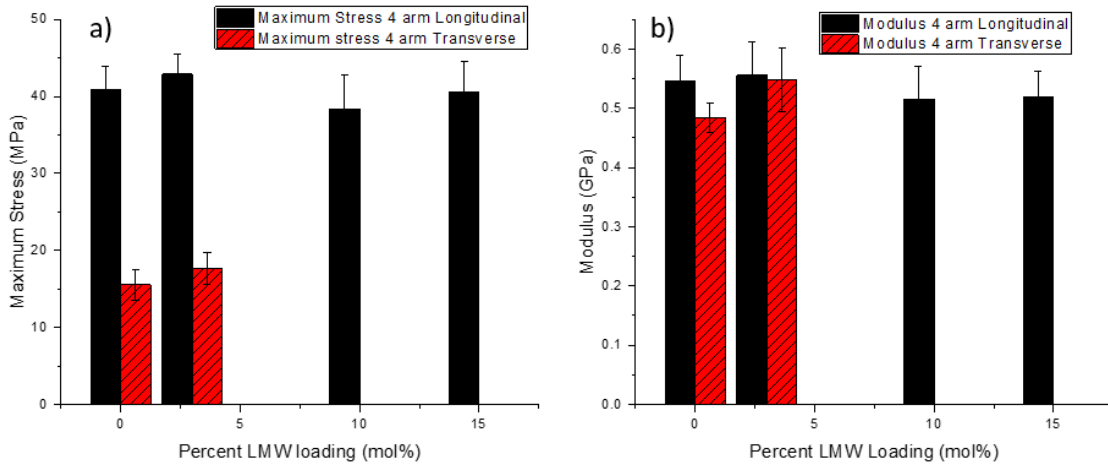
Figure 3.3 (a) Maximum stress and (b) modulus as a function of percent loading of the 4 arm LMW bimodal blends
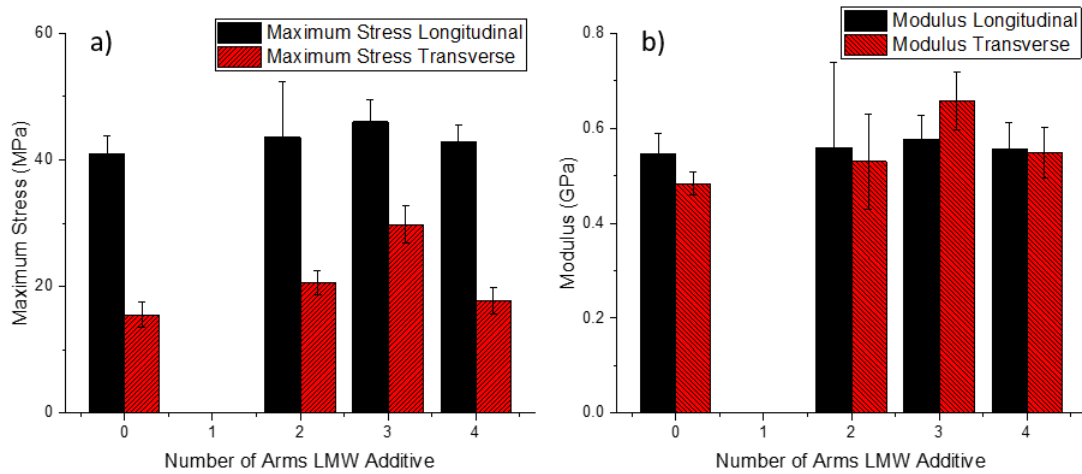

Figure 3.4 (a) Maximum stress and (b) modulus as a function of the number of arms of LMW bimodal blends

longitudinal direction. We ascribe the difference to the strong entanglement and strong interdiffusion of the star and linear polymers between layers.

Figure 3.5 plots the viscosity of the bimodal blends with varying architecture and LMW loading. This data shows that the neat material exhibits the highest viscosity, while the 4-arm star blends exhibit the next highest viscosity. The linear (2-arm) blend then follows, where the 3-arm stars exhibit the lowest viscosity. Interestingly, the addition of higher concentrations of LMW additive leads to further decreases in the viscosity. As mentioned previously, the viscosity of the 10 and 15 mol% samples were not obtained for the linear (2-arm) species, as these samples resulted in an unprintable material.

Figure 3.6 also plots the viscosity data, but in this case, the data of the neat sample and the bimodal blends with 3 mol% LMW additive are presented and plotted as a function of the LMW additive molecular weight. This data set also includes the bimodal blend with a 50k linear chain.
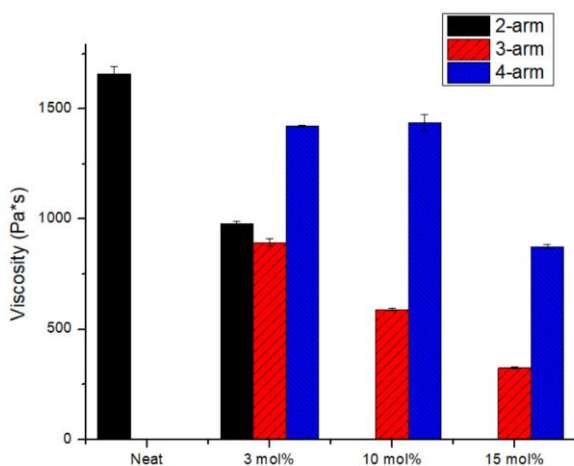

Figure 3.5 Apparent shear viscosity at 0.01 s^{-1} as a function of LMW loading for the various architectures
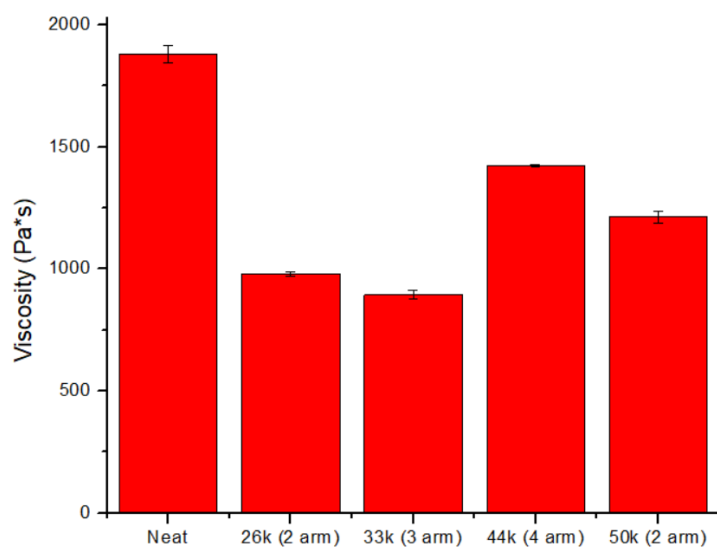
Figure 3.6 Apparent shear viscosity at 0.01 s^{-1} of 3 mol% bimodal blends as a function of LMW additive molecular weight.

SEM images of the fracture surfaces of FDM samples containing LMW additives

Figure 3.7 presents SEM images that document the amount of inter-filament void in the neat PLA FDM deposited samples as well as identical images for the samples printed with the bimodal blends with 3 mol% loading. This data shows that the addition of the LMW additive results in a drastic decrease in interfilamentous voids, regardless of the architecture of the LMW additive. Additionally, at 3 mol% loading, the magnitude by which the LMW additive reduces the interfilamentous void spacing is very similar for all LMW additive architectures.

DISCUSSION

Previous work in our group has shown that the interlayer adhesion of FDM printed samples drastically improved with the addition of a low molecular weight additive (LMW) to the base filament, as long as the polymer is sufficiently long to entangle yet diffuses faster than the large chains found in the commercial material. In these previous studies, the LMW species only consisted of linear polymers. These results led to the idea that altering the architecture of the LMW additive might further improve the mechanism, as branched polymers have an additional driving force to sequester at the interface. From these experiments, a better understanding of the mechanism that leads to drastically improved interlayer interfaces can be obtained.

The data presented in Figure 3.1-Figure 3.3 show that the overall bulk properties of the material are not detrimentally affected by the addition of the LMW species. This is consistent with the preferential migration of the LMW material to the inter-filament interface and indicates that they are not homogeneously distributed throughout the filament. Consequently, the improved layer adhesion resulting from the addition of low
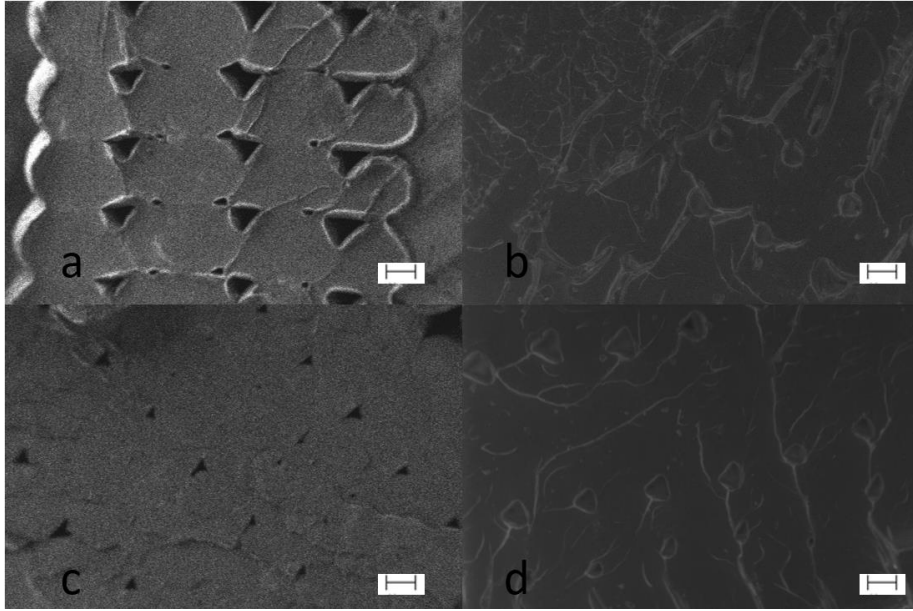
Figure 3.7 Longitudinal fracture surface of 3 mol% loading LMW additives with various architectures (a) Neat (b) 2-arm (linear) (c) 3-arm and (d) 4-arm (scale bars equal 100 μm)

concentrations of the LMW additive appears to reduce stress concentration points in the part, which leads to marginal improvements in the mechanical properties for samples printed in the longitudinal orientation. The observed mechanical properties of the transversely oriented parts, however, require a more in-depth discussion.

In our previous research, it was found that the behavior of the LMW additive is the results of the plasticizing effect of the LMW additive and its ability to sufficiently entangle across the interlayer interface. Investigation of the SEM images (Figure 3.7) shows that the addition of the LMW species drastically reduces the interfilamentous voids. Interestingly, regardless of the architecture of the LMW additive, this reduction in void space is approximately the same. If it were the case that the LMW additive acted purely as a plasticizing agent, then the resulting tensile properties of all the samples tested at this concentration should be nearly identical. As the tensile properties of these materials significantly vary, this data indicates that while the addition of the LMW additives indeed acts as a plasticizer, not all of them entangle with the linear polymer to the same extent.

In Figure 3.5, the viscosities of all the bimodal blends provides insight into the mechanism by which one architecture, such as the 3-arm star additive, can drastically strengthen the interlayer interface, while another, like the 4-arm star additive, results in only marginal improvements. In all instances, the blends containing LMW additives *decrease* the viscosity of the melt; however, the magnitude of this decrease is drastically different for differing architectures. These results further confirm a plasticizing effect of the LMW additives to the bulk, but also suggest that LMW chain entanglement must play a role in determining the viscosity of these blends.

74

Based on the data in Figure 3.5 and Figure 3.6, the presence of the 2-arm (linear) LMW chains decreases the viscosity of the matrix, allowing the polymers to diffuse into the adjacent layers more readily than the neat filament and become entangled. This results in an increase in the interlayer adhesion and a more isotropic part as shown in Figure 3.1a and Figure 3.1b. Moreover, the higher concentrations of 10 mol% and 15 mol% failed to print. The high concentrations of LMW linear polymer with this molecular weight plasticize the sample so that the filament is over-extruded and rough prints are formed that cause print failure. This behavior is consistent with previous experiments and is interpreted to be due to the LMW species saturating the interface. Ultimately, the analysis of the results of the 2-arm (linear) LMW additive is consistent with previous work indicating that the plasticizing effect of the LMW species must be balanced with the ability for the LMW additive to readily diffuse into the adjacent layers and become entangled.

The addition of a LMW 3-arm star additive at 3 mol% yields an *increase* in the tensile stress and modulus of over 100% and 45%, respectively. On the other hand, the addition of 4-arm star additives results in increases of only *ca.* 15% and 17%, respectively. Moreover, at higher concentrations of the star LMW additives, the mechanical properties of the printed sample drastically *decrease*, which is consistent with the surface saturation of the LMW additive, as found with the linear LMW additives. Interestingly, at 3 mol% loading, the 3-arm star bimodal blend exhibits a much lower viscosity than the 4-arm additive and the linear (2-arm) LMW additive that is a lower molecular weight than the 3-arm star. Thus, it is clear that the presence of the 3-arm star allows the polymers to diffuse much more readily than the sample with the 4-arm or 2-

arm star LMW additive. One interpretation of these results is that the presence of the 4-arm star slows the diffusion of the polymers relative to that in the bimodal blends that contain the linear or 3-arm star architectures. However, Figure 3.7 demonstrates that all the LMW additives provide sufficient mobility for the filaments to bond and nearly eliminate the inter-filament voids. Thus, the difference in the mechanical behavior must be the result of poor entanglement of the 4-arm star across the interface and thus weaker interlayer adhesion.

It is interesting that the 3-arm additive exhibits the lowest viscosity of all bimodal blends tested. If the molecular weight of the LMW additive were governing this behavior, the viscosities of these blends should rank as 26k (2-arm) < 33k (3-arm) < 44 K (4-arm) < 50k (2-arm), but inspection of Figure 7 shows that the viscosities rank as 33k (3-arm) < 26k (2-arm) < 50 K (2-arm) < 44k (4-arm). Thus, the architecture of the star polymers influences their flow properties where the 3-arm polymer flows more easily than an equivalent linear polymer and the flow of the 4-arm star is slower than a linear polymer with the same molecular weight.

Under reptative processes, a star polymer must recoil its arms back to the central branch point before moving an arm into a new tube. However, the 3-arm star architecture offers a unique transitional structure between linear and more highly branched star architectures, where the third arm can fold along the backbone of another branch.[121] In this way, a 3-arm star can attain a pseudo-linear structure and diffuse by reptation in a manner that is consistent with a linear species that is 2/3 the MW of the star.[121] This type of behavior nicely explains the observed results. The 3-arm LMW additives diffuse in a manner consistent with that of a slightly shorter linear LMW additive, but after diffusion

across the interface, the presence of the additional arm provides an opportunity for more entanglements and thus a greater *increase* in interlayer adhesion compared to a purely linear polymer. The 4-arm star does not have this mechanism available and thus its flow and formation of entanglements is hindered.

Therefore, the presented results agree with previous experiments and confirm the need to balance the plasticizing effect of a LMW additive with the entanglement of the LMW additive at the interlayer interface. A LMW additive that is too small to entangle will plasticize the filament and reduce the number of interfilamentous voids; however, it will not enhance the interlayer adhesion as the number of entanglements across the interface *decreases*. In the same way, high concentrations of a LMW additive may saturate the interface and *decrease* the interlayer adhesion. When the LMW additive can entangle, it must entangle readily with the mechanically robust high molecular weight filament preferentially. Entanglement among similar, shorter chains leads to a weakened interlayer bond as the mechanical properties of the pure LMW additive are not sufficient to handle high levels of mechanical stress. From these experiments, the 3-arm star type LMW additive provides the greatest improvement in interlayer adhesion, given its ability to readily diffuse across the interface and readily entangle with the adjacent filament layer. While the magnitude of improvement is not as high, linear species of similar MW also achieve drastically improved interlayer adhesion over that of the neat material.

CONCLUSION

The data presented here indicate and confirm that the addition of a low molecular additive to a polymer filament can reduce the anisotropy and improve the mechanical properties of an FDM printed sample. This occurs by the balance of the plasticizing

77

effect of adding a LMW additive and the entanglement of that additive across the interlayer interface. Furthermore, the architecture of the additive significantly impacts the ability of the LMW additives ability to strengthen parts fabricated by fused deposition modeling. Linear LMW additives of sufficient length readily diffuse and entangle with the adjacent matrix resulting in an improved interlayer interface. In a similar fashion, a 3-arm LMW additive diffuses in a manner consistent with a linear species. Also, the additional arm appears to provide an additional entanglement point leading to drastically *increased* interlayer adhesion and a significantly more isotropic part. A 4-arm star, however, exhibits a decrease in the mechanical properties of the FDM printed sample, which is attributed to the poor diffusion and entanglement of the additive across the interfilament interface. This analysis and previous experiments offer a methodology that is promising for the production of more isotropic and robust FDM printed parts. Additionally, the low cost of implementing such methodology makes it favorable to scaling for industrial type processes.

Chapter 4 - SURFACE SEGREGATING ADDITIVES: IMPROVING THE ISOTROPY OF ACRYLONITRILE-BUTADIENE-STYRENE PARTS PREPARED BY FUSED DEPOSITION MODELING

ABSTRACT

3D printed parts prepared by fused deposition modeling (FDM) are well known to exhibit large anisotropic mechanical properties. More precisely an object printed with layers orthogonal to the print bed (transverse) is significantly weaker than those printed parallel (longitudinal). The reason for this behavior is due to poor diffusion and entanglement of chains across the interlayer interface thus resulting in a weak interlayer bond. To combat anisotropy in FDM, our group has utilized bimodal blends of a chemically identical low molecular weight surface-segregating additive (LMW-SuSA) blended with a bulk, commercially available poly(lactide) (PLA). By this process, drastic improvements in the interlayer adhesion and a more isotropic part is realized. To expand this methodology to other materials and to understand the impact the chemical identity of the LMW-SuSA has on interlayer adhesion, we report the introduction of LMW-SuSAs of miscible styrene-co-acrylonitrile (SAN), poly(methyl methacrylate) (PMMA) and immiscible PLA to ABS and the impact on mechanical properties of a printed FDM part. Decreases in the anisotropy of mechanical properties of ABS blends containing SAN (8.5k, 33k, and 75k), PMMA (33k, 67k, and 100k) and PLA (33k-3 arm and 220k) are tested utilizing a protocol previously developed in the group. With the addition of 33k PMMA and 33k-3 arm PLA the transversely oriented parts maximum stress increases by 40% and 25% respectively. A significant improvement in isotropy is therefore realized. Interestingly, LMW-SuSAs of SAN do not improve the isotropy of the part. Further, experiments utilizing energy dispersive x-ray spectroscopy (EDS) confirms the surface segregation of LMW PMMA and PLA suggesting that improvements in layer adhesion

are a result of increased diffusion and entanglement of chains across the interlayer interface.

INTRODUCTION

3D printing utilizing the fused deposition modeling (FDM) method has exploded in the last decade in its use in a broad range of applications, from industry to desktop do-it-yourselfers. With the boom of FDM usage, mitigating issues associated with the technique have garnered significant attention. Specifically, improving the well-known mechanical anisotropy in FDM printed parts has become a focal point for much research.[19,115,122,123] This mechanical anisotropy in parts fabricated by FDM is a result of poor interlayer adhesion which leads to weak interfaces between filaments. As a result, mechanical usefulness is limited in parts prepared by this method.[115] In FDM, a molten polymer is deposited onto a build platform via a hot extruding nozzle. By way of the deposition process, polymer chains are laid in a highly oriented manner along the print path. This, coupled with the complex thermal history of the printing environment, minimizes entanglement of polymer chains between adjacent layers.[124] Ultimately, entanglement across this interface is limited and weak interfaces result.[67,70,71] Furthermore, the raster orientation of the printed sample has been shown to impact the mechanical properties of a printed specimen tremendously.[72,103,104] In other words, a longitudinally oriented part (printed parallel to the build platform) exhibits substantially higher tensile properties relative to a sample that is prepared with a transverse orientation (printed orthogonal to the build platform).[115] Many studies have quantified the extent to which parts prepared by the FDM method suffer from poor interfacial adhesion between layers.[16,19,105,48]

Viewed from a molecular level perspective, the diffusion of large, bulky polymer chains across the interfilament interface is slow. Additionally, there is minimal thermal energy available during a standard FDM deposition to allow the diffusion of the polymers between filaments to form strong interfaces.[67,71] Therefore, improved interlayer adhesion can be achieved in the standard FDM process by improving the diffusion of polymers across the interface during the deposition to increase entanglement of chains between layers.

As discussed in the previous chapters, under identical printing conditions to that of the bulk polymer, the introduction of low molecular weight surface-segregating additives (LMW-SuSAs) to the filament substantially improve the interlayer adhesion of parts prepared by FDM.[115] These improvements are facilitated by the LMW-SuSAs ability to more readily diffuse across the interlayer interface and, when of sufficient length, improve chain entanglement between layers.[106,116] In Chapter 3, it was shown that the addition of 3 arm star LMW-SuSA to an FDM filament doubles the mechanical properties in the transverse orientation of a printed part.[123] This methodology employs the entropically favorable migration of small chains to the interface.[51,60,70,107,108] In these experiments, the addition of a 3 arm star LMW-SuSA of poly(lactide) (PLA) with M_w-33,000 kilodaltons (k) at 3 mol% loading to the filament led to an *increase* of up to 100% in the maximum tensile stress and an *increase* of 45% in the tensile modulus of the printed part over that of a part fabricated from the neat filament in the transverse orientation. A drastic improvement in the isotropy of the part due to increased interlayer adhesion is thus realized by this methodology.

While these results are exciting for improving the isotropy of FDM printed objects, they have focused on a model system of PLA. To extend this methodology to other systems, ABS blends containing LMW additives of 3 different materials are tested for their ability to reduce the anisotropy of 3D printed parts. Furthermore, the additives are selected based on a continuum of their chemical similarity and miscibility to the styrene-acrylonitrile continuous phase of ABS: styrene-co-acrylonitrile (SAN) [Chemically similar and miscible]; poly(methyl methacrylate) (PMMA) [chemically different and miscible]; and poly(lactide) (PLA) [chemically different and immiscible].[125,126] From this continuum, information on the necessity of the additive to be miscible with the bulk matrix component to improve mechanical properties is obtained. Additionally, the incorporation of PMMA and PLA as a chemically different additive provides additional analytical techniques to monitor the segregation of the additive in the printed sample and provide additional insight into the mechanism by which the LMW-SuSA decreases part anisotropy.

In our previous work, a combination of thermodynamic principles, mechanical properties, imaging techniques, and rheological measurements has led to the interpretation that the improvement in part properties and reduction of anisotropy is the result of the surface segregation of the low molecular weight component. Moreover, this LMW component improves the extent of diffusion and entanglement between filaments for a given FDM deposition process that translates to improved properties.[115,123] However, experimental verification that the LMW species segregates to the interface has remained elusive. In utilizing a LMW additive that is chemically different than the matrix, we can exploit this contrast in energy dispersive X-ray spectroscopy (EDS).

Elemental analysis of various areas of a given printed part provides a qualitative assessment of the location of the LMW additive within a printed specimen. Therefore, a better understanding of the surface segregation of the LMW additive and insight into the mechanism by which these additives improve the mechanical properties of 3D printed parts is obtained.

EXPERIMENTAL

Materials

Styrene (Sty, Sigma Aldrich 99%), Acrylonitrile (AN, Acros Organics 99%) and Methyl Methacrylate (MMA, Acros Organics 99%) were purified by passing through a column filled with neutral alumina. Acrylonitrile-Butadiene-Styrene (ABS) Pellets (Filabot, Barre, VT), NatureWorks Poly(lactide) (PLA) 4043D Pellets (M_w-220,000 (220k), 4043D, Filabot, Barre, VT), Poly(methyl methacrylate) (PMMA) pellets (M_w-100,000 (100k), Polymer Science), Benzoyl Peroxide (BPO, Sigma Aldrich), DL-Lactide (DL-LA, Fisher Scientific), Trimethylolpropane (TMP, Sigma Aldrich), Stannous Octoate ($Sn(Oct)_2$, Sigma Aldrich), Isopropanol (iPrOH, Fisher Scientific), Anisole (Acros Organics 99%), Tri(2-(dimethylamino)ethylamine (Me6TREN, Sigma Aldrich 97%), Ethyl 2-bromoisobutyrate (EBiB, Acros Organics 99%), Copper(II) Chloride (Acros Organics 99%), Toluene (Fisher Scientific), and Anisole (Fischer Scientific) were used as received. All glassware and magnetic stirrers were stored in an oven at 110 °C and cooled before reaction.

Synthesis of styrene-co-acrylonitrile by ARGET ATRP

Poly(styrene-co-acrylonitrile) (SAN) with a target molecular weight of 75k was prepared by ARGET ATRP following the procedure utilized by Pietrasik, et al.[127] Styrene

84

(17.0 mL), acrylonitrile (7.5 mL), and anisole (13.9 mL) were added to a dry 3 necked flask. A solution of $CuCl_2$ (0.257 mg)/Me_6TREN (0.43 μL) in anisole (2.64 mL) was added. EBiB initiator (27.8 μL) was then added. The mixture was degassed by four freeze-pump-thaw cycles. After melting the mixture, a solution of $Sn(Oct)_2$ (31.0 μL)/Me_6TREN (22.0 μL) in anisole (1.65 mL) was added. The flask was placed in an oil bath at 80°C for 24 h. Polymer was precipitated from cold stirring isopropanol, re-dissolved in methylene chloride and then dried under vacuum. 8.5k and 33k SAN were prepared analogously (molecular weight distributions may be found in the Appendix Table S4.1 and GPC chromatograms may be found in the Appendix Figure S4.3- Figure S4.5).

Synthesis of linear poly(methyl methacrylate) (PMMA)

PMMA with a target molecular weight of 67k was synthesized by ATRP. To a 2-neck round bottom flask, 20.0 g of MMA, 0.0416 g of Copper(I) Bromide (CuBr), 66.6 of μL N, N, N', N", N'- Pentamethyldiethylenetriamine (PMDETA) and 20 mL of Toluene were added. The solution was degassed with three freeze-pump-thaw cycles and then placed under an inert nitrogen atmosphere. The reaction vessel was placed in an oil bath thermostatted at 90°C. The vessel was kept under an N_2 purge throughout the reaction. Once the temperature was stabilized, 41.9 μL of EBiB was added to the vessel. The reaction was carried out for 16 hrs. The resulting PMMA was precipitated into cold, stirring isopropanol and redissolved into methylene chloride. Methylene chloride was evaporated and the PMMA dried at 120 °C under vacuum for 24 hrs. prior to use. PMMA with a target molecular weight of 33k was synthesized analogously. Molecular weight characterization was performed by gel permeation chromatography (GPC) on a Tosoh

EcoSEC equipped with a RI detector and THF as eluent. PMMA and SAN molecular weights are presented relative to a PMMA standard (molecular weight distributions may be found in the Appendix Table S4.1 and GPC chromatograms may be found in the Appendix Figure S4.6- Figure S4.8).

Synthesis of 3 arm poly(lactide) (PLA) stars

The target molecular weight of the PLA stars is 33k. Addition of the reagents was carried out under an inert nitrogen atmosphere. To a 2-neck round bottom flask, 20.0g of DL-LA, 53 mg of TMP, and 70 mL of Toluene were added. The reaction vessel was stoppered and transferred to an oil bath where it was thermostatted at 90°C. The vessel was kept under an N_2 purge throughout the reaction. Once the temperature stabilized, 3.5 mL of an $Sn(Oct)_2$ solution (7.00 g $Sn(Oct)_2$ / 100 mL Toluene) was added to the flask. The reaction was carried out for 4 hrs. The resulting PLA was precipitated into cold, stirring isopropanol and redissolved into methylene chloride. Methylene chloride was removed by evaporation and the PLA was dried at 90°C in a vacuum oven for 24 hrs. prior to use. Molecular weight characterization was performed by gel permeation chromatography (GPC) on a Polymer Labs GPC 220 equipped with a refractometer, differential viscometer, and static light scattering with THF as eluent (molecular weight distributions may be found in the Appendix Table S4.1 and GPC chromatograms may be found in Appendix Figure S3.5).

Preparation of 3 mol% ABS/33k PMMA blend

All blends were prepared by a masterbatch process. ABS and the synthesized 33k PMMA were dissolved in methylene chloride and mixed for 24h. Methylene chloride was removed by evaporation and the resulting blend was dried under vacuum at 120°C for

24h. prior to use. Blends were prepared by mechanical mixing in a Filabot Original™ single screw extruder where masterbatched ABS/33k PMMA was mixed with neat ABS pellets to the desired 3 mol% concentration of PMMA. The filament was extruded at 195 °C, to a diameter of 2.75+/- 0.05mm. 100k PMMA, 33k-3 arm PLA, and 220k PLA were also blended with ABS at 3 mol% to prepare analogous filaments.

ASTM D638-V tensile specimens

Tensile specimens (Figure 1.4) were cut from an FDM printed cube, as previously described.[115] Samples were printed by FDM on a LulzBot TAZ 5 3D printer with a 0.5mm nozzle. The extruder nozzle was heated to 230°C and the build platform heated to 110°C.

Scanning electron microscopy image analysis (SEM)

The void space of the printed tensile specimens was analyzed by Scanning Electron Microscopy (SEM). All printed samples were imaged at the Joint Institute for Advanced Materials Microscopy Facility at Knoxville, TN on a Zeiss EVO MA15 SEM with variable pressure and a Bruker eFlash Electron Backscattered Detector.

Energy dispersive x-ray spectroscopy (EDS)

Energy dispersive x-ray spectroscopy was carried out on the printed tensile specimens in the above SEM utilizing a Bruker xFlash 6130 energy dispersive X-ray spectrometer.

RESULTS

Mechanical properties of FDM printed ABS blends

Filament containing Neat ABS and blended with SAN (8.5k, 33k, and 75k), PMMA (33k, 67k, and 100k) or PLA (33k-3 arm, 220k) at concentrations of 3 mol% were prepared. Actual molecular weights and their distributions of the base material and additives are presented in Table S4.1 of the appendix. For all blends, a printable filament was obtained. Three sets of additives were chosen based on the miscibility of the additive with the matrix. SAN is the most miscible and similar to the matrix of ABS, PMMA is miscible but chemically different than the continuous phase of ABS, and PLA is immiscible and chemically different from the ABS constituents. The MW of the SAN additives were chosen based on our previous results that examined the improvement of the tensile properties of 3D printed PLA with the addition of low molecular weight PLA.[115,123] Following these studies, one molecular weight is selected that is near but below the entanglement weight M_e (10.5k for SAN)[128] and then two that are above the critical molecular weight M_c (21k for SAN).[128] In this study, 33k is slightly above M_c and 75k is well above M_c and approximately half of the bulk ABS molecular weight of 150k. Examining the behavior of this range of molecular weights provides insight into the relative importance of the plasticizing effect of the lower molecular weight material (which will dominate for the 8.5k SAN) and the improvement of inter-filament entanglement (which will become increasingly dominant for the 33k and 75k additives). PMMA molecular weights were selected based on the results obtained from the SAN analysis and from previous results with PLA where layer adhesion only appears to improve substantially when the additive is above M_c (~27.5k for PMMA).[123,126] The three

PMMA molecular weights encompass an additive that is just above M_c (33k), double M_c (67k), and a high molecular weight (HMW) additive of 100k. Here the HMW additive gives insight into any improvements in the blends due to the increased stiffness of the PMMA, as surface segregation of the additive is unlikely to occur. Lastly, the two PLA molecular weights were selected for similar reasons to PMMA. The 33k-3 arm star PLA was selected as it is above PLA M_c (20k), should surface segregate and because it has shown to improve the layer adhesion to the greatest degree in previous experiments with bimodal blends of PLA.[123] Additionally, 220k PLA is well above M_c and should not surface segregate.

Figure 4.1a illustrates how the maximum tensile stress of 3D printed parts in the transverse and longitudinal directions changes with the addition of SAN at 3 mol% loading to ABS. From this Figure, no improvement (or decrease) in the strength of the sample in the longitudinal orientation is observed for all molecular weights of the SAN additive tested. Additionally, a small decrease in the transverse orientation is observed with the addition of 8.5k and 75k SAN, but a small increase is observed for the 33k SAN additive. While changes in the maximum stress for all SAN additives are small, the tensile modulus of all samples with LMW SAN added *increases* in both orientations (Figure 4.1b). Figure 4.1b also illustrates that with the addition of 33k SAN, a large *increase* in the tensile modulus is observed for both orientations. Figure 4.2 shows the tensile properties of the samples that are printed with 3 mol% PMMA additives included in the filament. The addition of 33k PMMA at 3 mol%, as shown in Figure 4.2a, *increases* the maximum stress of the transversely oriented parts by a substantial ~40% with a large *increase* in the tensile modulus for both orientations. Interestingly, the
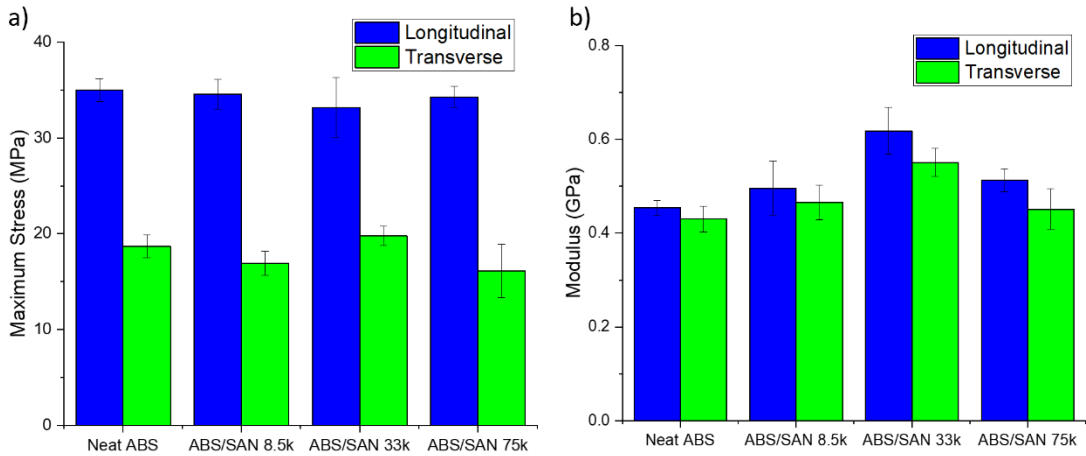
Figure 4.1 (a) Maximum tensile stress and (b) tensile modulus for 3 mol% ABS/SAN blends
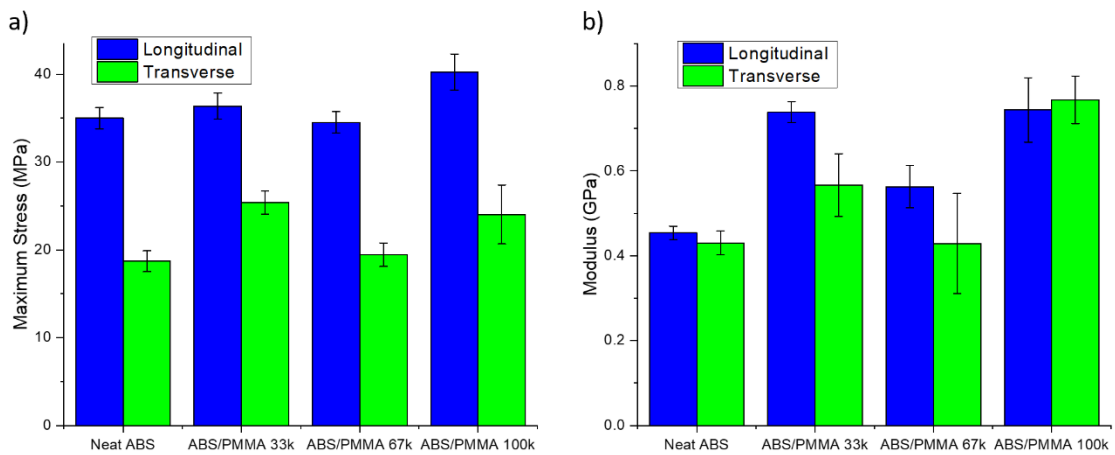
Figure 4.2 (a) Maximum tensile stress and (b) tensile modulus for 3 mol% ABS/PMMA blends

addition of 67k PMMA does not improve the maximum tensile stress nor does the tensile modulus *increase* as substantially as for the sample printed with the 33k PMMA. The addition of 100k PMMA to the filament appears to *increase* both the longitudinal and transverse maximum tensile stress, while the tensile modulus of these samples drastically *increases* and appears near equivalent in both transverse and longitudinal directions. Similarly, Figure 4.3 shows the tensile properties of the samples that are printed with 3 mol% PLA additives included in the filament. Figure 4.3a shows that the addition of 33k-3 arm PLA to the ABS filament, which was the most efficient LMW additive in our examination of PLA bimodal blends, results in an *increase* in the transverse orientations maximum stress by ~25%.[123] Additionally, the tensile modulus in both orientations drastically *increases* (Figure 4.3b). Lastly, the addition of 220k PLA results in a small *increase* in the maximum stress for the longitudinally oriented sample, but a large *decrease* for the transverse orientation. Like the HMW PMMA, the tensile modulus for both orientations substantially *increases* and are essentially equal within error, indicating a more isotropic part with regard to the modulus.

Void space analysis of fracture surfaces of FDM printed ABS blends

Figure 4.4 presents the longitudinal cross-sectional images of the printed tensile bars and documents the interfilament voids of the various ABS blends tested utilizing SEM imaging. Upon inspection and utilizing image analysis as described previously group[115], the percent voids in the samples that contain 75k SAN and 220k PLA ~35% for 33k-3arm PLA relative to the voids in the part that is printed from neat ABS. Table 4.1 summarizes the percent voids that exist between filaments for each sample, as well as the change in percent voids relative to that of the sample printed from neat ABS, where a
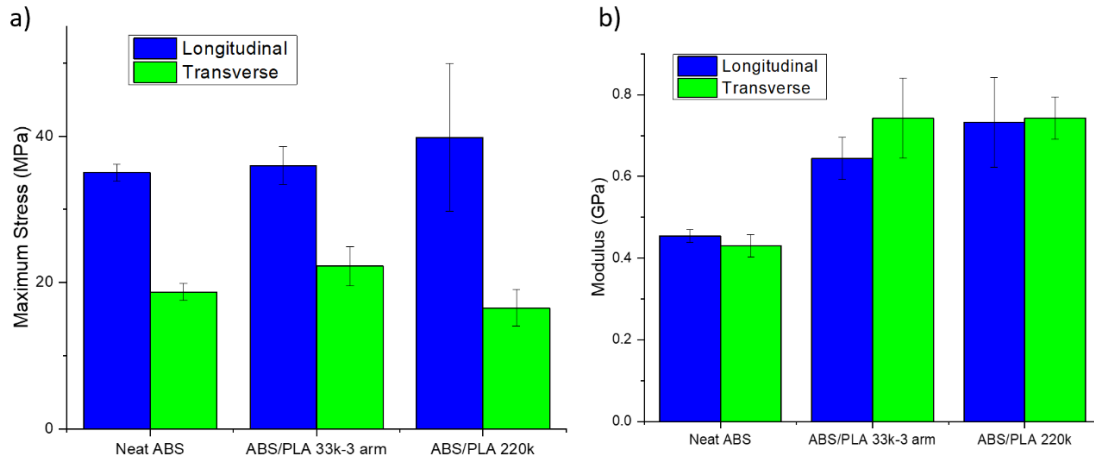
Figure 4.3 (a) Maximum tensile stress and (b) tensile modulus for 3 mol% ABS/PLA blends
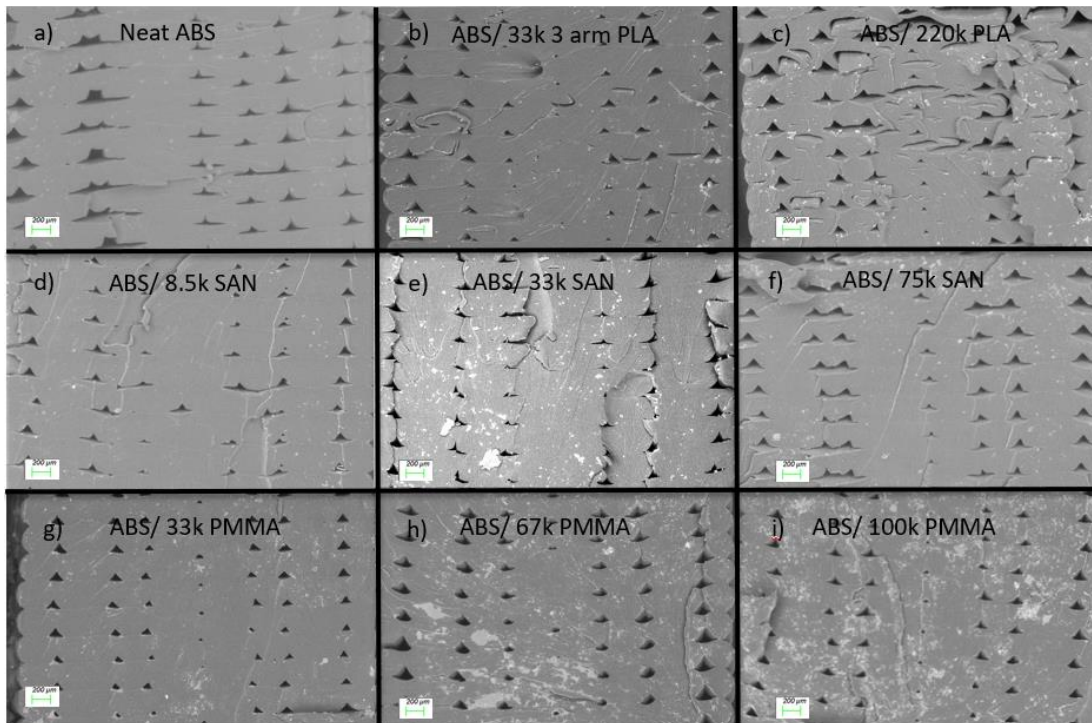
Figure 4.4 Longitudinal fracture surface of 3 mol% loading of various additives with ABS (a) Neat, (b) 33k-3 arm PLA, (c) 220k PLA (d) 8.5k SAN, (e) 33k SAN, (f) 75k SAN, (g)33k PMMA, (h) 67k PMMA, (i) 100k PMMA (scale bars equal 200 μm)

negative sign indicates the voids are smaller in the blend printed part than in the neat ABS part.

Compositional maps of fracture surfaces in FDM printed ABS blends using SEM-EDS

Scanning electron microscopy-energy dispersive X-ray spectroscopy (SEM-EDS) was employed to qualitatively monitor the position of the additives in the ABS blends in the cross-section of the filaments. Exploiting the contrast between the oxygen-containing additives (PMMA and PLA) and nitrogen-containing ABS in EDS provides a mechanism to qualitatively monitor the location of the additives in the printed part. As there is no contrast between the SAN matrix and SAN additives, these blends are excluded from this analysis. To provide insight into whether the LMW additive resides in the center of a filament or near the surface of the filament, three scans were performed for each blend as illustrated in Figure 4.5. The first scan provides the relative population of oxygen and nitrogen averaged over 4 filaments, including the center and edge of the filaments. A second scan focuses the analysis on the center of each filament, which provides a composition of the center of the bulk of the filament. The final scan focuses on the area around the inter-filament voids, where this provides insight into the composition of the blend near the filament-filament interface. In each scan, the ratio of the oxygen to nitrogen peaks is used to characterize the composition (additive/ABS) of the blend in a given area (Figure 4.6). Additional EDS spectra are provided in the appendix, Figures

Table 4.1Percentage interfilamentous void as compared to the Neat ABS for all ABS Blends analyzed

ABS Blend at 3 mol%	Percent Void	Variation in % Void Relative to Neat ABS
Neat ABS	5.4 +/- 1.5	0.0
ABS/SAN 8.5k	3.4+/-0.5	-38.0+/-5.6
ABS/SAN 33k	3.5+/-0.5	-35.1+/-5.0
ABS/SAN 75k	7.3+/-0.6	34.7+/-2.9
ABS/PMMA 33k	2.5+/-0.4	-53.9+/-8.6
ABS/PMMA 67k	2.8+/-0.5	-48.6+/-8.7
ABS/PMMA 100k	2.5+/-0.1	-54.1+/-2.2
ABS/PLA 33k 3 arm	2.7+/-0.5	-50.5+/-9.4
ABS/PLA 220k	6.3+/-1.0	16.0+/-2.5

Center (scan 2)

Void (scan 3)

Average (scan 1)
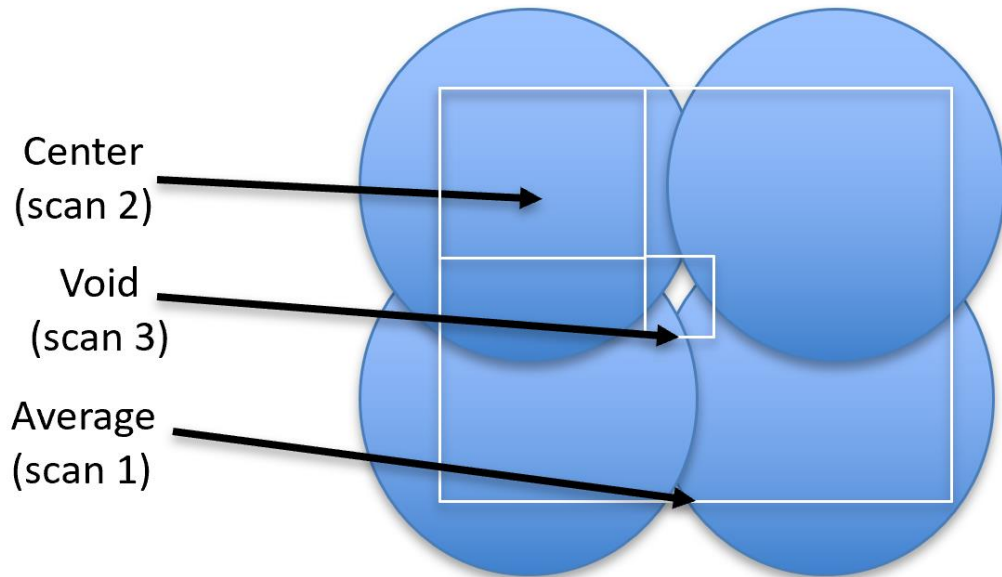
Figure 4.5 EDS areas of analysis for PMMA and PLA blends with ABS
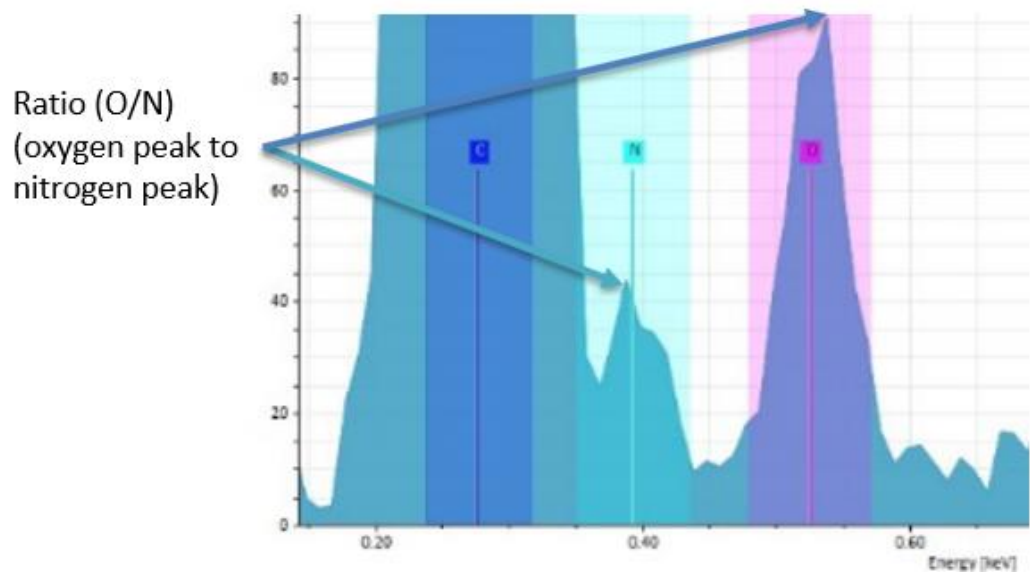
Figure 4.6 Example EDS Spectrum emphasizing the ratio of oxygen to nitrogen peaks used in the analysis

S41-S18. Table 4.2 summarizes this analysis where the O/N ratio of the filament centers

(scan 2) and voids (scan 3) are normalized to the O/N ratio of the average over 4

filaments (scan 1). Inspection of Table 4.2 shows that there is no change in the

composition of the filament between the center and void in the Neat ABS sample.

Further, inspection shows that the LMW 33k PMMA preferentially enriches the inter-

filament interface, as does LMW 33k-3 arm PLA, denoted by an increase in the ratio of

O/N within the void scan and a decrease in the O/N ratio in the filament center.

Interestingly, the 220k PLA also appears to enrich the interface. The higher molecular

weights of PMMA (67k and 100k) exhibit the opposite behavior, where the additives

appear to segregate to the bulk and are depleted at the filament-filament interface.

Table 4.2 Summary of EDS analysis for ABS/PMMA and ABS/PLA blends at 3 mol%

Sample	Void (O/N)/Average (O/N)	Center (O/N)/Average (O/N)
Neat	1.14	1.14
PMMA 33k	1.08	0.80
PMMA 67k	0.77	1.17
PMMA 100k	1.00	1.23
PLA 33k	1.07	0.79
PLA 220k	1.33	0.92

DISCUSSION

Recent work in our group has shown that the addition of LMW additives to PLA drastically improves the mechanical properties of the interlayer interface in fused deposition modeling (FDM) printed parts.[115,123] Moreover, improvements in the interlayer strength can be achieved by adding either a linear LMW additive or a 3-arm star type LMW additive. From these analyses, we have shown that improvements in the interlayer interface and the subsequent improvement in isotropy requires an additive that surface segregates, readily diffuses across the interface and must entangle across the interface. To expand on these previous results and to extend this methodology to other materials systems, we have studied the impact of including LMW additives to ABS.

ABS is the most prominent FDM printed material and has a large presence in industrial and makerspace applications. ABS is a complex system that incorporates styrene-co-acrylonitrile (SAN) as a matrix mixed with poly(butadiene) (PBd) domains. In some SAN systems, the SAN is grafted to the PBd domains, while in others these two phases are merely mixed. In a typical ABS composition, SAN makes up 85%-90% of the total.[129–131] For this reason, three LMW SAN additives were chosen to be tested as interfacial modifiers in the SAN filament. The 8.5k LMW SAN additive is below M_e and therefore should not improve entanglement across the inter-filament interface but may plasticize the filament. Figure 4.1a suggests there is no plasticization as there is a small *decrease* in the maximum tensile stress. If 8.5k LMW SAN surface segregates, an increase in the number of unentangled chains at the interface could weaken the interface. This satisfactorily explains the *decrease* in maximum tensile stress of the transverse samples. Figure 4.4d and Table 4.1 highlight that the interfilamentous voids for the 8.5k

SAN blend decrease by 38%. While this may suggest a plasticization effect, it does not enhance the interlayer adhesion. The result is consistent with previous experiments where the surface-segregating species must readily diffuse AND entangle to improve the interlayer adhesion. For the 33k LMW SAN component, the addition of LMW SAN above its M_c should improve interlayer adhesion between adjacent filaments. Figure 4.1a illustrates that this occurs, but only slightly. However, from Figure 4.1b, the tensile modulus of the 33k SAN samples drastically increases in both orientations. Inspection of the SEM image e also suggests that addition of 33k LMW SAN leads to a decrease in void % by ~35%. This is nearly equivalent to the reduction in void % for the 8.5k blend and further suggests that the changes in tensile stress and modulus are not merely a function of plasticization. It would seem instead that the 33k SAN additive surface segregates to the inter-filament interface, which leads to better entanglement between printed layers, albeit minimally. As shown in Figure 4.1a, the addition of 75k SAN results in a decrease in the transverse orientation's maximum stress with a small increase in the modulus. These results suggest that while the 75k is SAN is well above the entanglement threshold, it is too large and inhibits diffusion across the interface. The SEM image of the 75k SAN nicely confirms this as the void % in these samples *increases* by ~35% (Figure 4.4f).

The above results indicate that SAN added to ABS provides minimal to no beneficial plasticization effect nor does it appreciably increase entanglement between filaments. As a result, only a small improvement in the maximum stress for the 33k SAN additive is observed. However, as mentioned before, Figure 4.1b shows that addition of all SAN additives yields a printed part with a higher modulus, where the 33k SAN

98

additive blends result in the samples with the highest modulus. In ABS, the SAN component is the high stiffness component with a Young's modulus of 3.8 GPa and the PBd is low stiffness with a Young's modulus of 2.0 GPa.[132] The results presented here show that, unsurprisingly, the additional SAN added to the ABS matrix increases the tensile modulus. For the 33k SAN, the large increase in modulus may be explained by surface segregation of the additive. A higher concentration of the additive at the interface may lead to a beneficial increase in the observed modulus where the application of stress results in an elastic response from the SAN preferentially over the polybutadiene dispersed in the bulk. While the 8.5k SAN may also surface segregate, it is below M_e and does not appreciably contribute to the modulus. Intuitively, the 75k SAN should increase the modulus to the greatest extent, but this is not the case. It may be that the 75k SAN does not surface segregate and instead remains dispersed in the bulk, which minimizes its impact on tensile properties, as it is dispersed rather than concentrated at the interface.

As the addition of SAN to ABS did not significantly improve the tensile properties of the 3D printed parts, we turned our attention to additives that are chemically different from the matrix. Often, polymer blends are utilized to introduce orthogonal yet beneficial properties from two different polymers.[133] One such example are blends composed of ABS and PMMA. The high strength and stiffness of PMMA results in a relatively brittle material; however, PMMA added to ABS has been shown to increase tensile strength while maintaining the beneficial toughness and durability of ABS.[134] To this end, PMMA was chosen as a LMW additive for ABS filament. To further understand the impact PMMA has on FDM printed ABS blends, 3 PMMA molecular weights were chosen that encompass an additive that is near M_c and should surface segregate (33k), an

additive that is above M_c and may surface segregate (67k) and an additive that is well above M_c and may not surface segregate (100k). Additionally, PMMA contains oxygen while ABS uniquely contains nitrogen, providing elemental contrast between the two blend components. This provides an opportunity to use energy dispersive x-ray spectroscopy (EDS) to gain a qualitative understanding of the location of the PMMA additive in the printed part. This coupled with SEM imaging and measured tensile properties of the blends provides a fundamental understanding of the mechanism by which LMW additives improve the properties of 3D printed parts. More precisely, these results provide insight into whether an additive increases interlayer adhesion by surface segregation and subsequent diffusion and entanglement across the filament interface or if the additive merely disperses in the filament and imparts its mechanical properties to the blend and printed part.

From Figure 4.2a, the parts printed from the 33k PMMA blend exhibit a large *increase*, ~40%, in the transverse orientation maximum stress. However, the maximum stress in the longitudinal orientation does not change. Moreover, Figure 4.2b shows that the modulus drastically increases for both orientations. Since the increase in the maximum stress only occurs in the transverse orientation, it appears that the 33k PMMA additive surface segregates, entangles with the adjacent layer and *increases* the interlayer adhesion of the part. Analysis of the EDS data in Table 4.2 strongly supports this interpretation, where a higher concentration of PMMA is found in the void area scan; indicating a higher concentration of PMMA at the interface between filaments and layers. Interestingly for the 67k PMMA blends, there is no increase in the transverse orientation maximum stress. Moreover, the modulus only *increases* marginally. EDS analysis of the

blend indicates that the 67k PMMA is concentrated in the bulk, but not segregated at the inter-filament interface. Since the 67k PMMA is dispersed within the bulk of the filament, it does not readily diffuse and entangle between layers resulting in little to no change in the transverse properties. Lastly, with the addition of 100k PMMA to ABS, the maximum stress *increases* in both orientations. Likewise, the modulus drastically *increases* in both orientations and appears near equivalent. As shown in the EDS analysis, the 100k PMMA, like the 67k PMMA, preferentially disperses into the bulk of the filament. From these results, the 100k PMMA is merely imparting its high strength and stiffness to the blend, but not selectively modifying the inter-filament interface. Advantageously, this results in an improvement in the interlayer strength; however, it does not result in an overall reduction of the anisotropy of the part. The increase in the modulus follows the trend for the ABS/SAN and other ABS/PMMA blends where the introduction of a higher stiffness material to the matrix results in an increased modulus. As a last note, the SEM images for all 3 PMMA blends show that the addition of PMMA decreases the void size of the part by nearly the same magnitude as the LMW SAN additives tested (Figure 4.4g-i). This could be interpreted that the LMW additives all provide similar plasticizing to the filament. However, the different mechanical properties obtained for the 3 PMMA MWs tested clearly show that the plasticization of the filament does not explain the observed changes in properties for all samples.

The data presented above analyzes two sets of ABS blends where the second component is miscible with SAN and shows that with an appropriate molecular weight additive, it will surface segregate to the inter-filament interface, which leads to improved interlayer adhesion and improved isotropy of the part. To further probe what constitutes a

good LMW-SuSA, the performance of PLA additives was investigated. The addition of LMW PLA to a PLA matrix yields drastically improved interlayer properties in parts printed by FDM from these PLA blends. Since PLA is immiscible with ABS, it is interesting to probe whether improvements from surface segregation of the additive can still be realized despite this immiscibility. For these experiments, 2 molecular weight additives were chosen, a LMW 33k-3 arm star PLA and a HMW 220k PLA. In our previous work, blends that contained the 33k-3 arm PLA exhibited the best tensile properties and isotropy of a PLA FDM part.[123] Figure 4.3a demonstrates that the addition of the 33k-3 arm PLA star to ABS results in an *increase* in the maximum stress of ~25%. As for the 33k PMMA sample, the maximum stress in the longitudinal orientation does not change, which is consistent with the surface segregation of the PLA to the filament-filament interface where it improves entanglement between adjacent filaments. This interpretation is corroborated by the EDS results in Table 4.2 which indicates that the 3-arm PLA is in excess between filaments. As with all additives tested, the modulus increases substantially due to the higher stiffness of PLA (Figure 4.3b). However, the addition of the 220k PLA to the ABS filament results in a drastic *decrease* in the maximum stress in the transverse orientation (Figure 4.3a). This is interesting as the EDS analysis indicates that the 220k PLA appears to preferentially enrich the interface. This is not an entropically driven surface segregation, but rather is a result of the lower viscosity of the PLA relative to the ABS. This lower viscosity, coupled with the immiscibility of ABS and PLA evidently drives the HMW PLA to the surface. Moreover, the larger 220k PLA chains are too bulky and slow to readily diffuse and entangle between filaments during the deposition process. Thus, the addition of the larger PLA results in a weakened

102

interlayer interface. In a similar manner to the ABS filament with added 100k PMMA, the modulus drastically *increases* in both orientations from the high stiffness of the high molecular weight polymer. SEM image analysis of the 33k-3 arm PLA blend shows that the number of voids is reduced and similar to the void size observed in the ABS/PMMA blends. This is further proof that the additive itself is important and that plasticization does not dominate in determining the tensile properties of the printed sample. The cross-sectional image of the 220k PLA blend further confirms this interpretation, as the increase in voids is smaller than that of the 75k SAN blend, yet the interlayer properties are weaker.

Addition of 3 sets of additives ranging from chemically identical and miscible to chemically different and immiscible confirms that LMW additives of sufficient length will surface segregate. Further, surface segregation of the additive *increases* the interlayer adhesion and reduces the anisotropy of the printed part. This occurs because of increased diffusion and entanglement of the LMW chains with adjacent filaments. Additionally, for the first time, energy dispersive x-ray spectroscopy gives definitive proof of the additives location in the part and provides consistent evidence with surface segregation and entanglement of LMW-SuSAs.

CONCLUSION

The results of this study show that the addition of LMW-SuSAs to commercially available ABS improves the isotropy and tensile properties of FDM printed parts. Moreover, energy dispersive x-ray spectroscopy provides evidence that LMW additives preferentially enrich the interface of an FDM filament. During the standard printing process, these LMW additives can diffuse and readily entangle with adjacent layers to

significantly improve the interlayer adhesion of an FDM part. LMW-SuSAs of SAN, PMMA, and PLA provide *increases* to the strength of the interlayer interface of the part, where 33k PMMA provides the greatest improvement. Further, the data presented suggests the HMW PMMA disperses throughout the filament, increasing the tensile properties of the printed parts, but the anisotropy does not decrease. The higher molecular weight additives exhibit poorer tensile properties in the transverse direction, presumably due to the poorer diffusion of the additive across the filament-filament interface and weaker interlayers. Interestingly, miscibility of the additive with the ABS did not appear to play a vital role in the properties of the parts printed from blends with the LMW additives. For the smallest molecular weights studied, the added PMMA and PLA both led to *increases* in the isotropy of the part, yet PLA is immiscible in the matrix. These studies thus provide a better understanding of the mechanism by which LMW-SuSAs improve the isotropy. Ultimately, success in expanding this methodology to ABS systems verifies the broad applicability of this methodology to improve the isotropy of FDM printed parts as a cost-effective and straightforward mechanism to provide more robust and mechanically useful products across multiple material platforms.

Chapter 5 – REACTIVE PROCESSING IN FUSED DEPOSITION MODELING TO FACILITATED IMPROVED ISOTROPY

ABSTRACT

Minimizing anisotropy in parts prepared by fused deposition modeling (FDM) remains a key area of research in the development of robust and mechanically useful 3D printed objects. Due to the bulky nature of polymer chains and the complex thermal environment experienced by adjacent filaments during the printing process, interactions of polymer chains between layers is minimized. Weak interfaces and poor layer adhesion results. In recent years, our group has addressed these issues through the introduction of low molecular weight surface-segregating additives (LMW-SuSAs). LMW-SuSAs are smaller than the polymer chains of the neat material and can more readily diffuse and entangle in adjacent layers during the printing process, yet still entangle. In the current research, we report a novel reactive processing protocol for extrusion-based 3D printing, where bimodal blends containing linear and 3-arm PLA LMW-SuSAs that are terminated with methacrylate groups and coupled by UV irradiation during the 3D printing process. *In-situ* irradiation of the printed layers results in drastic increases in the transverse maximum tensile stress of the printed structures, where an increase of up to ~140% and ~200% for the linear and 3-arm LMW-SuSAs is observed. Additional experiments document the effect of *in-situ* UV intensity on the reactive processing protocol.

INTRODUCTION

Fused deposition modeling (FDM) remains a growing tool in the manufacturing community. The technology has been readily implemented to fabricate prototyping tools, molds for industrial processes, and tailored parts across many industrial fields.[32,45,135] While its use in industry has expanded, the anisotropic mechanical properties observed in the final structure remains a hurdle to the production of mechanically robust printed

106

parts.[32,47,105] In the FDM process, a polymeric filament is passed through a heated nozzle and deposited in a layer by layer fashion. Due to the deposition method and the complex thermal history experienced by the filaments, poor diffusion and entanglement of chains in adjacent layers is observed.[43] Additionally, a number of parameters affect the welding of adjacent layers which in turn affects the observed mechanical properties of the part.[25,45,48,123] In recent years, a vast amount of research has been dedicated to modeling these parameters that influence the bonding and adhesion between printed layers.[25,32,40,48,104,136] The research has provided valuable information to improve the mechanical isotropy of printed parts but focuses primarily in the optimization of the print parameters such as layer height, print orientation, print speed, and print temperatures with modest success. Our group has focused on material design as a pathway to improve the isotropy of FDM fabricated structures, which remains a key aspect in advancing the FDM process. Furthermore, our studies have found that the introduction of low molecular weight polymeric species that surface segregate results in drastic improvements to the layer adhesion, bonding of adjacent filaments, and mechanical isotropy.[115,123] These low molecular weight surface-segregating additives, deemed LMW-SuSAs, function two-fold. First, LMW-SuSAs preferentially segregate to the interface where increased entanglement between adjacent printed layers is afforded by the better diffusion of the LMW species compared to their bulky and slow counterparts.[51,67,116,118] Secondly, LMW-SuSAs act as a plasticizer wherein interfilamentous voids are minimized. Importantly, the molecular characteristics of the additive including molecular weight and architecture have a large impact on the ability of the additive to improve the bonding and adhesion of

printed layers. Thus, a balance between the plasticization and entanglement of the additive is vitally important to producing robust and more isotropic printed objects.

With the addition of LMW-SuSAs, substantial improvements to the isotropy of the printed parts have been realized; however, the structures still exhibit anisotropy and further improvement is needed. To this end, we report the development of a reactive processing protocol that expands on the behavior of LMW SuSAs to form covalent bonds between layers and filaments to further strengthen these interfaces. In this protocol, polylactide (PLA) LMW-SuSAs modified with methacrylate end-groups is added to commercially available PLA that contains a photoinitiator to facilitate the formation of crosslinks between layers. It is well known that crosslinks between polymer chains substantially increase the tensile strength and toughness of materials.[87,88,137] The addition of crosslinkable sites to the LMW-SuSAs provides a reactive processing platform to initiate crosslinks via UV light between printed layers in a similar fashion to those created by stereolithographic printing (SLA).[6,8,138] Furthermore, UV induced crosslinking in FDM offers the opportunity to induce crosslinking only after the filament is deposited and only where it is desired. This holds a distinct advantage over other crosslinking systems such as thermally initiated reactions where control of the reaction is difficult. Therefore, we have studied and elucidated the effect of implementing this reactive processing protocol on the mechanical properties of the printed objects with *in-situ* irradiation. Moreover, we probe the effect of UV power on the *in-situ* irradiation process to control the speed of the crosslinking reaction. Lastly, UV DSC is presented to better quantify the reaction process of the PLA LMW-SuSAs.

EXPERIMENTAL

Materials

NatureWorks Poly(lactide) 4043D pellets (4043D, Filabot, Barre, VT), DL-Lactide (DL-LA, Fisher Scientific), 2-hydroxyethyl methacrylate (HEMA, Sigma Aldrich), Trimethylolpropane (TMP, Sigma Aldrich), Stannous Octoate (Sn(Oct)$_2$, Sigma Aldrich), Methacryloyl chloride (MethCl, Sigma Aldrich), Triethylamine (TEA, Sigma Aldrich), 2,2-Dimethoxy-2-phenylacetophenone (DMPA, 99%, Sigma Aldrich), Dichloromethane (Acros), and Toluene (Fisher Scientific) were used as received. All glassware and magnetic stirrers were stored in an oven at 110°C and cooled before reaction. Molecular weight characterization of linear and star-shaped PLA was performed by gel permeation chromatography (GPC) on a Polymer Labs GPC 220 equipped with a refractometer, differential viscometer, and static light scattering. ^{1}H-NMR was performed on a Jeol 400MHZ NMR.

Synthesis of 35k low molecular weight linear poly(lactide) (PLA)

Addition of the reagents was carried out under an inert nitrogen atmosphere. To a 2-neck round bottom flask, DL-LA, HEMA, and Toluene were added. The reaction vessel was stoppered and immediately transferred to an oil bath. A temperature probe was added to the vessel and the temperature set to 90˚C. The vessel was kept under an N$_2$ purge throughout the reaction. Once the vessel reached the set temperature and stabilized, Sn(Oct)$_2$ was added to the flask. The reaction was carried out for approximately 4 hrs. The resulting PLA was precipitated into cold, stirring isopropanol and re-dissolved into methylene chloride. Methylene chloride was evaporated, and the PLA dried at 90 °C

under vacuum for 24 hrs. prior to use. 3-arm PLA stars were prepared analogously substituting the HEMA for TMP.

Synthesis of dimethacrylated (PLADM) and trimethacrylated (PLATM) Poly(lactide)

HEMA initiated PLA was dissolved in dichloromethane in a round bottom flask. Upon dissolution, TEA was added. Over a 30 minute period, methCl was slowly added and the reaction flask was stoppered. The reaction was carried out for 4 days at room temperature. After 4 days, the solution was passed through a neutral alumina column and then precipitated into cold stirring isopropanol. Precipitated polymer was dried for 24 h. in a vacuum oven at 90°C. Trimethacrylated PLA was prepared analogously, substituting HEMA initiated PLA with 3-arm star PLA. The resultant polymers were characterized by GPC and ^{1}H-NMR experiments described above (Figure 5.1) (GPC chromatograms may be found in the Appendix Figure S5.1 and Figure S5.2).
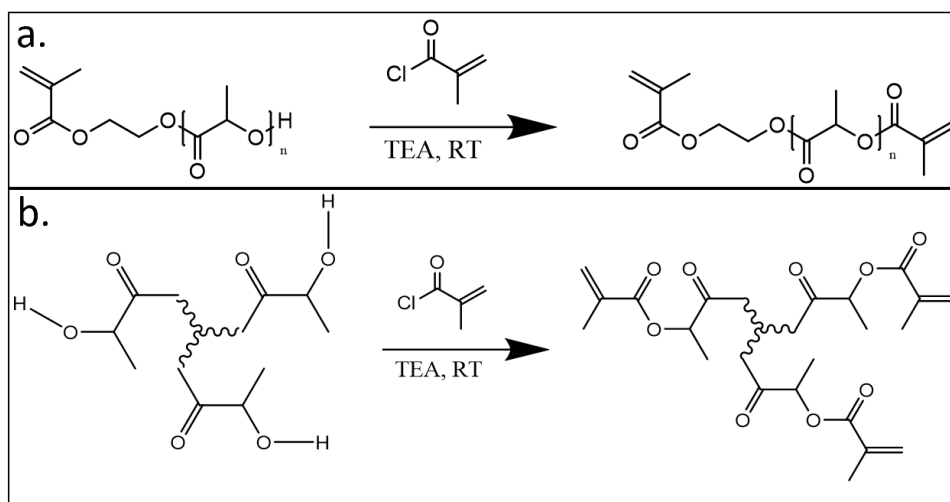
Figure 5.1 (a) PLADM and (b) PLATM reaction schemes

Preparation of Tensile Specimens

4043D pellets (M_w- 220k), LMW PLA additives, and DMPA photoinitiator were dried under vacuum prior to use. Filaments were prepared by mechanical mixing of the LMW PLA, DMPA, and virgin PLA pellets in a Filabot Original™ single screw extruder. Filaments were extruded at 147-152°C to a diameter of 2.85+/- 0.1 mm. Dogbone specimens were prepared utilizing a method used previously in the group by printing a cube and laser cutting dogbones longitudinal and transverse to the printing direction.[123] All samples were printed by FDM on a LulzBot TAZ 5 3D printer with a 0.5mm nozzle. The extruder nozzle was heated to 210°C and the build platform heated to 70 °C.

Scanning electron microscopy image analysis

Cross-sections of the fractured tensile specimens were imaged at the Joint Institute for Advanced Materials Microscopy Facility by a Zeiss EVO MA15 SEM with variable pressure and a Bruker eFlash Electron Backscattered Detector.

UV irradiation of samples *in situ*

For *in situ* UV irradiation, a fiber-optic UV LED from Thor Labs was affixed to the print head and positioned to illuminate the deposited filament (Figure 5.2). UV LED max output is 9.8 milliwatts (mW), 1400 milliamps (mA) at a wavelength of 365 nm. Illuminance was controlled by Thor Labs LEDD1B T-Cube driver with trigger mode. Illuminance of the LED was measured by a Fisher Scientific light meter.

UV differential scanning calorimetry (DSC) of 35k trimethacrylated poly(lactide)

UV DSC experiments were carried out on a TA Instruments Q2000 DSC equipped with a TA instruments photocalorimeter accessory with a 200 watt (W) mercury high-pressure mercury source that transmits UV and visible light in the 320-500 nm
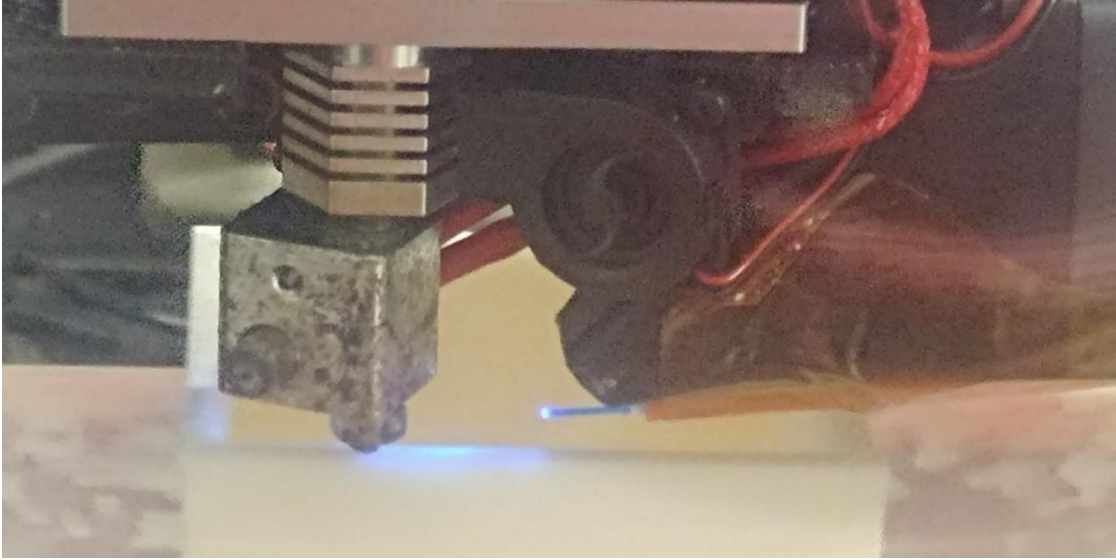
Figure 5.2 In situ UV irradiation set up

range. All samples were equilibrated at 40°C followed by a 5 min. isotherm. After the 5 min. isotherm, the UV shutter was opened, and samples were exposed to light, with the intensity that can vary between 15 and 53 mW/cm^2 for 6 min. before the shutter was closed. A final isotherm of 1 min. finished the experiment.

RESULTS

UV irradiated dimethacrylated poly(lactide) (PLADM) and trimethacrylated FDM printed samples

For all samples, 3 mol% of the LMW-SuSA is utilized. Weight percent (wt.%) of DMPA is given as a function of the total blends weight. Figure 5.3a compares the maximum stress and Figure 5.3b the modulus of printed neat PLA and blends of PLA containing 3 mol% of LMW-SuSA and 0.5 wt.% of DMPA photoinitiator with UV on and UV off. The mechanical properties for the neat PLA samples that were irradiated with UV and those of neat PLA samples that are not irradiated showed no difference. They are therefore excluded from the analysis for clarity. Interestingly, Figure 5.3a illustrates that with the addition of 0.5 wt.% DMPA, a large *increase* is observed in the transverse orientation maximum stress from 15 MPa to 30 MPa for the non-UV irradiated samples. With UV on, the maximum stress likewise shows a similar *increase*. Moreover, the modulus of the non-UV irradiated samples slightly *decreases* compared to Neat PLA; however, the modulus *increases* for UV irradiated samples (Figure 5.3b). The addition of PLADM 35k and 0.5 wt% DMPA printed with no UV irradiation leads to an increase from 15 MPa to 23 MPa. Furthermore, the modulus in the transverse orientation overtakes the modulus of the longitudinal orientation and *increases* from ~0.85 GPa to

113
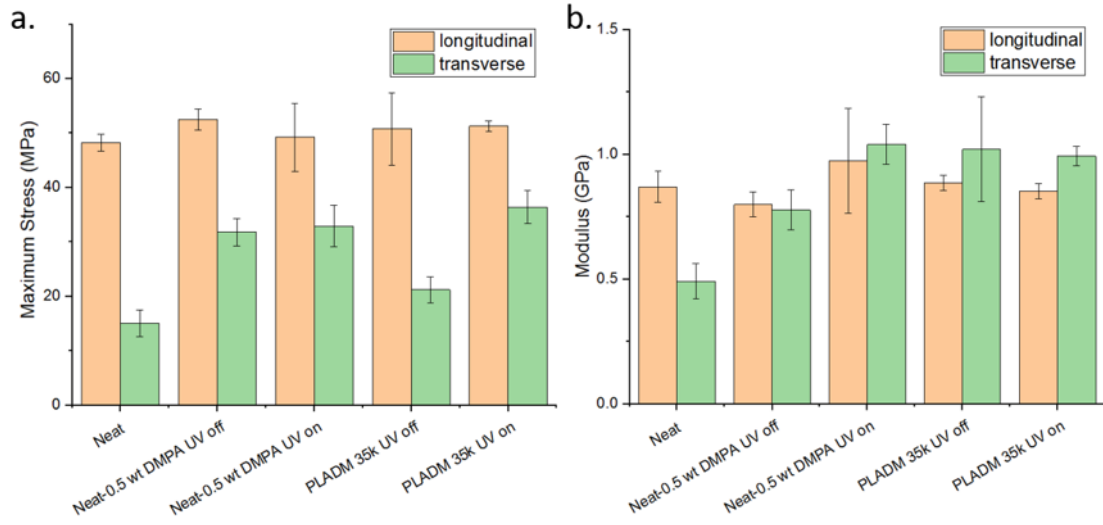
Figure 5.3 (a) Maximum stress and (b) modulus for PLADM series at 3 mol% loading with 0.5 wt% DMPA loading

~1.0 GPa. Lastly, blends containing PLADM 35k and 0.5 wt% DMPA printed with *in-situ* UV irradiation shows a drastic *increase* in the maximum stress from 15 to 35 MPa where the modulus results in a similar trend to the PLADM blends with no UV irradiation. Furthermore, the *increase* in the maximum stress of the UV irradiated PLADM is ~50% greater than that of the non-UV irradiated PLADM.

In Figure 5.4a and Figure 5.4b, the mechanical properties of the non-UV irradiated blends containing PLATM LMW-SuSA and 0.5 wt.% DMPA printed are compared to the mechanical properties of blends exposed to *in-situ* UV irradiation. From Figure 5.4a, it is observed that with the addition of PLATM with 0.5 wt% DMPA and no UV irradiation, an *increase* in the maximum stress from 15 MPa to 30 MPa is observed. This observed result is similar to previous experiments where a 3-arm star LMW-SuSA added to neat PLA yields a stronger interlayer interface.[123] Interestingly, the resulting max stress is nearly identical to previous experiments even though these samples contain a photoinitiator. The modulus in the transverse orientation *increases* but remains smaller than in the longitudinal orientation. When the PLATM blends are printed with *in-situ* UV irradiation, a drastic *increase* in the max stress for the transverse orientation is observed (15 to 45 MPa). Moreover, this is a ~50% *increase* in the transverse maximum stress over that of the non-UV irradiated PLATM. Finally, the modulus for these samples *increases* in the transverse orientation similarly to the PLADM series where the transverse orientation modulus is greater than the longitudinal orientation modulus.

In Figure 5.5, SEM images of the fractured cross-sections of longitudinally oriented dogbones are presented for both the PLADM and PLATM series. At the print
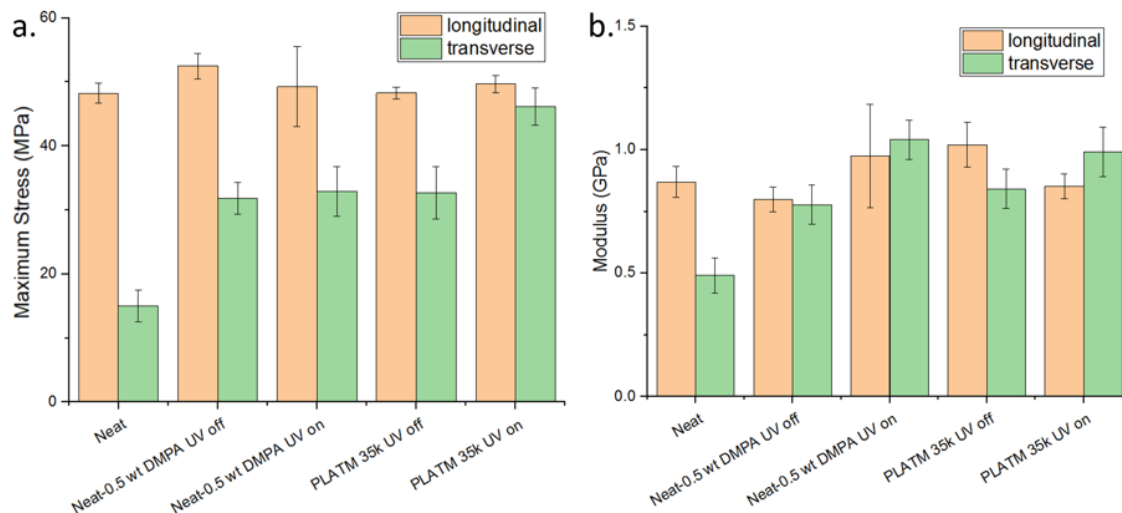
Figure 5.4 (a) Maximum stress and (b) modulus for PLATM series at 3 mol% loading with 0.5 wt% DMPA loading.
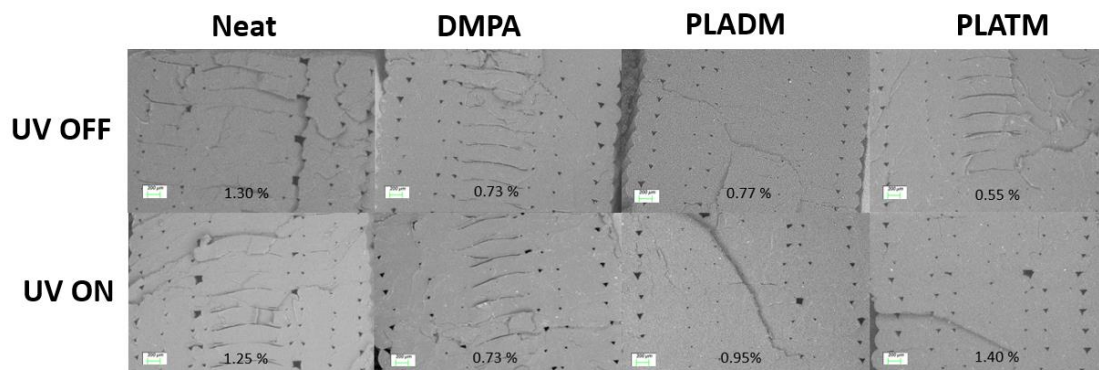
Figure 5.5 SEM print cross-sections of neat, PLA with 0.5 wt.% DMPA, PLA with 0.5 wt.% DMPA and 3 mol% PLADM, PLA with 0.5 wt.% DMPA and 3 mol% PLATM with UV on (Top) and UV off (Bottom)

gives the percent void present in each sample (Figure 5.5).[115] shows that the PLATM

with *in situ* UV irradiation exhibits the largest percent voids followed by the neat PLA,

PLADM with *in situ* UV irradiation and PLATM with no UV irradiation. Moreover, the

non-UV irradiated PLADM structure and PLA containing 0.5 wt% DMPA exhibit similar

void percentages.

Effect of UV irradiation power on PLATM printing

The void analysis suggests that the UV induced reaction impacts the extent of

inter-filament diffusion. A closer investigation that elucidates the correlation between UV

power during in-situ UV curing, and thus the extent of reaction and the extent of

interfilamentous voids is necessary. PLA blends containing 3 mol% PLATM with 0.5

wt.% DMPA were printed with varying levels of UV intensity from 25% to 100% as a

function of irradiance. Figure 5.6a and Figure 5.6b, illustrate the change in maximum

stress and modulus of the printed samples as a function of UV intensity. With increasing

intensity up to 75%, the transverse maximum stress appears to decrease slightly. The

maximum stress in the longitudinal orientation also appears to be higher in 25%, 50%,

and 75% UV irradiated samples than 100%. This trend seems to follow in the results

reported for the modulus as well where the lower illumination intensities exhibit a higher

modulus. Peculiarly, the 75% illuminated samples exhibit a higher tensile modulus in the

transverse orientation but exhibit the lowest transverse stress. Lastly, Figure 5.7 compares

the SEM images of the fractured tensile specimens. From Figure 5.7, it is clear that the

interfilamentous voids are nearly eliminated in the samples irradiated at 25% and 50%.

At 75%, the voids are likewise small but the sample fractures in a less brittle fashion
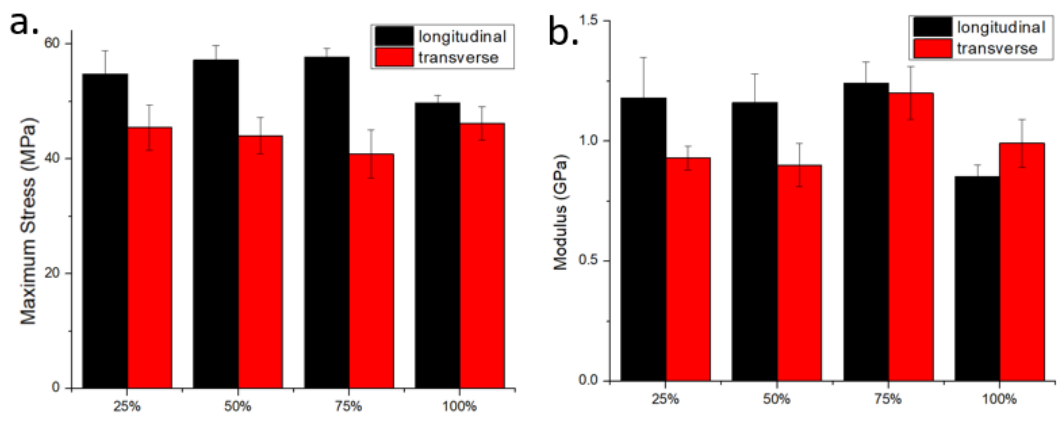
Figure 5.6 (a) Maximum stress and (b) modulus of PLATM LMW-SuSAs at 3 mol% and 0.5 wt% DMPA as a function of UV irradiation intensity (100% = 260 Lux)
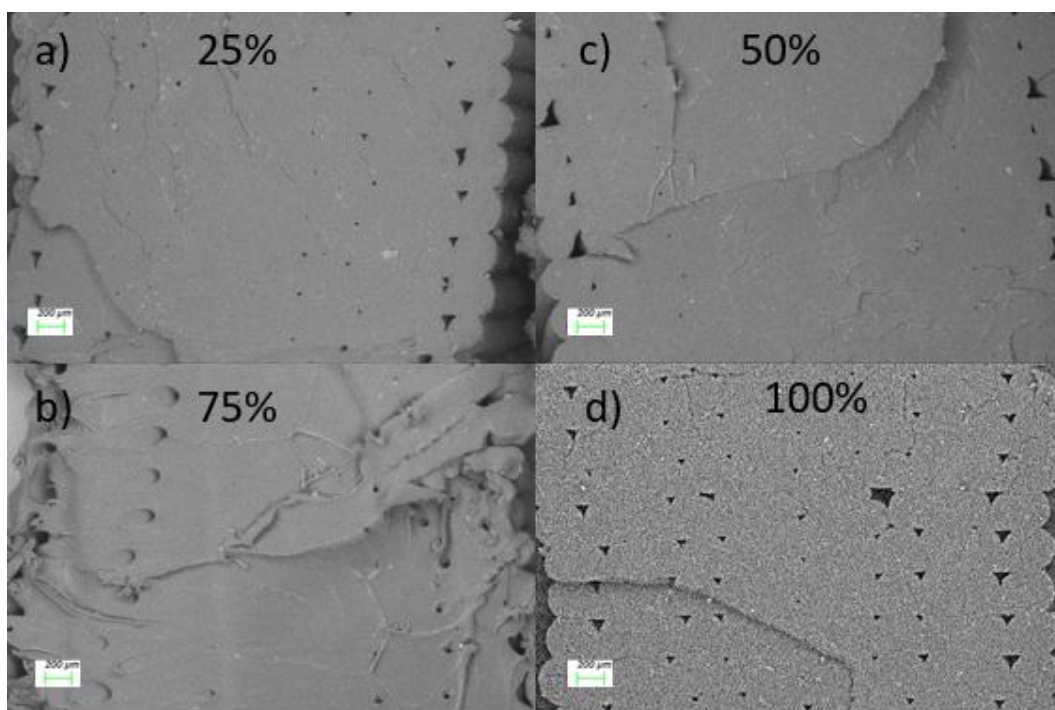
Figure 5.7 SEM cross-sections of PLATM LMW-SuSAs at 3 mol% with 0.5 wt% DMPA as a function of UV irradiation intensity a) 25%, b) 50%, c) 75%, and d) 100% (100% = 260 Lux)

temperature of 210°C, Figure 5.5 highlights the presence of interfilamentous voids in the printed specimens. Image analysis of the SEM images, as described in previous work,

compared to the other specimens. With 100% UV irradiation, larger voids are again prevalent.

UV DSC of trimethacrylated PLA

Controlling the UV intensity in-situ has a profound effect on the observed interfilamentous voids which seems to indicate a level of control over the crosslinking reaction of PLATM. To verify this interpretation, UV DSC was employed to monitor the impact of UV intensity on the extent of reaction of the methacrylated end groups. For all UV DSC samples, 0.5 wt% DMPA was added to the PLA/PLATM mixtures, as well as 40 wt% dioctyl phthalate to reduce the Tg of the samples such that it fell within the operating temperatures of the UV DSC instrument. Figure 5.8 shows a representative DSC thermogram of a PLATM sample irradiated at 24 mW/cm2. From the thermogram, a distinctive peak is observed immediately after the shutter is opened at 5 minutes. This is a clear indication of a reaction, where the area under the peak is proportional to the extent of reaction. Table 5.1 summarizes the results of the UV DSC experiments. When a sample was irradiated at 35°C no reaction was observed; however, at 40°C reactions are observed in all instances except the 50 mW/cm2 intensity (Table 5.1, sample 7) where the detector was flooded by the UV light. Unfortunately, the observed reaction signal is close to the baseline, which makes precise quantification of the methacrylate conversion difficult, but the calculated conversions show semi-quantitatively that at lower intensities, fewer methacrylate moieties react.

119
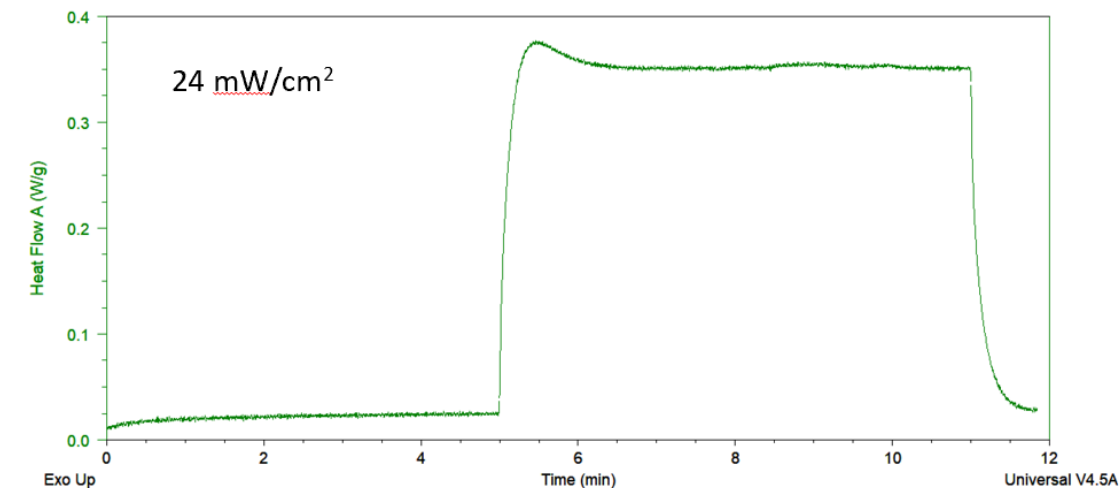
Figure 5.8 UV DSC curve of PLATM cured with 24 mW/cm² UV light

Table 5.1 UV DSC curing experiments comparing temperature and UV intensity to the enthalpy of reaction and percent conversion of PLATM samples

Sample	Temperature (°C)	Intensity (mW/cm²)	ΔH (kJ/mol)	% Conversion
1	35	24	0	0
2	40	15	17.15	19.9
3	40	23	37.62	43.7
4	40	24	39.77	46.2
5	40	24	58.01	67.5
6	40	24	48.11	55.9
7	40	53	0	0

DISCUSSION

In-situ UV irradiated FDM printed PLA LMW-SuSA blends

UV initiation is commonly used to induce crosslinks in systems such as hydrogels and in stereolithography.[6,8,138] To utilize these chemistries to promote improved interlayer adhesion in FDM, PLA LMW-SuSAs were modified to include methacrylate end-groups.Blends containing these additives with the photoinitiator DMPA were then printed and exposed to UV as the filament was extruded (Figure 5.2) to execute this reactive processing protocol. Under these print conditions, it was believed that the surface segregation of the LMW species to the interface coupled with a UV initiated crosslinking reaction between the methacrylate groups could drastically improve the interlayer adhesion of adjacent filament layers by creating covalent bonds across those interfaces. As shown in Figure 5.3, at print temperatures of 210°C, significant anisotropy in the mechanical properties is observed in the neat PLA sample regardless of UV irradiation; however, when 0.5 wt.% DMPA is added, the transverse maximum stress _increases_ to ~30 MPa compared to the neat PLA at 15 MPa. Additionally, the difference between the longitudinal and transverse maximum stress values is substantially reduced; indicating a more isotropic part. This result would seem to suggest some level of thermal initiation of the methacrylated PLA by DMPA, but further results are needed to verify this. Since adding only DMPA to PLA results in transverse maximum stresses of ~30 MPa, it is interesting that when dimethacrylated 35k LMW PLA is added at 3 mol% to PLA with 0.5 wt.% DMPA, the transverse maximum stress only increases to ~23 MPa. Additionally, the magnitude of improvement for this LMW additive is similar to previous results with no DMPA.[123] It would seem that the surface segregation of the LMW species

121

dictates the development of the interlayer interface in these systems. In other words, the faster diffusion of the LMW-SuSA relative to the bulky high molecular weight (HMW) chains of the neat PLA is the key driving force to the entanglement and strengthening of that interface. Moreover, the 35k PLATM LMW-SuSA with DMPA yields similar properties to that of a 33k 3-arm PLA additive without DMPA. The results further indicate the self-assembly of these LMW additives to the interface where they can potentially react across adjacent filaments.

As observed in Figure 5.3 and Figure 5.4, a reaction initiated by UV irradiation of the methacrylated blends appears to readily occur. When exposed to UV irradiation during the print, the PLADM blends exhibit a large *increase* in the transverse maximum stress from ~25 to ~35 MPa. This large *increase* is also observed in the PLATM blends where the transverse maximum stress *increases* from ~33 MPa to ~45 MPa. Moreover, the transverse maximum stress for the PLATM blends becomes nearly equivalent to that in the longitudinal orientation. A substantially more isotropic part is therefore realized seemingly facilitated by the UV initiated crosslinking of the methacrylated additives. A further indication of reaction lies in the cross-sectional SEM images obtained for the blends. From Figure 5.5, the calculated void space shows that when the samples are UV irradiated, larger interfilamentous voids are observed. This behavior is interpreted to indicate that reactions occur between LMW species where the mobility of the reacted blend is hindered and is no longer able to readily flow. Moreover, the observed change in void space does not occur within the neat samples or those PLA samples containing just DMPA. The results suggest that the UV reaction of the methacrylated LMW-SuSAs

122

occurs quickly, covalently bonding the layers together and inhibiting inter-filament diffusion.

Effect of UV irradiation power on PLATM printing

In blends printed without UV irradiation, small interfilamentous voids are observed. This is preferred, as the interaction between adjacent layers is maximized and a more cohesive part is fabricated. Unfortunately, these samples exhibit poorer mechanical properties than those exposed to UV irradiation during the print. Thus, it appears there is a need to balance the rate of formation of the crosslinks between filaments such that the reaction is slow enough so that their formation does not hinder diffusion between filaments, but the reaction is fast enough to create sufficient covalent bonds between filaments in the final sample. In an attempt to determine reaction conditions that identify this balance and minimize inter-filament voids but maximize reaction, we looked to tune the speed of the methacrylate coupling reaction by controlling the UV intensity and thus initiation. Moreover, tuning the reaction affords a level of control to minimize interfilamentous voids while retaining the drastic improvements to interlayer adhesion due to covalent reactions observed for the *in-situ* UV irradiated samples. To control this process, the *in-situ* UV power was tuned. Figure 5.6a and Figure 5.6b illustrate the effect of UV power on the mechanical properties of the PLATM blends. Even at 25% power, the observed transverse maximum stress is equivalent to those samples at 100% power. Additionally, the modulus is substantially higher than in the 100% power samples. Inspection of Figure 5.7 illustrates that the interfilamentous voids are extremely small in the fractionally irradiated samples, similar to non-irradiated samples. As the power increases to 50%, the observed mechanical properties are nearly identical to those

123

samples at 25% UV power. Likewise, the voids are small. For these irradiation levels, the reaction still proceeds, albeit, at a slower rate such that the chains have adequate time to flow between filaments during the printing process. At 75% UV power, however, the properties diverge slightly. Samples irradiated at 75% UV power exhibit transverse maximum stresses that are lower than all other irradiation levels, but these samples exhibit the highest modulus. Within this sample, the voids are small as in the 25% and 50% illuminated samples, but the fracture does not appear to occur in as brittle a fashion. It appears that 75% UV power is a transitional point where the voids are minimized yet the reaction occurs more quickly than at the lower irradiation levels. At this point, the flow of the chains between filaments is inhibited by the reaction, yet still flow enough to minimize voids. This interpretation nicely explains the small *decrease* in the transverse maximum stress and *increase* in modulus where increased voids mean less interfacial interaction of the chains. Lastly, at 100% irradiation, it appears that the presence of large voids indicates a very quick reaction that inhibits interfilament chain diffusion due to the fast reaction, but this is counteracted by the formation of covalent bonds across the interface that substantially strengthens the inter-layer adhesion. Thus, at low irradiation levels (25-50%), a reaction occurs, but not as readily as in the high irradiation regime. Furthermore, low levels of UV irradiation allow minimization of the voids, but not at the expense of interlayer adhesion. Irradiation levels between 50 and 75% UV power appear to be optimal conditions where voids are minimized, tensile strength and modulus are maximized, and the printed part is the most isotropic.

UV DSC of 35k PLATM

Modification of the *in-situ* UV power illustrates a level of control over the percent conversion of the methacrylate moieties in the PLATM printed specimens. To corroborate this interpretation, UV DSC was utilized. From the results presented in Figure 5.8 and Table 5.1, the LMW additive PLATM does indeed react with a maximum of 67% conversion at a UV intensity of 24 mW/cm^2. The peak observed in the DSC is indicative of the enthalpy of reaction of the methacrylate functionalities and illustrates that the reaction readily occurs over approximately a 1 min. span. In a typical FDM print, the layers cool very quickly only reaching the nozzle temperature for 1-2 secs; however, recent work has shown that the layers maintain an elevated temperature on the time scale of minutes. The results of the UV DSC, therefore, indicate that even at only 10°C above the T$_g$, PLATM reaction occurs. The print conditions are therefore sufficient to allow adequate reaction to occur. Furthermore, while the signal to background is small making quantification imprecise, the data shows that less reaction occurs at an intensity of 15 mW/cm^2 than with illumination at 23 and 24 mW/cm^2. This is consistent with the mechanical property and SEM data presented above where more voids are present in samples exposed to high intensities of UV because of a higher extent of conversion. Thus, by controlling the UV intensity, the extent of reaction can be tuned, reducing the presence of interfilamentous voids, and yielding a printed part that is mechanically robust and nearly isotropic.

CONCLUSION

The introduction of LMW-SuSAs to a neat polymer blend offers improved interlayer adhesion and improved isotropy of FDM printed objects. To further improve

the interlayer adhesion and isotropy, we report a novel reactive processing protocol for extrusion-based 3D printing, where the LMW-SuSAs were modified to include methacrylate end-groups that can undergo crosslinking reactions between filaments. The addition of the methacrylate groups and a photoinitiator to the blends offer the ability to reactively process printed parts via *in-situ* UV irradiation and induce coupling reactions across the interlayer interface. From these experiments, we have achieved parts with transverse maximum stresses that are ~200% stronger than the neat samples. Additionally, the samples become substantially more isotropic. Control of the reaction *in-situ* by modification of the UV power offers a pathway to balance the inhibition of chain motion by the fast formation of crosslinks and the strengthening of inter-filament interfaces with the covalent bonds. Ultimately, the ease of implementation of this methodology offers reactive processing capabilities within the FDM space across multiple material platforms bringing the industry closer to mechanically isotropic printed objects.

Chapter 6 - CONCLUSIONS AND FUTURE WORK

CONCLUSIONS

Through this dissertation work, a series of low molecular weight surface-segregating additives were developed and tested for their ability to direct enhanced interlayer adhesion and improve isotropy in FDM printed objects. A comprehensive study of the effect of molecular weight, additive concentration, polymer architecture, and chemical identity clearly indicates that substantial improvements to the interlayer adhesion may be obtained with the addition of surface-segregating additives. The experiments illustrate the importance of utilizing an additive that is sufficiently long to entangle yet readily surface segregates and diffuses between adjacent printed layers. Furthermore, entropically driven surface segregation facilitates improved interlayer adhesion through the concentration of low molecular weight components to the interface. Subsequently, the faster diffusion of the low molecular weight additive relative to its bulky, high molecular weight counterpart leads to an increased number of chain entanglements between layers and a more robust interface. The experiments also illustrate the potential for reactive processing where nearly isotropic parts may be realized by the inclusion of crosslinkable moieties to the low molecular weight additive. Covalent crosslinking of adjacent layers stimulated by the application of UV light in the presence of a photoinitiator leads to substantially more robust and isotropic FDM printed parts. The methodology presented in this work is easily implemented and expandable across multiple material platforms making it amenable to not only FDM printing but many current polymer processing technologies. Further, the experiments highlight the importance of understanding the polydispersity of polymer blends and the large impact the addition of additives, such as LMW-SuSAs, have on the processability of polymer melts.

Bimodal molecular weight samples and interlayer diffusion

Investigation of a series of LMW polylactide components introduced to a commercial PLA filament yields substantial improvements to the interlayer adhesion and isotropy of FDM printed objects. The work presented provides convincing evidence that this is due to the lower molecular weight polymer's quick diffusion across the inter-filament interface during the 3D printing process. A more robust interface is realized. Investigation of the effect of molecular weight and loading illustrates that improvements to the isotropy are governed by a balance between the plasticization of the blend and the requirement that the additive is sufficiently long to entangle across the interface. Furthermore, the developed methodology illustrates that a reduction in the interfilamentous voids prevalent in typical FDM printed objects is not sufficient nor an indication of the interlayer adhesion and isotropy. For example, in the presented work the addition of an 8.5k poly(lactide) LMW-SuSA at 10 mol% loading leads to nearly no interfilamentous voids, yet the mechanical strength of the interface is poorer than that of the neat material. At molecular weights below the entanglement length, M_e, of the polymer, the additive only functions as a traditional plasticizer. While this is shown to reduce the interfilamentous voids in the printed objects and in certain instances may lead to enhanced interlayer adhesion, it is not sufficient to the development of isotropic FDM objects. Conversely, at high molecular weights, diffusion of the additive is inhibited also leading to poor interlayer adhesion and anisotropic printed objects. A balance between these two extremes is thus a vital component to increasing interlayer adhesion and improving isotropy in FDM objects.

Building on these observations, the architecture of the additive also significantly impacts the ability of the LMW-SuSA to increase the interlayer adhesion of parts fabricated by FDM. In a similar fashion to linear additives, the addition of a branching arm to make a 3-arm star LMW additive results in improved diffusion consistent with a linear additive of similar molecular weight. However, the additional branching arm provides another point of entanglement which leads to drastically improved interlayer properties relative to a linear additive. The addition of a second arm to make a 4-arm star, however, inhibits the formation of robust interfacial welds. This may be attributed to the poor diffusion and entanglement of the additive across the interfilament interface. From these experiments, it is clear that both faster diffusion and increased entanglement of the additive is vitally important to the observed interfacial mechanical properties.

Experimental verification of surface segregation in FDM printed objects

Substantial evidence provided by adhesion testing, mechanical testing, void image analysis, and rheological measurements indicates that the addition of LMW additives to create bimodal blends may only significantly improve interlayer adhesion and reduce the isotropy when the additive readily diffuses and is of sufficient length to entangle. The experiments suggest that this is a result of the entropically driven surface segregation of low molecular weight components to the interface. To confirm the surface segregation of the LMW-SuSAs, energy dispersive x-ray spectroscopy was employed. Exploitation of the contrast afforded by the difference between additive and matrix in ABS printed objects provides a mechanism to identify the location of the additive within the part. Investigation of the resultant blends by SEM-EDS provides evidence that the LMW additives do indeed preferentially enrich the interface of an FDM filament. Therefore, the

130

experiments provide confirmation that LMW additives concentrate at the interface where they may readily diffuse and entangle with adjacent layers under standard FDM deposition conditions. Significantly improved interlayer adhesion and more isotropic FDM objects result. As an extension of this work, miscibility of the additive with the ABS did not appear to play a vital role in the observed interlayer properties. At the lowest molecular weights studied, both PMMA and PLA led to increases in the isotropy of the part. Interestingly though, PLA is immiscible in the matrix. Ultimately, these studies provide a more fundamental understanding of the mechanisms that drive enhanced interlayer adhesion and improved isotropy with the addition of LMW-SuSAs.

UV initiated reactive processing

The remarkable properties observed with the addition of LMW-SuSAs provided an excellent platform to build upon. To this end, the introduction of reactive processing type methodologies could be employed. By the simple addition of methacrylate groups to the LMW-SuSA, in the presence of a photoinitiator and UV stimulus, nearly isotropic and superior printed objects were obtained. Where un-modified LMW-SuSAs increased the tensile strength of transversely oriented parts by 100%, methacrylate modified and UV reactively processed LMW-SuSAs increased the tensile strength by over 200%. The experiments suggest that UV irradiation of the methacrylate moieties induces covalent crosslinks. Crosslinking between layers is then responsible for the observed interlayer properties. Further evidence that LMW-SuSAs indeed surface segregate is provided within these experiments where the addition of modified LMW-SuSAs without UV leads to a smaller magnitude increase to the interlayer mechanical properties than that of a blend containing just photoinitiator. The results suggest, that the interfacial properties are

131

thus dictated by the presence of the LMW additive. Interestingly, the data provided does indicate that the photoinitiator may additionally function as a thermal initiator in the melt, facilitating a level of crosslinking/branching of the PLA chains. This seemingly works in conjunction with the plasticization of the blend afforded by the small molecule to beneficially increase the interlayer adhesion of printed objects. However, UV initiation of the LMW additives in the blend provides substantially more robust printed objects than those obtained by only the presence of a photoinitiator. While room temperature post UV irradiation was shown to provide no beneficial improvements to the interfacial properties of printed blends, control of the reaction, in-situ, by modification of the UV power affords a level of control of the reaction. Investigation of these reactively processed blends indicates that UV crosslinking inhibits the mobility of the deposited polymers. Larger interfilamentous voids are observed. By adjusting the UV power, the reaction can be attenuated to minimize these voids producing a printed object that is both more cohesive and mechanically robust. Ultimately, the presented experiments illustrate the generation of robust and nearly isotropic printed objects can be realized by the UV initiated crosslinking of LMW-SuSAs between interfilament layers.

Summary

The overall goal of the presented work has been to develop and understand the underlying mechanisms that lead to improved isotropy in FDM printed objects with the introduction of low molecular weight surface-segregating additives. The methodology developed begins simply with the introduction of linear low molecular weight additives to commercially available polymer materials. The success of that work prompted a more in-depth investigation of the additives to further understand the effects of molecular weight

and architecture on the LMW-SuSAs role within the blend. Ultimately, the work provided insight into the necessity of the additives to readily diffuse and also readily entangle. A balance between these two requirements being fundamental to realize *increased* interlayer adhesion and more isotropic FDM printed objects. Further experiments expanded the developed methodology to other material platforms and confirmed the surface segregation of LMW components within the blends to the interface. Vital insight into the mechanisms that leads to the observed mechanical properties was therefore realized. Continuing to build upon the LMW methodology, reactively processed additives were prepared. The results of these experiments led to nearly isotropic printed objects facilitated by the crosslinking of the modified LMW-SuSA between printed layers. UV initiation of these systems *in-situ* holds a distinct advantage to post-modification by eliminating wasted time while providing drastically improved interlayer properties.

Thus, the ease of implementing LMW-SuSAs and their subsequent reactive modifications into current polymer processing technologies, across multiple material platforms, makes it a distinctly advantageous system. With this developed methodology, the FDM and 3D printing industry moves closer to mechanically isotropic printed objects suitable for use within the industrial space.

FUTURE WORK

The experiments presented above illustrate the vast potential in utilizing LMW additives to direct enhanced interlayer adhesion in FDM printed objects. The experiments presented prove the viability of the methodology and illuminate some of the underlying mechanisms that lead to more isotropic FDM objects, yet future work can expand on these

insights to provide better quantification of the UV reactions and how the reactions are affected by the complex thermal environment of FDM.

Quantifying the extent of reaction in reactively processed blends

It is clear that the use of reactively modified LMW-SuSAs to induce crosslinking between printed layers leads to substantially more isotropic FDM printed objects. From these experiments, it is also clear that UV light is necessary to initiate the reaction, but the extent of reaction and the number of crosslinks is unknown. In the previous work, photo-DSC was employed to confirm the reaction of the methacrylated PLA in the presence of a plasticizer. Temperature limits of the UV fixture limited access to print temperatures; however, future experiments should look to revisit both photo-DSC and photo-rheology instruments with the appropriate high-temperature probe. From these experiments, the extent of the reaction in the blend at print temperatures can be obtained. Additional information can be gleaned by varying the UV intensity to corroborate and quantify the effect of UV intensity on the extent of crosslinking and ultimately the observed mechanical properties.

UV penetration depth and thermal history

Another important experiment will look to understand the penetration depth of UV within the printed samples. This is important to better understand the reaction mechanism throughout the print and to understand how subsequent passes of the print nozzle and UV light may induce further crosslinking. In typical FDM prints, the filament spends only 1-2s at print temperature and then rapidly decays. Subsequent passes of the heated nozzle re-heat the deposited layers to a small degree where layers typically spend most of the print around 50°C. For PLA, this is below but near the T_g. To carry out these experiments a light

probe will be affixed to the bottom of the print. A solid layer will be printed followed by UV light exposure. The decay in the flux as read by the light meter with the addition of subsequent layers allows one to determine the UV penetration depth. IR thermography will monitor the individual layer height and allow one to couple the layer temperature to the UV flux. These experiments will provide insight into the potential for additional crosslinking with subsequent passes of the UV light. Further, the results of these experiments may be coupled with the results obtained from photo-DSC and rheology to provide a more comprehensive and quantitative picture of the crosslinking reaction under the complex thermal conditions of FDM printing.

Tailoring reactivity of LMW-SuSA by end group choice

Methacrylate end groups served as a great option for UV crosslinking in the examined blends; however, it is of interest to probe other reactive end groups and how this impacts the properties of reactively processed FDM objects. In the case of methacrylated PLA, large voids were present within the sample presumably due to the fast crosslinking reaction that immobilized polymers after deposition. While adjusting UV power was capable of minimizing these voids and maintaining the robust interlayer adhesion properties, tuning the end group reactivity may also serve this function and provide further tunability in terms of strength, modulus, and toughness. To probe this, a number of double bond terminated end groups will be selected. By varying the size of the adjacent side groups, we can intuitively inhibit the crosslinking reaction and monitor how this impacts the ability of the additive to crosslink under FDM processes. In terms of end group size, we can introduce from smallest to largest, acrylate, methacrylate, and styrenic moieties to the polymer chain. Bimodal blends will be prepared and printed by FDM with *in-situ* UV

135

as previously reported. This will then be coupled to the extent of crosslinking and observed mechanical properties. Going a step further, these moieties may be introduced at additional points along the chain to provide more reactive centers. More reactive centers should equate to more crosslinking reactions and more robust prints. This can be coupled to the size of interfilamentous voids and the reactive functionalities present to provide a comprehensive correlation of number of reactive groups to the observed mechanical properties.

LIST OF REFERENCES

(1)   Tofail, S. A. M.; Koumoulos, E. P.; Bandyopadhyay, A.; Bose, S.; O'Donoghue, L.; Charitidis, C. Additive Manufacturing: Scientific and Technological Challenges, Market Uptake and Opportunities. *Mater. Today* **2018**, *21* (1), 22–37.

(2)   Gao, W.; Zhang, Y.; Ramanujan, D.; Ramani, K.; Chen, Y.; Williams, C. B.; Wang, C. C. L.; Shin, Y. C.; Zhang, S.; Zavattieri, P. D. The Status, Challenges, and Future of Additive Manufacturing in Engineering. *CAD Comput. Aided Des.* **2015**, *69*, 65–89.

(3)   Wong, K. V.; Hernandez, A. A Review of Additive Manufacturing. *Mech. Eng.* **2015**, *2012* (1), 1–11.

(4)   Leal, R.; Barreiros, F. M.; Alves, L.; Romeiro, F.; Vasco, J. C.; Santos, M.; Marto, C. Additive Manufacturing Tooling for the Automotive Industry. *Int. J. Adv. Manuf. Technol.* **2017**, *92* (5–8), 1671–1676.

(5)   Bose, S.; Vahabzadeh, S.; Bandyopadhyay, A. Bone Tissue Engineering Using 3D Printing. *Mater. Today* **2013**, *16* (12), 496–504.

(6)   Wang, X.; Jiang, M.; Zhou, Z.; Gou, J.; Hui, D. 3D Printing of Polymer Matrix Composites: A Review and Prospective. *Compos. Part B Eng.* **2017**, *110*, 442–458.

(7)   Zein, I.; Hutmacher, D. W.; Tan, K. C.; Teoh, S. H. Fused Deposition Modeling of Novel Scaffold Architectures for Tissue Engineering Applications. *Biomaterials* **2002**, *23* (4), 1169–1185.

(8)   Melchels, F. P. W.; Feijen, J.; Grijpma, D. W. A Review on Stereolithography and Its Applications in Biomedical Engineering. *Biomaterials* **2010**, *31* (24), 6121–6130.

(9)   Rahmat, M. Silane Crosslinking of Poly(Lactic Acid): The Effect of Simultaneous Hydrolytic Degradation. *Express Polym. Lett.* **2015**, *9* (12), 1133–1141.

(10)   Redwood, B. Additive Manufacturing Technologies: An Overview https://www.3dhubs.com/knowledge-base/additive-manufacturing-technologies-overview (accessed Feb 19, 2019).

(11)   Taormina, G.; Sciancalepore, C.; Messori, M.; Bondioli, F. 3D Printing Processes for Photocurable Polymeric Materials : Technologies , Materials , and Future Trends. **2018**.

(12)   Tumbleston, J. R.; Shirvanyants, D.; Ermoshkin, N.; Janusziewicz, R.; Johnson, A. R.; Kelly, D.; Chen, K.; Pinschmidt, R.; Rolland, J. P.; Ermoshkin, A.; et al. Continuous Liquid Interface Production of 3D Objects. **2015**, *347* (6228), 635–639.

(13)   Tyge, E.; Pallisgaard, J. J.; Lillethorup, M.; Hjaltalin, N. G.; Thompson, M. K.; Clemmensen, L. H. Characterizing Digital Light Processing (DLP) 3D Printed Primitives; Springer, Cham, 2015; pp 302–313.

(14)   Gordeev, E. G.; Galushko, A. S.; Ananikov, V. P. Improvement of Quality of 3D

Printed Objects by Elimination of Microscopic Structural Defects in Fused Deposition Modeling. **2018**.

(15) Lee, C. S.; Kim, S. G.; Kim, H. J.; Ahn, S. H. Measurement of Anisotropic Compressive Strength of Rapid Prototyping Parts. *J. Mater. Process. Technol.* **2007**, *187–188*, 627–630.

(16) Ahn, S. H.; Montero, M.; Odell, D.; Roundy, S.; Wright, P. K. Anisotropic Material Properties of Fused Deposition Modeling ABS. *Rapid Prototyp. J.* **2002**, *8* (4), 248–257.

(17) Motaparti, K. P.; Taylor, G.; Leu, M. C.; Chandrashekhara, K.; Castle, J.; Matlack, M. Experimental Investigation of Effects of Build Parameters on Flexural Properties in Fused Deposition Modelling Parts. *Virtual Phys. Prototyp.* **2017**, *12* (3), 207–220.

(18) Levenhagen, N. P.; Dadmun, M. D. Interlayer Diffusion of Surface Segregating Additives to Improve the Isotropy of Fused Deposition Modeling Products. *Polymer (Guildf).* **2018**, *152*.

(19) Shaffer, S.; Yang, K.; Vargas, J.; Di Prima, M. A.; Voit, W. On Reducing Anisotropy in 3D Printed Polymers via Ionizing Radiation. *Polymer (Guildf).* **2014**, *55* (23), 5969–5979.

(20) Levenhagen, N. P.; Dadmun, M. D. Bimodal Molecular Weight Samples Improve the Isotropy of 3D Printed Polymeric Samples. *Polym. (United Kingdom)* **2017**, *122*, 232–241.

(21) Anisotropy https://www.britannica.com/science/anisotropy (accessed Mar 1, 2019).

(22) Kurabayashi, K. Anisotropic Thermal Properties of Solid Polymers. *Int. J. Thermophys.* **2001**, *22* (1), 277–288.

(23) Arruda, E. M.; Boyce, M. C. Evolution of Plastic Anisotropy in Amorphous Polymers During Finite Straining. *Int. J. Plast.* **1993**, *9*, 697–720.

(24) Hennig, J. Anisotropy and Structure in Uniaxially Stretched Amorphous High Polymers. *J. Polym. Sci. Part C Polym. Symp.* **1967**, *16* (5), 2751–2761.

(25) Anitha, R.; Arunachalam, S.; Radhakrishnan, P. Critical Parameters Influencing the Quality of Prototypes in Fused Deposition Modelling. *J. Mater. Process. Technol.* **2001**, *118* (1–3), 385–388.

(26) Chockalingam, K.; Jawahar, N.; Praveen, J. Enhancement of Anisotropic Strength of Fused Deposited ABS Parts by Genetic Algorithm. *Mater. Manuf. Process.* **2016**, *31* (15), 2001–2010.

(27) Tian, X.; Liu, T.; Yang, C.; Wang, Q.; Li, D. Interface and Performance of 3D Printed Continuous Carbon Fiber Reinforced PLA Composites. *Compos. Part A Appl. Sci. Manuf.* **2016**, *88* (October 2017), 198–205.

(28) Costa, S. F.; Duarte, F. M.; Covas, J. A. Thermal Conditions Affecting Heat Transfer in FDM/FFE: A Contribution towards the Numerical Modelling of the Process: This Paper Investigates Convection, Conduction and Radiation Phenomena in the Filament Deposition Process. *Virtual Phys. Prototyp.* **2015**, *10* (1), 35–46.

(29) Comminal, R.; Serdeczny, M. P.; Pedersen, D. B.; Spangenberg, J. Numerical Modeling of the Strand Deposition Flow in Extrusion-Based Additive Manufacturing. *Addit. Manuf.* **2018**, *20*, 68–76.

(30) Seppala, J. E.; Migler, K. D. Infrared Thermography of Welding Zones Produced by Polymer Extrusion Additive Manufacturing. *Addit. Manuf.* **2016**, *12*, 71–76.

(31) Sun, Q.; Rizvi, G. M.; Bellehumeur, C. T.; Gu, P. *Experimental Study of the Cooling Characteristics of Polymer Filaments in FDM and Impact on the Mesostructures and Properties of Prototypes*.

(32) Chacón, J. M.; Caminero, M. A.; García-Plaza, E.; Núñez, P. J. Additive Manufacturing of PLA Structures Using Fused Deposition Modelling: Effect of Process Parameters on Mechanical Properties and Their Optimal Selection. *Mater. Des.* **2017**, *124*, 143–157.

(33) Swallowe, G. M. Tensile and Compressive Testing. In *Mechanical Properties*; Swalloe, G. M., Ed.; 1999; pp 242–247.

(34) Kulkarni, P.; Dutta, D. Deposition Strategies and Resulting Part Stiffnesses in Fused Deposition Modeling. *J. Manuf. Sci. Eng.* **1999**, *121* (1), 93.

(35) Pan, A. Q.; Huang, Z. F.; Guo, R. J.; Liu, J. Effect of FDM Process on Adhesive Strength of Polylactic Acid(PLA) Filament. *Key Eng. Mater.* **2015**, *667*, 181–186.

(36) Croccolo, D.; De Agostinis, M.; Olmi, G. Experimental Characterization and Analytical Modelling of the Mechanical Behaviour of Fused Deposition Processed Parts Made of ABS-M30. *Comput. Mater. Sci.* **2013**, *79*, 506–518.

(37) Mohamed, O. A.; Masood, S. H.; Bhowmik, J. L. Experimental Investigations of Process Parameters Influence on Rheological Behavior and Dynamic Mechanical Properties of FDM Manufactured Parts. *Mater. Manuf. Process.* **2016**, *31* (15), 1983–1994.

(38) Aliheidari, N.; Tripuraneni, R.; Ameli, A.; Nadimpalli, S. Fracture Resistance Measurement of Fused Deposition Modeling 3D Printed Polymers. *Polym. Test.* **2017**, *60*, 94–101.

(39) Ahmed, O.; Hasan, S.; Lal, J.; Somers, A. E. Investigation on the Tribological Behavior and Wear Mechanism of Parts Processed by Fused Deposition Additive Manufacturing Process. *J. Manuf. Process.* **2017**, *29*, 149–159.

(40) Alafaghani, A.; Qattawi, A.; Alrawi, B.; Guzman, A. Experimental Optimization of Fused Deposition Modelling Processing Parameters: A Design-for-Manufacturing Approach. *Procedia Manuf.* **2017**, *10*, 791–803.

(41) Bellini, A.; Güçeri, S. Mechanical Characterization of Parts Fabricated Using Fused Deposition Modeling. *Rapid Prototyp. J.* **2003**, *9* (4), 252–264.

(42) Bagsik, A.; Schöoppner, V. Mechanical Properties of Fused Deposition Modeling Parts Manufactured with ULTEM 9085. *Antec* **2011**.

(43) McIlroy, C.; Olmsted, P. D. Disentanglement Effects on Welding Behaviour of Polymer Melts during the Fused-Filament-Fabrication Method for Additive Manufacturing. *Polymer (Guildf).* **2017**, *123*, 376–391.

(44) Practical Applications for Melt Rheology in Polymer Processing. *Plastics Engineering*. 2000, pp 38–38.

(45) Ahn, S. H.; Montero, M.; Odell, D.; Roundy, S.; Wright, P. K. Anisotropic Material Properties of Fused Deposition Modeling ABS. *Rapid Prototyp. J.* **2002**, *8* (4), 248–257.

(46) Gurrala, P. K.; Regalla, S. P. Multi-Objective Optimisation of Strength and Volumetric Shrinkage of FDM Parts: A Multi-Objective Optimization Scheme Is Used to Optimize the Strength and Volumetric Shrinkage of FDM Parts Considering Different Process Parameters. *Virtual Phys. Prototyp.* **2014**, *9* (2), 127–138.

(47) Boschetto, A.; Bottini, L. Design for Manufacturing of Surfaces to Improve Accuracy in Fused Deposition Modeling. *Robot. Comput. Integr. Manuf.* **2016**, *37*, 103–114.

(48) Bellehumeur, C.; Li, L.; Sun, Q.; Gu, P. Modeling of Bond Formation between Polymer Filaments in the Fused Deposition Modeling Process. *J. Manuf. Process.* **2004**, *6* (2), 170–178.

(49) Acrawal, C.; Jose, S.; Ahn, S.-H. H.; Montero, M.; Odell, D.; Roundy, S.; Wright, P. K.; Anitha, R.; Arunachalam, S.; Radhakrishnan, P.; et al. Temperature (°C). *Polymer (Guildf).* **2016**, *9* (2), 2–3.

(50) Hiemenez, P. C.; Lodge, T. *Polymer Chemistry*, 2nd ed.; Boca Raton: CRC Press, 2007.

(51) Homma, H.; Kuroyagi, T.; Mirley, C. L.; Ronzello, J.; Boggs, S. a. Diffusion of Low Molecular Weight Siloxane from Bulk to Surface [Outdoor Insulators]. *IEEE Trans. Dielectr. Electr. Insul.* **1999**, *6* (3), 370–375.

(52) Zhao, W.; Zhao, X.; Rafailovich, M. H.; Sokolov, J.; Composto, R. J.; Smith, S. D.; Satkowski, M.; Russell, T. P.; Dozier, W. D.; Mansfield, T. Segregation of Chain Ends to Polymer Melt Surfaces and Interfaces. *Macromolecules* **1993**, *26* (3), 561–562.

(53) Gardella, J. A.; Mahoney, C. M. Determination of Oligomeric Chain Length Distributions at Surfaces Using ToF-SIMS: Segregation Effects and Polymer Properties. *Appl. Surf. Sci.* **2004**, *231–232*, 283–288.

(54) Minnikanti, V. S.; Archer, L. A. Entropic Attraction of Polymers toward Surfaces

and Its Relationship to Surface Tension. *Macromolecules* **2006**, *39* (22), 7718–7728.

(55) Brosetav, D.; Fredrickson, G. H.; Helfand, E.; Leibler, L. Molecular Weight and Polydispersity Effects at Polymer-Polymer Interfaces. *Macromolecules* **1990**, *23* (1), 132–139.

(56) Yethiraj, A.; Kumar, S.; Hariharan, A.; Schweizer, K. S. Surface Segregation in Polymer Blends Due to Stiffness Disparity. *J. Chem. Phys.* **1994**, *100* (6), 4691–4694.

(57) Hariharan, A.; Kumar, S. K.; Russel, T. P. A Lattice Model for the Surface Segregation of Polymer Chains Due to Molecular Weight Effects. *Macromolecules* **1990**, *23* (15), 3584–3592.

(58) Kajiyama, T.; Tanaka, K.; Takahara, A. Surface Segregation of the Higher Surface Free Energy Component in Symmetric Polymer Blend Films. *Macromolecules* **1998**, *31* (11), 3746–3749.

(59) Tretinnikov, O.; Ohta, K. Surface Segregation in Stereochemically Asymmetric Polymer Blends. *Langmuir* **1998**, *7463* (15), 915–920.

(60) Shimizu, R. N.; Moreira, J. C.; Demarquette, N. R.; Kamal, M. R.; Samara, M. Influence of Temperature, Molecular Weight, and Molecular Weight Dispersity on the Surface Tension of Polystyrene, Polypropylene, and Polyethylene. II. Theoretical. *J. Appl. Polym. Sci.* **2002**, *83* (10), 2201–2212.

(61) De Gennes, P.-G. *Scaling Concepts in Polymer Physics*; Cornell University Press: Ithaca, 1979.

(62) Doi, M.; Edwards, S. F. *The Theory of Polymer Dynamics*; Oxford Oxfordshire: Clarendon Press, 1928.

(63) Milner, S. T.; Mc Leish, T. C. B. Reptation and Contour-Length Fluctuations in Melts of Linear Polymers. *Phys. Rev. Lett.* **1998**, *81* (3), 725–728.

(64) Su, W.-F. *Principles of Polymer Design and Synthesis*; 2013; Vol. 82.

(65) Lodge, T. P. Reconciliation of the Molecular Weight Dependence of Diffusion and Viscosity in Entangled Polymers. *Phys. Rev. Lett.* **1999**, *83* (16), 3218–3221.

(66) Crank, J. THE MATHEMATICS OF DIFFUSION. **1975**.

(67) Agrawal, G.; Wool, R. P.; Dozier, W. D.; Felcher, G. P.; Zhou, J.; Pispas, S.; Mays, J. W.; Russell, T. P. Interdiffusion of Polymers across Interfaces. *J. Polym. Sci. Part B Polym. Phys.* **1996**, *34* (17), 2919–2940.

(68) Habuchi, S.; Fujiwara, S.; Yamamoto, T.; Tezuka, Y. Single-Molecule Imaging Reveals Topological Isomer-Dependent Diffusion by 4-Armed Star and Dicyclic 8-Shaped Polymers. *Polym. Chem.* **2015**, *6* (22), 4109–4115.

(69) Wischnewski, A.; Richter, D. Polymer Dynamics in Melts. In *Soft Matter Vol 1: Polymer Melts and Mixtures*; Gompper, G., Schick, M., Eds.; Wiley-VCH Verlag

GmbH & Co. KGaA: Weinheim; Vol. 1, pp 17–83.

(70) Kausch, H. H. Polymer Interdiffusion. *Annu. Rev. Mater. Sci.* **1989**, *19* (1), 341–377.

(71) Wool, R. P.; Willett, J. L.; McGarel, O. J.; Yuan, B. L. Strength of Polymer Interfaces. *Am. Chem. Soc. Polym. Prepr. Div. Polym. Chem.* **1987**, *28* (2), 38–39.

(72) Eastwood, E.; Viswanathan, S.; Brien, C. P. O.; Kumar, D.; Dadmun, M. D. Methods to Improve the Properties of Polymer Mixtures : Optimizing Intermolecular Interactions and Compatibilization. **2005**, *46*, 3957–3970.

(73) Rana, A. K.; Mandal, A.; Mitra, B. C.; Jacobson, R.; Rowell, R.; Banerjee, A. N.; Al, R. E. T. Short Jute Fiber-Reinforced Polypropylene Composites : Effect of Compatibilizer. **1997**, 329–338.

(74) Sailaja, R. R. N.; Deepthi, M. V. Mechanical and Thermal Properties of Compatibilized Composites of LDPE and Esterified Unbleached Wood Pulp. **2011**.

(75) JM Frechet. Functional Polymers and Dendrimers: Reactivity, Molecular Architecture, and Interfacial Energy. *Science (80-.).* **1994**, *263* (5154), 1710–1715.

(76) Ball, R. C.; McLeish, T. C. B. Dynamic Dilution and the Viscosity of Star Polymer Melts. *Macromolecules* **1989**, *22* (4), 1911–1913.

(77) Colley, F. R.; Collins, S. A.; Richards, R. W. Tracer Diffusion of Four Arm Polystyrene Star Molecules into Linear and Star Polymer Matrices from Nuclear Reaction Analysis. *J. Mater. Chem.* **2003**, *13* (11), 2765–2770.

(78) McLeish, T. C. B.; O'Connor, K. P. Rheology of Star-Linear Polymer Blends: Molecular Tube Models. *Polymer (Guildf).* **1993**, *34* (14), 2998–3003.

(79) McLeish, T. C. B.; Milner, S. T. Entangled Dynamics and Melt Flow of Branched Polymers. *Adv. Phys.* **1999**, *143*, 195–256.

(80) Milner, S. T.; McLeish, T. C. B.; Young, R. N.; Hakiki, A.; Johnson, J. M. Dynamic Dilution, Constraint-Release, and Star - Linear Blends. *Macromolecules* **1998**, *31* (26), 9345–9353.

(81) Diesendruck, C. E.; Sottos, N. R.; Moore, J. S.; White, S. R. Biomimetic Self-Healing. *Angew. Chemie - Int. Ed.* **2015**, *54* (36), 10428–10447.

(82) Bekas, D. G.; Tsirka, K.; Baltzis, D.; Paipetis, A. S. Self-Healing Materials: A Review of Advances in Materials, Evaluation, Characterization and Monitoring Techniques. *Compos. Part B Eng.* **2016**, *87*, 92–119.

(83) Liu, Y. L.; Chuo, T. W. Self-Healing Polymers Based on Thermally Reversible Diels-Alder Chemistry. *Polym. Chem.* **2013**, *4* (7), 2194–2205.

(84) Chen, W.; Zhou, Y.; Li, Y.; Sun, J.; Pan, X.; Yu, Q.; Zhou, N.; Zhang, Z.; Zhu, X. Shape-Memory and Self-Healing Polyurethanes Based on Cyclic Poly(ε-

Caprolactone). *Polym. Chem.* **2016**, 6789–6797.

(85)   Semba, T.; Kitagawa, K.; Ishiaku, U. S.; Hamada, H. The Effect of Crosslinking on the Mechanical Properties of Polylactic Acid/Polycaprolactone Blends. *J. Appl. Polym. Sci.* **2006**, *101* (3), 1816–1825.

(86)   Decker, C.; Nguyen Thi Viet, T. Photocrosslinking of Functionalized Rubbers. IX. Thiol-Ene Polymerization of Styrene-Butadiene-Block-Copolymers. *Polymer (Guildf).* **2000**, *41* (11), 3905–3912.

(87)   Krumova, M.; López, D.; Benavente, R.; Mijangos, C.; Pereña, J. M. Effect of Crosslinking on the Mechanical and Thermal Properties of Poly(Vinyl Alcohol). *Polymer (Guildf).* **2000**, *41* (26), 9265–9272.

(88)   Khonakdar, H. A.; Morshedian, J.; Wagenknecht, U.; Jafari, S. H. An Investigation of Chemical Crosslinking Effect on Properties of High-Density Polyethylene. *Polymer (Guildf).* **2003**, *44* (15), 4301–4309.

(89)   Oster, G.; Oster, G. K.; Moroson, H. Ultraviolet Induced Crosslinking and Grafting of Solid High Polymers. *J. Polym. Sci.* **1959**, *34* (127), 671–684.

(90)   Decker, C. The Use of UV Irradiation in Polymerization. *Polym. Int.* **1998**, *45* (2), 133–141.

(91)   Lin-Gibson, S.; Bencherif, S.; Cooper, J. A.; Wetzel, S. J.; Antonucci, J. M.; Vogel, B. M.; Horkay, F.; Washburn, N. R. Synthesis and Characterization of PEG Dimethacrylates and Their Hydrogels. *Biomacromolecules* **2004**, *5* (4), 1280–1287.

(92)   Martens, P.; Anseth, K. S. Characterization of Hydrogels Formed from Acrylate Modified Poly(Vinyl Alcohol) Macromers. *Polymer (Guildf).* **2000**, *41* (21), 7715–7722.

(93)   Xanthos, M.; Dagli, S. S. Compatibilization of Polymer Blends by Reactive Processing. *Polym. Eng. Sci.* **1991**, *31* (13), 929–935.

(94)   Kirchmajer, D. M.; Gorkin, R.; In Het Panhuis, M. An Overview of the Suitability of Hydrogel-Forming Polymers for Extrusion-Based 3D-Printing. *J. Mater. Chem. B* **2015**, *3* (20), 4105–4117.

(95)   Nakamura, Y.; Yamaguchi, M.; Kitayama, A.; Iko, K.; Okubo, M.; Matsumoto, T. Internal Stress of Epoxy Resin Modified with Acrylic Polymers Produced by in Situ UV Radiation Polymerization. *J. Appl. Polym. Sci.* **1990**, *39* (5), 1045–1060.

(96)   Decker, C.; Nguyen Thi Viet, T.; Decker, D.; Weber-Koehl, E. UV-Radiation Curing of Acrylate/Epoxide Systems. *Polymer (Guildf).* **2001**, *42* (13), 5531–5541.

(97)   Timpe, H.-J.; Strehmel, B. Light Induced Polymer and Polymerization Reactions, 35. Influence of Monomer Structure and Binder Composition on the Photoinduced Polymerization of Multifunctional Acrylic Esters. *Angew. Makromol. Chemie* **1990**, *178* (1), 131–142.

(98) Radiation Curing of Polymeric Materials. **1990**, *417* (11), 1990.

(99) Eibel, A.; Fast, D. E.; Gescheidt, G. Choosing the Ideal Photoinitiator for Free Radical Photopolymerizations: Predictions Based on Simulations Using Established Data. *Polym. Chem.* **2018**, *9* (41), 5107–5115.

(100) Rocha, C. R.; Perez, A. R. T.; Roberson, D. a. Novel ABS-Based Binary and Ternary Polymer Blends for Material Extrusion 3D Printing. *J. Mater. Res.* **2014**, *29* (17), 1859–1866.

(101) Rengier, F.; Mehndiratta, A.; Von Tengg-Kobligk, H.; Zechmann, C. M.; Unterhinninghofen, R.; Kauczor, H. U.; Giesel, F. L. 3D Printing Based on Imaging Data: Review of Medical Applications. *Int. J. Comput. Assist. Radiol. Surg.* **2010**, *5* (4), 335–341.

(102) Lim, S.; Buswell, R. A.; Le, T. T.; Austin, S. A.; Gibb, A. G. F.; Thorpe, T. Developments in Construction-Scale Additive Manufacturing Processes. *Autom. Constr.* **2012**, *21* (1), 262–268.

(103) Es-Said, O. S.; Foyos, J.; Noorani, R.; Mendelson, M.; Marloth, R.; Pregger, B. A. Effect of Layer Orientation on Mechanical Properties of Rapid Prototyped Samples. *Mater. Manuf. Process.* **2000**, *15* (1), 107–122.

(104) Lee, B. H.; Abdullah, J.; Khan, Z. A. Optimization of Rapid Prototyping Parameters for Production of Flexible ABS Object. *J. Mater. Process. Technol.* **2005**, *169* (1), 54–61.

(105) Ziemian, C.; Sharma, M.; Ziemi, S. Anisotropic Mechanical Properties of ABS Parts Fabricated by Fused Deposition Modelling. In *Mechanical Engineering*; Gokcek, M., Ed.; InTech: online, 2012; pp 159–180.

(106) Osswald, T. A. Mechanical Behaviors of Polymers. In *Understanding Polymer Processing*; Hanser: Munich, 2010; pp 27–54.

(107) Schonhorn, H. Surface Free Energy of Polymers. *J. Phys. Chem.* **1965**, *69* (3), 1084–1085.

(108) Scalettar, B. a; Abney, J. R.; Owicki, J. C. Theoretical Comparison of the Self Diffusion and Mutual Diffusion of Interacting Membrane Proteins. *Proc. Natl. Acad. Sci. U. S. A.* **1988**, *85* (18), 6726–6730.

(109) Dorgan, J. R.; Williams, J. S.; Lewis, D. N. AdvPolymSci1999McLeish.Pdf. *J. Rheol. (N. Y. N. Y).* **1999**, *43*, 1141.

(110) Applications, M.; Information, P. Ingeo ™ Biopolymer 4043D Technical Data Sheet 3D Printing Monofilament – General Purpose Grade. No. 4, 1–4.

(111) PolyPlus PLA Technical Data Sheet. **2015**, 2015.

(112) Tábi, T.; Sajó, I. E.; Szabó, F.; Luyt, A. S.; Kovács, J. G. Crystalline Structure of Annealed Polylactic Acid and Its. *eXPRESS Polym. Lett.* **2010**, *4* (10), 659–668.

(113) Haas, T. W.; Maxwell, B. Effects of Shear Stress on the Crystallization of Linear

Polyethylene and Polybutene-1. *Polym. Eng. Sci.* **1969**, *9* (4), 225–241.

(114) Talagani, M. R.; Dormohammadi, S.; Dutton, R.; Godines, C.; Baid, H.; Abdi, F. Numerical Simulation of Big Area Additive Manufacturing (3D Printing) of a Full Size Car. *SAMPE J.* **2015**, *51* (4), 27–36.

(115) Levenhagen, N. P.; Dadmun, M. D. Bimodal Molecular Weight Samples Improve the Isotropy of 3D Printed Polymeric Samples. *Polymer (Guildf).* **2017**, *122*, 232–241.

(116) Tead, S. F.; Kramer, E. J. Polymer Diffusion in Melt Blends of Low and High Molecular Weight. *Macromolecules* **1988**, *21* (5), 1513–1517.

(117) Dorgan, J. R.; Williams, J. S.; Lewis, D. N. Melt Rheology of Poly(Lactic Acid): Entanglement and Chain Architecture Effects. *J. Rheol. (N. Y. N. Y).* **1999**, *43* (5), 1141–1155.

(118) Klein, J.; Fletcher, D.; Fetters, L. J. Diffusional Behaviour of Entangled Star Polymers. *Nature* **1983**, *304* (5926), 526–527.

(119) Khajeheian, Mohammad B., Rosling, A. Preparation and Characterization of Linear and Star-ShapedpolyL-Lactide Blends. *J. Appl. Polym. Sci.* **2016**, *133* (2), 42231.

(120) Nunez, C. M.; Chiou, B.; Andrady, A. L.; Khan, S. A. Solution Rheology of Hyperbranched Polyesters and Their Blends with Linear Polymers. *Macromolecules* **2000**, *33* (5), 1720–1726.

(121) Klein, J. Dynamics of Entangled Linear, Branched, and Cyclic Polymers. **1986**, *118* (33), 105–118.

(122) Davidson, J. R.; Appuhamillage, G. A.; Thompson, C. M.; Voit, W.; Smaldone, R. A. Design Paradigm Utilizing Reversible Diels-Alder Reactions to Enhance the Mechanical Properties of 3D Printed Materials. *ACS Appl. Mater. Interfaces* **2016**, *8* (26), 16961–16966.

(123) Levenhagen, N. P.; Dadmun, M. D. Interlayer Diffusion of Surface Segregating Additives to Improve the Isotropy of Fused Deposition Modeling Products. *Polymer (Guildf).* **2018**, *152*, 35–41.

(124) Abbott, A. C.; Tandon, G. P.; Bradford, R. L.; Koerner, H.; Baur, J. W. Process-Structure-Property Effects on ABS Bond Strength in Fused Filament Fabrication. *Addit. Manuf.* **2018**, *19*, 29–38.

(125) Kim, Y. J.; Shin, G. S.; Lee, I. T.; Kim, B. K. Miscible and Immiscible Blends of ABS with PMMA. I. Morphology and Rheology. *J. Appl. Polym. Sci.* **1993**, *47* (2), 295–304.

(126) Prentice, P. Influence of Molecular Weight on the Fracture of Poly(Methyl Methacrylate) (PMMA). *Polymer (Guildf).* **1983**, *24* (3), 344–350.

(127) Pietrasik, J.; Dong, H.; Matyjaszewski, K. Synthesis of High Molecular Weight

Poly(Styrene-Co-Acrylonitrile) Copolymers with Controlled Architecture. *Macromolecules* **2006**, *39* (19), 6384–6390.

(128) Lomellini, P.; Lavagnini, L. Molecular Weight Polydispersity Effects on the Melt Viscoelasticity of Styrene-Acrylonitrile Random Copolymers. *Rheol. Acta* **1992**, *31* (2), 175–182.

(129) Shepherd, L.; Laboratories, B.; Hill, M. 13C-NMR of ABS in the Solid State . Characterization and Relaxation Studies. *J. Polym. Sci. Part A Polym. Chem.* **1982**, *20*, 3285–3296.

(130) Fischer, G.; Lüderwald, I.; Ottenbreit, P. Characterization of Acrylonitrile-butadiene-styrene Terpolymers by Computer Aided FT-IR Spectroscopy. *Die Angew. Makromol. Chemie* **1987**, *149* (1), 179–187.

(131) Duh, Y. S.; Ho, T. C.; Chen, J. R.; Kao, C. S. Study on Exothermic Oxidation of Acrylonitrile-Butadiene-Styrene (ABS) Resin Powder with Application to ABS Processing Safety. *Polymers (Basel).* **2010**, *2* (3), 174–187.

(132) AZoM. Polybutadiene- Properties, Applications, Processing and Types of Polybutadiene (BR) https://www.azom.com.

(133) Parameswaranpillai, J.; Thomas, S.; Grohens, Y. Characterization of Polymer Blends: Miscibility, Morphology and Interfaces. In *Characterization of Polymer Blends: Miscibility, Morphology and Interfaces*; Thomas, S., Grohens, Y., Jyotishkumar, P., Eds.; Wiley-VCH Verlag GmbH & Co. KGaA: Weinheim, 2015; pp 1–942.

(134) Han, C. D.; Yang, H. -H. Rheological Behavior of Blends of Poly(Methyl Methacrylate) (PMMA) and Poly(Acrylonitrile-stat-styrene)-graft-polybutadiene (ABS). *J. Appl. Polym. Sci.* **1987**, *33* (4), 1221–1229.

(135) Masood, S. H.; Song, W. Q. Development of New Metal/Polymer Materials for Rapid Tooling Using Fused Deposition Modelling. *Mater. Des.* **2004**, *25* (7), 587–594.

(136) Costa, S. F.; Duarte, F. M.; Covas, J. A. Estimation of Filament Temperature and Adhesion Development in Fused Deposition Techniques. *J. Mater. Process. Technol.* **2017**, *245*, 167–179.

(137) Kannurpatti, A. R.; Anderson, K. J.; Anseth, J. W.; Bowman, C. N. Use of "Living" Radical Polymerizations to Study the Structural Evolution and Properties of Highly Crosslinked Polymer Networks. *J. Polym. Sci. Part B Polym. Phys.* **1997**, *35* (14), 2297–2307.

(138) Scalera, F.; Esposito Corcione, C.; Montagna, F.; Sannino, A.; Maffezzoli, A. Development and Characterization of UV Curable Epoxy/Hydroxyapatite Suspensions for Stereolithography Applied to Bone Tissue Engineering. *Ceram. Int.* **2014**, *40* (10), 15455–15462.

(139) Cernicki, B. K.; Miihl, J. V; Janovic, Z. J.; Sliepcevic, Z. K. *Determination of the Composition of Styrene-Acrylonitrile Copolymers by Nuclear Magnetic*

Resonance.

APPENDIX
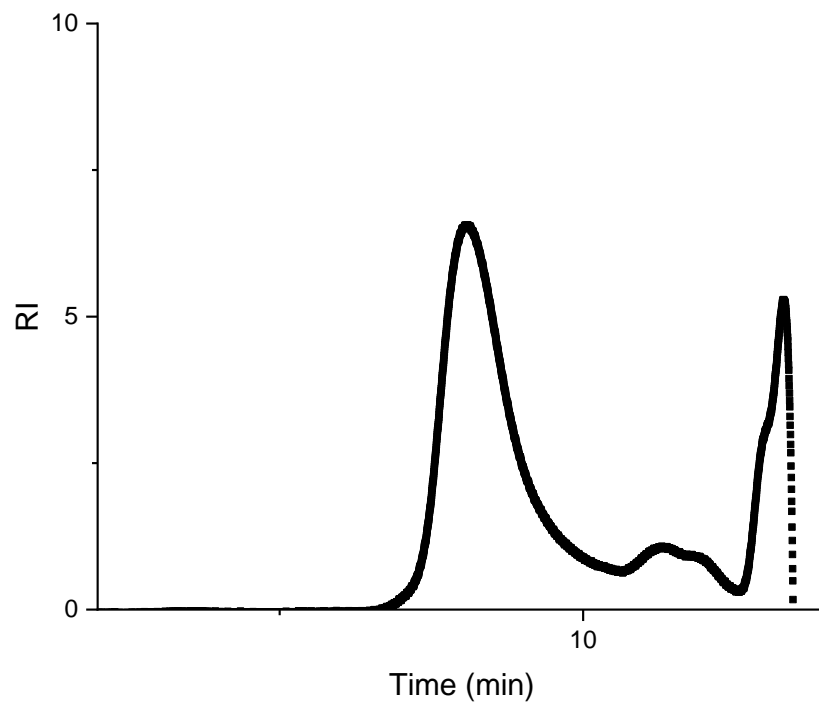
Figure S2.1 GPC trace of 8.5 kDa PLA
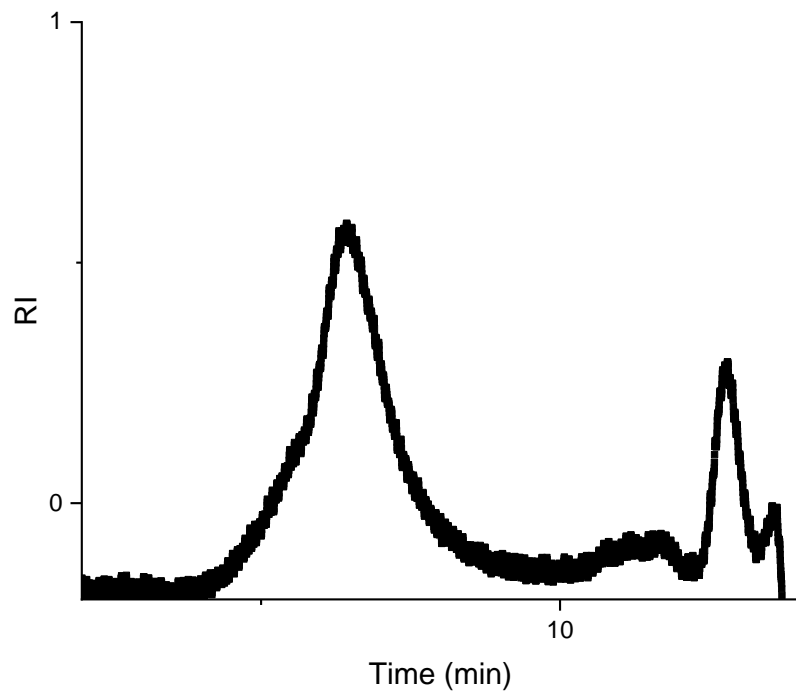
Figure S2.2 GPC trace of 50 kDa PLA
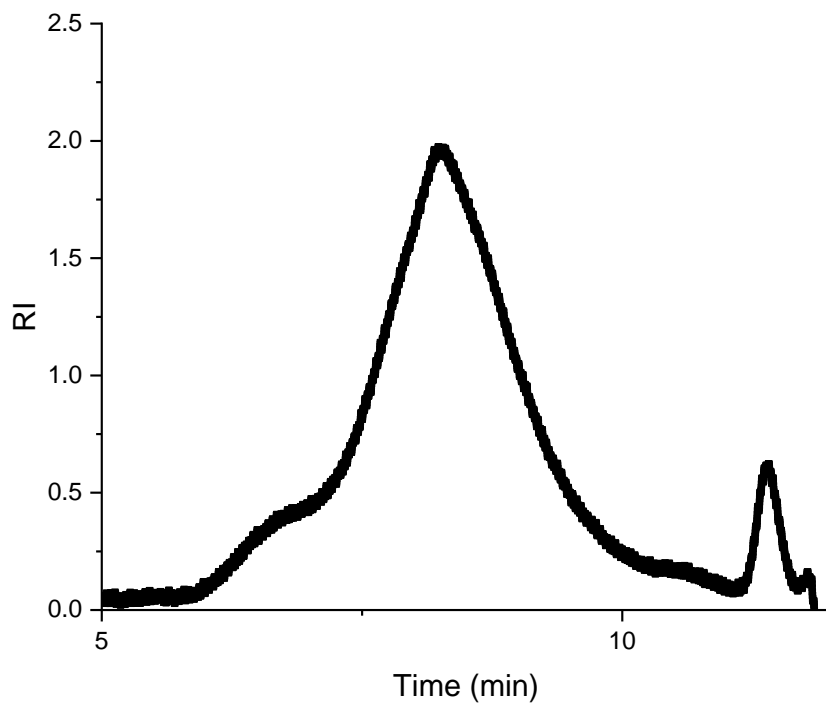
Figure S2.3 GPC trace of 100 kDa PLA
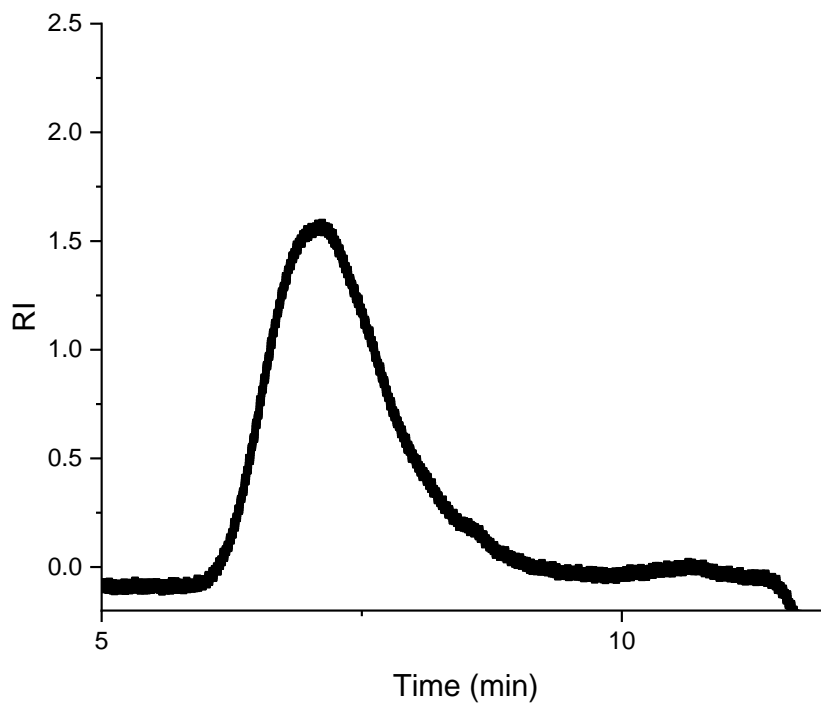
Figure S2.4 GPC trace of 220 kDA PLA (Neat)
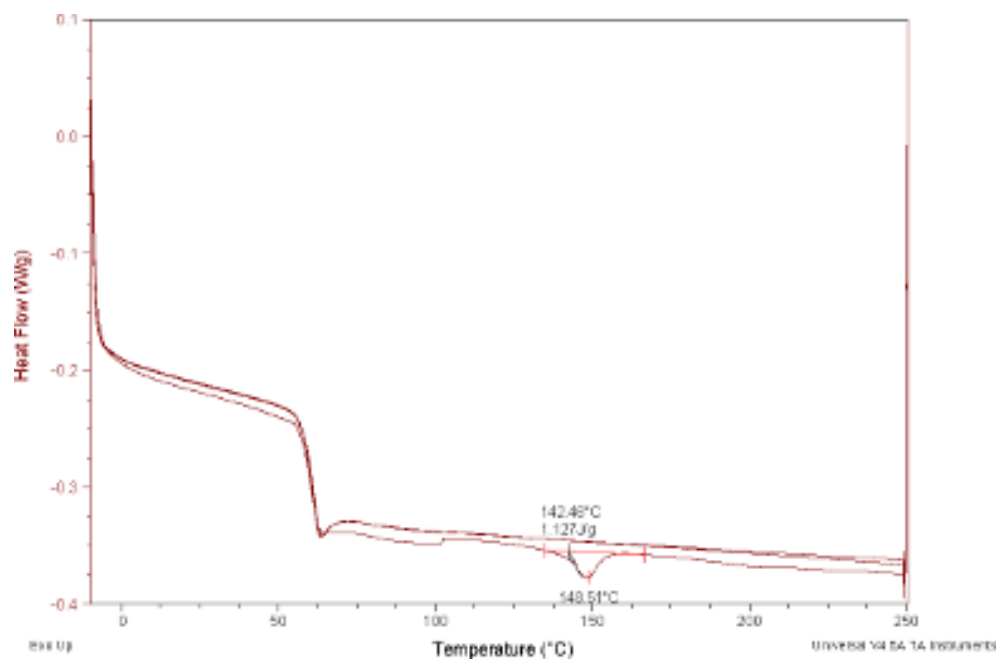
Figure S2.5 DSC thermogram of commercial HMW PLA
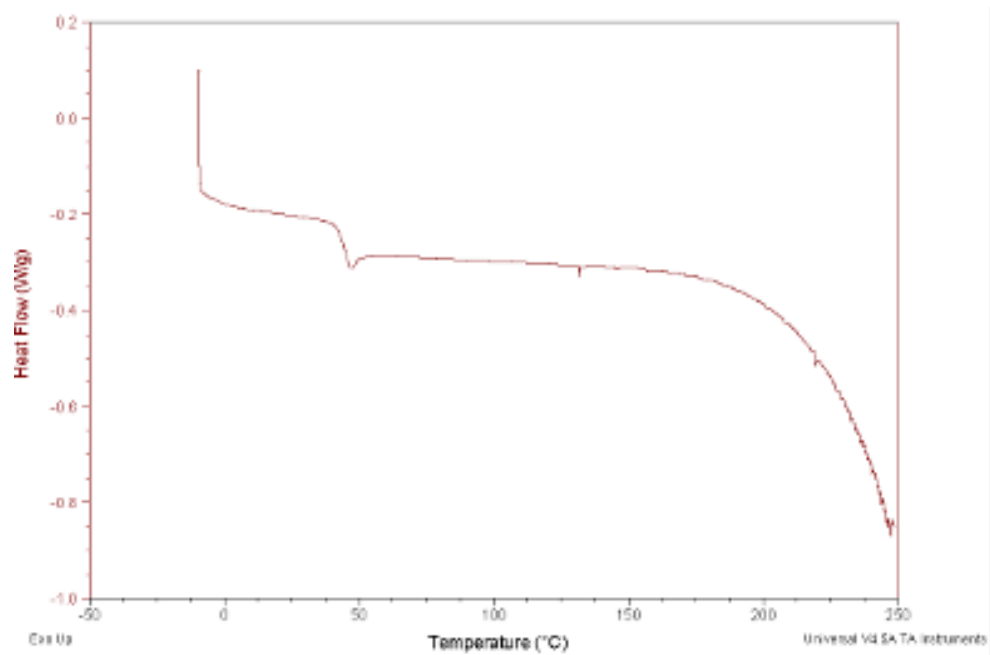
Figure S2.6 DSC thermogram of synthesized 50k PLA

Table S2.1 Thermal properties of 50k LMW and commercial HMW PLA

Sample	T_m(ºC)	T_c(ºC)	Enthalpy (J/g)	% Crystallinity
NL_1_121_50k	N/A	N/A	N/A	0
Natureworks 4043D	148.5	142.3	1.145	1.51
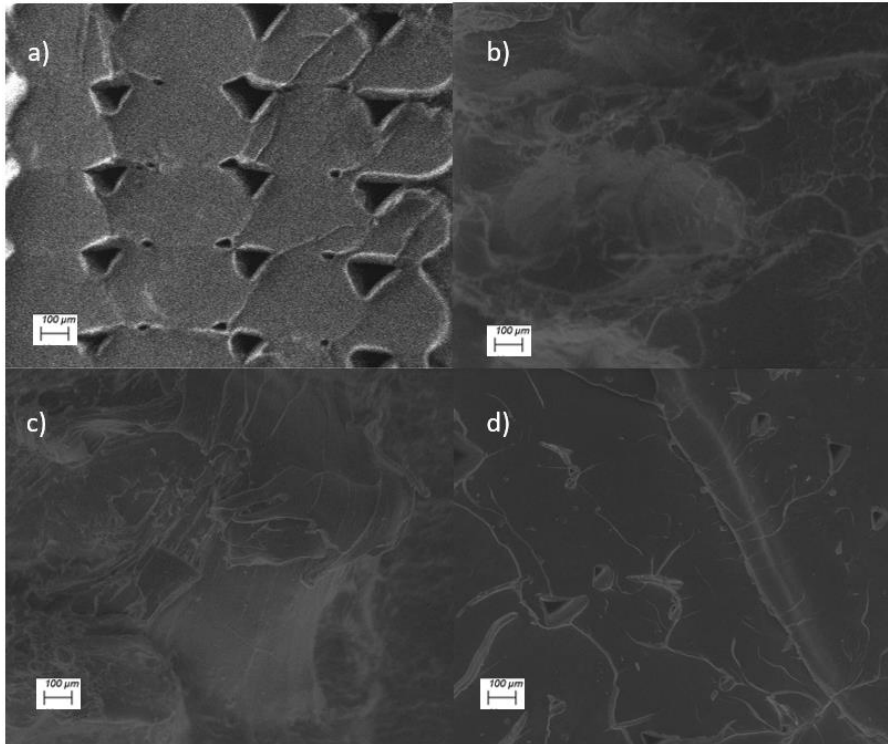
Figure S2.7 SEM image of PLA tensile specimens fracture surface in the longitudinal orientation a) neat b) 8.5k at 3 mol% c) 50k at 3 mol% and d) 100k at 3 mol%
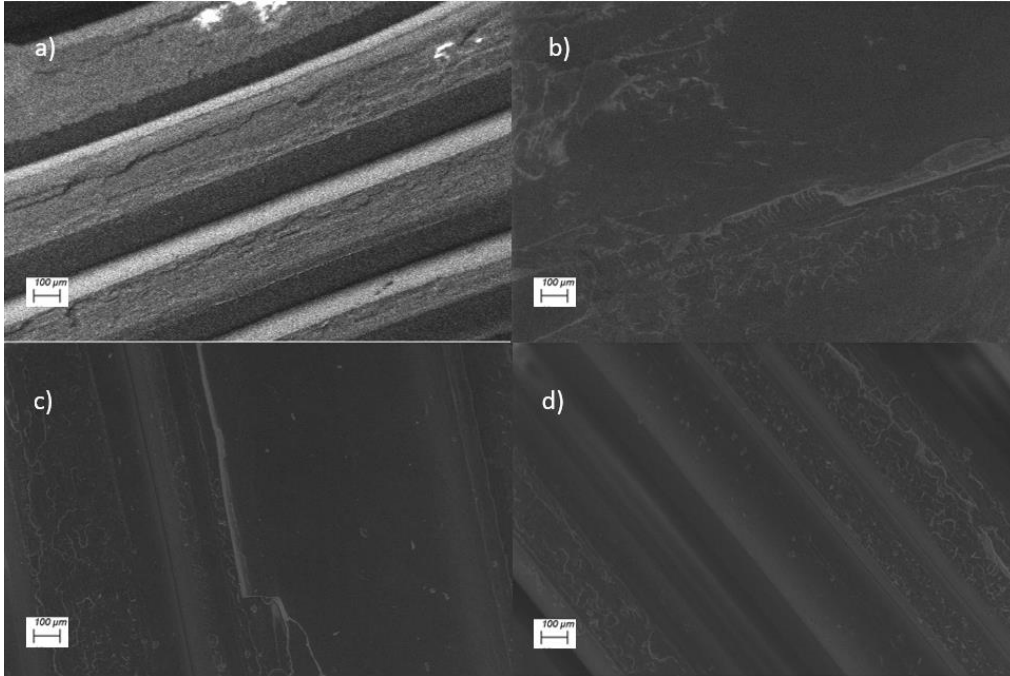
Figure S2.8 SEM image of PLA tensile specimens fracture surface in the transverse orientation a) neat b) 8.5k at 3 mol% c) 50k at 3 mol% and d) 100k at 3 mol%
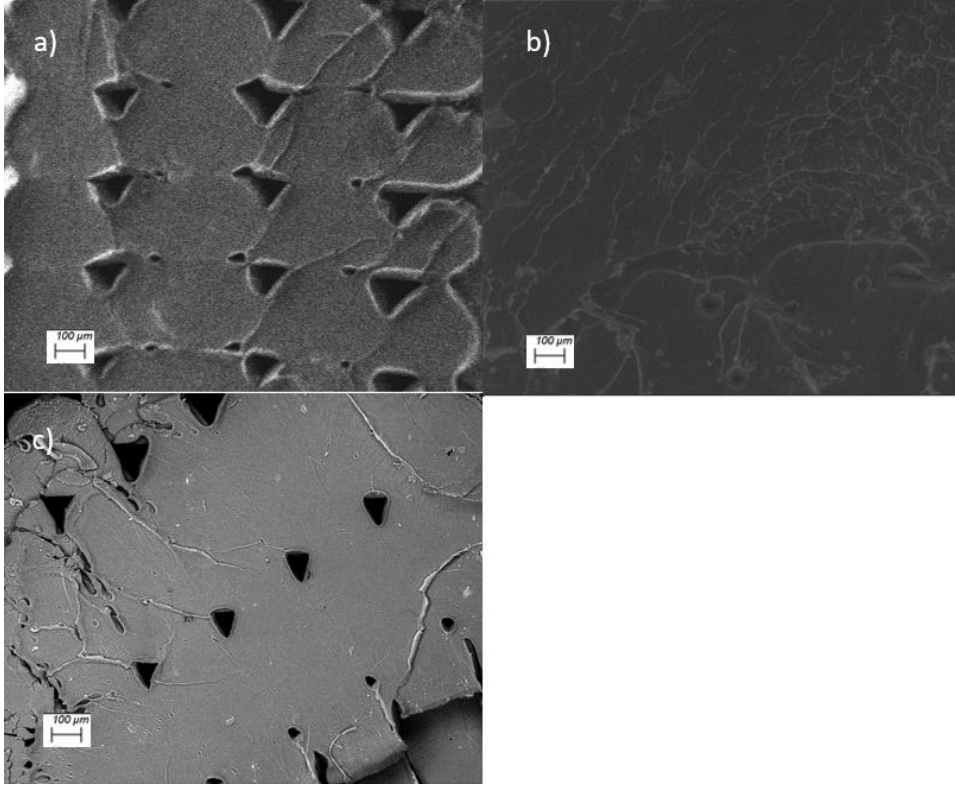
Figure S2.9 SEM image of PLA tensile specimens fracture surface in the longitudinal orientation a) neat b) 8.5k at 15 mol% and c) 50k at 15 mol%
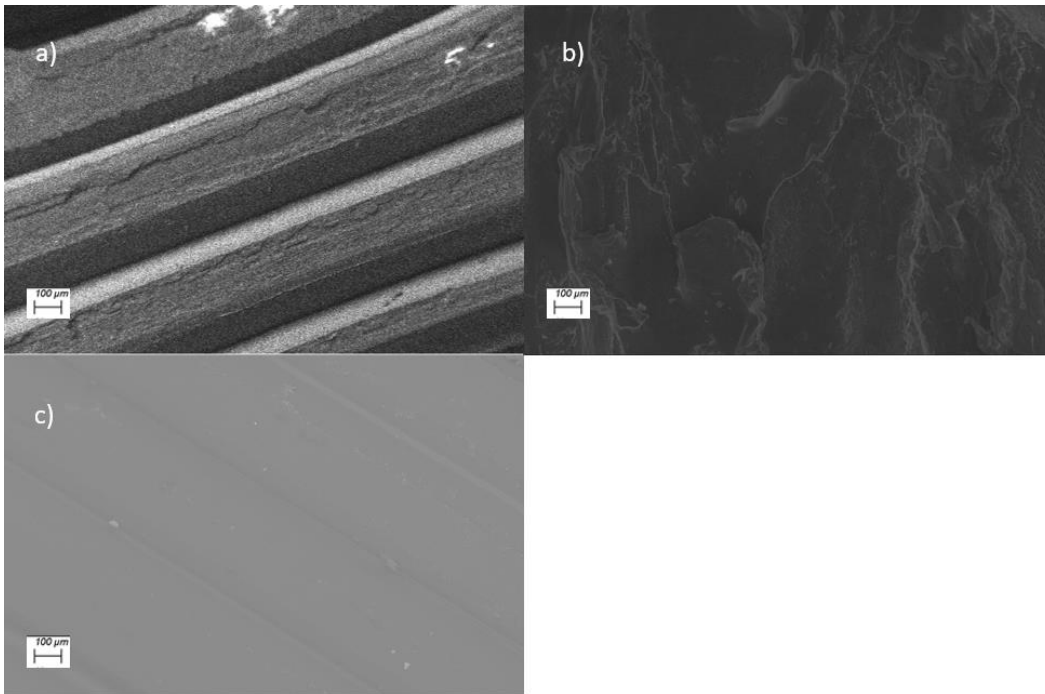
Figure S2.10 SEM image of PLA tensile specimens fracture surface in the transverse orientation a) neat b) 8.5k at 15 mol% and c) 50k at 15 mol%

Tensile data for Chapter 2 showing all specimens, which is presented as load (N) vs. extension (mm). The data for a single specimen is plotted as stress (MPa) vs strain (mm/mm) to provide the correlation of load to stress and extension to strain.
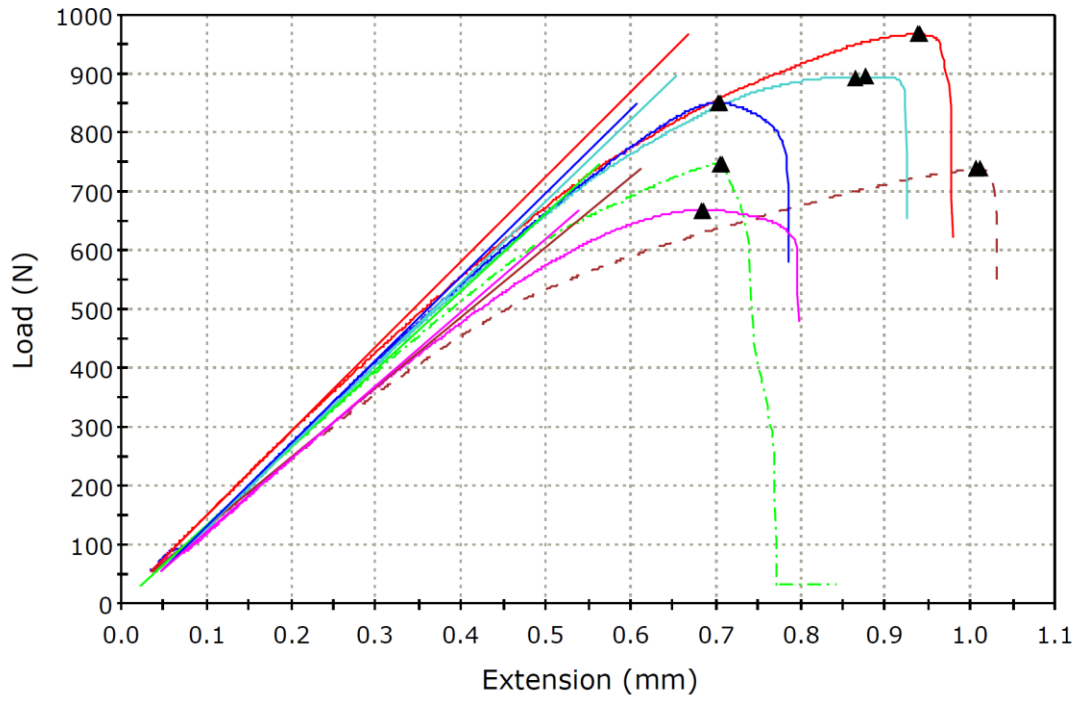
Figure S2.11 Load vs. extension curves for 220 kDa PLA (Neat) in the longitudinal orientation (colors represent multiple test specimens of the same bimodal blend)
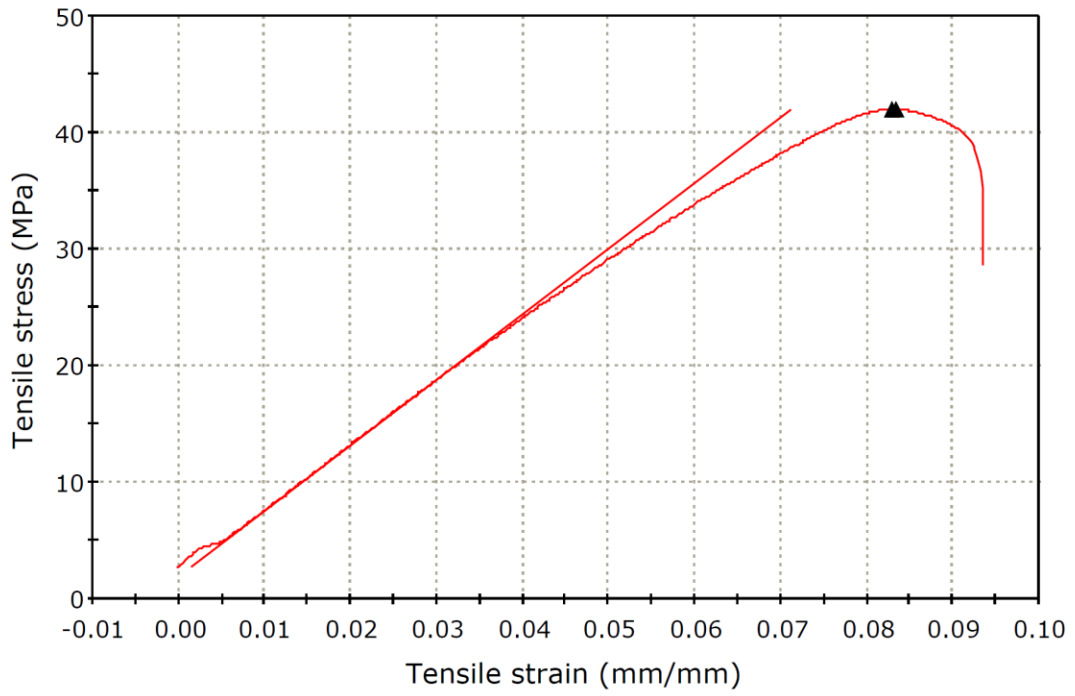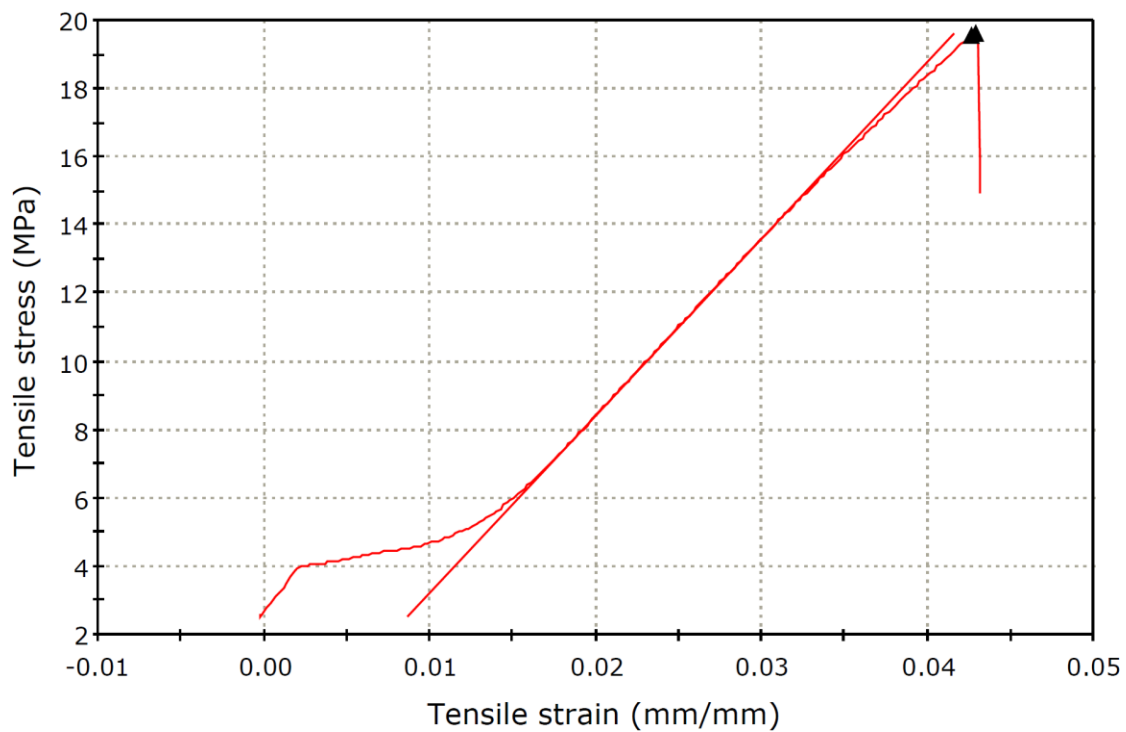
Figure S2.12 Stress vs strain curve of 220 kDa PLA (Neat) in the longitudinal orientation
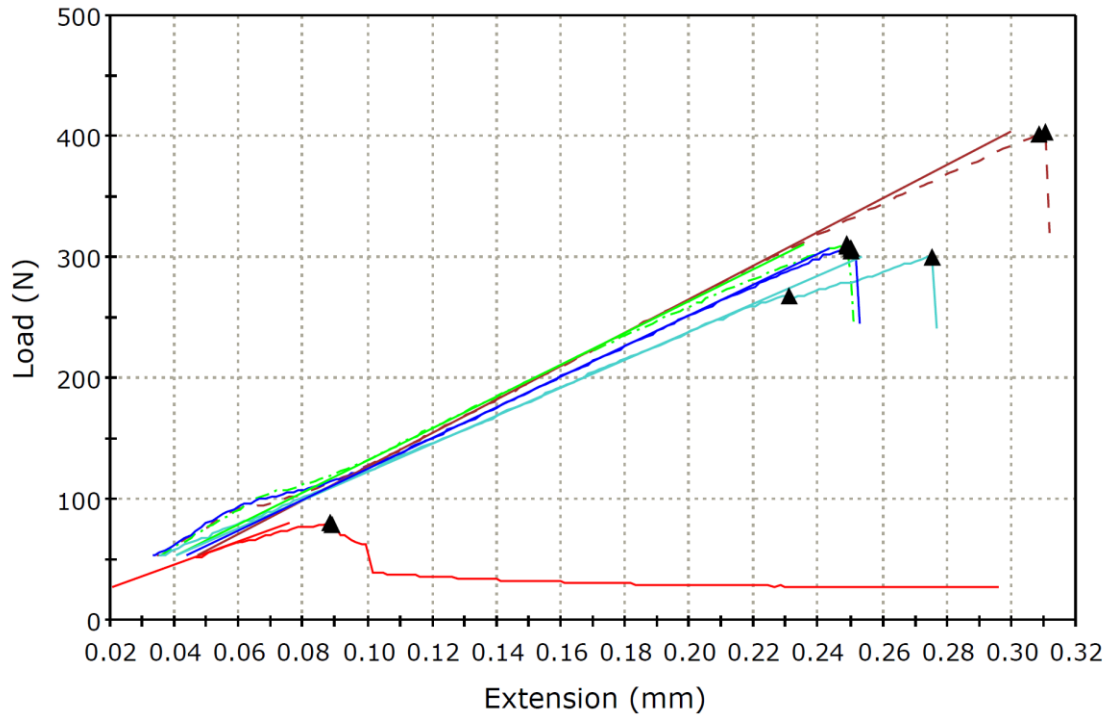
Figure S2.13 Load vs. extension curves for 220 kDa PLA (Neat) in the transverse orientation (colors represent multiple test specimens of the same bimodal blend)
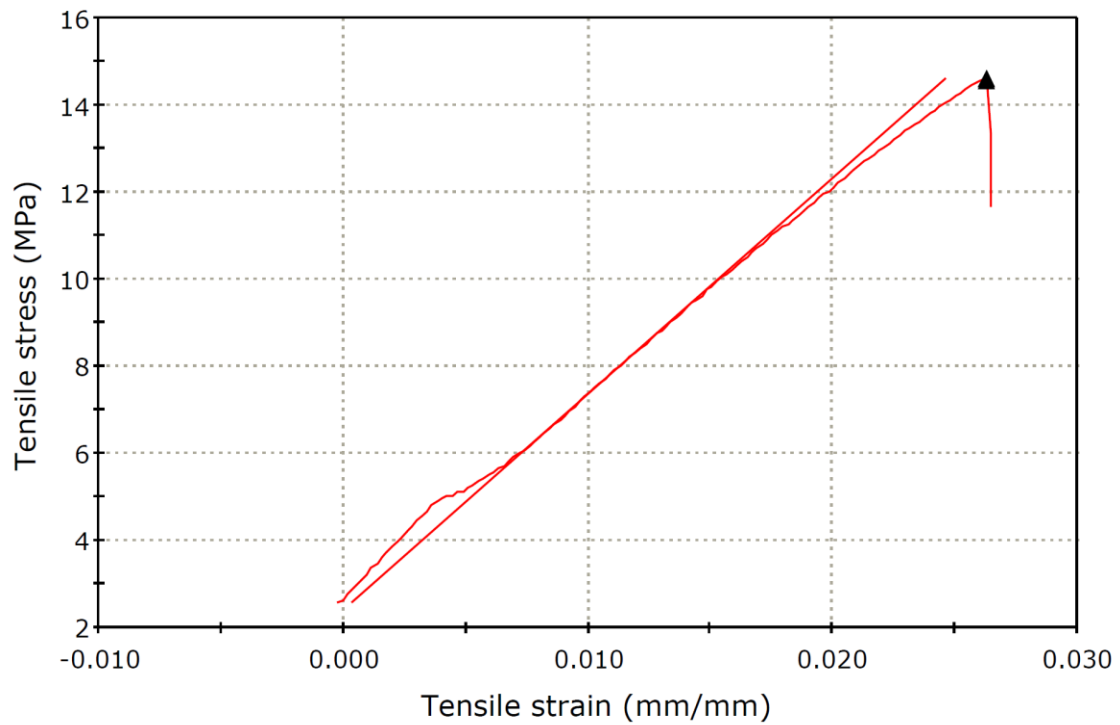
**Figure S2.14 Stress vs strain curve of 220 kDa PLA (Neat) in the transverse orientation**
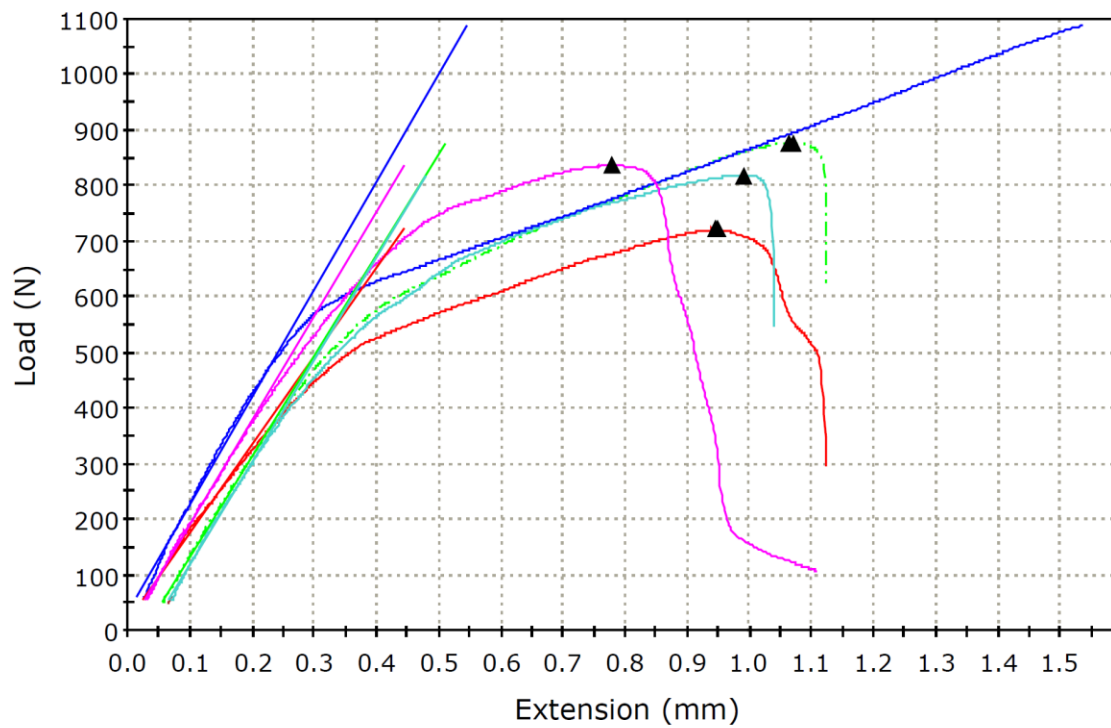
Figure S2.15 Load vs. extension curves for 3 mol% 8.5 kDa PLA in the longitudinal orientation (colors represent multiple test specimens of the same bimodal blend)
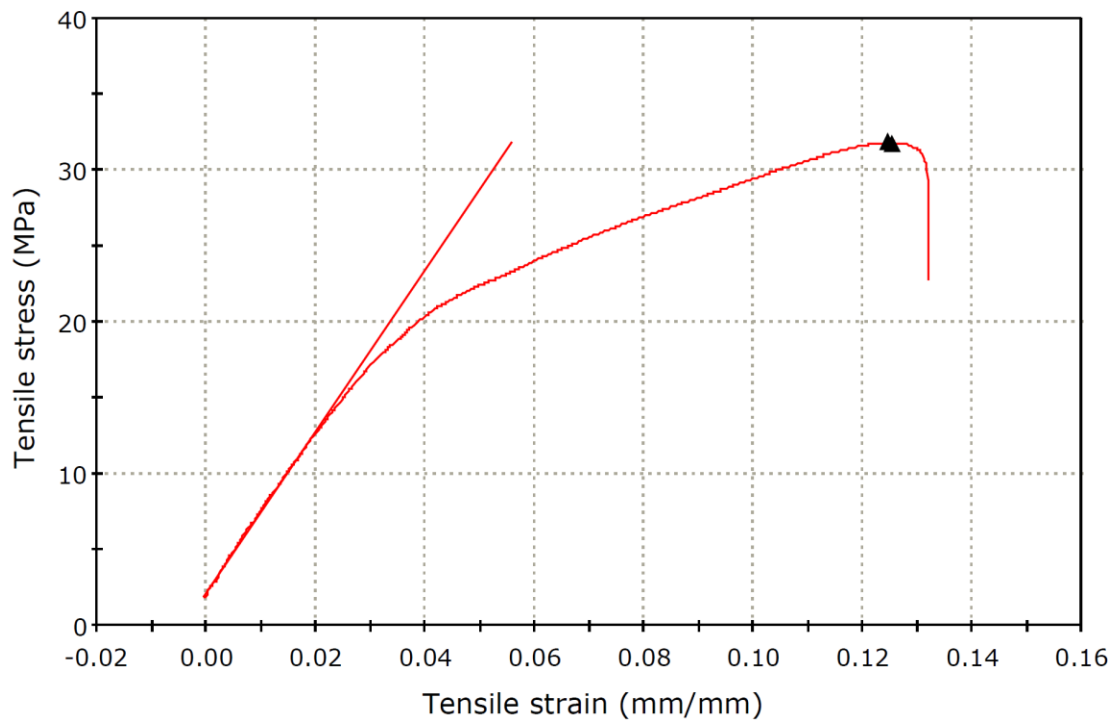
Figure S2.16 Stress vs strain curve of 3 mol% 8.5 kDa PLA in the longitudinal orientation
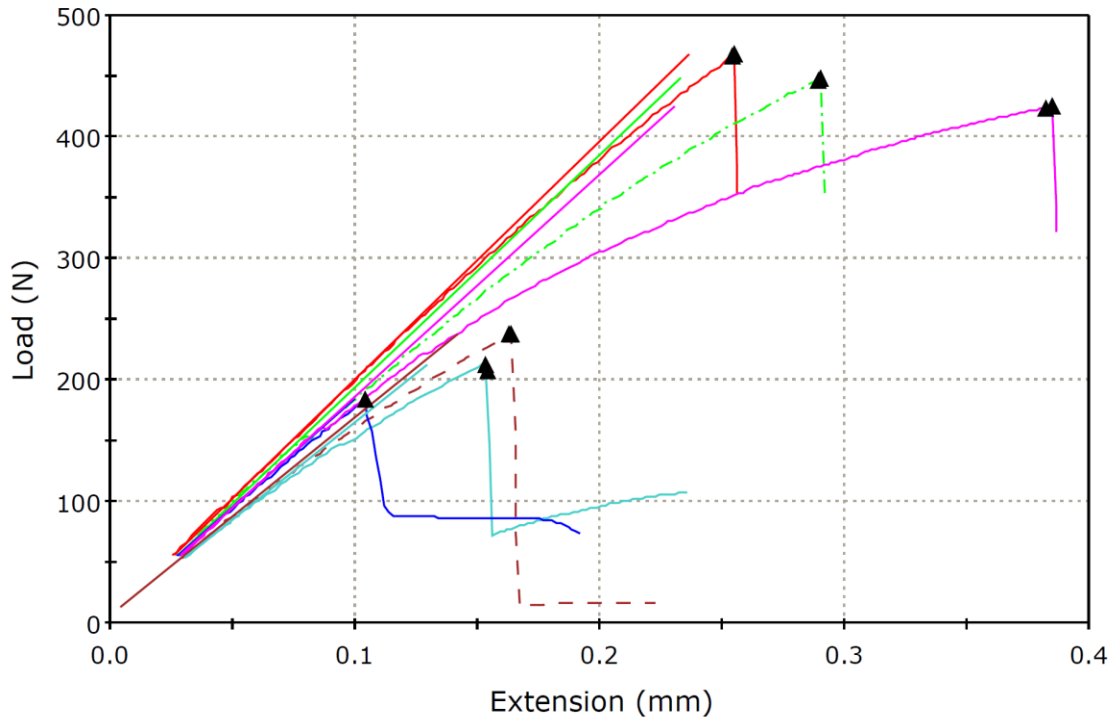
Figure S2.17 Load vs. extension curves for3 mol% 8.5 kDa PLA in the transverse orientation (colors represent multiple test specimens of the same bimodal blend)
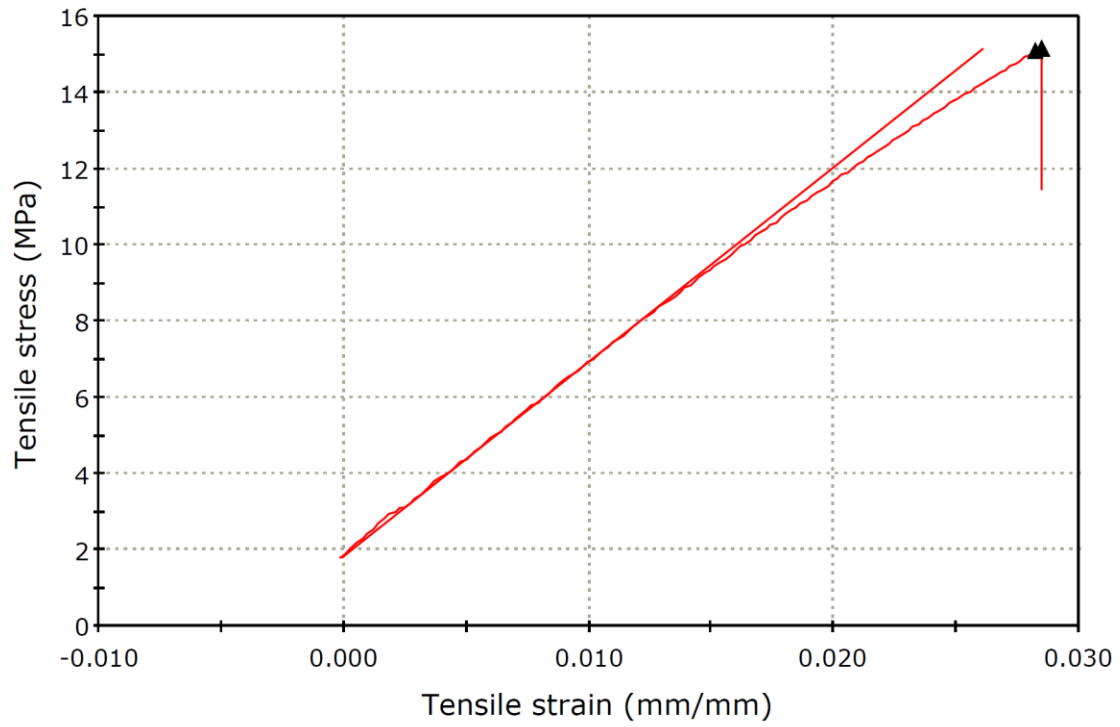
Figure S2.18 Stress vs strain curve of 3 mol% 8.5 kDa PLA in the transverse orientation
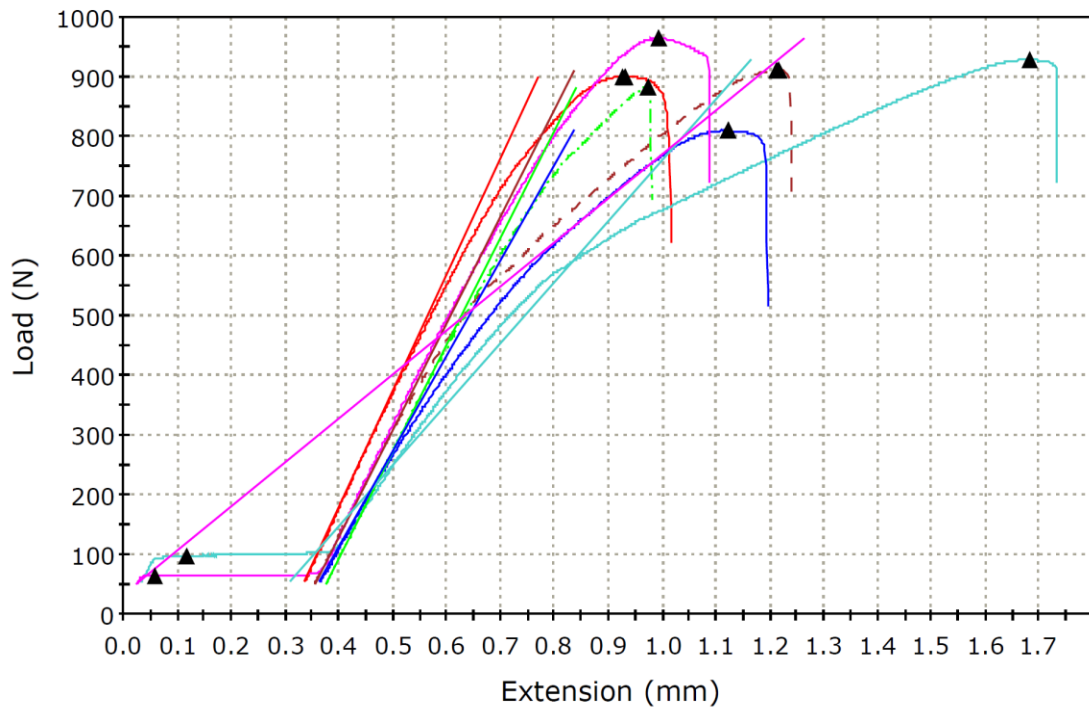
Figure S2.19 Load vs. extension curves for 3 mol% 50 kDa PLA in the longitudinal orientation (colors represent multiple test specimens of the same bimodal blend)
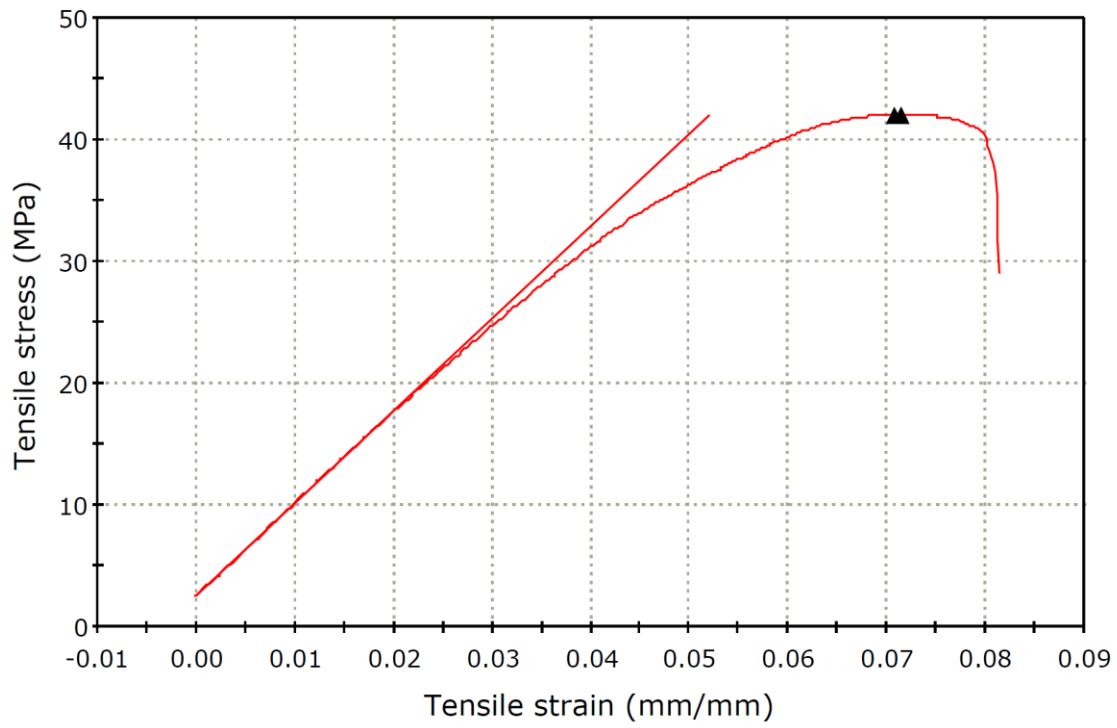
Figure S2.20 Stress vs strain curve of 3 mol% 50 kDa PLA in the longitudinal orientation
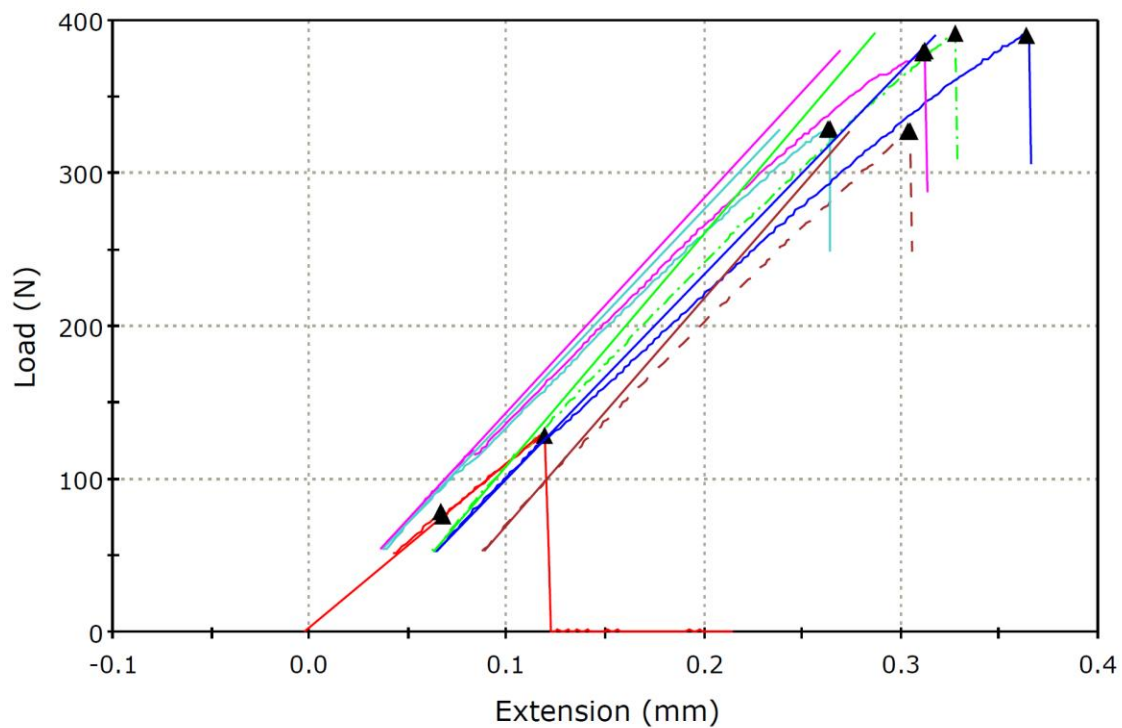
Figure S2.21 Load vs. extension curves for 3 mol% 50 kDa PLA in the transverse orientation (colors represent multiple test specimens of the same bimodal blend)
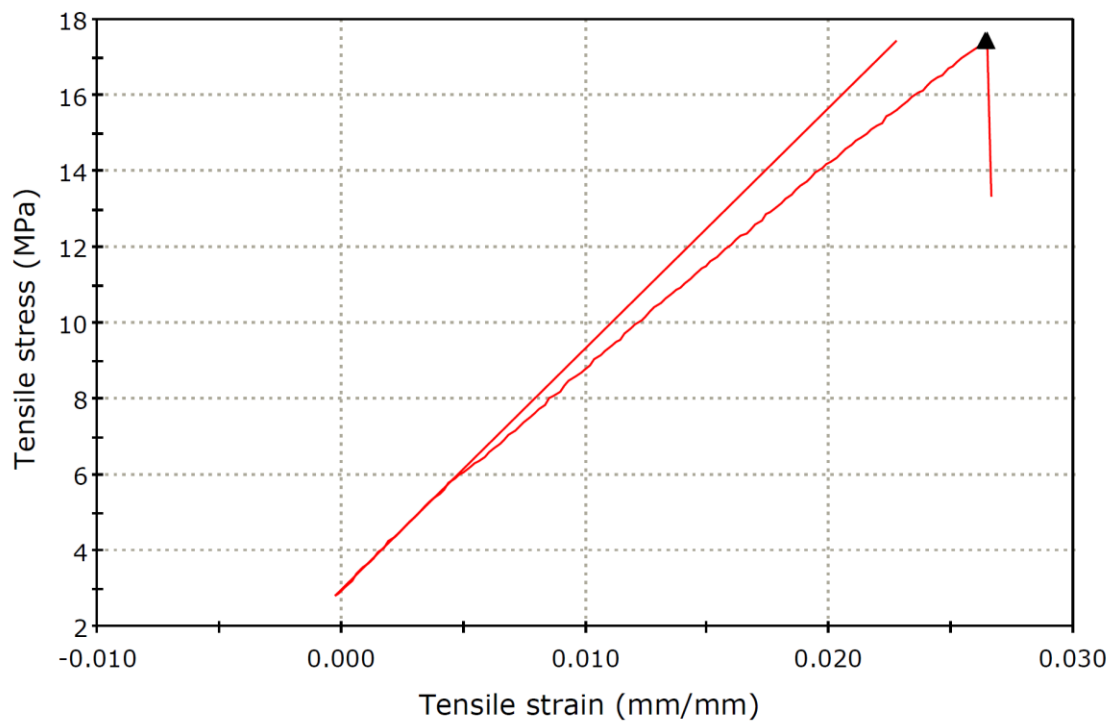
Figure S2.22 Stress vs strain curve of 3 mol% 50 kDa PLA in the transverse orientation
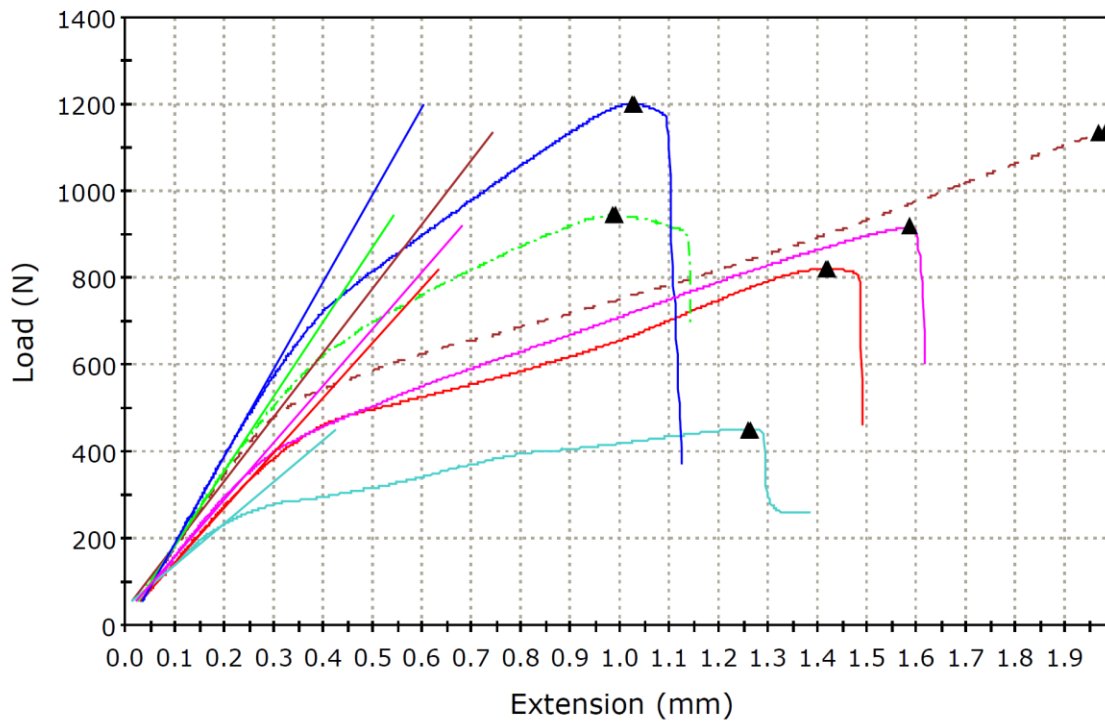
Figure S2.23 Load vs. extension curves for 3 mol% 100 kDa PLA in the longitudinal orientation (colors represent multiple test specimens of the same bimodal blend)
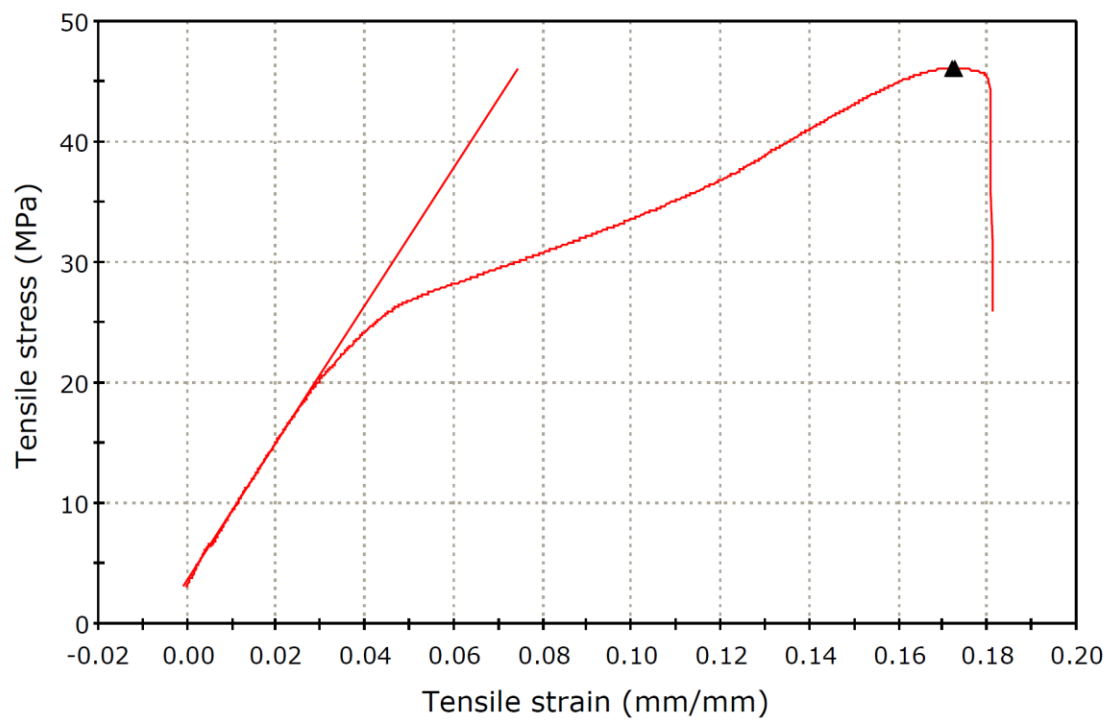
Figure S2.24 Stress vs strain curve of 3 mol% 100 kDa PLA in the longitudinal orientation
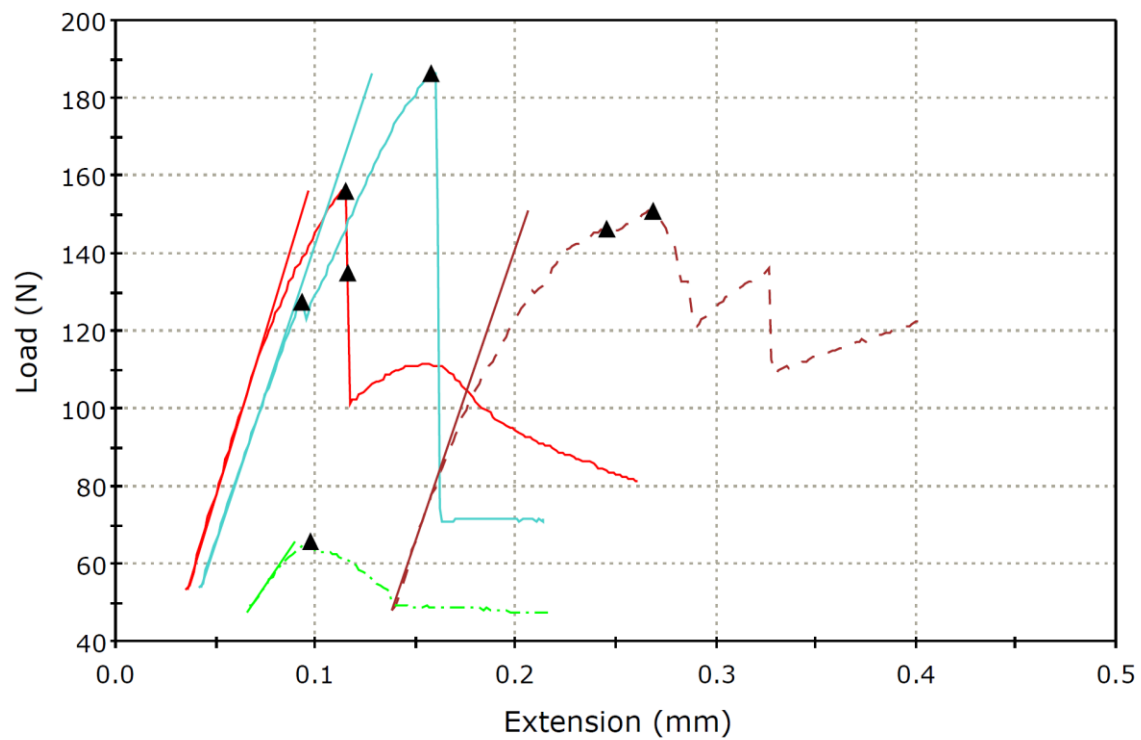
Figure S2.25 Load vs. extension curves for 3 mol% 100 kDa PLA in the transverse orientation (colors represent multiple test specimens of the same bimodal blend)
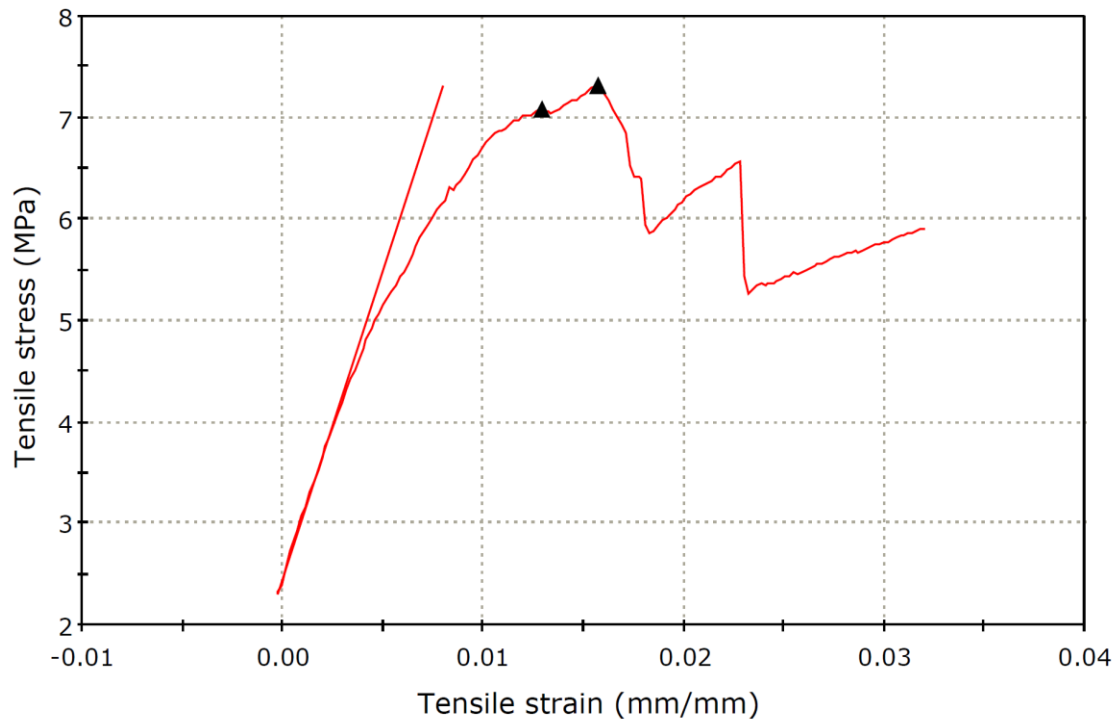
Figure S2.26 Stress vs strain curve of 3 mol% 100 kDa PLA in the transverse orientation
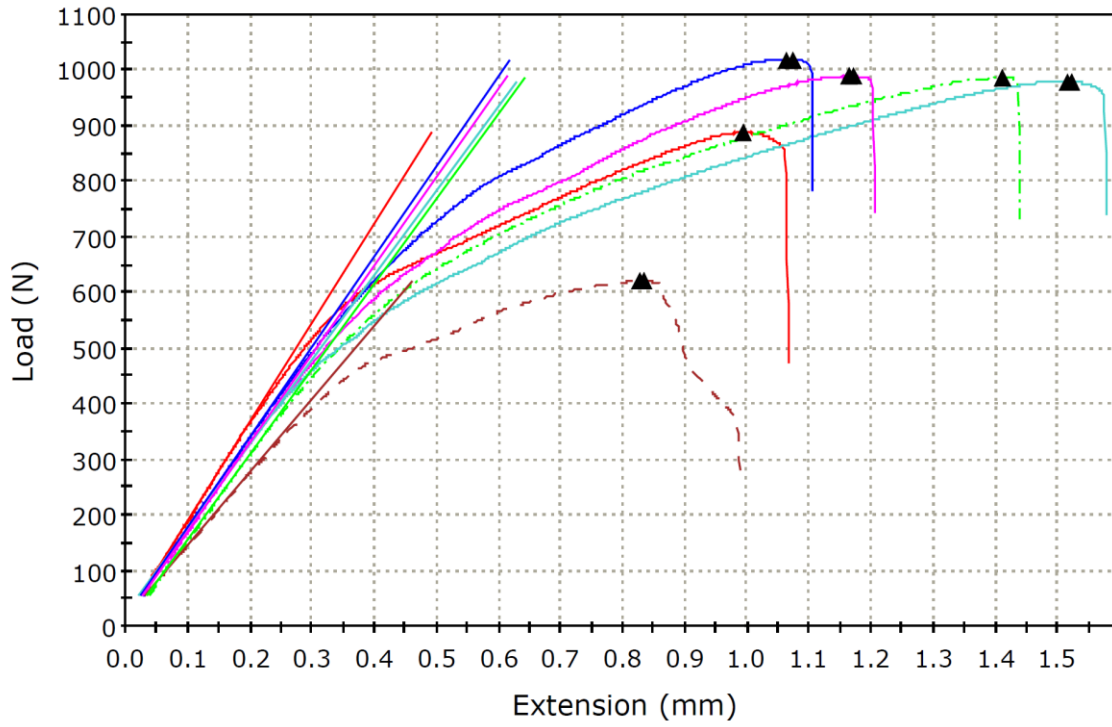
Figure S2.27 Load vs. extension curves for 10 mol% 8.5 kDa PLA in the longitudinal orientation (colors represent multiple test specimens of the same bimodal blend)
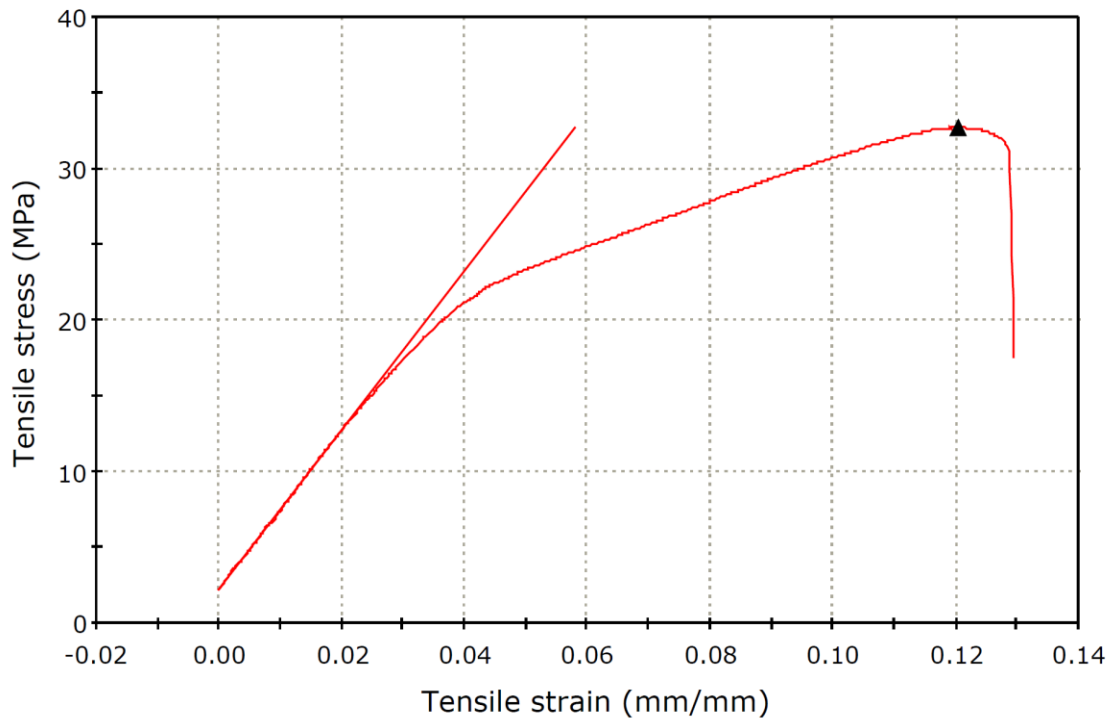
Figure S2.28 Stress vs strain curve of 10 mol% 8.5 kDa PLA in the longitudinal orientation
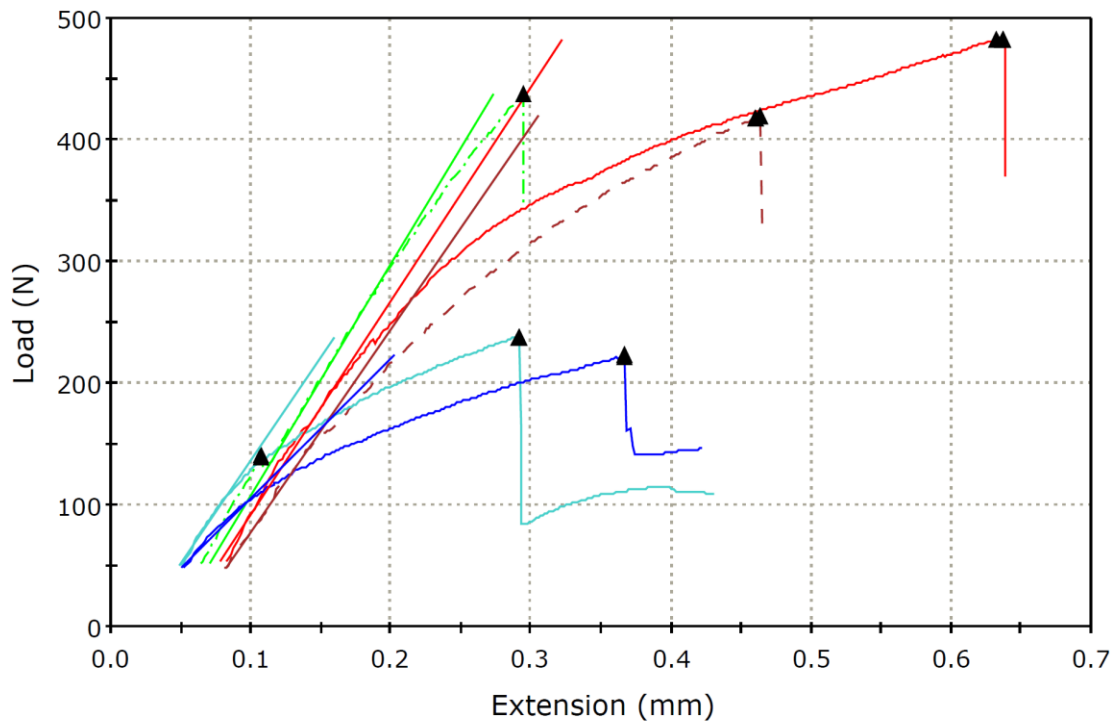
Figure S2.29 Load vs. extension curves for 10 mol% 8.5 kDa PLA in the transverse orientation (colors represent multiple test specimens of the same bimodal blend)
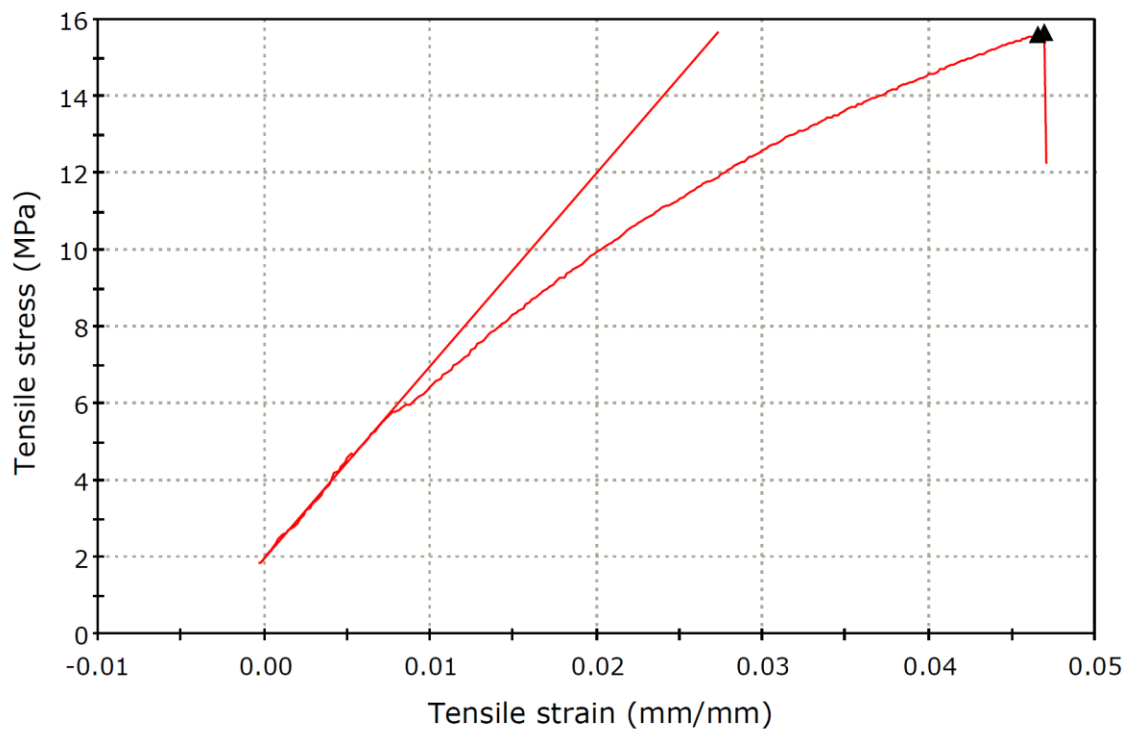
Figure S2.30 Stress vs strain curve of 10 mol% 8.5 kDa PLA in the transverse orientation
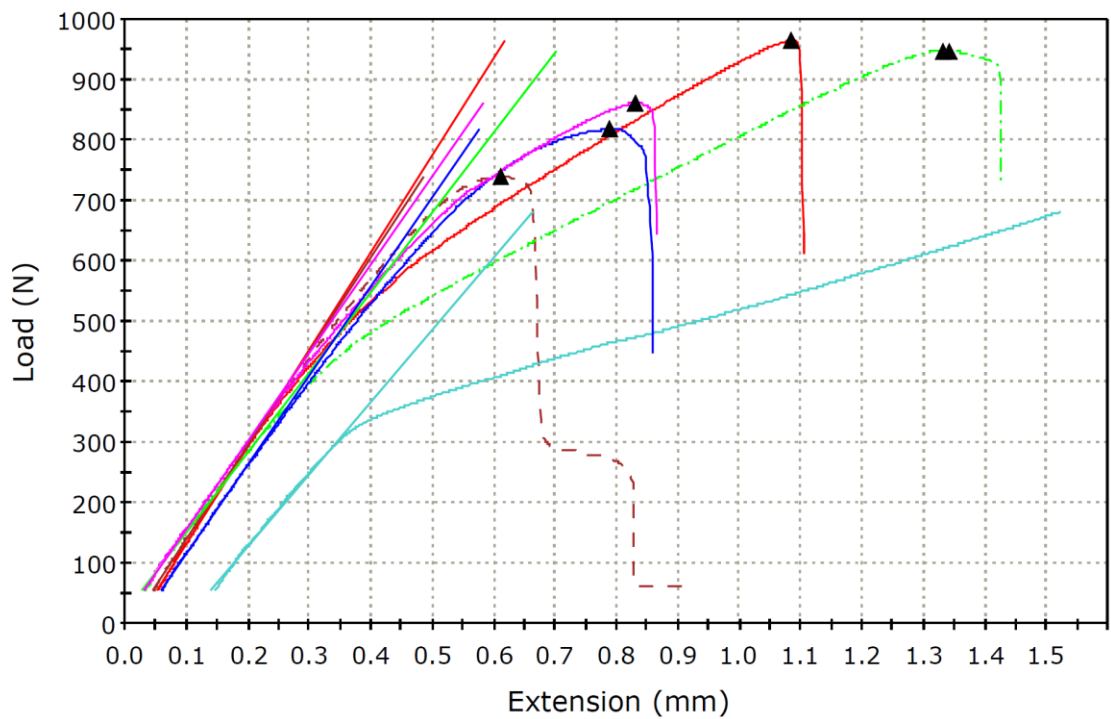
Figure S2.31 Load vs. extension curves for 10 mol% 50 kDa PLA in the longitudinal orientation (colors represent multiple test specimens of the same bimodal blend)
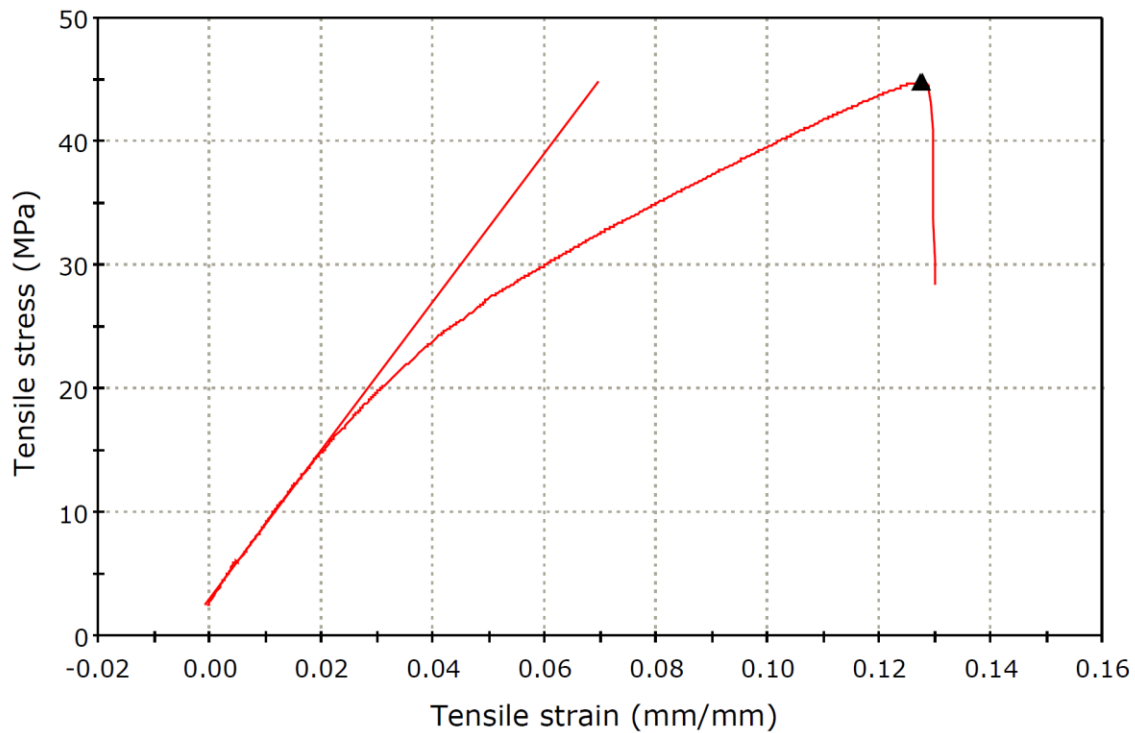
Figure S2.32 Stress vs strain curve of 10 mol% 50 kDa PLA in the longitudinal orientation
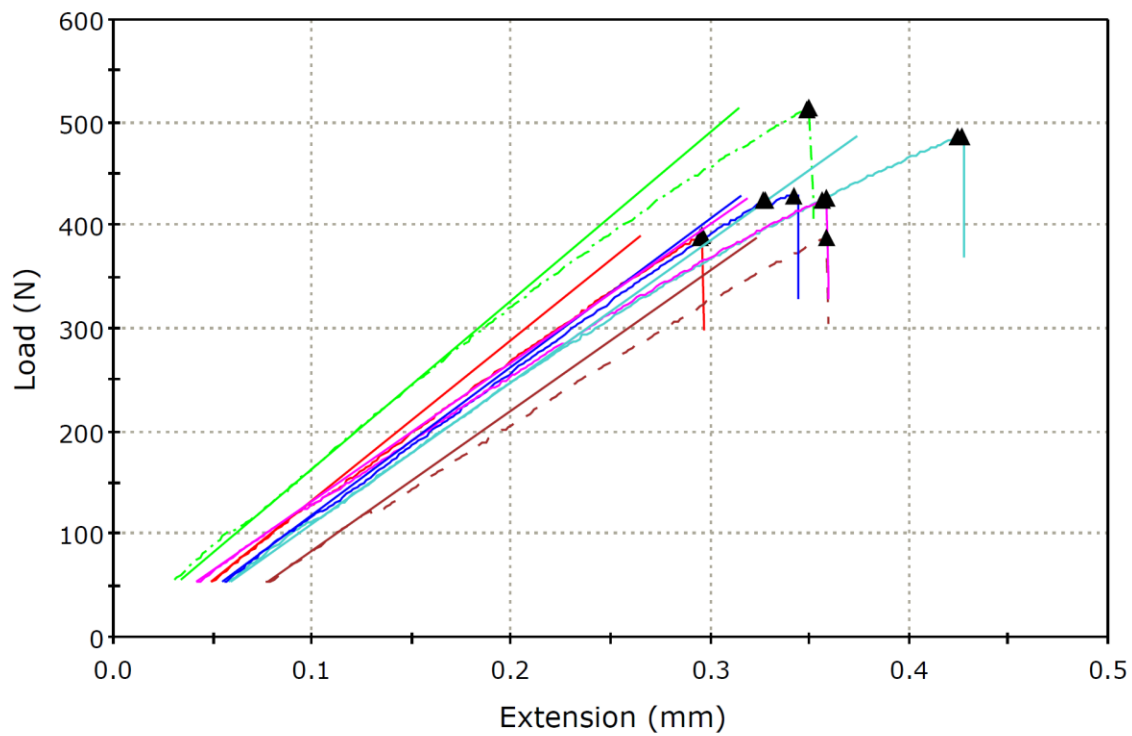
Figure S2.33 Load vs. extension curves for 10 mol% 50 kDa PLA in the transverse orientation (colors represent multiple test specimens of the same bimodal blend)
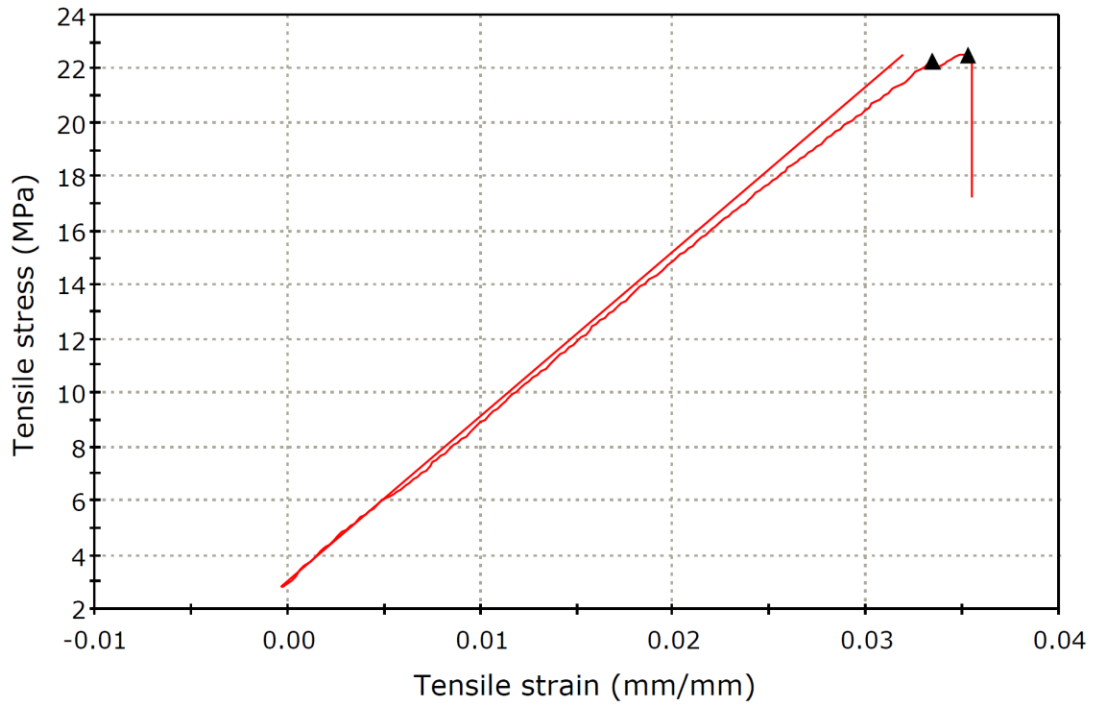
Figure S2.34 Stress vs strain curve of 10 mol% 50 kDa PLA in the transverse orientation
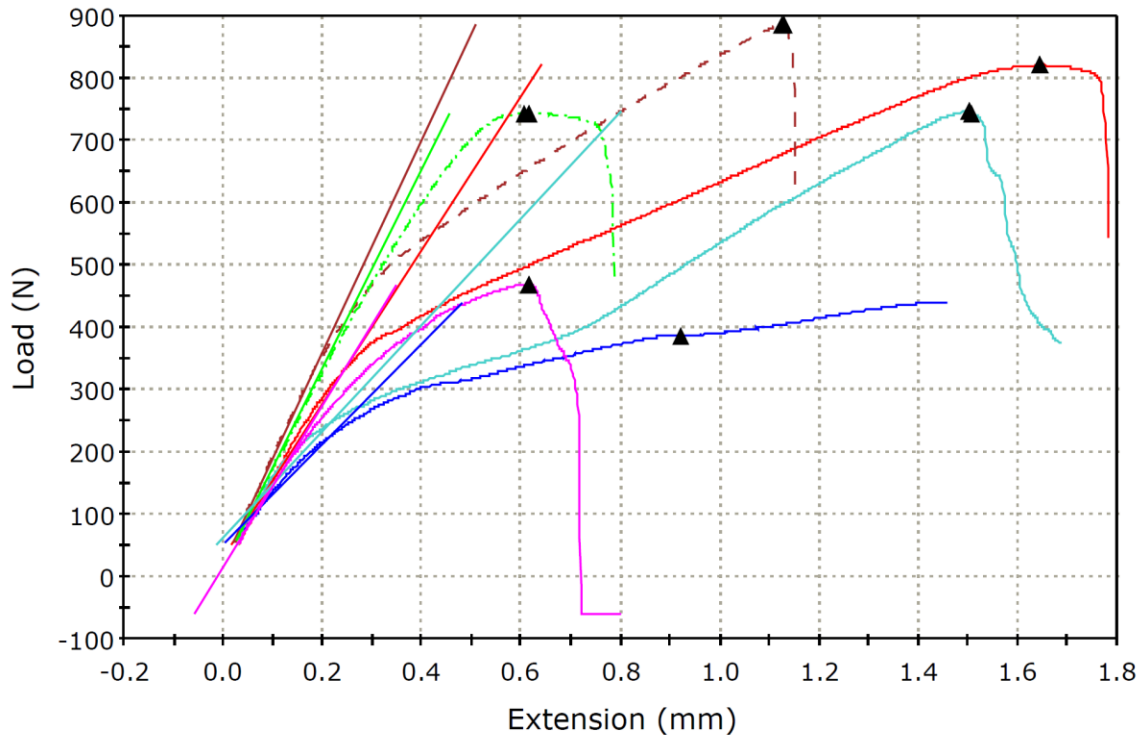
Figure S2.35 Load vs. extension curves for 10 mol% 100 kDa PLA in the longitudinal orientation (colors represent multiple test specimens of the same bimodal blend)
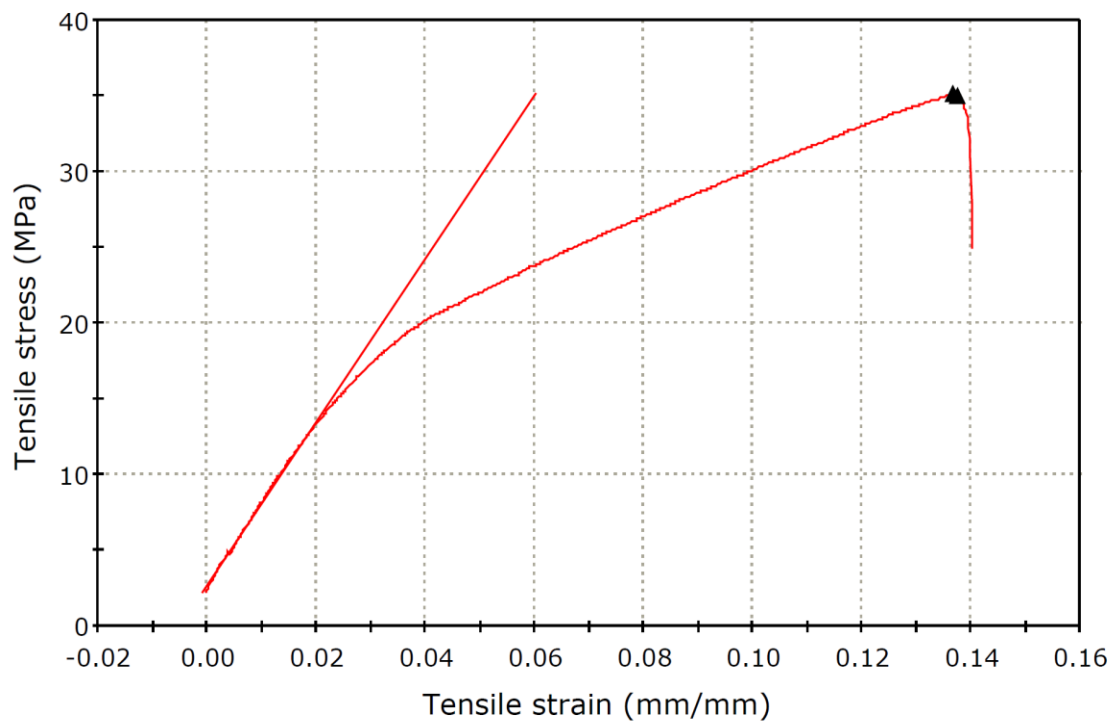
Figure S2.36 Stress vs strain curve of 10 mol% 100 kDa PLA in the longitudinal orientation
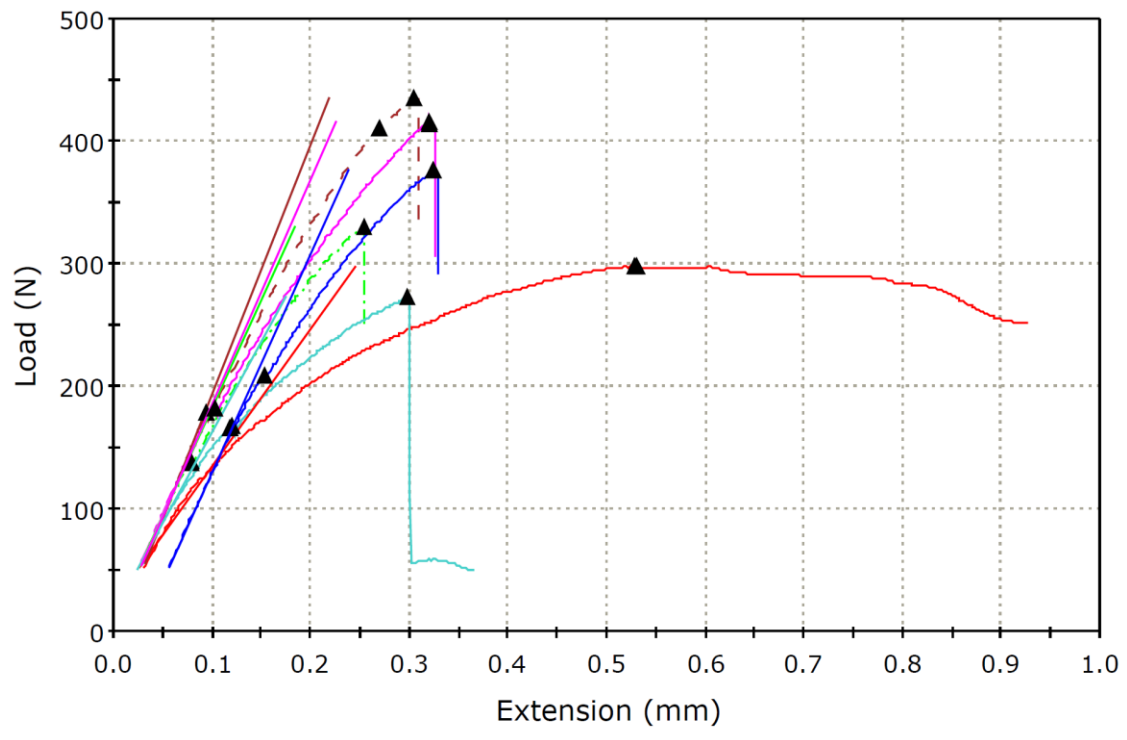
Figure S2.37 Load vs. extension curves for 10 mol% 100 kDa PLA in the transverse orientation (colors represent multiple test specimens of the same bimodal blend)
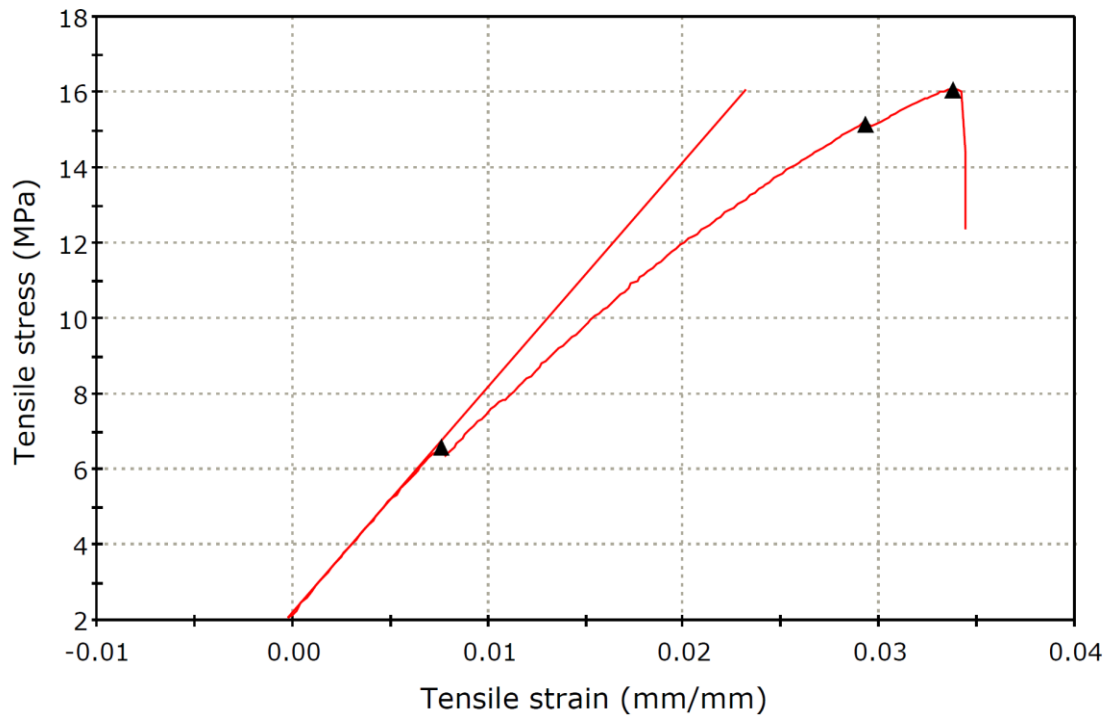
Figure S2.38 Stress vs strain curve of 10 mol% 100 kDa PLA in the transverse orientation
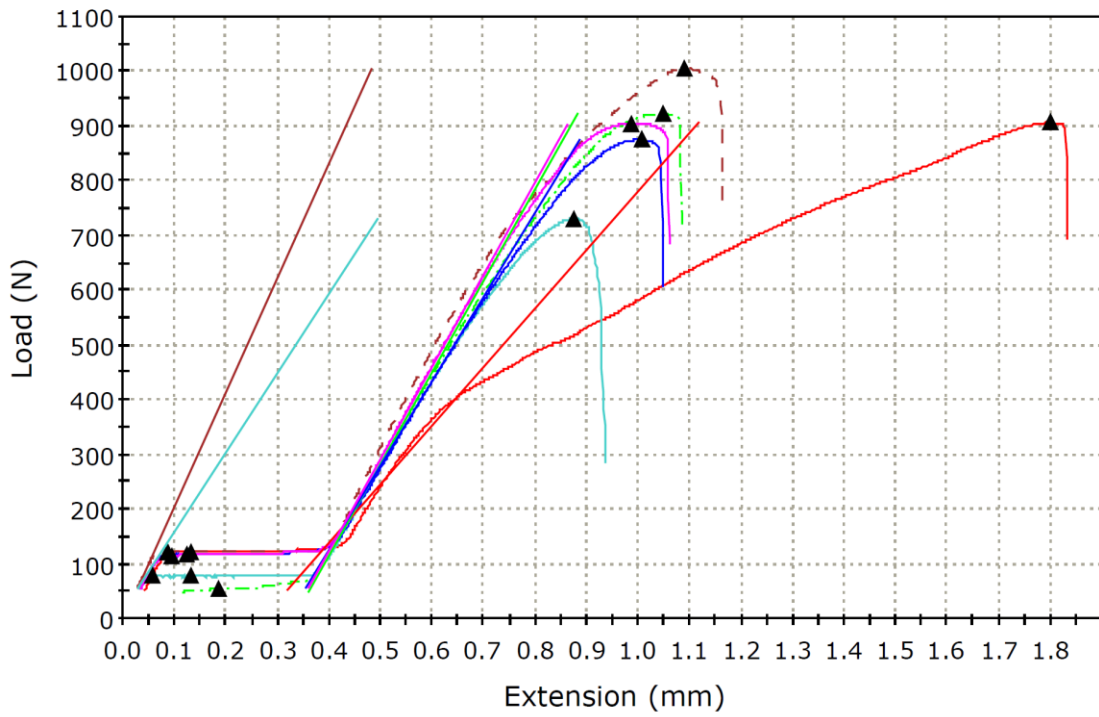
Figure S2.39 Load vs. extension curves for 15 mol% 50 kDa PLA in the longitudinal orientation (colors represent multiple test specimens of the same bimodal blend)
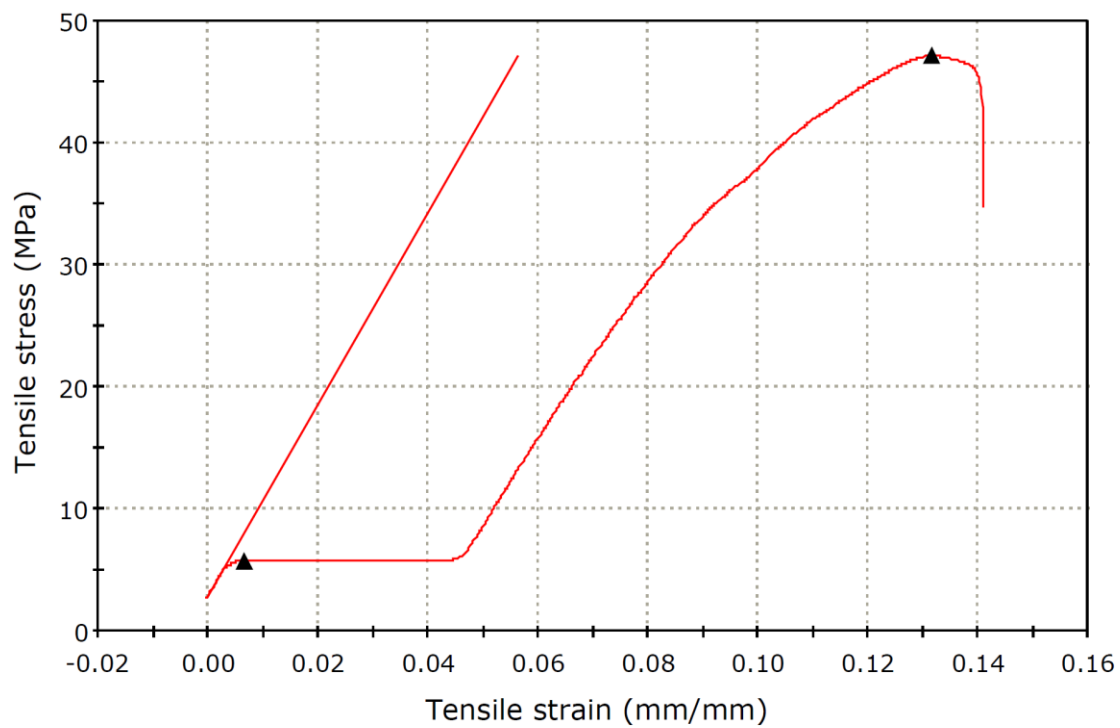
Figure S2.40 Stress vs strain curve of 15 mol% 50 kDa PLA in the longitudinal orientation
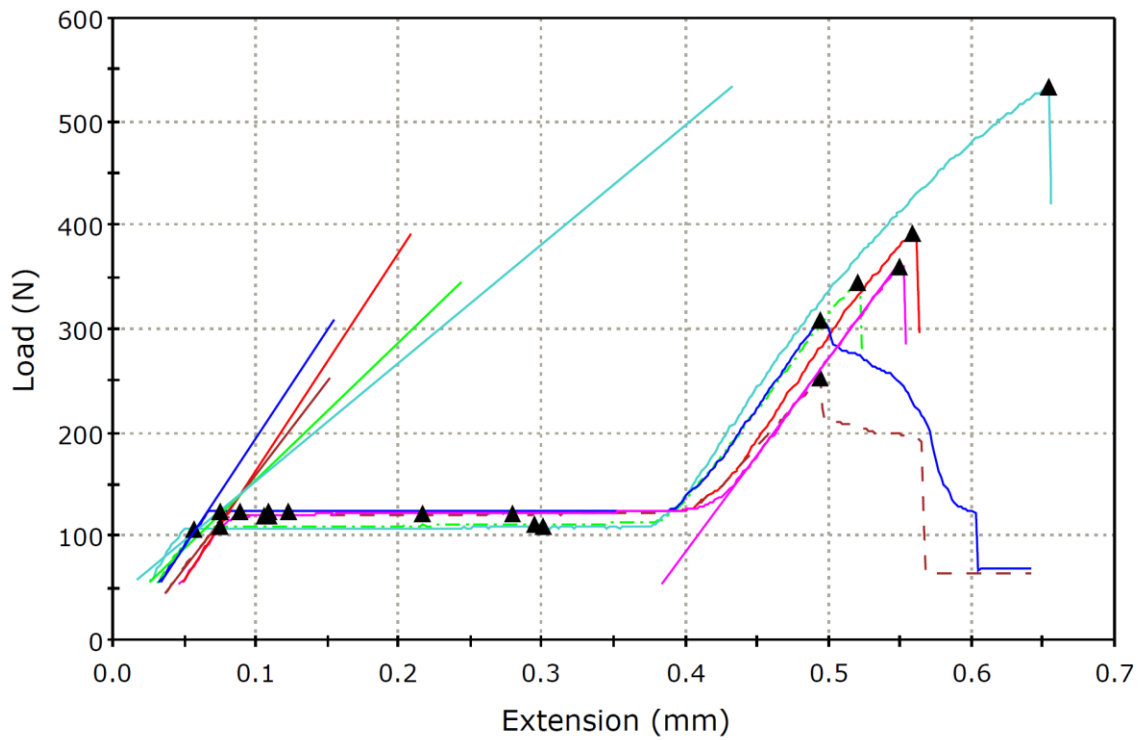
Figure S2.41 Load vs. extension curves for 15 mol% 50 kDa PLA in the transverse orientation (colors represent multiple test specimens of the same bimodal blend)
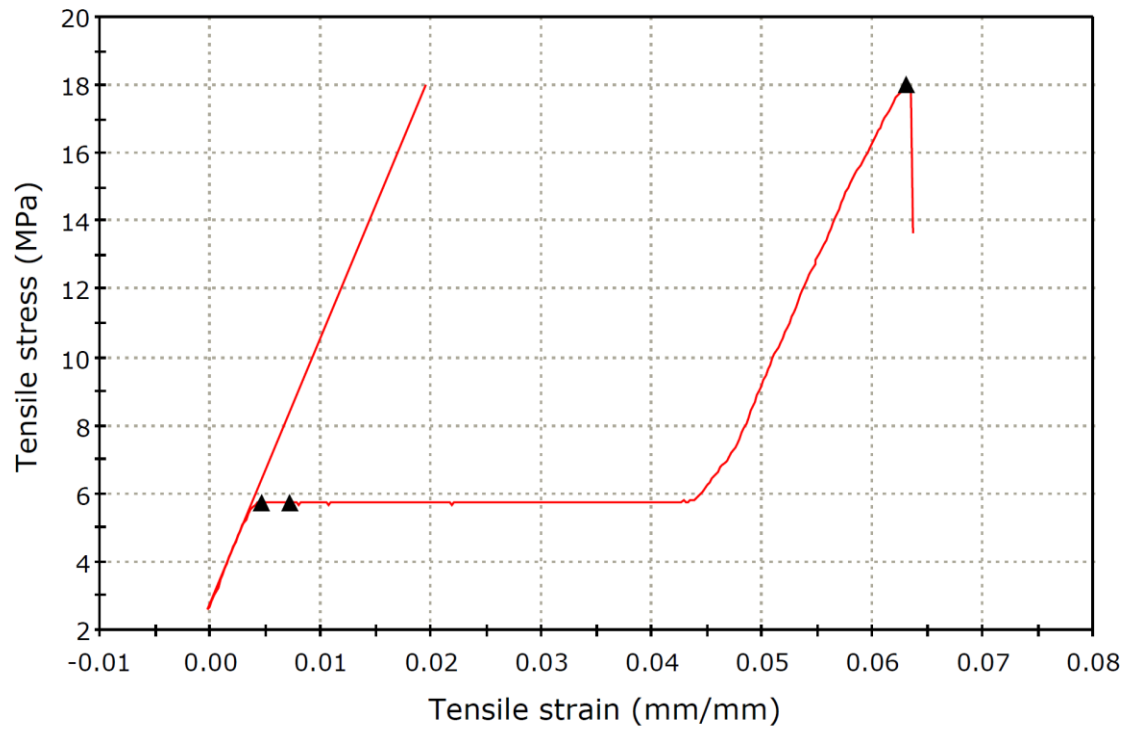
Figure S2.42 Stress vs strain curve of 15 mol% 50 kDa PLA in the transverse orientation
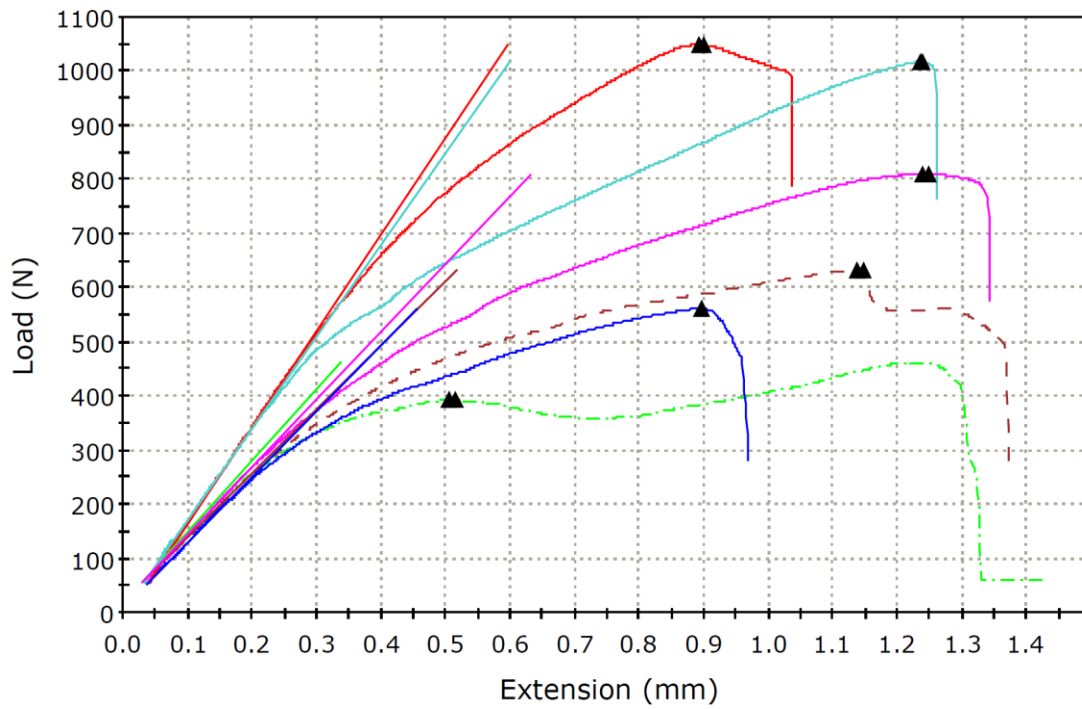
Figure S2.43 Load vs. extension curves for 15 mol% 100 kDa PLA in the longitudinal orientation (colors represent multiple test specimens of the same bimodal blend)
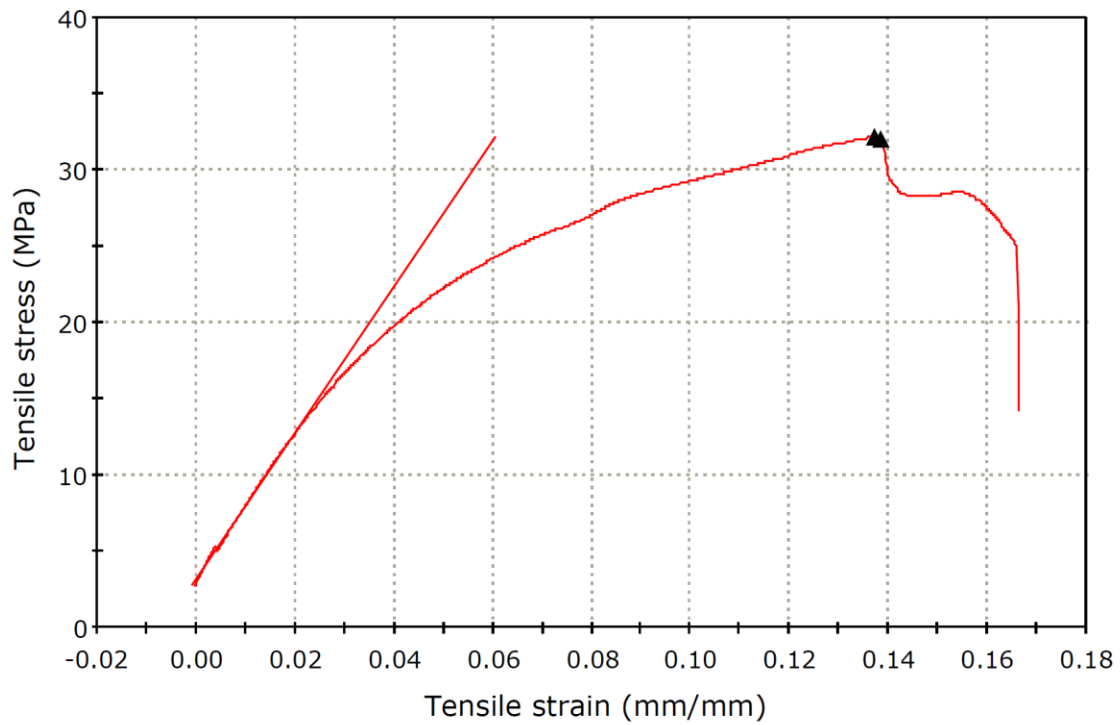
Figure S2.44 Stress vs strain curve of 15 mol% 100 kDa PLA in the longitudinal orientation
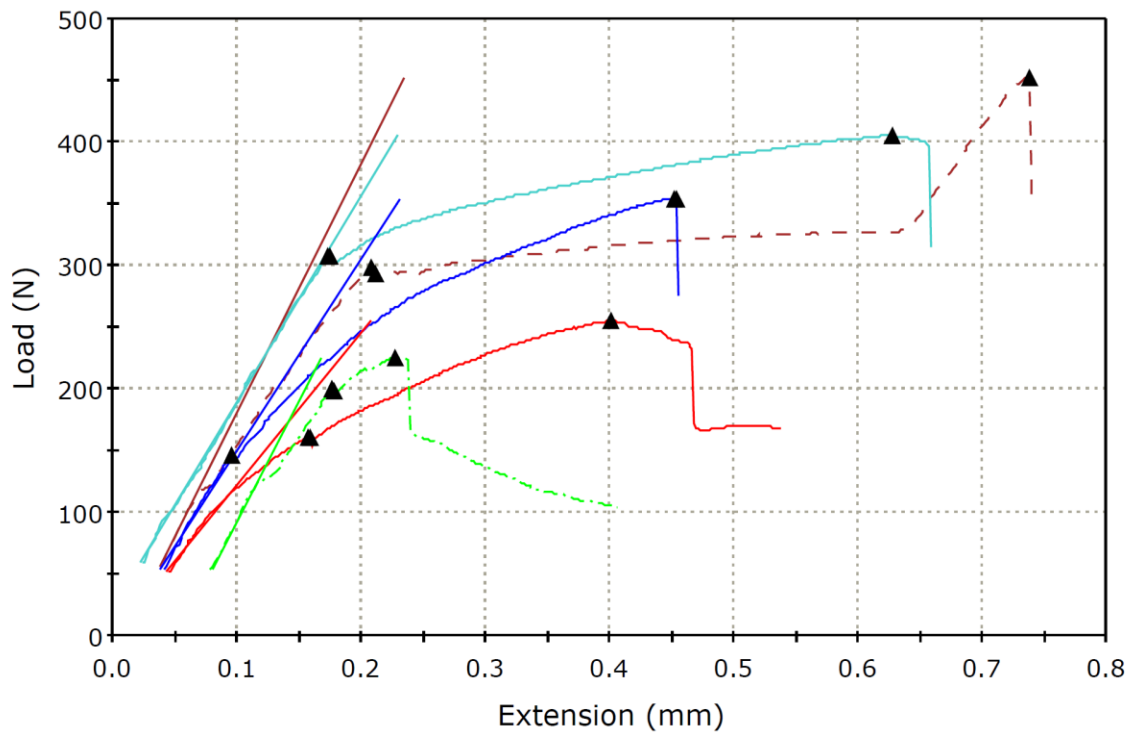
Figure S2.45 Load vs. extension curves for 15 mol% 100 kDa PLA in the transverse orientation (colors represent multiple test specimens of the same bimodal blend)
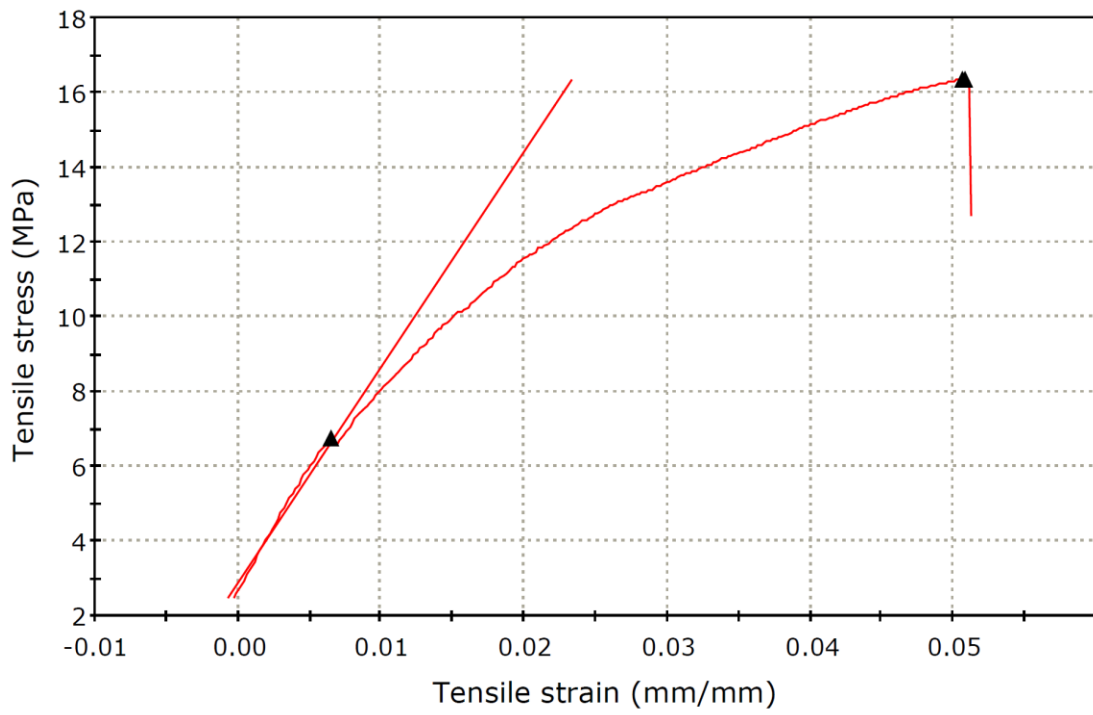
Figure S2.46 Stress vs strain curve of 15 mol% 100 kDa PLA in the transverse orientation
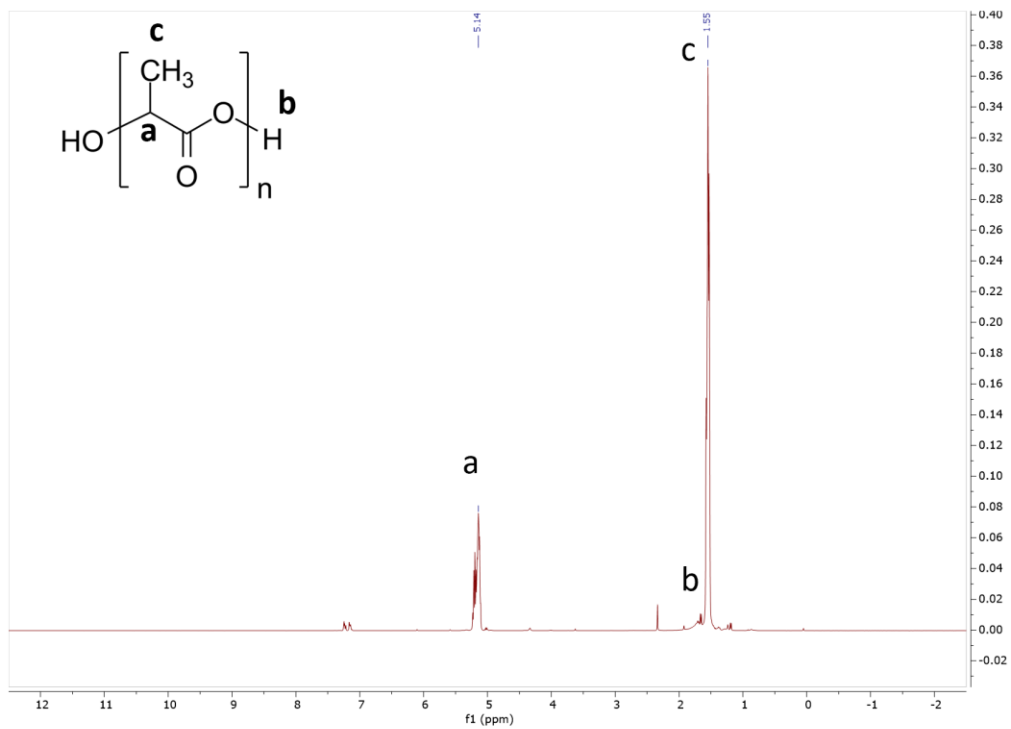
Figure S3.1 H-NMR of linear poly(lactide) (PLA)
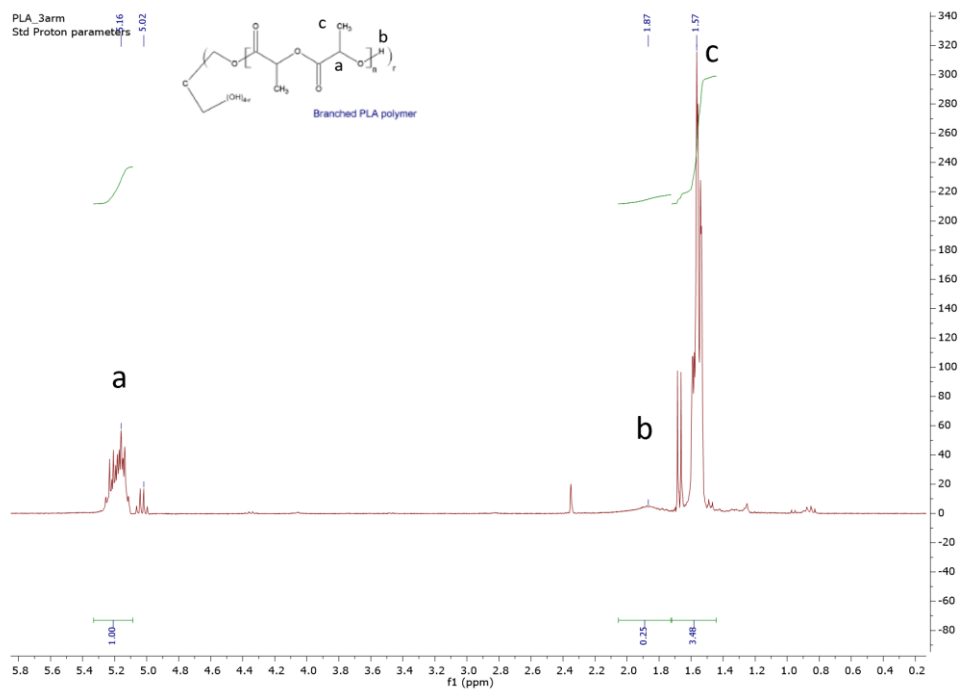
Figure S3.2 H-NMR of 3-arm poly(lactide) (PLA)
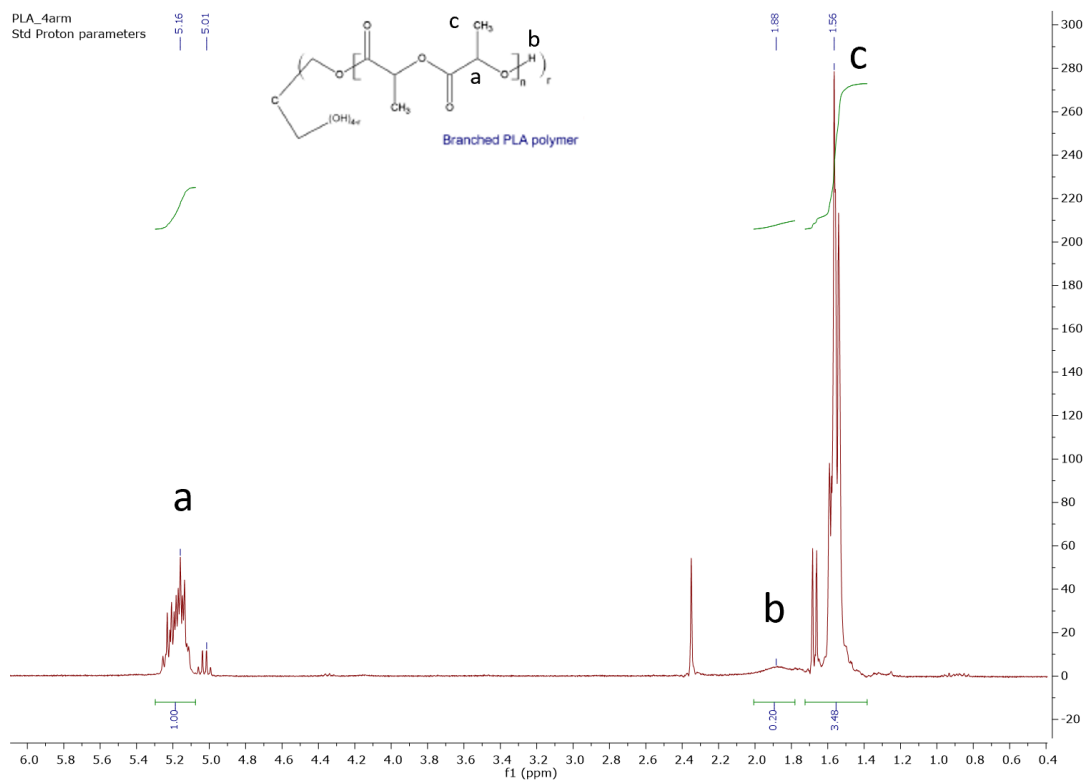
Figure S3.3 H-NMR of 4-arm poly(lactide) (PLA)

Table S3.1 Molecular weight characteristics of the PLA low molecular weight additives

SAMPLE	M_n (1 x 10^3)	M_w (1 x 10^3)	PDI
2 ARM (26K)	25	27	1.1
2 ARM (50K)	36	54	1.5
3 ARM (33K)	33	35	1.1
4 ARM (44K)	31	44	1.4
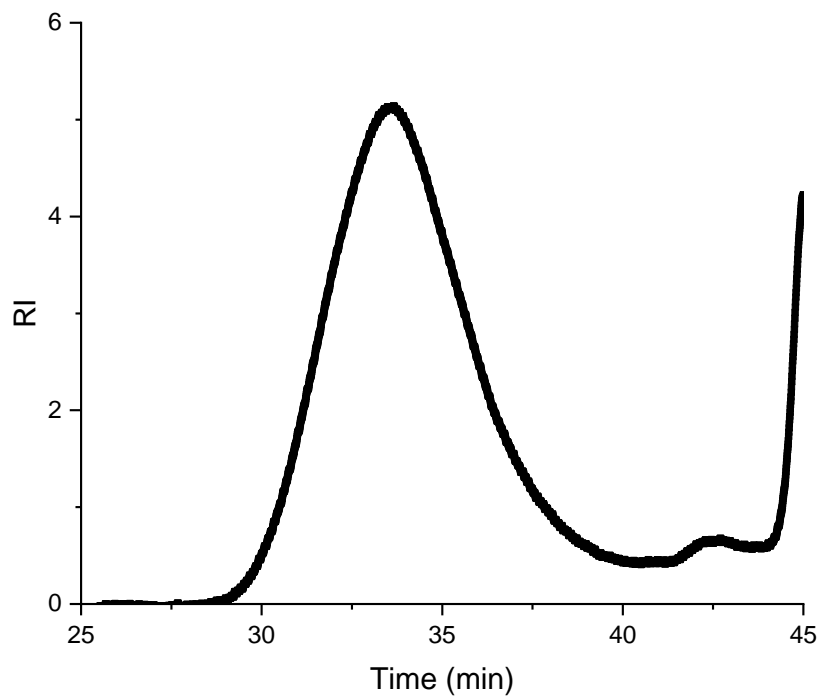
Figure 3.4GPC trace of 26k PLA
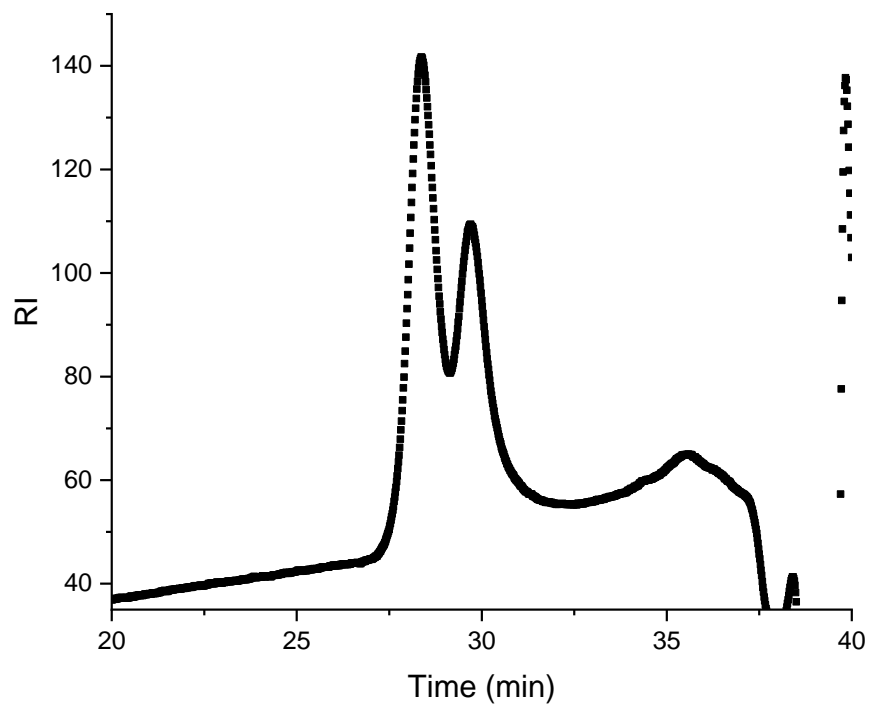
Figure S3.5 GPC trace of 3-arm PLA
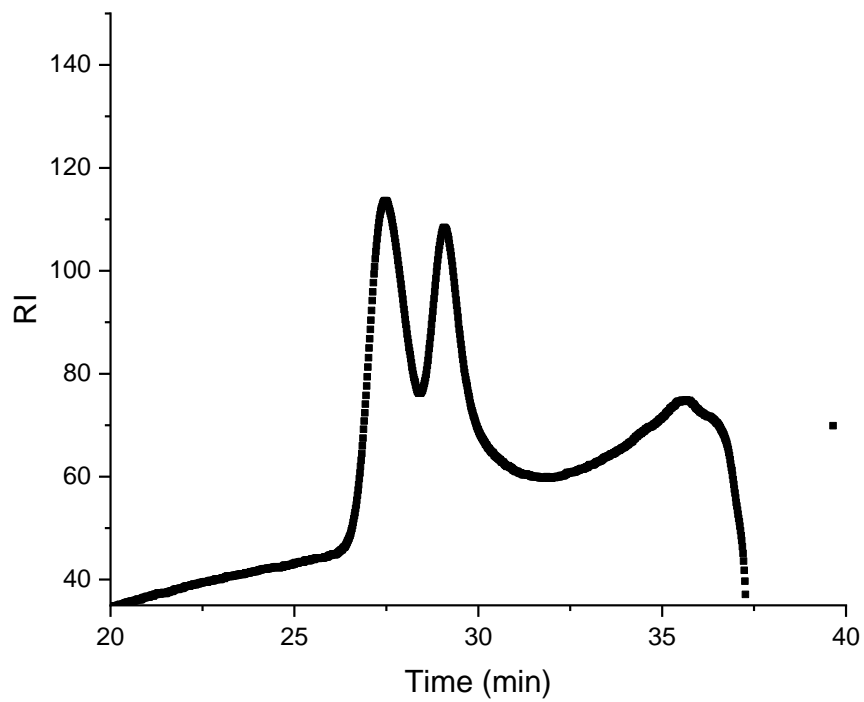
Figure S3.6 GPC trace of 4-arm PLA

Tensile data for Chapter 3 showing all specimens, which is presented as load (N) vs. extension (mm). The data for a single specimen is plotted as stress (MPa) vs strain (mm/mm) to provide the correlation of load to stress and extension to strain.
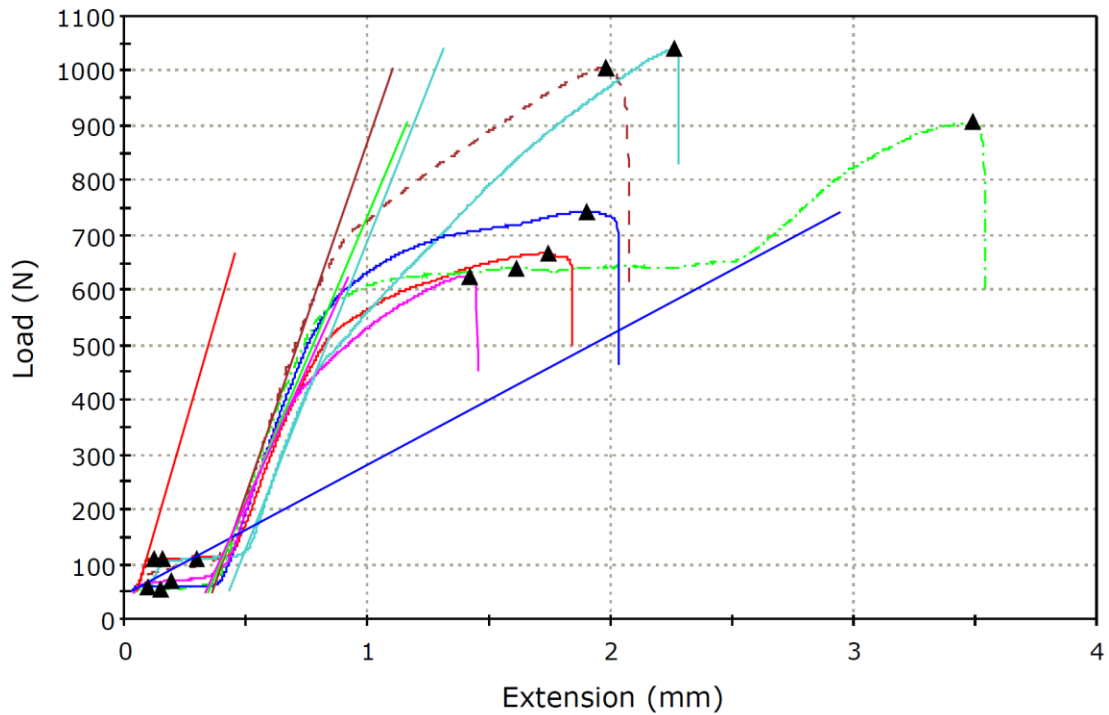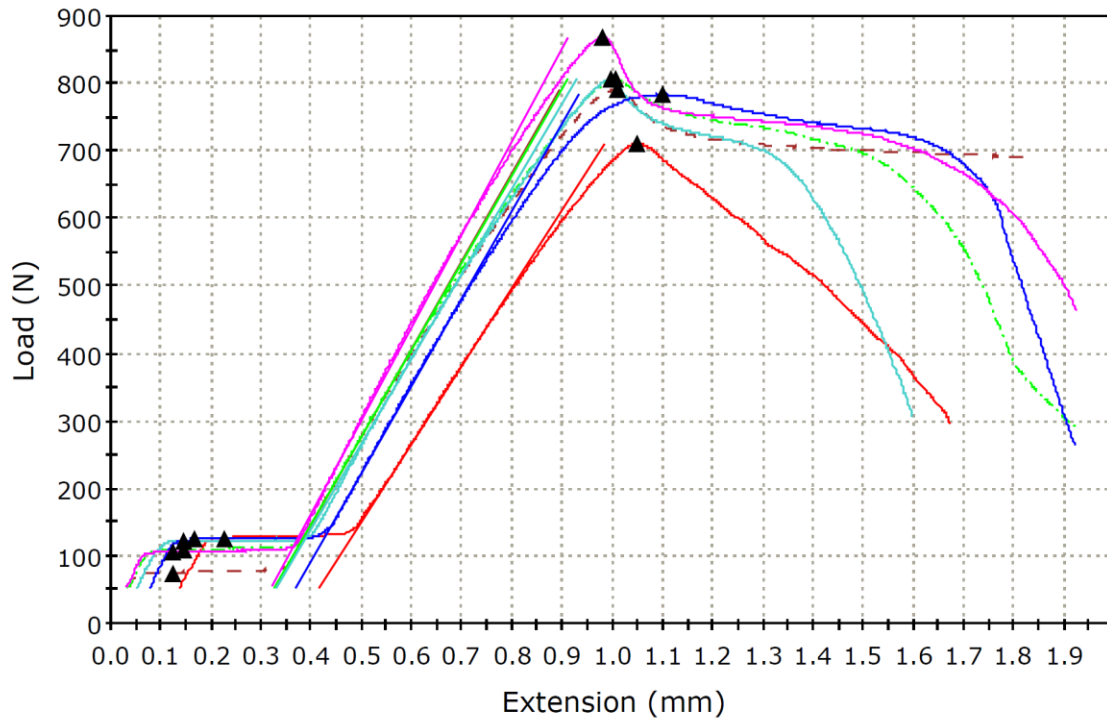

Figure S3.7 Load vs. extension curves for 3 mol% 26 kDa PLA in the longitudinal orientation (colors represent multiple test specimens of the same bimodal blend)
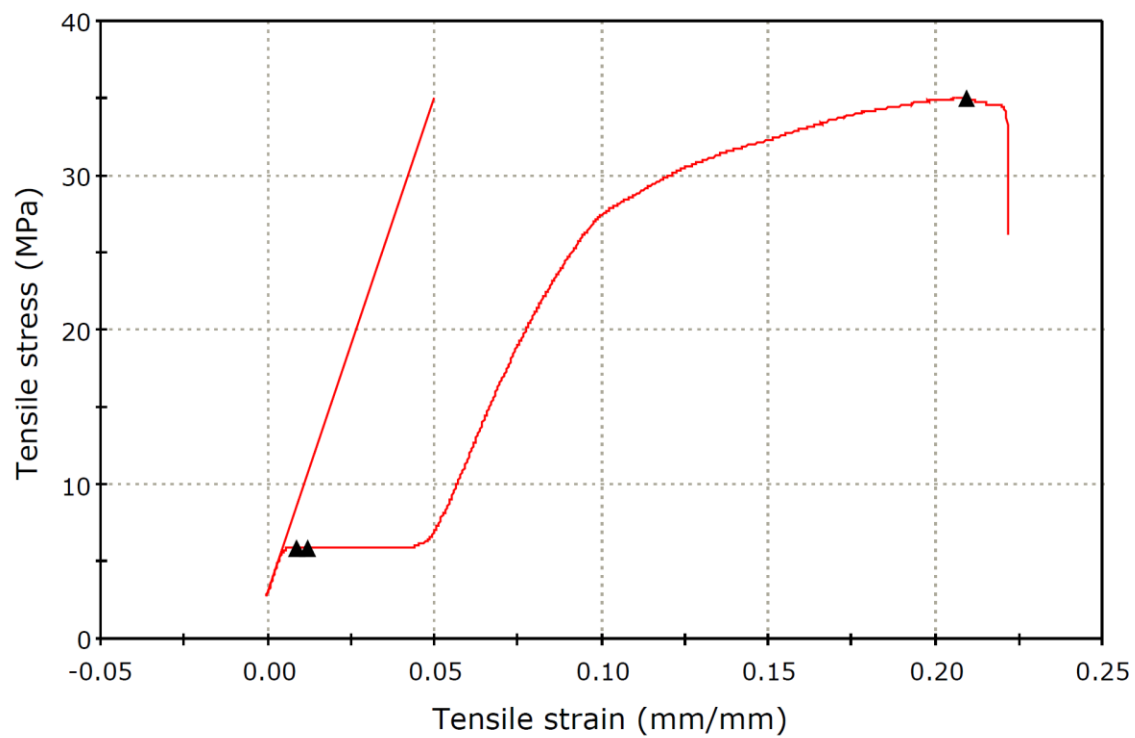
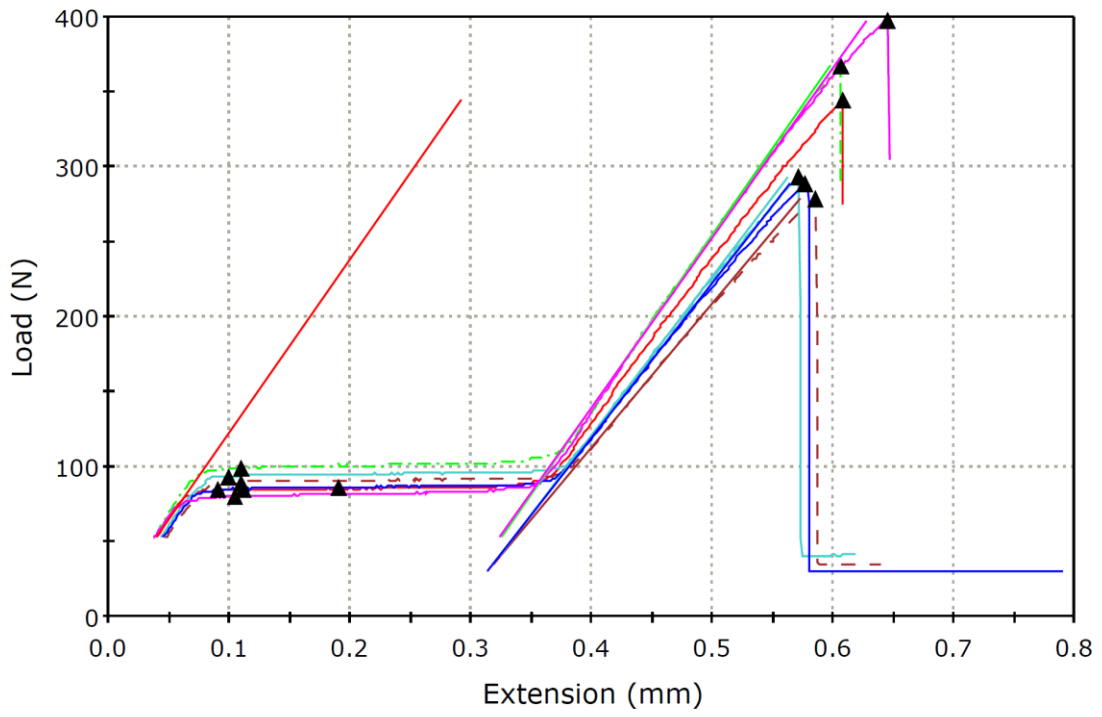**Figure S3.8 Stress vs strain curve of 3 mol% 26 kDa PLA in the longitudinal orientation**
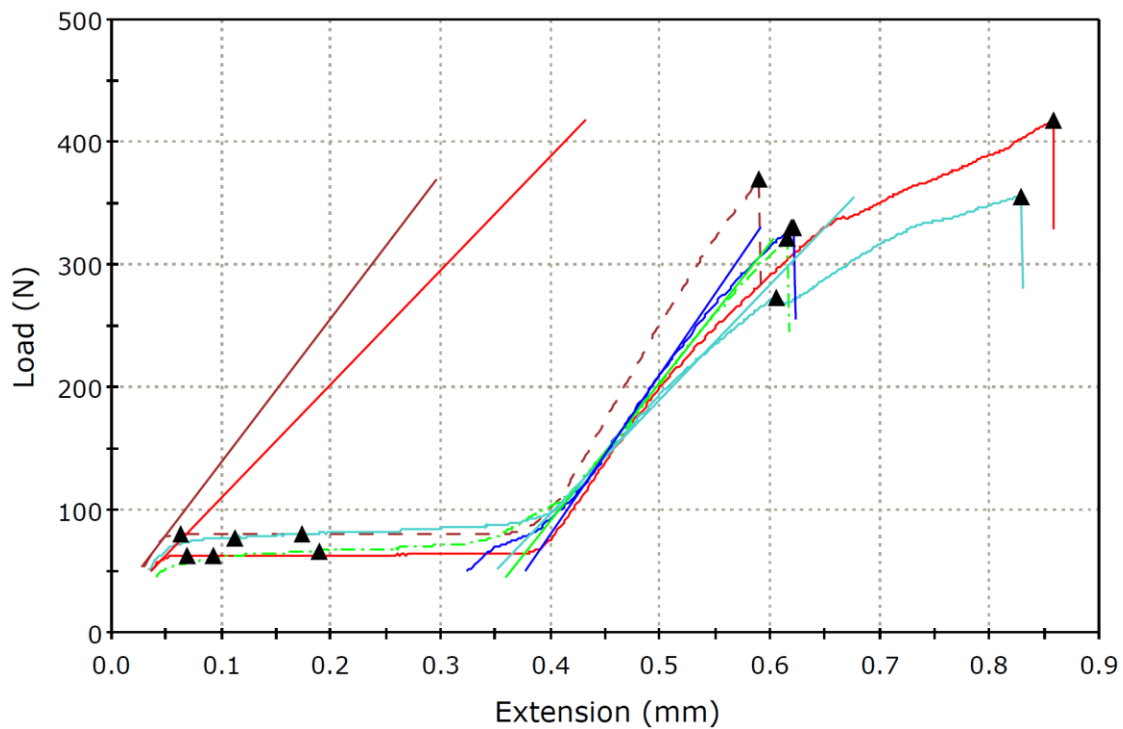
Figure S3.9 Load vs. extension curves for 3 mol% 26 kDa PLA in the transverse orientation (colors represent multiple test specimens of the same bimodal blend)
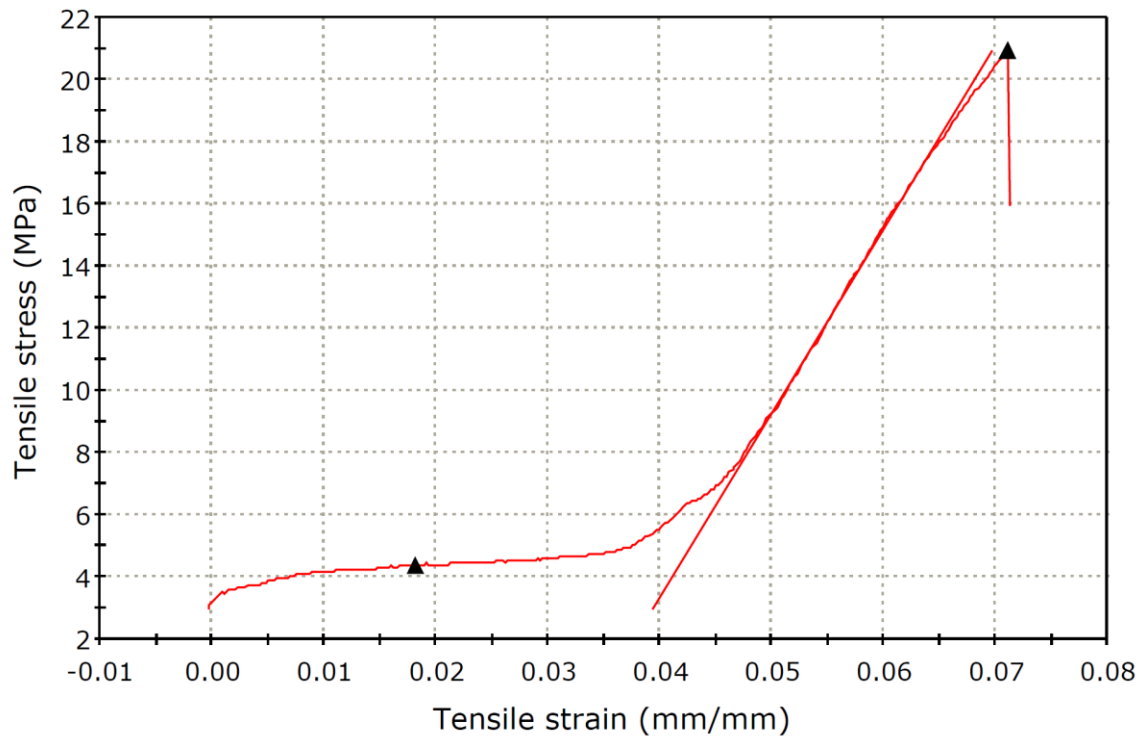
Figure S3.10 Stress vs strain curve of 3 mol% 26 kDa PLA in the transverse orientation
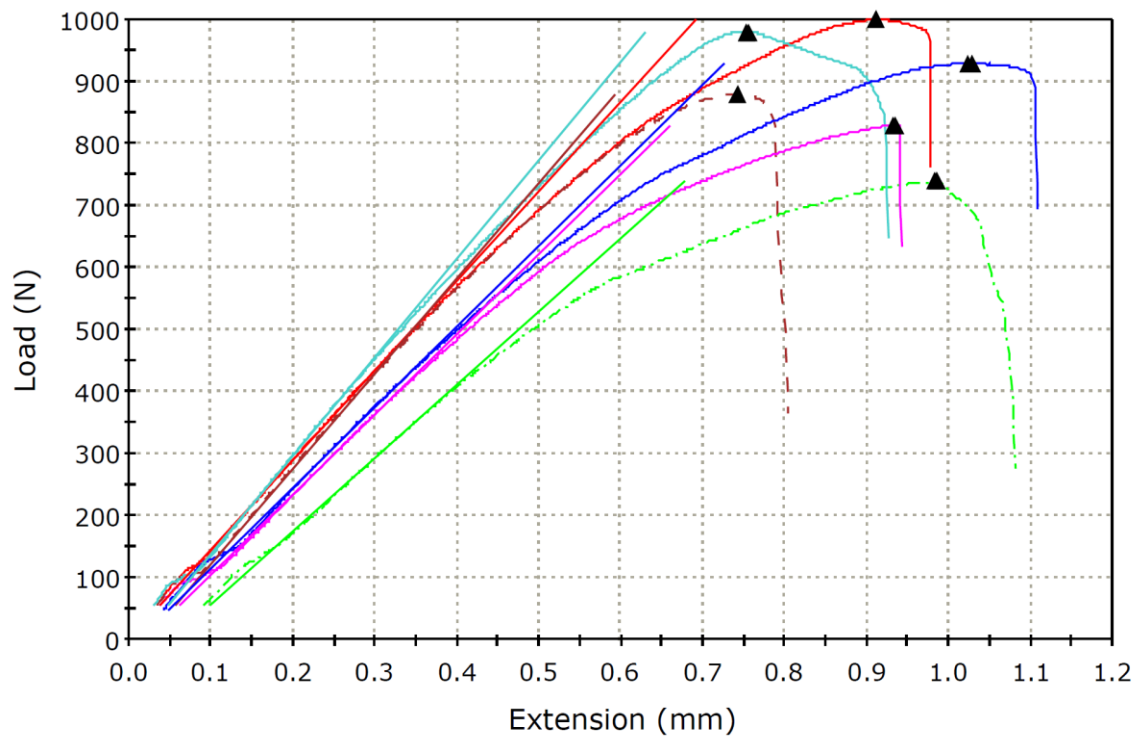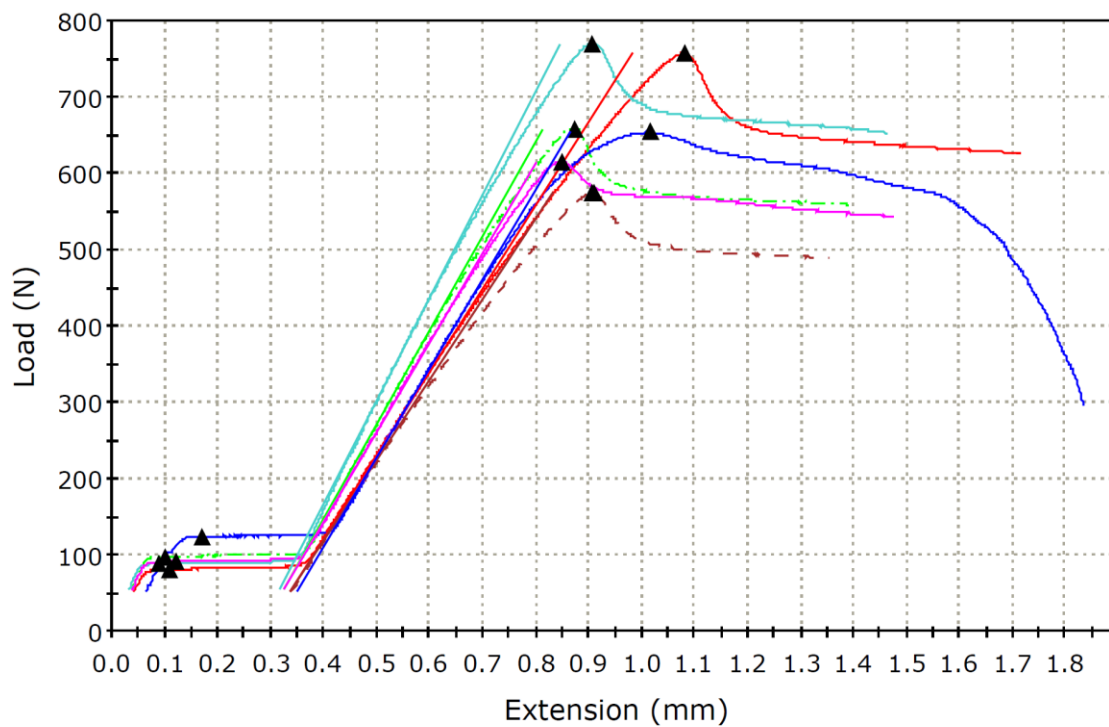
Figure S3.11 Load vs. extension curves for 3 mol% 3-arm 33 kDa PLA in the longitudinal orientation (colors represent multiple test specimens of the same bimodal blend)
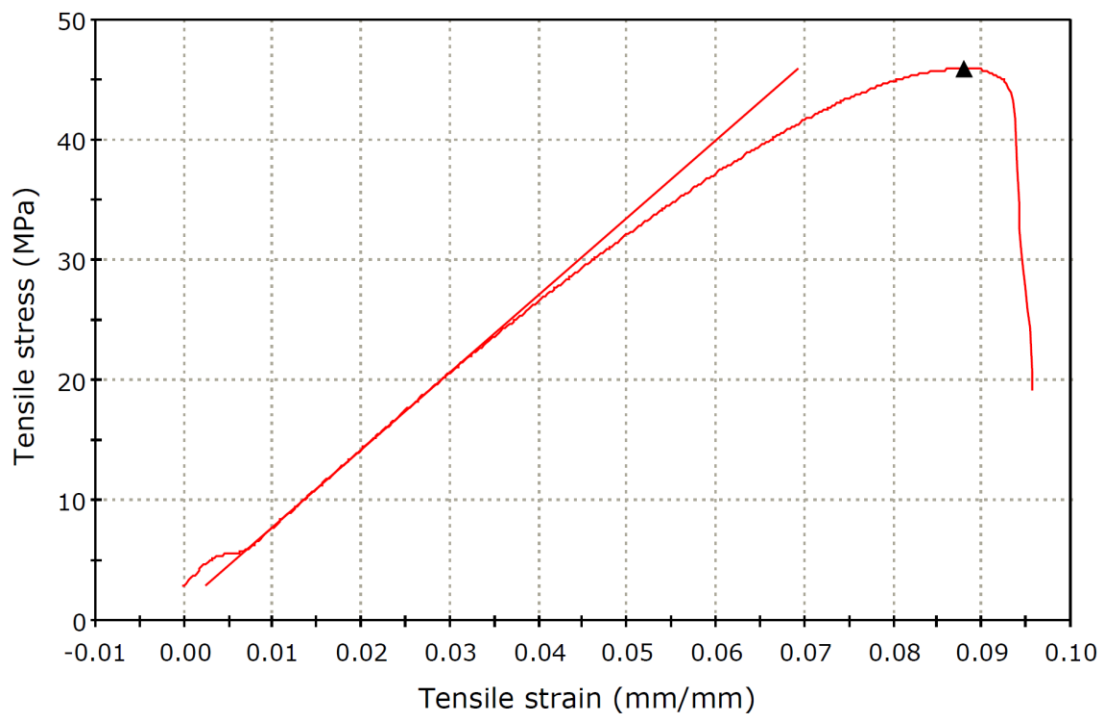
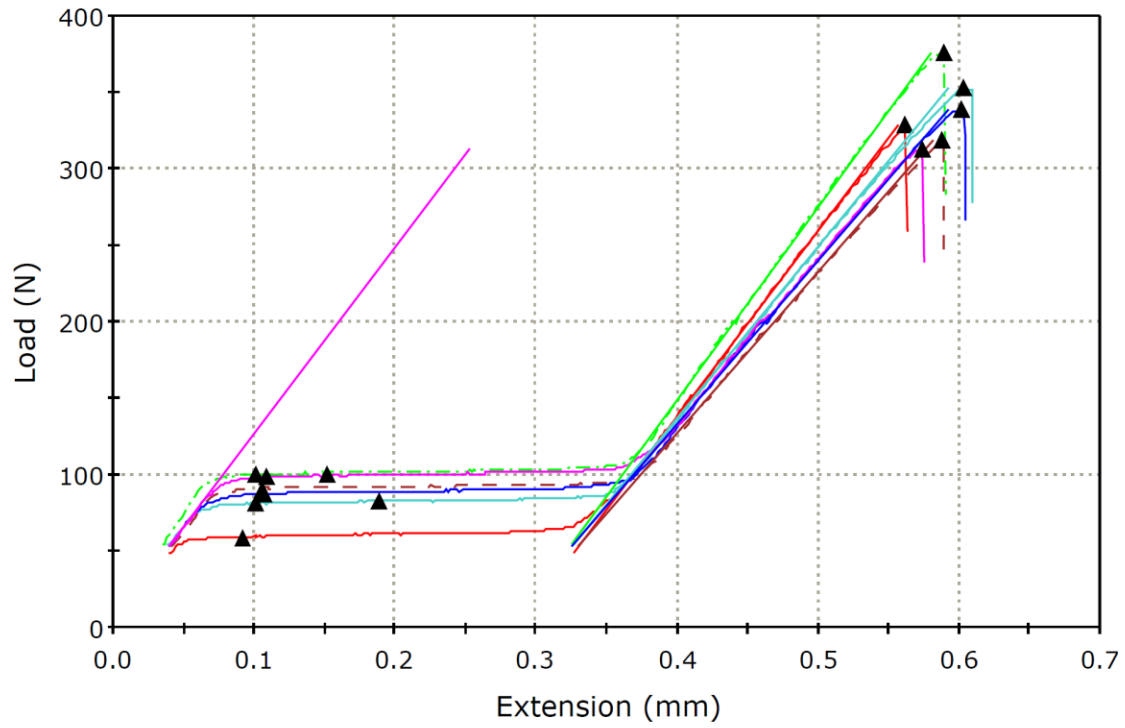**Figure S3.12 Stress vs strain curve of 3 mol% 3-arm 33 kDa PLA in the longitudinal orientation**
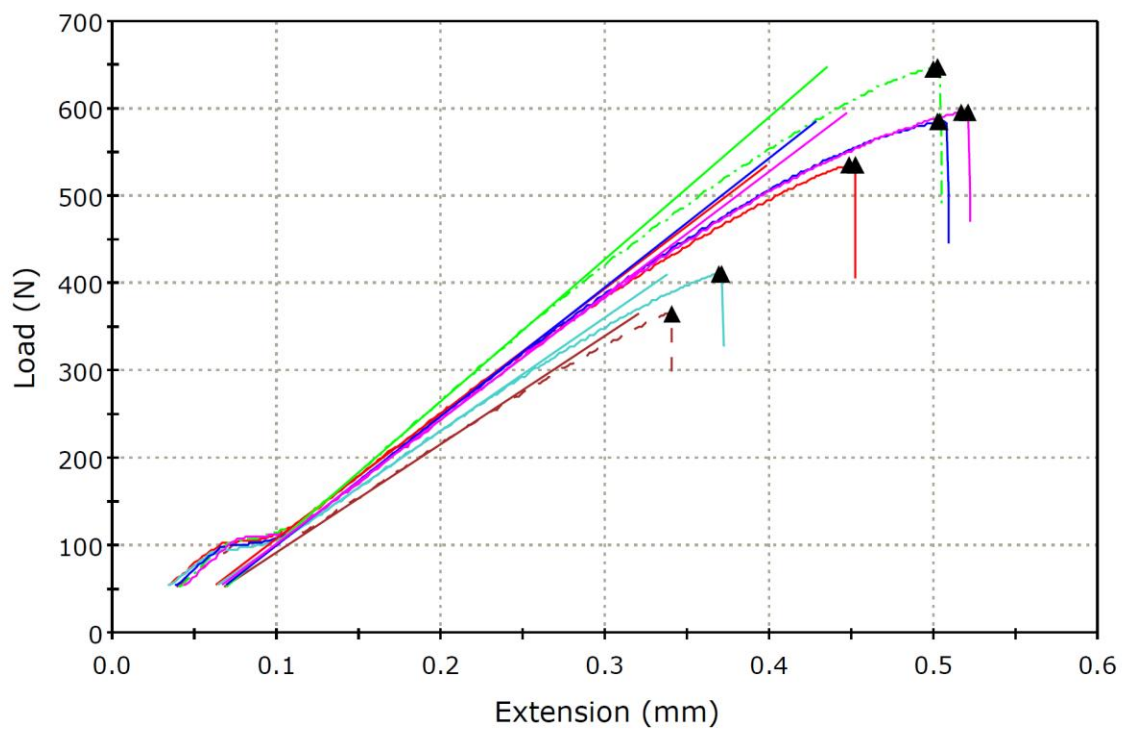
Figure S3.14 Load vs. extension curves for 3 mol% 33 kDa PLA in the transverse orientation (colors represent multiple test specimens of the same bimodal blend)
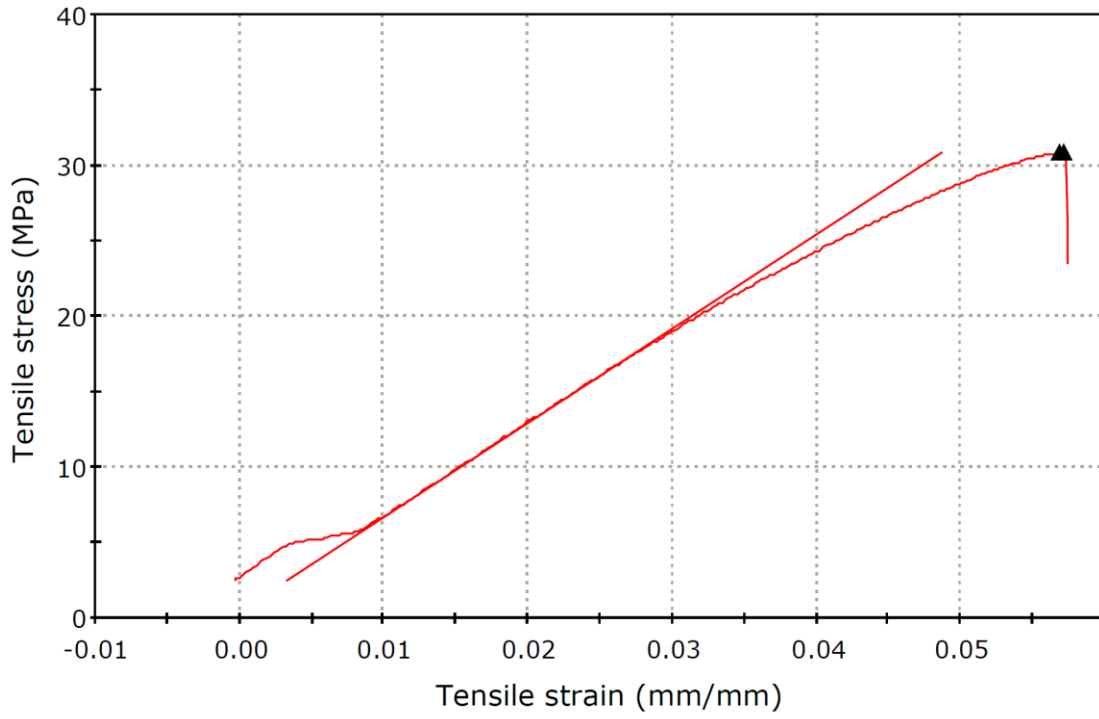
Figure S3.15 Stress vs strain curve of 3 mol% 3-arm 33 kDa PLA in the transverse orientation
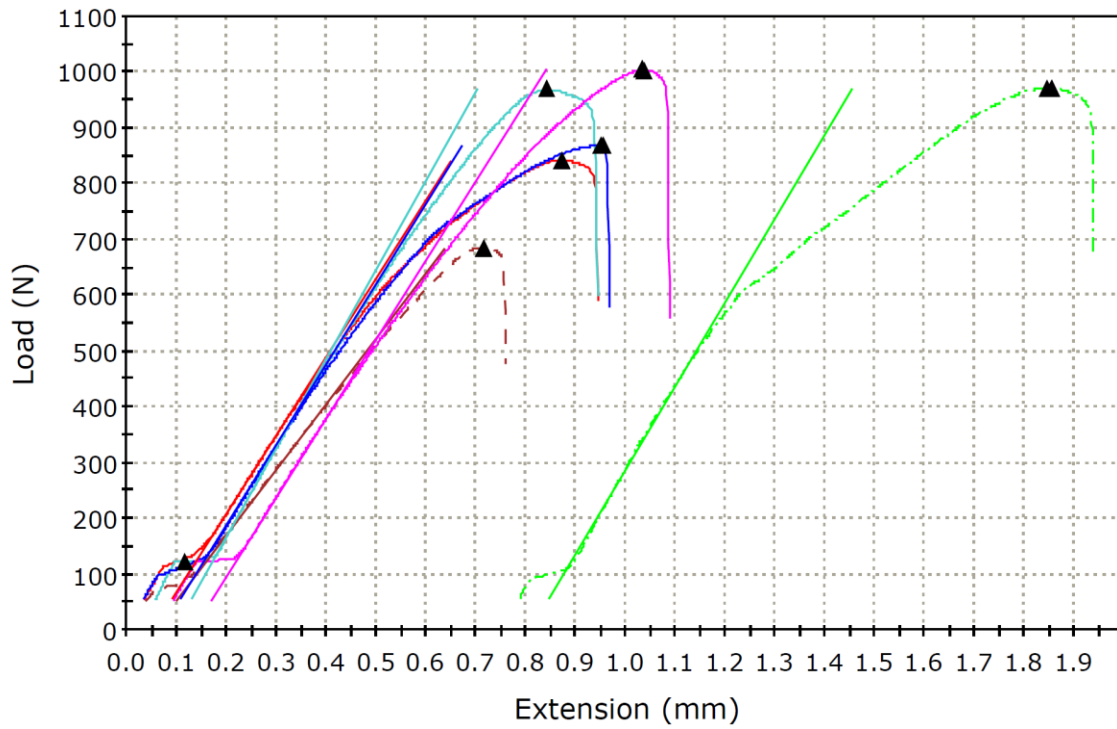
Figure S3.16 Load vs. extension curves for 3 mol% 4-arm 44 kDa PLA in the longitudinal orientation (colors represent multiple test specimens of the same bimodal blend)
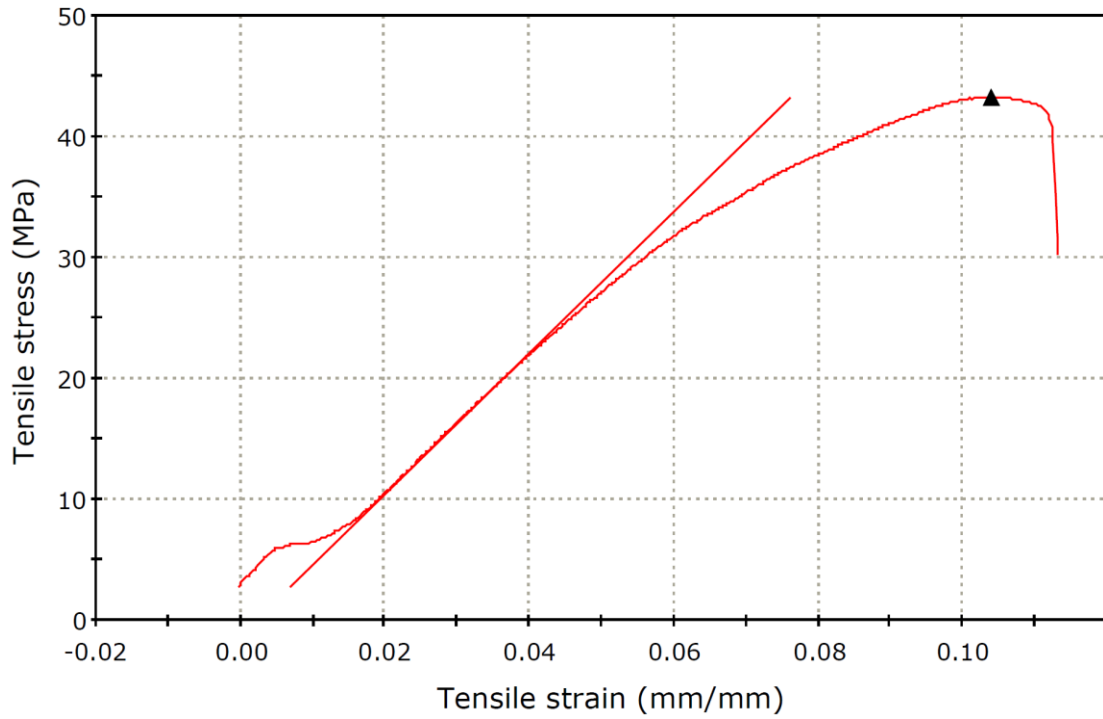
Figure S3.17 Stress vs strain curve of 3 mol% 4-arm 44 kDa PLA in the longitudinal orientation
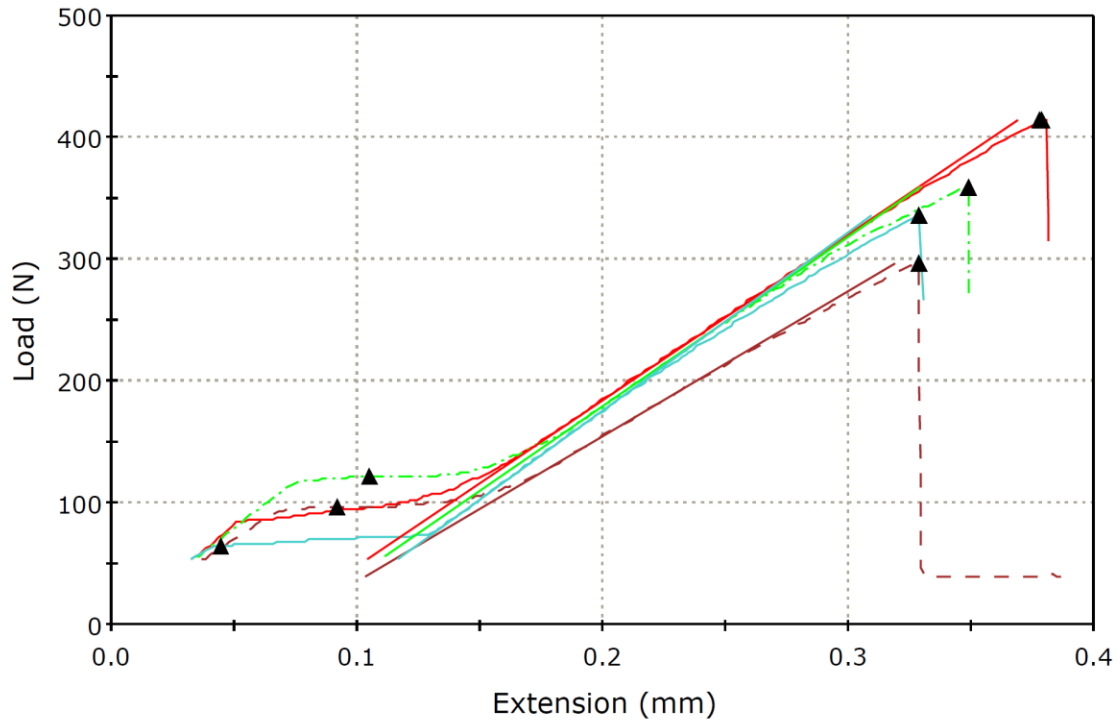
Figure S3.18 Load vs. extension curves for 3 mol% 4-arm 44 kDa PLA in the transverse orientation (colors represent multiple test specimens of the same bimodal blend)

Figure S3.19 Stress vs strain curve of 3 mol% 4-arm 44 kDa PLA in the transverse orientation
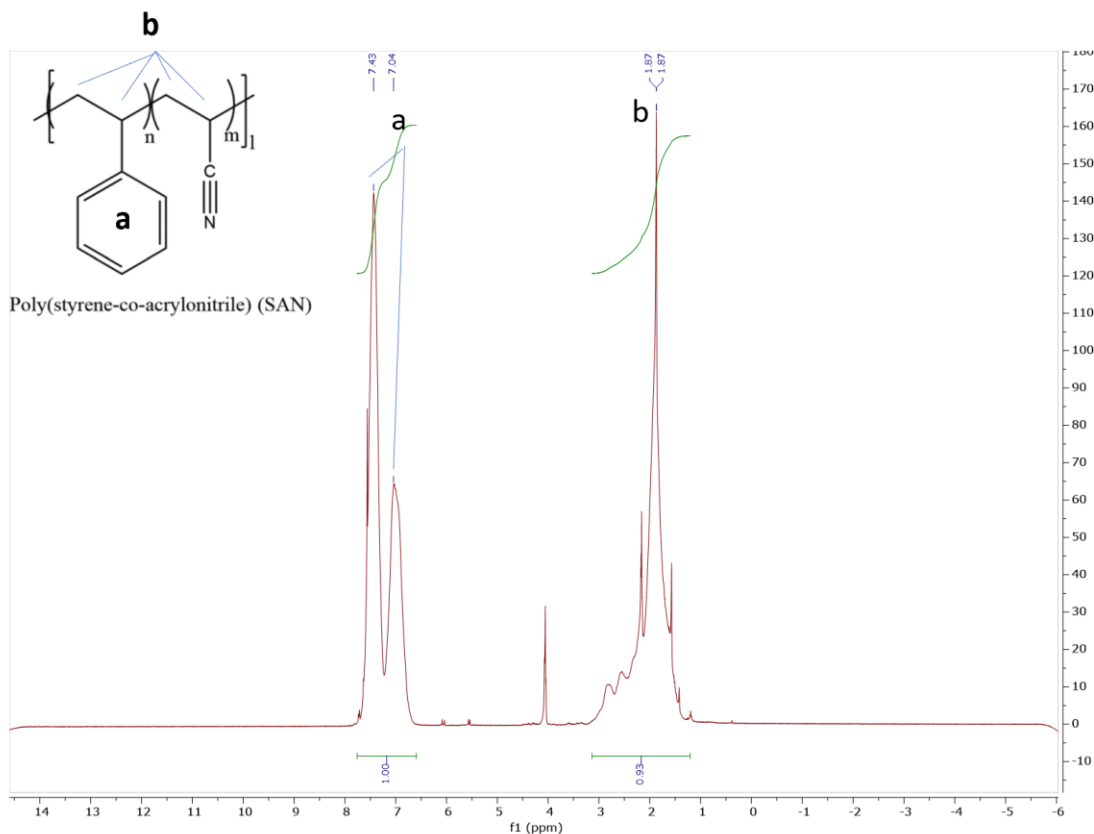
Figure S4.1 H-NMR of poly(styrene-co-acrylonitrile) (SAN)

We can determine the composition of the SAN copolymer utilizing the equation

$$S = 60(a/b)$$

Where S equals the mol% percentage of styrene and (a/b) represents the ratio between the ring protons of the styrene and the backbone protons of the entire chain respectively.[139] Thus, the SAN synthesized for these experiments is 65% styrene.

Table S4.1 Molecular weight characteristics of low molecular weight additives for ABS

SAMPLE	M_n (1 x 10^3)	M_w (1 x 10^3)	PDI
SAN (8.5K)	6.07	8.5	1.4
SAN (33K)	33	34	1.07
SAN (75K)	41	75	1.80
PMMA (33K)	31	35	1.13
PMMA (67K)	52	66	1.29
PMMA (100K)	72	120	1.68
PLA (33K-3ARM)	33	35	1.10
PLA (220K)	109	220	2.00
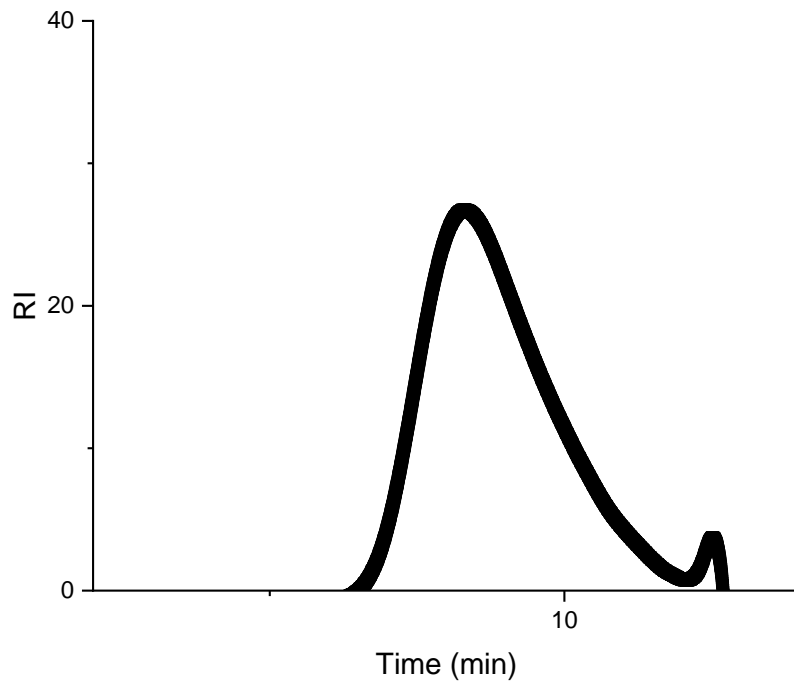
Figure S4.3 GPC trace of 8.5 kDa SAN
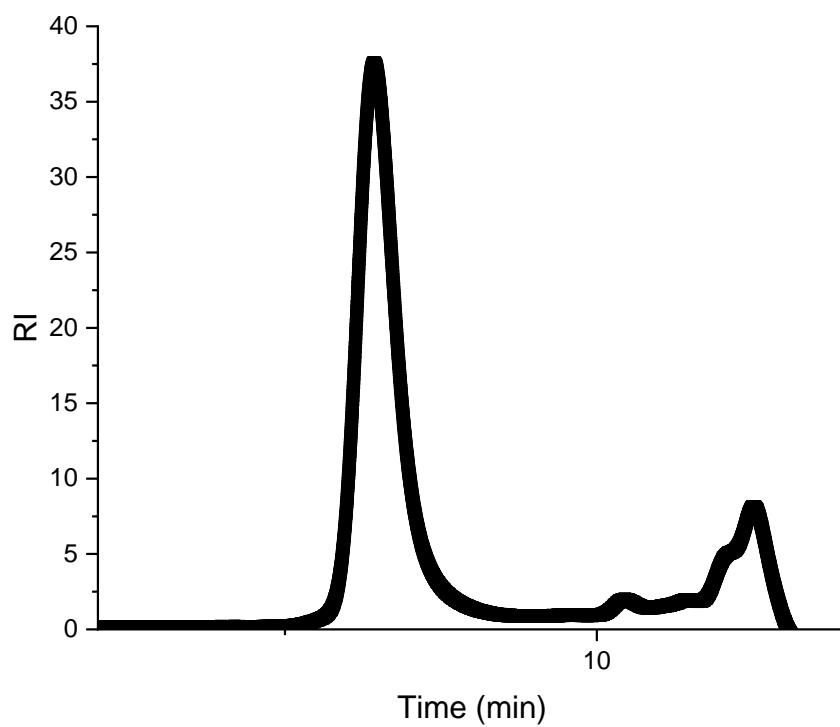
Figure S4.4 GPC trace of 33 kDa SAN
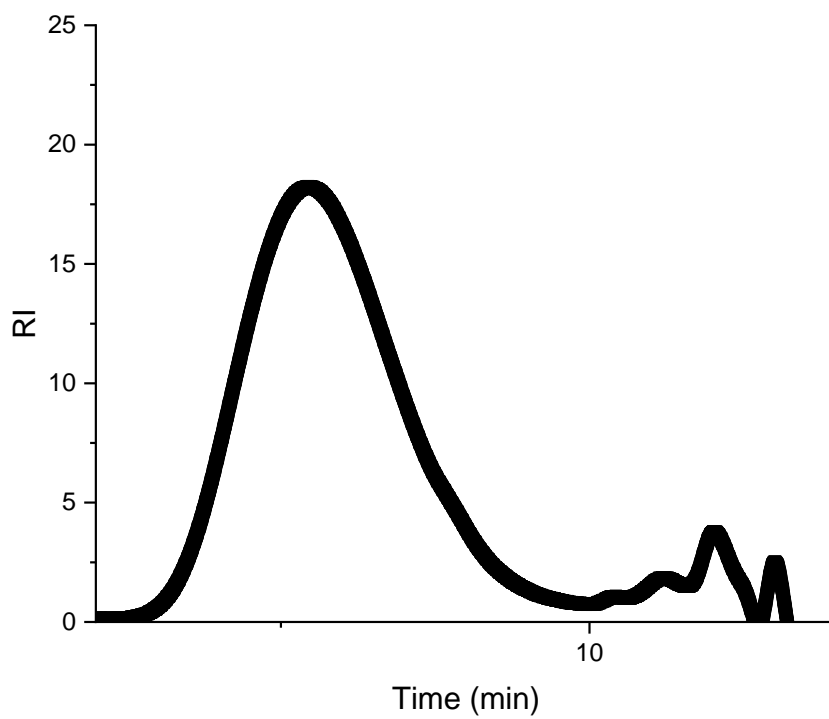
Figure S4.5 GPC trace of 75 kDa SAN
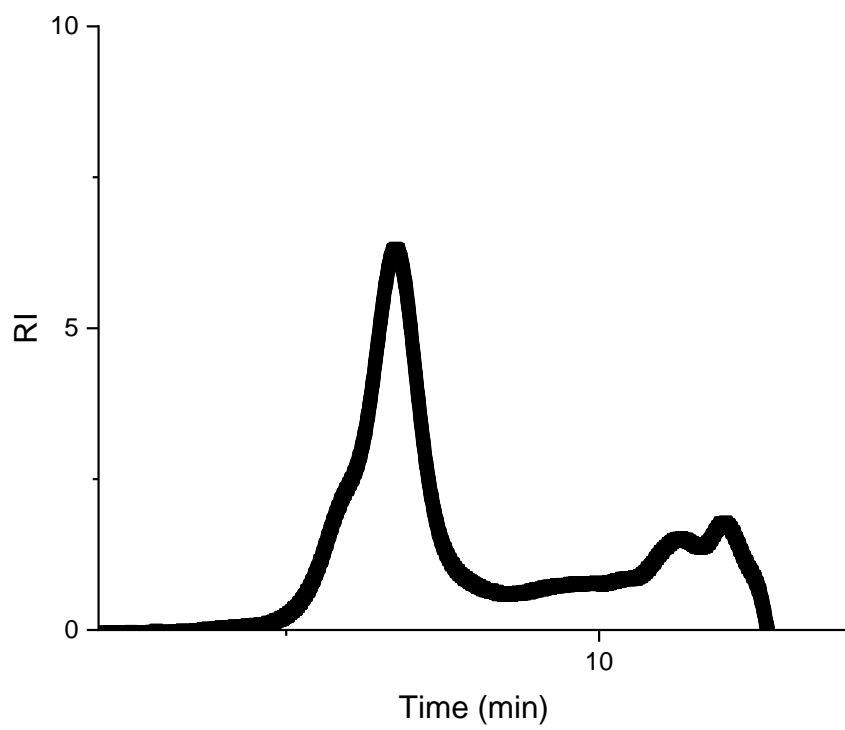
Figure S4.6 GPC trace of 33 kDa PMMA
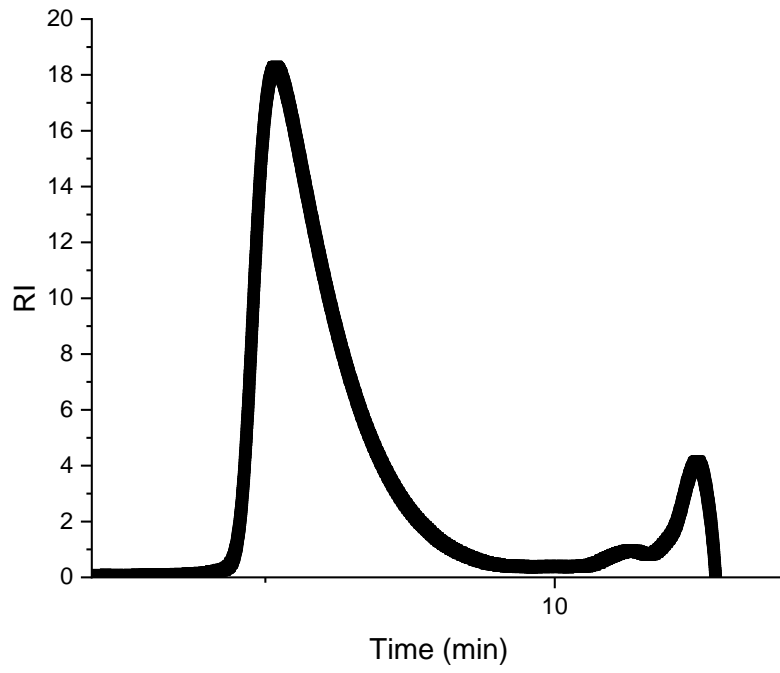
Figure S4.7 GPC trace of 67 kDa PMMA
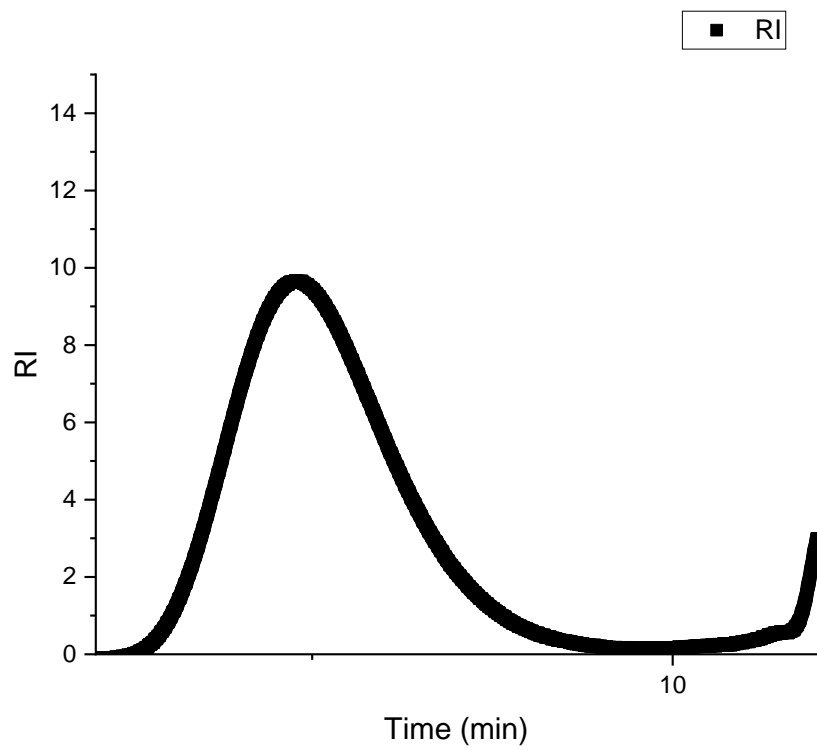
Figure S4.8 GPC trace of 100 kDa PMMA
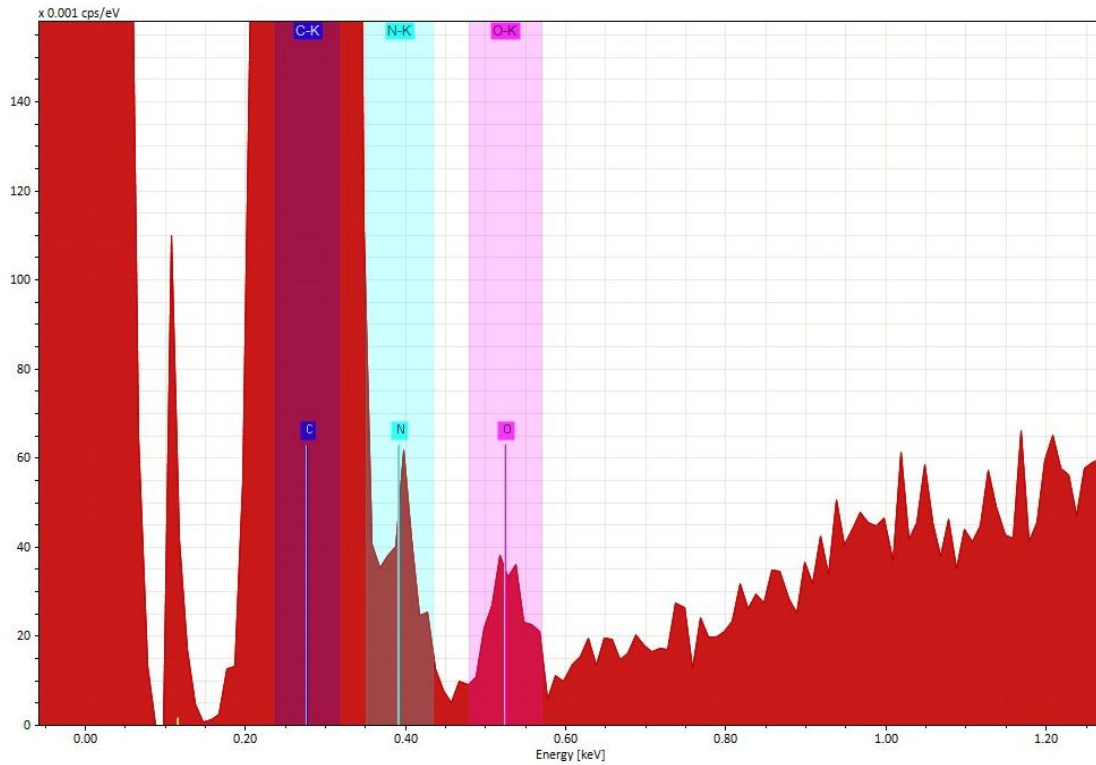
Figure S4.11 EDS spectra of ABS average scan
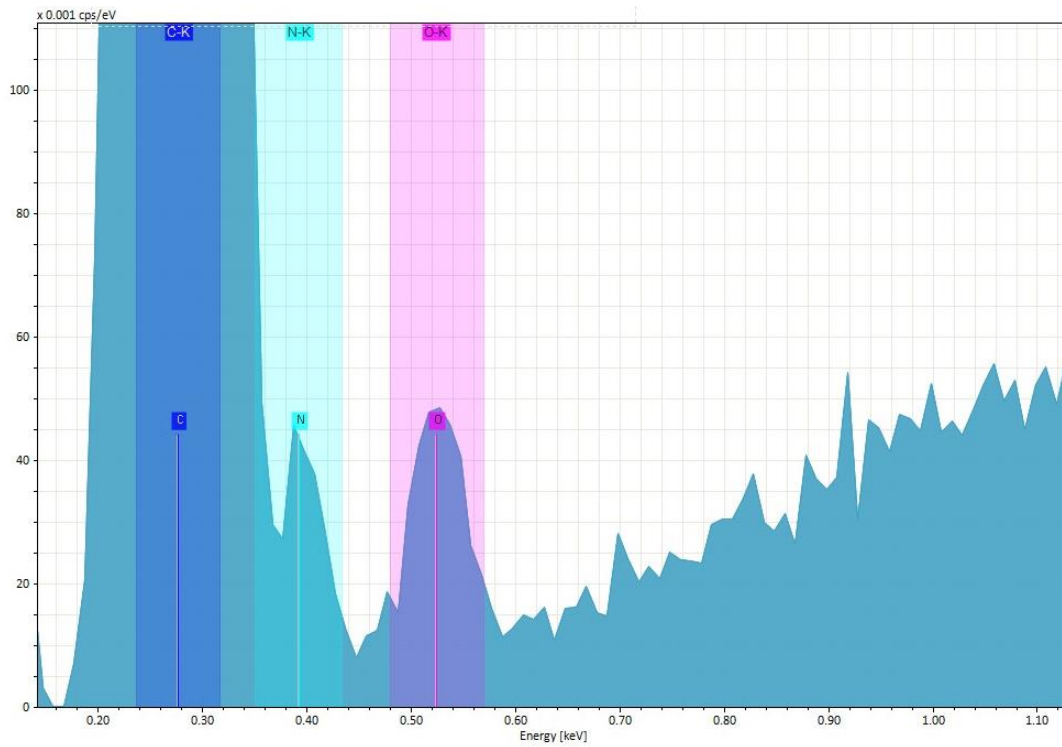
Figure S4.12 EDS spectra of ABS center scan
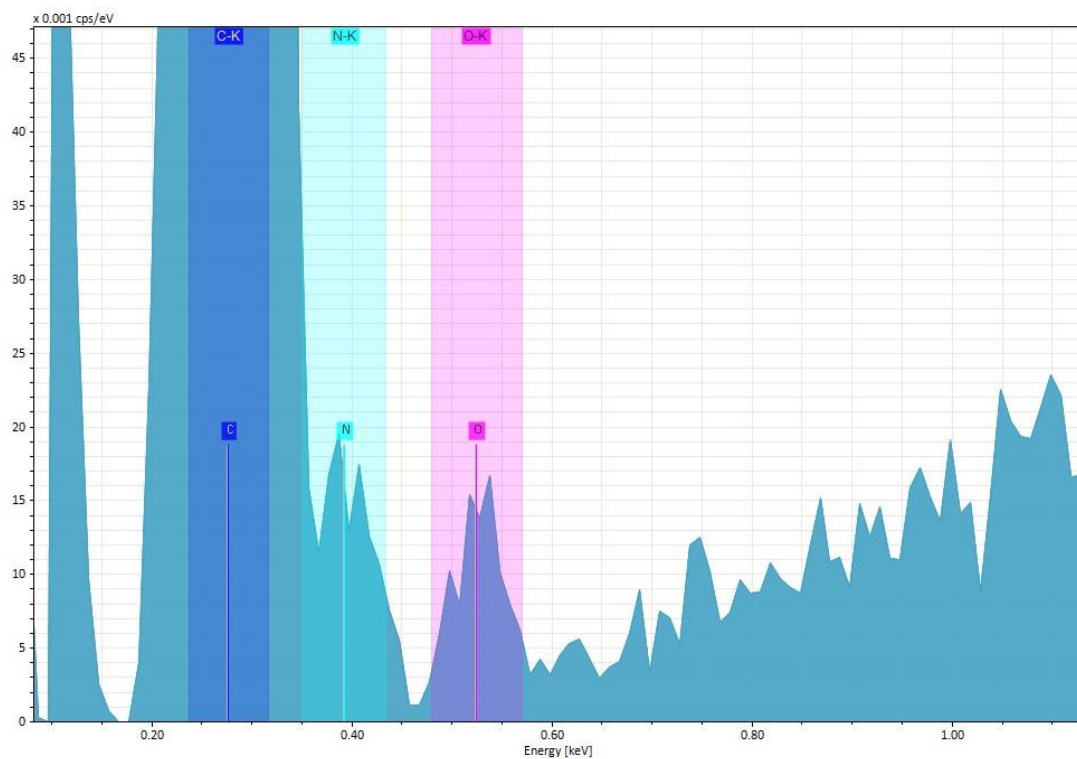
Figure S4.13 EDS spectra of ABS void scan
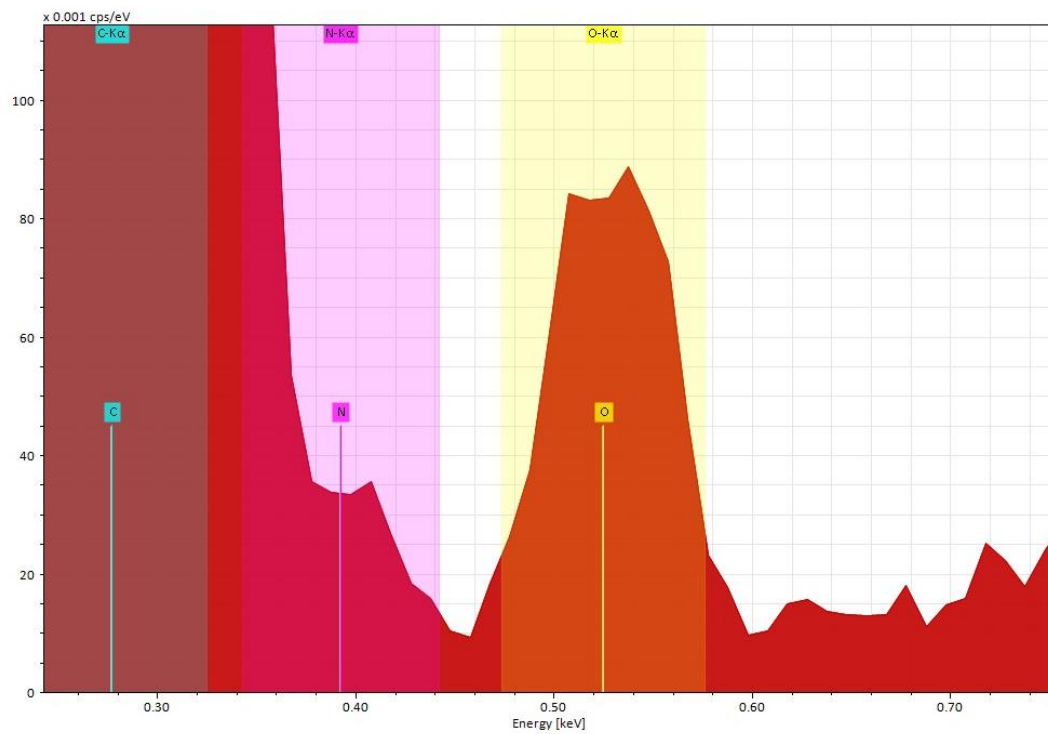
Figure S4.14 EDS spectra of ABS/ 33k PMMA 3 mol blend average scan
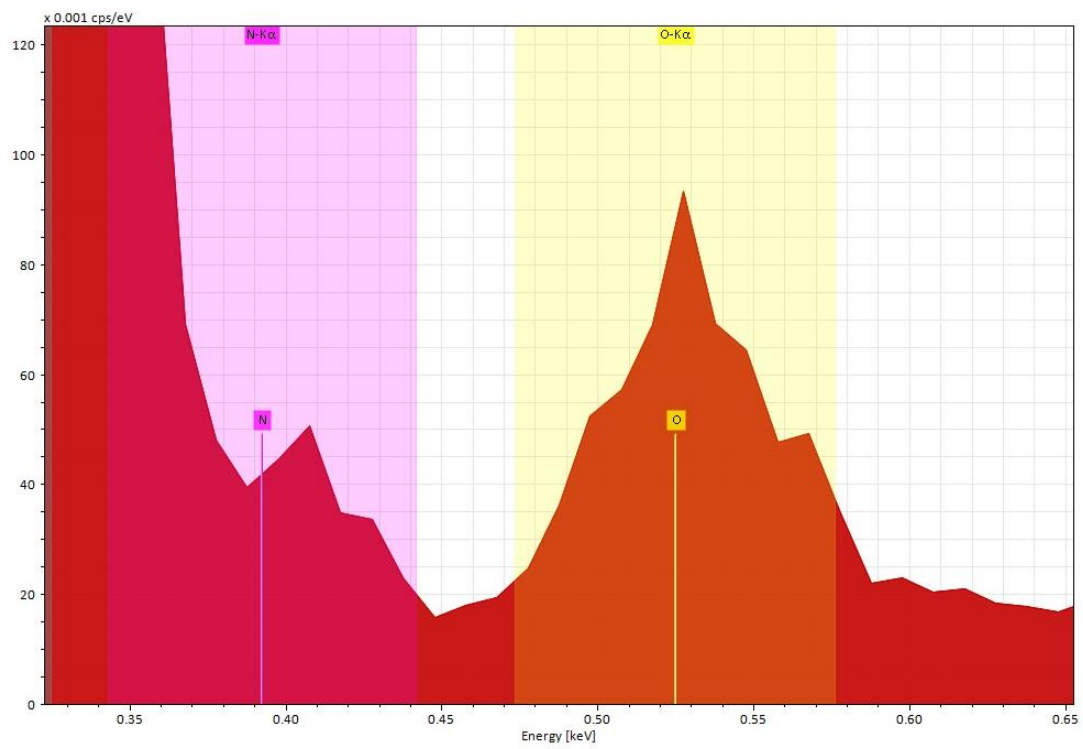
Figure S4.15 EDS spectra of ABS/ 33k PMMA 3 mol blend center scan
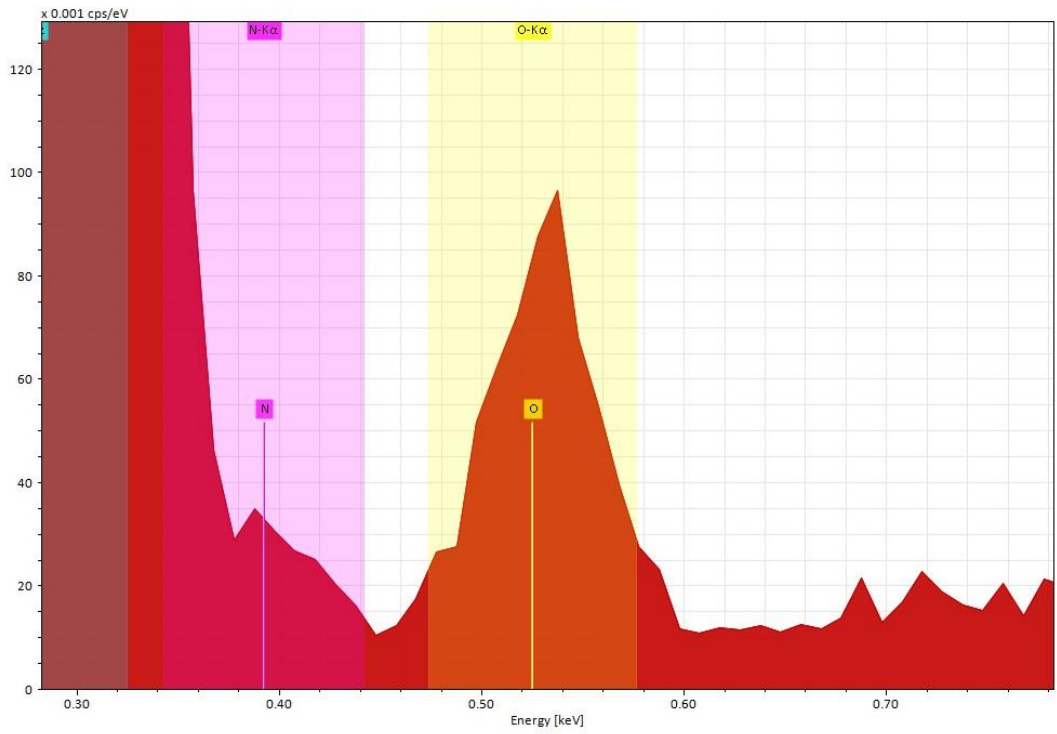
Figure S4.16 EDS spectra of ABS/ 33k PMMA 3 mol blend void scan
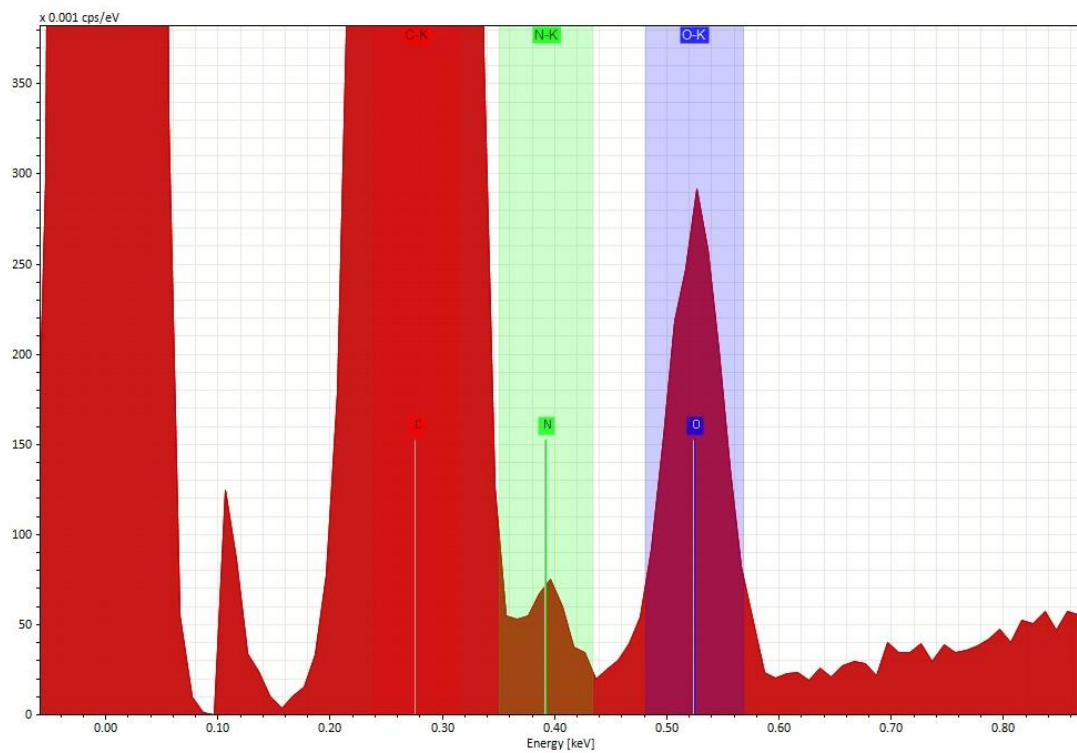
Figure S4.17 EDS spectra of ABS/ 67k PMMA 3 mol average scan
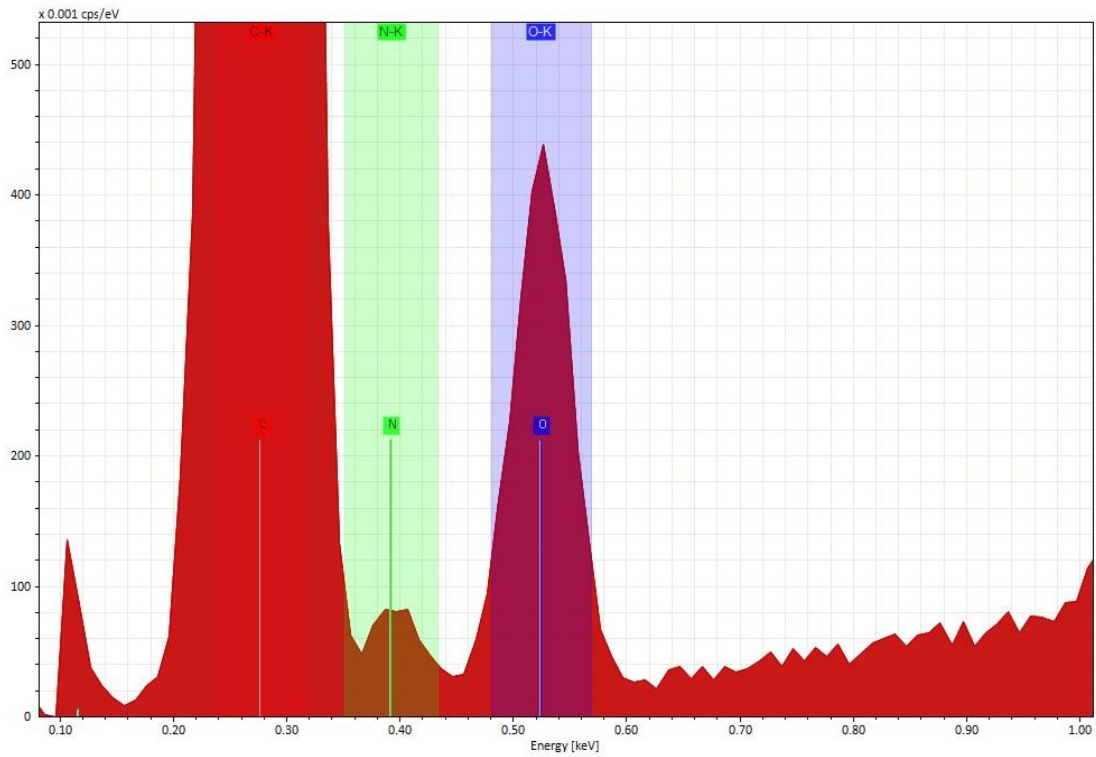
Figure S4.18 EDS spectra of ABS/ 67k PMMA 3 mol center scan
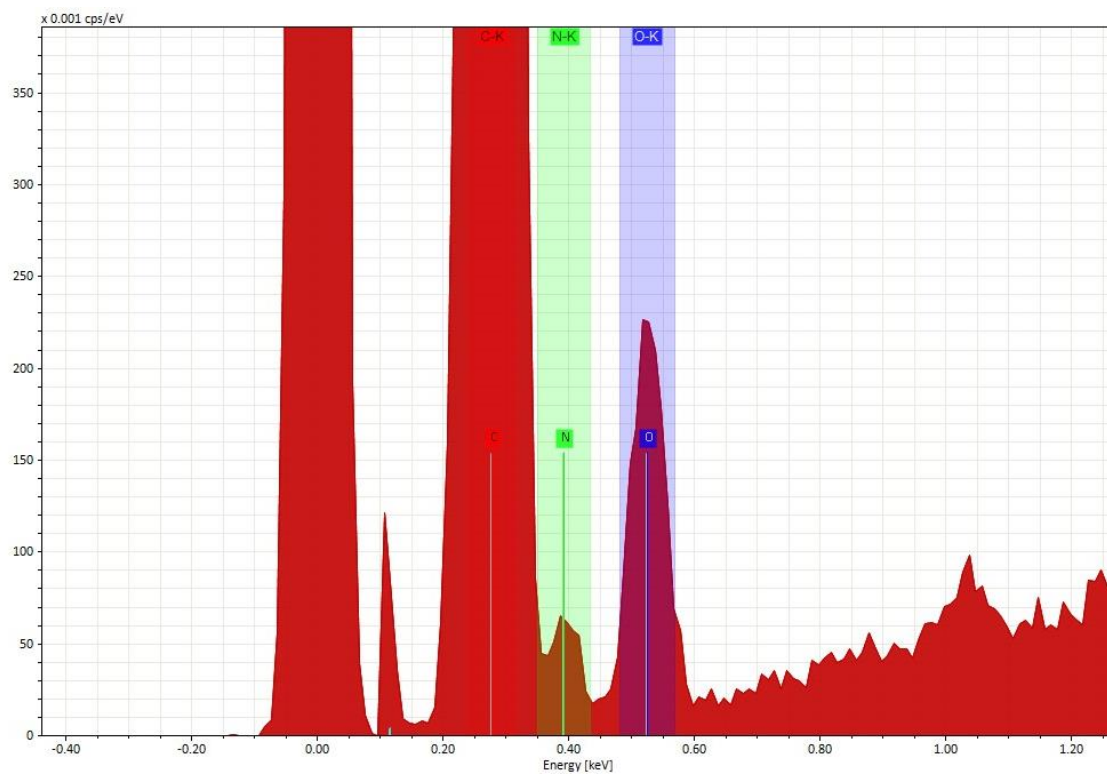
Figure S4.19 EDS spectra of ABS/ 67k PMMA 3 mol void scan
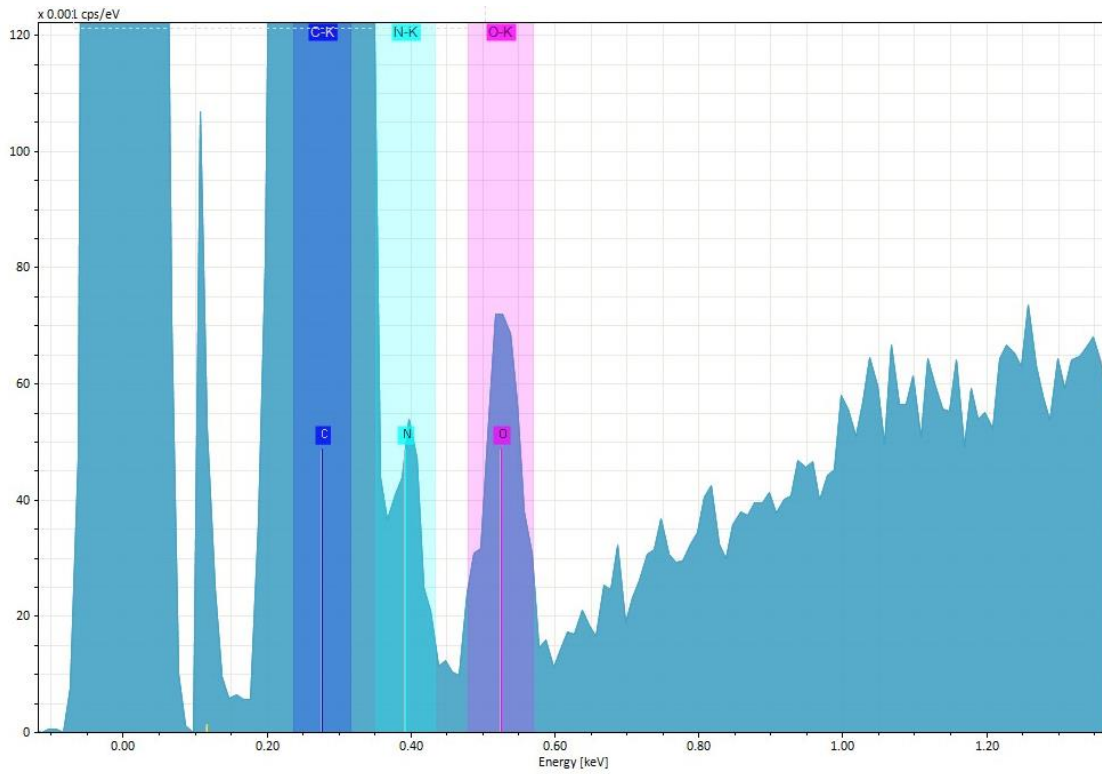
Figure S4.20 EDS spectra of ABS/ 100k PMMA 3 mol average scan
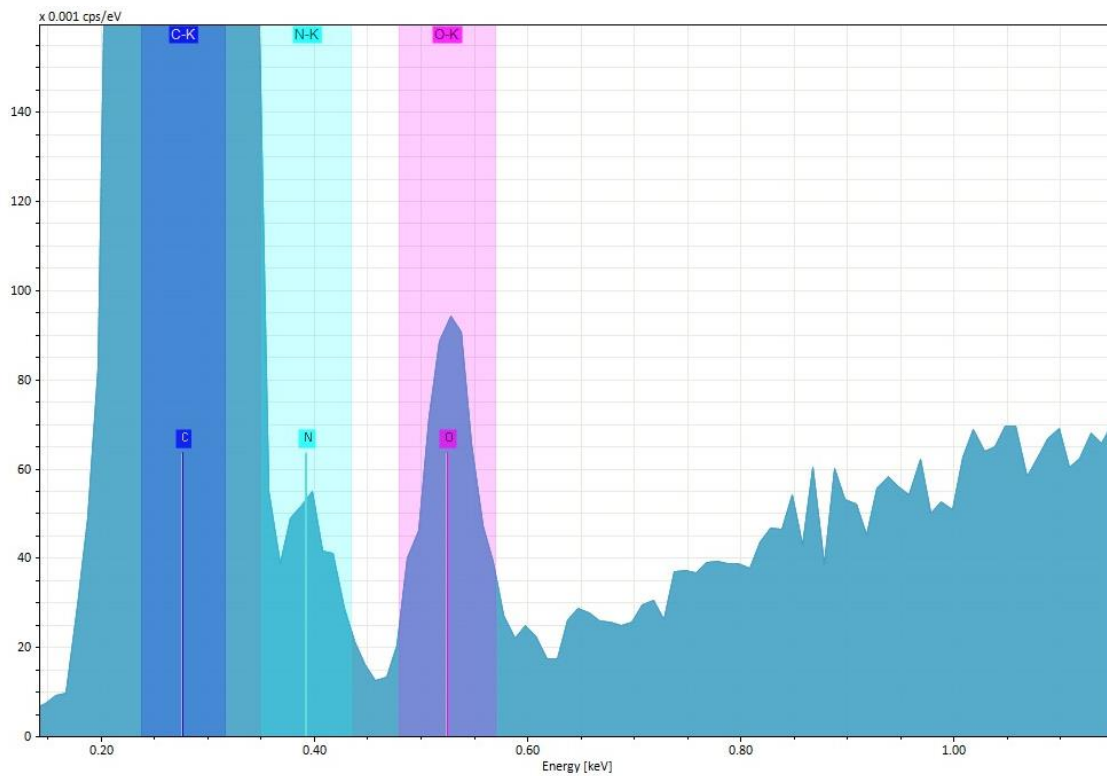
Figure S4.21 EDS spectra of ABS/ 100k PMMA 3 mol center scan
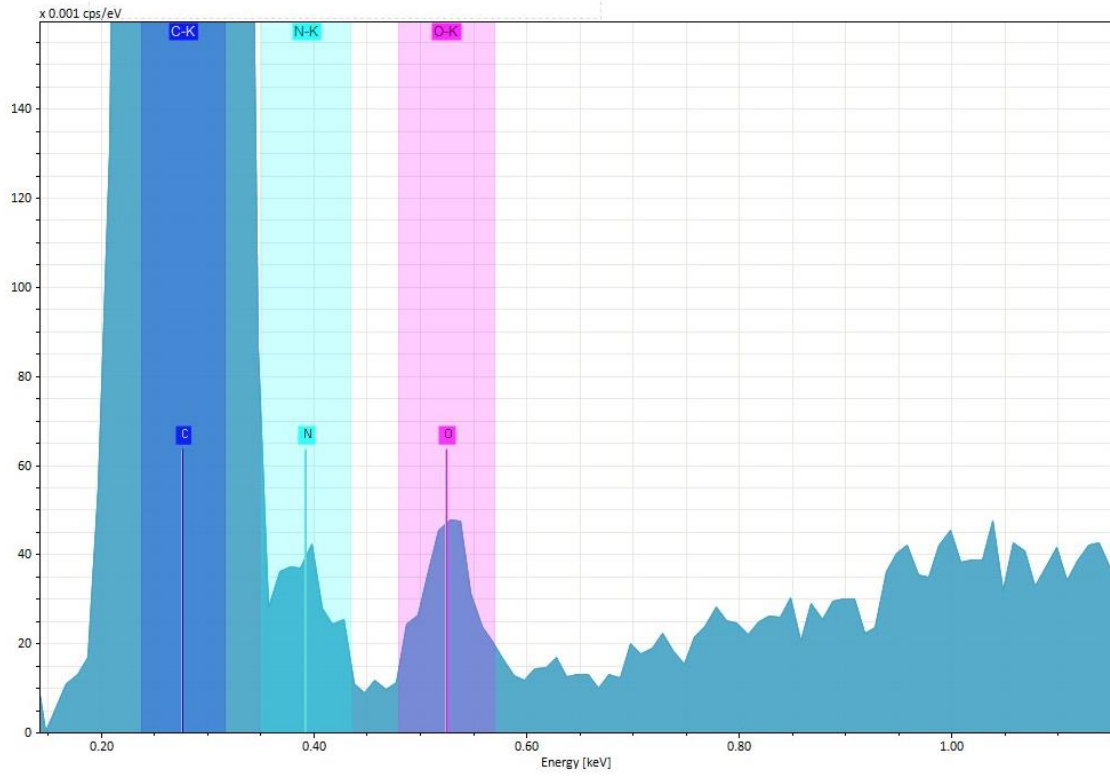
Figure S4.22 EDS spectra of ABS/ 100k PMMA 3 mol void scan
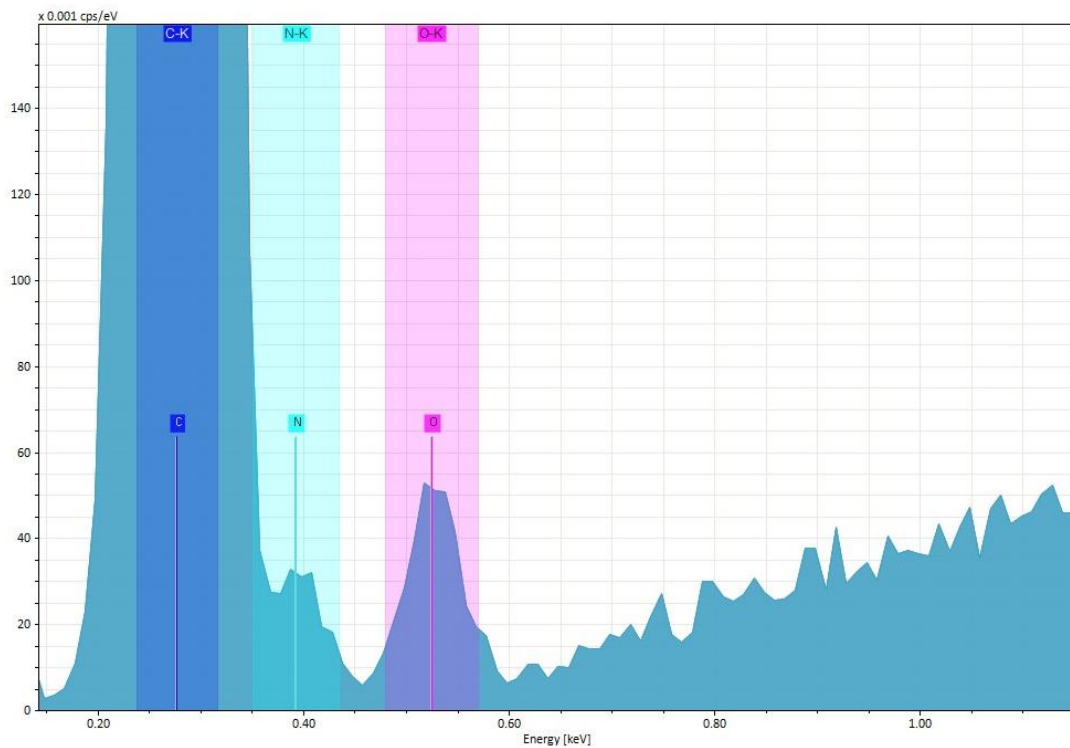
Figure S4.23 EDS spectra of ABS/ 33k-3 arm PLA 3 mol average scan
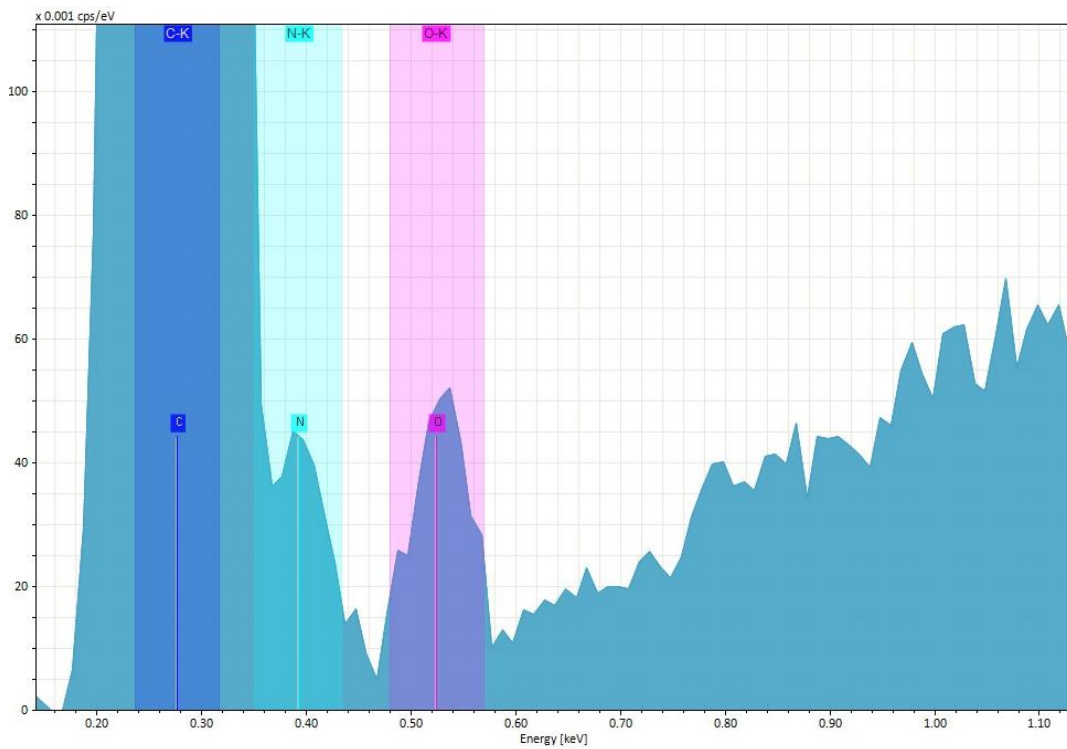
Figure S4.24 EDS spectra of ABS/ 33k-3 arm PLA 3 mol center scan
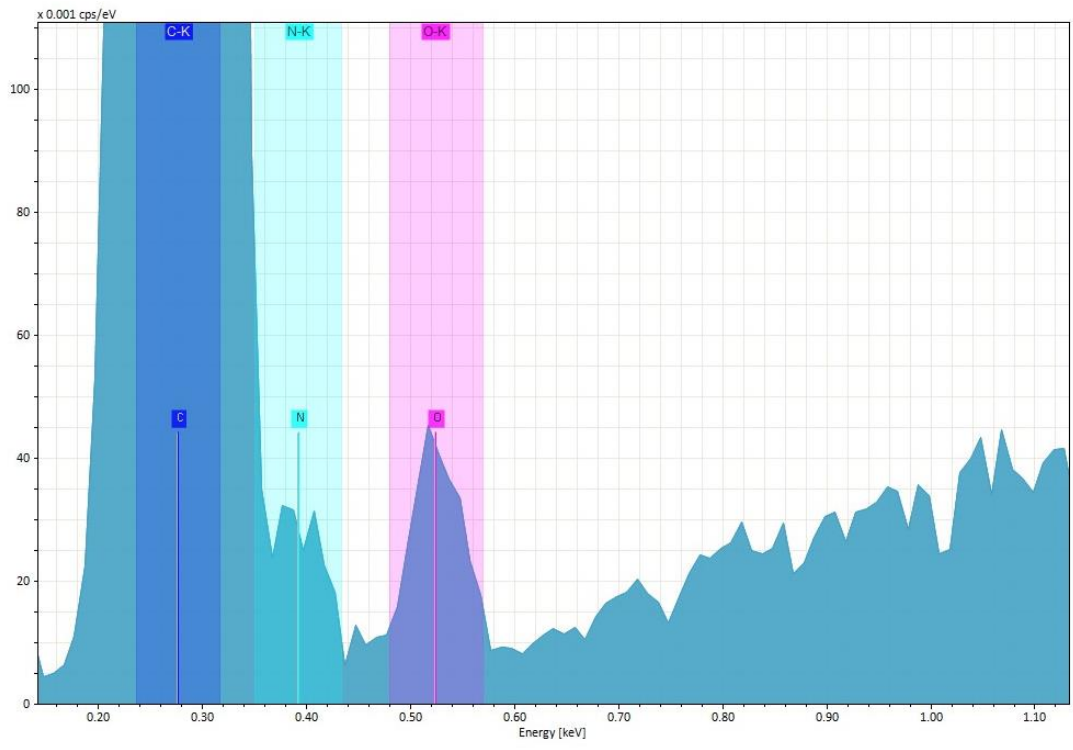
Figure S4.25 EDS spectra of ABS/ 33k-3 arm PLA 3 mol void scan
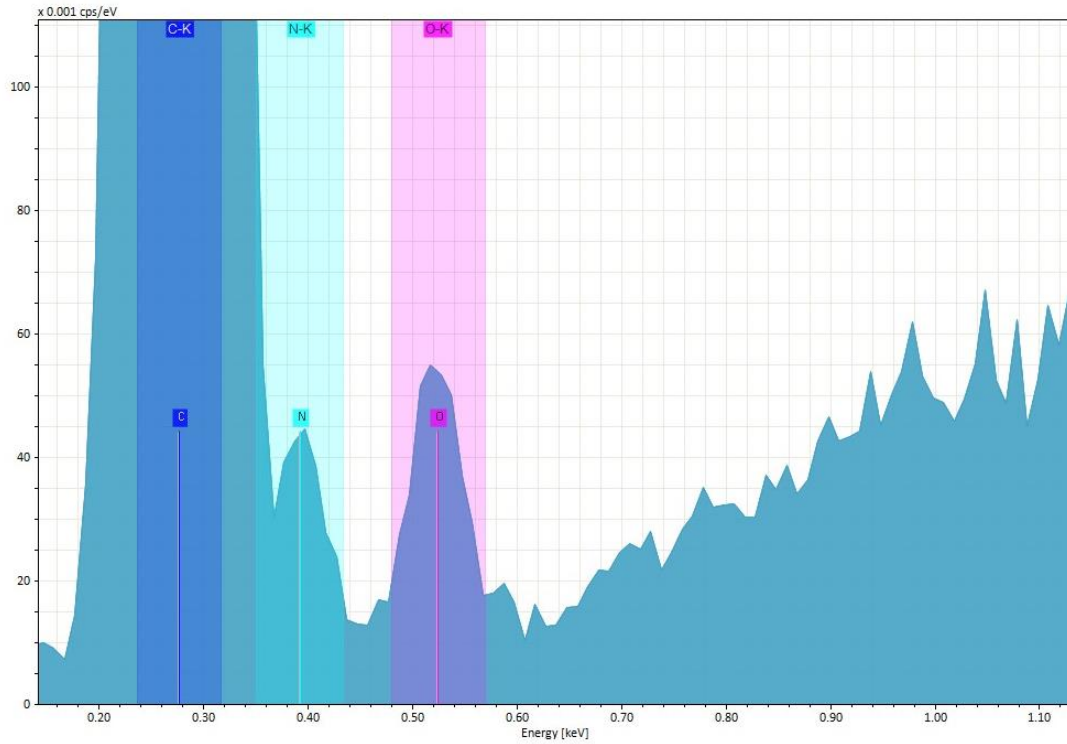
Figure S4.26 EDS spectra of ABS/ 220k PLA 3 mol average scan
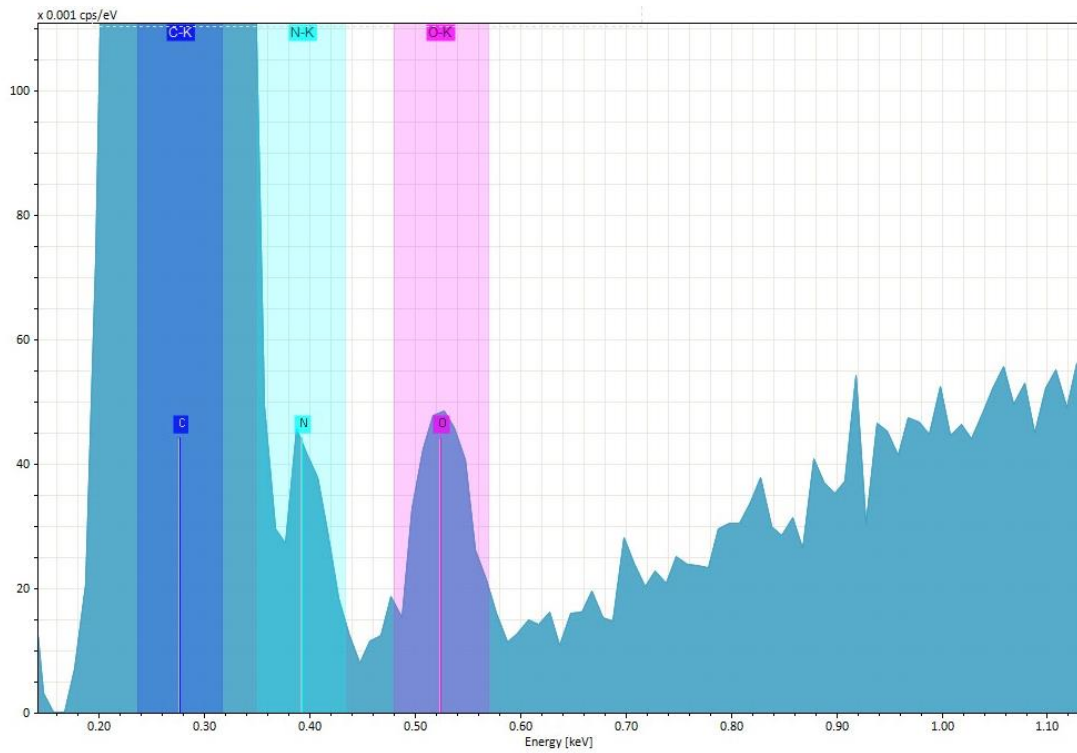
Figure S4.27 EDS spectra of ABS/ 220k PLA 3 mol center scan
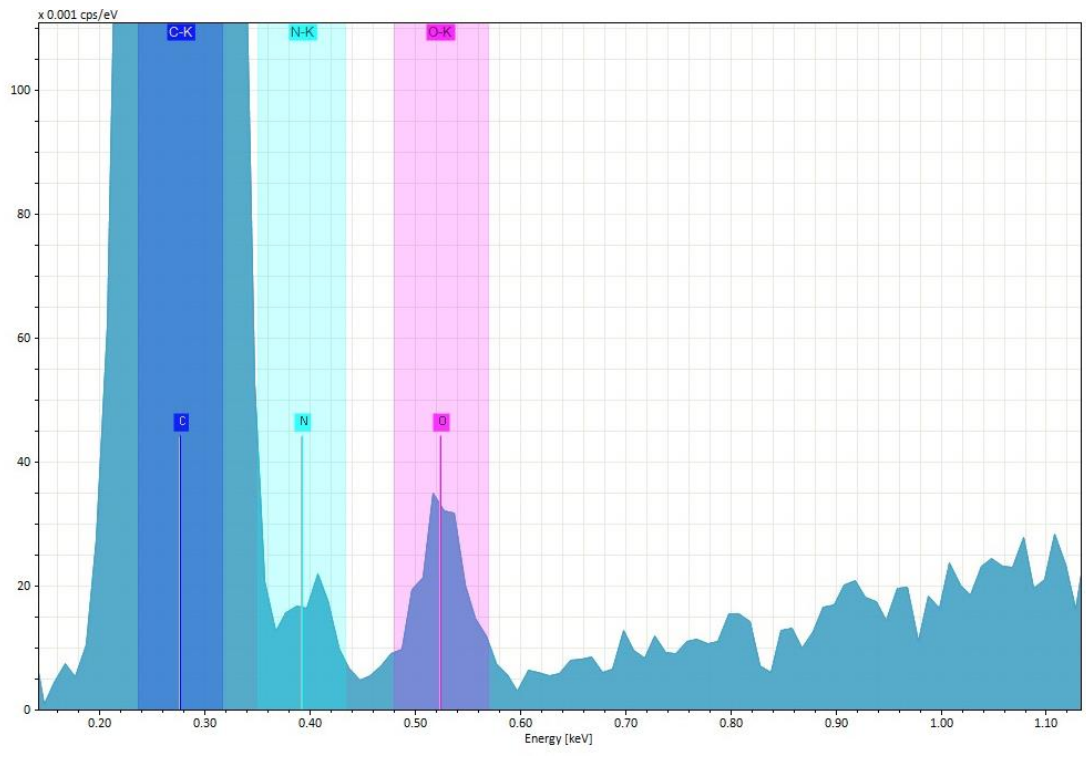
Figure S4.28 EDS spectra of ABS/ 220k PLA 3 mol void scan

Tensile data for Chapter 4 showing all specimens, which is presented as load (N) vs.

extension (mm).

Figure S4.29 Load vs. extension curves for 150 kDa ABS (Neat) in the longitudinal orientation (colors represent multiple test specimens of the same bimodal blend)

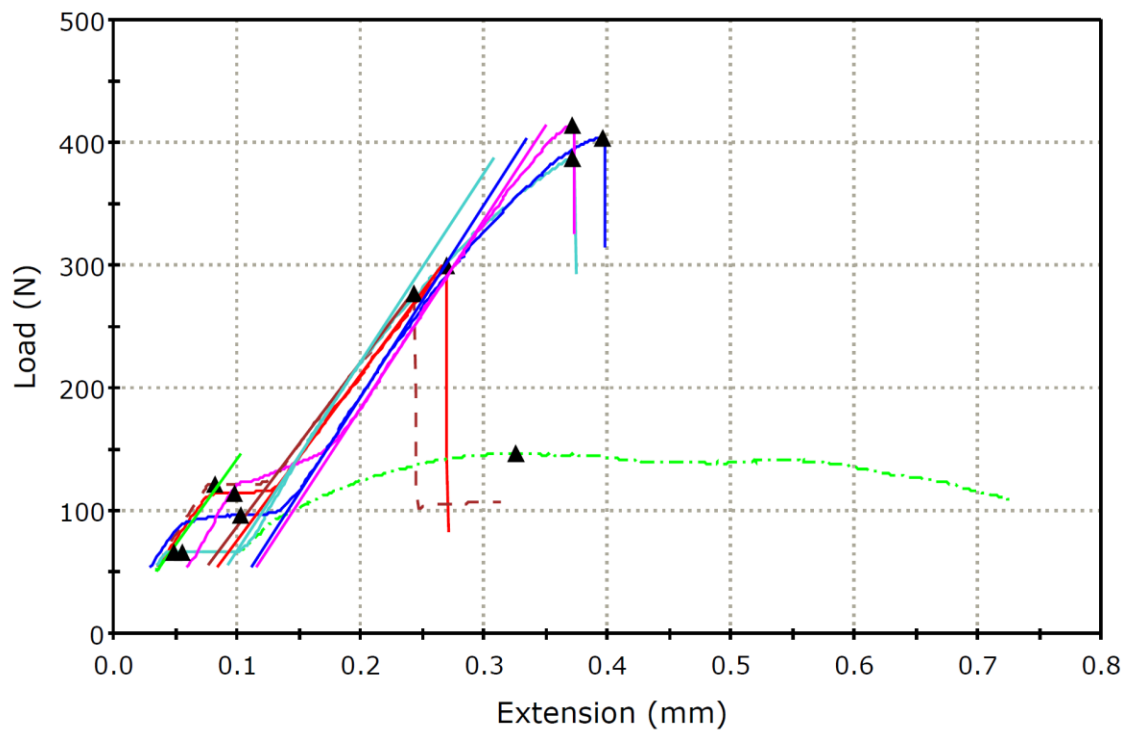**Figure S4.30 Load vs. extension curves for 150 kDa ABS (Neat) in the transverse orientation (colors represent multiple test specimens of the same bimodal blend)**

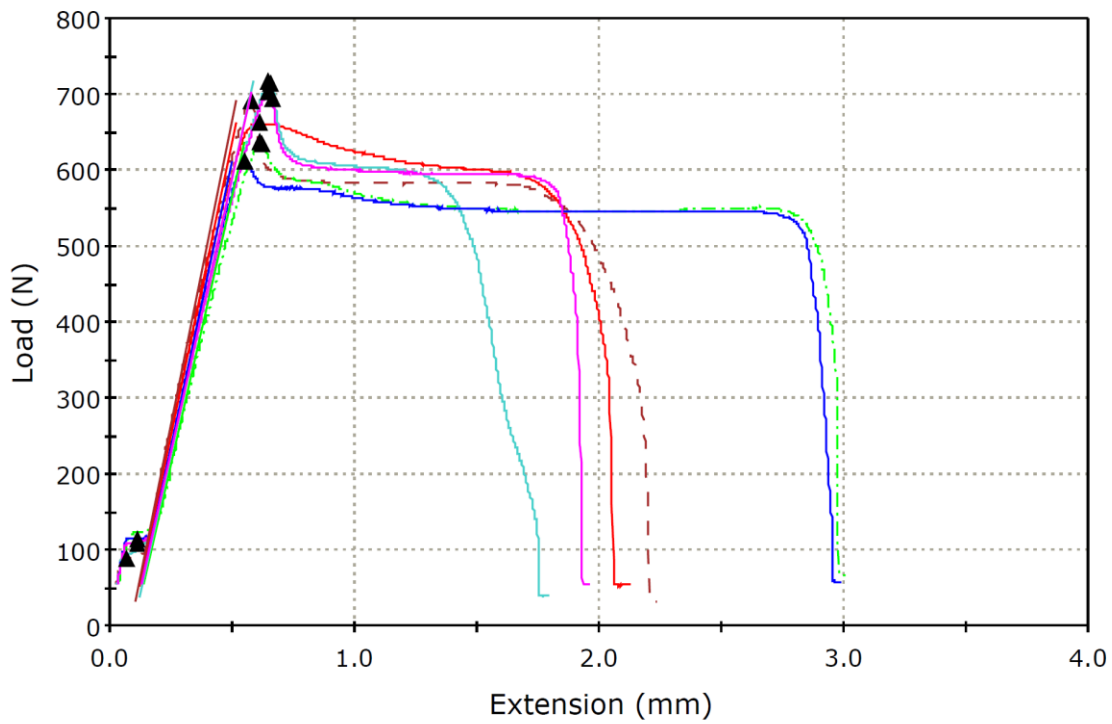**Figure S4.31 Load vs. extension curves for 3 mol% 8.5 kDa ABS in the longitudinal orientation (colors represent multiple test specimens of the same bimodal blend)**
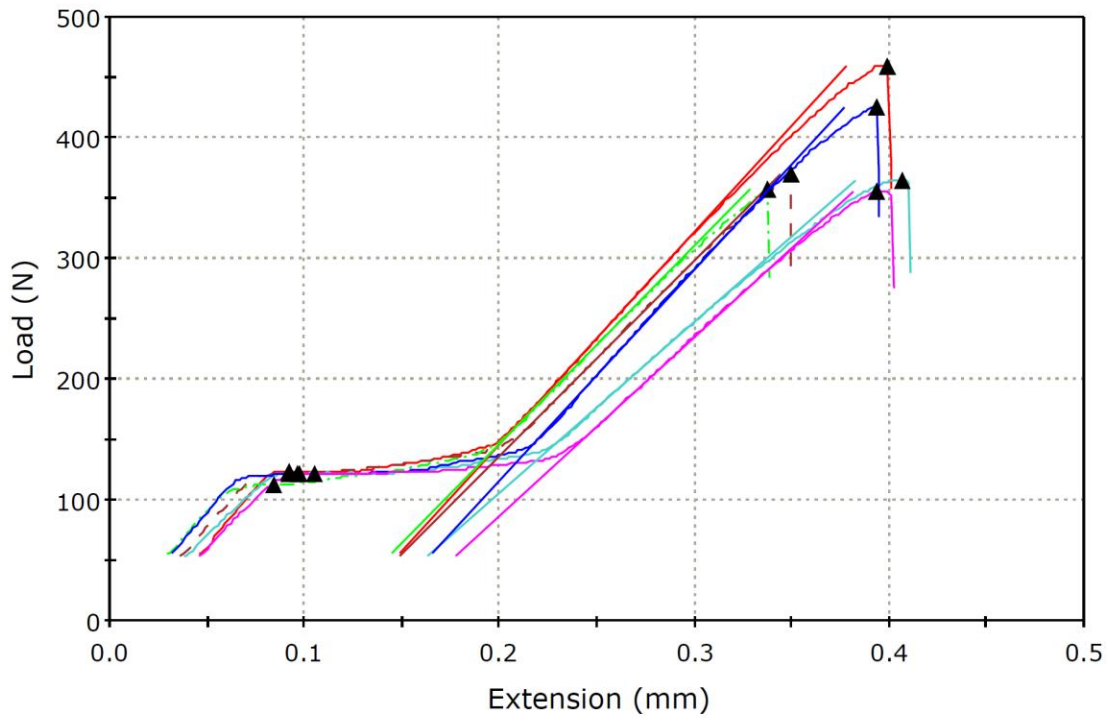
Figure S4.32 Load vs. extension curves for 3 mol% 8.5 kDa SAN in ABS in the transverse orientation (colors represent multiple test specimens of the same bimodal blend)
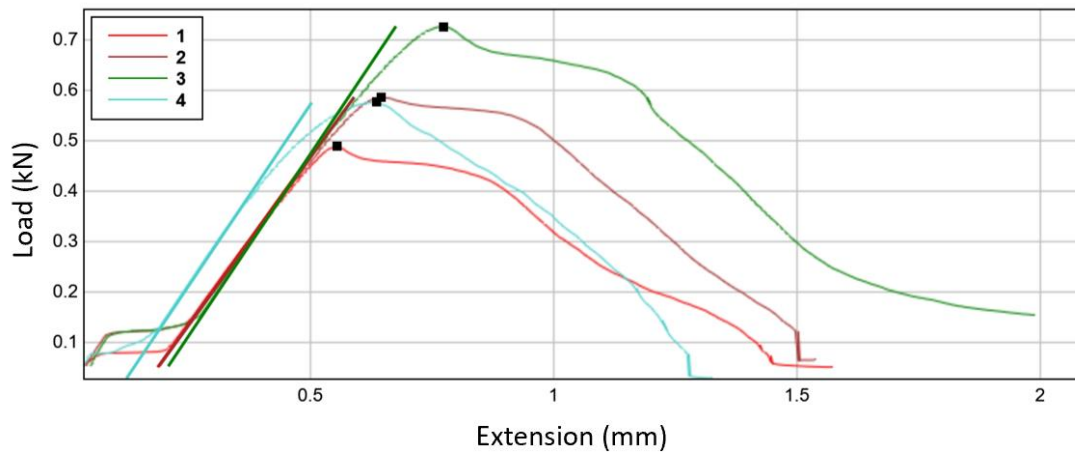
Figure S4.33 Load vs. extension curves for 3 mol% 33 kDa SAN in ABS in the longitudinal orientation (colors represent multiple test specimens of the same bimodal blend)
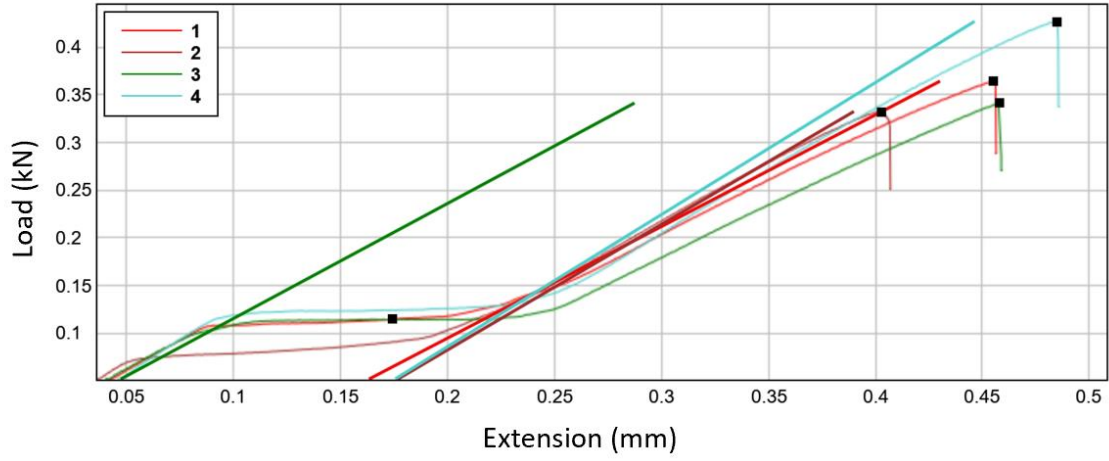
Figure S4.34 Load vs. extension curves for 3 mol% 33 kDa SAN in ABS in the transverse orientation (colors represent multiple test specimens of the same bimodal blend)
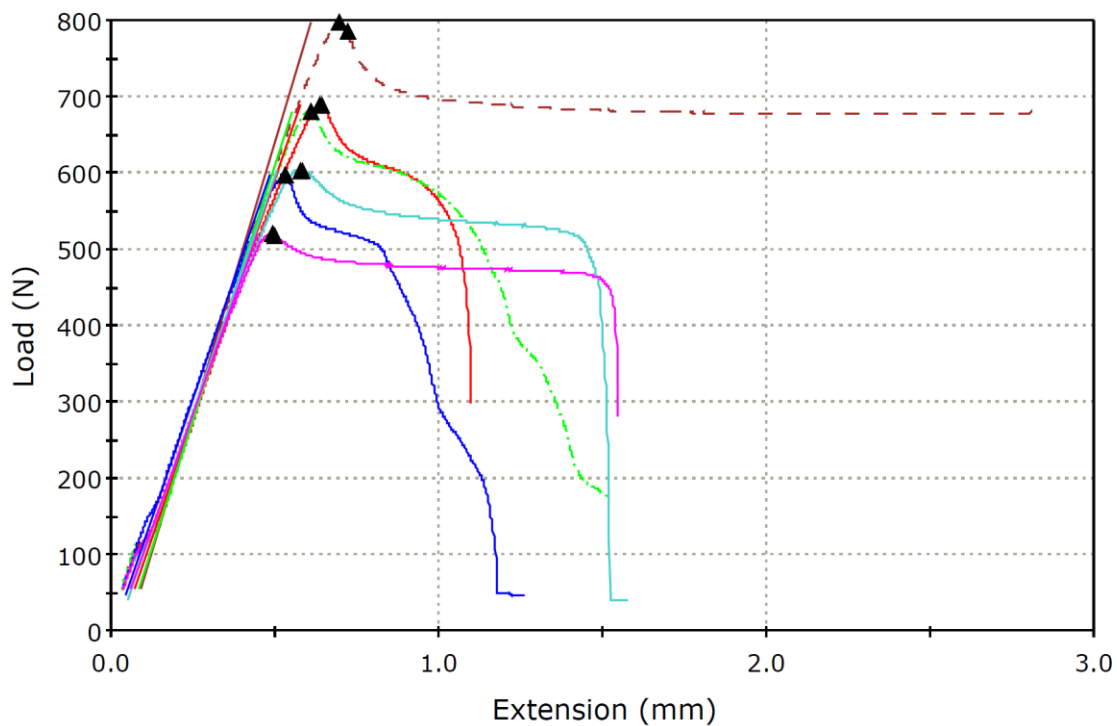
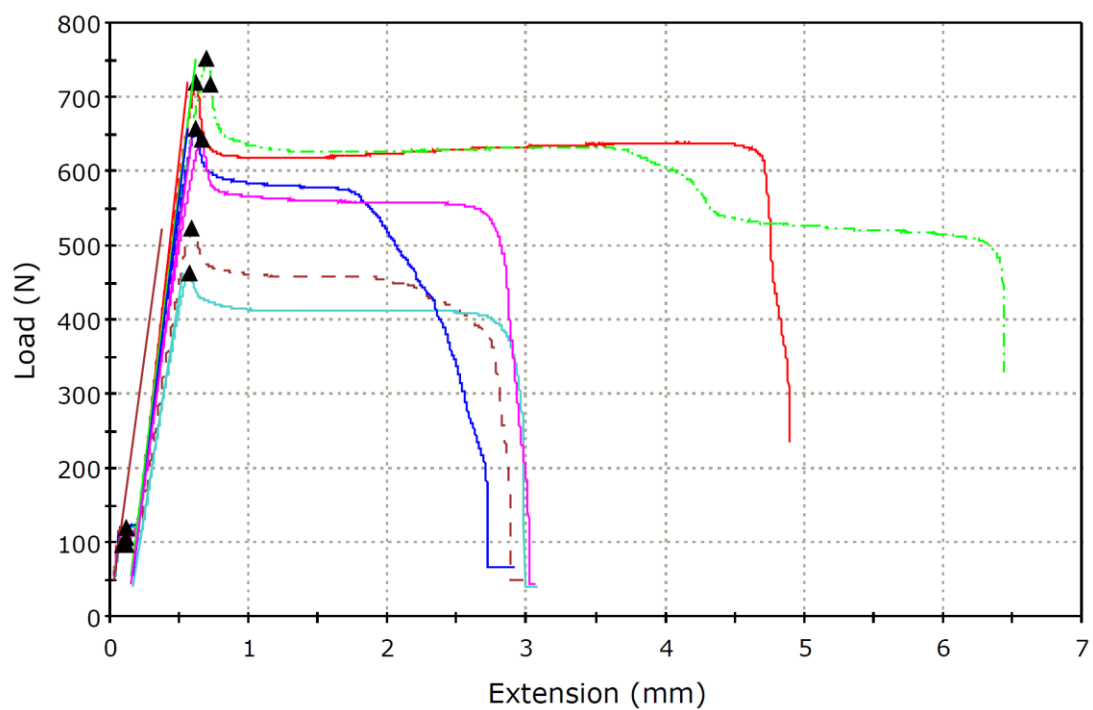**Figure S4.35 Load vs. extension curves for 3 mol% 75 kDa SAN in ABS in the longitudinal orientation (colors represent multiple test specimens of the same bimodal blend)**
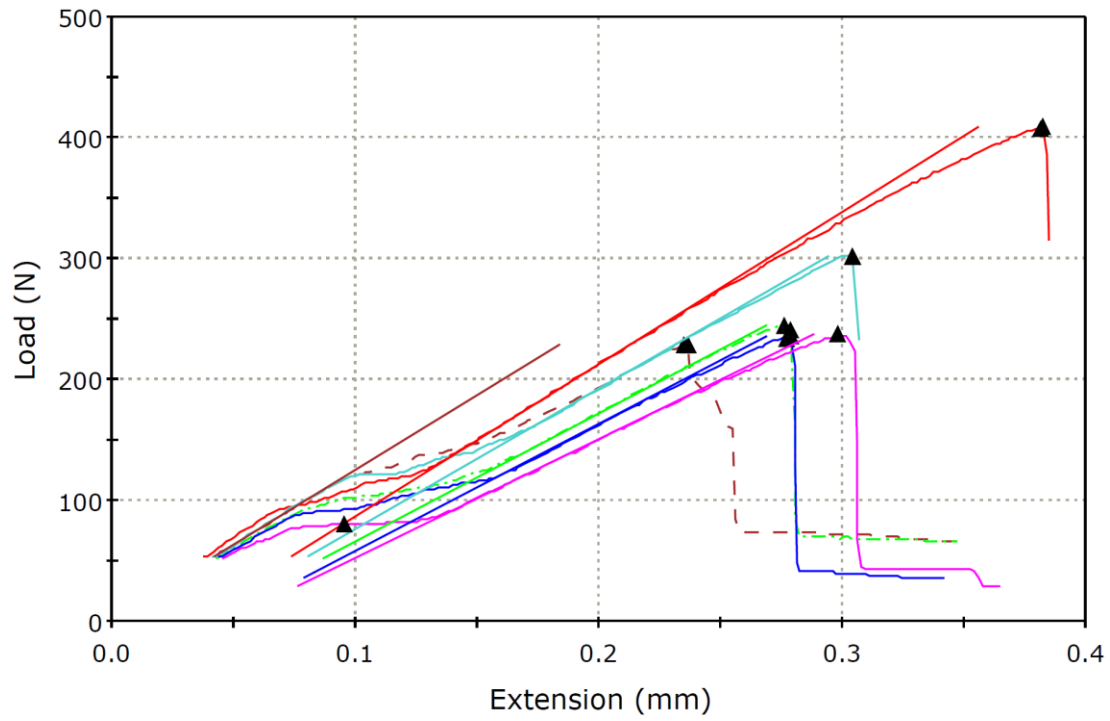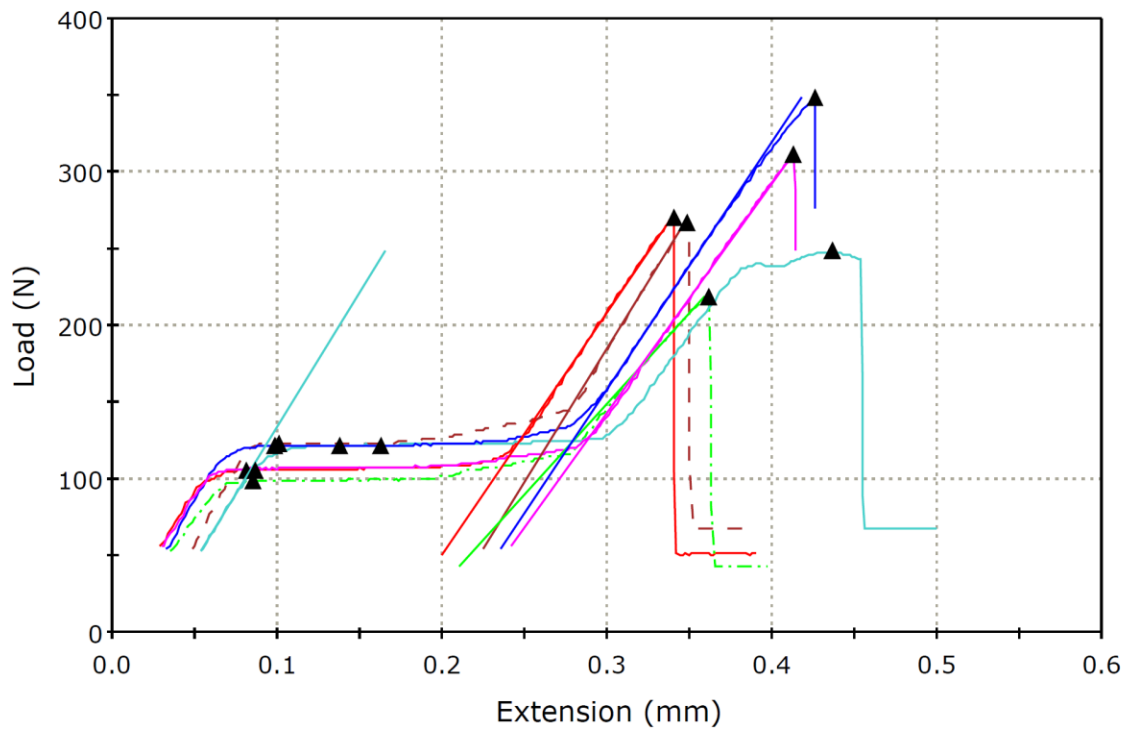
Figure S4.36 Load vs. extension curves for 3 mol% 75 kDa SAN in ABS in the transverse orientation (colors represent multiple test specimens of the same bimodal blend)
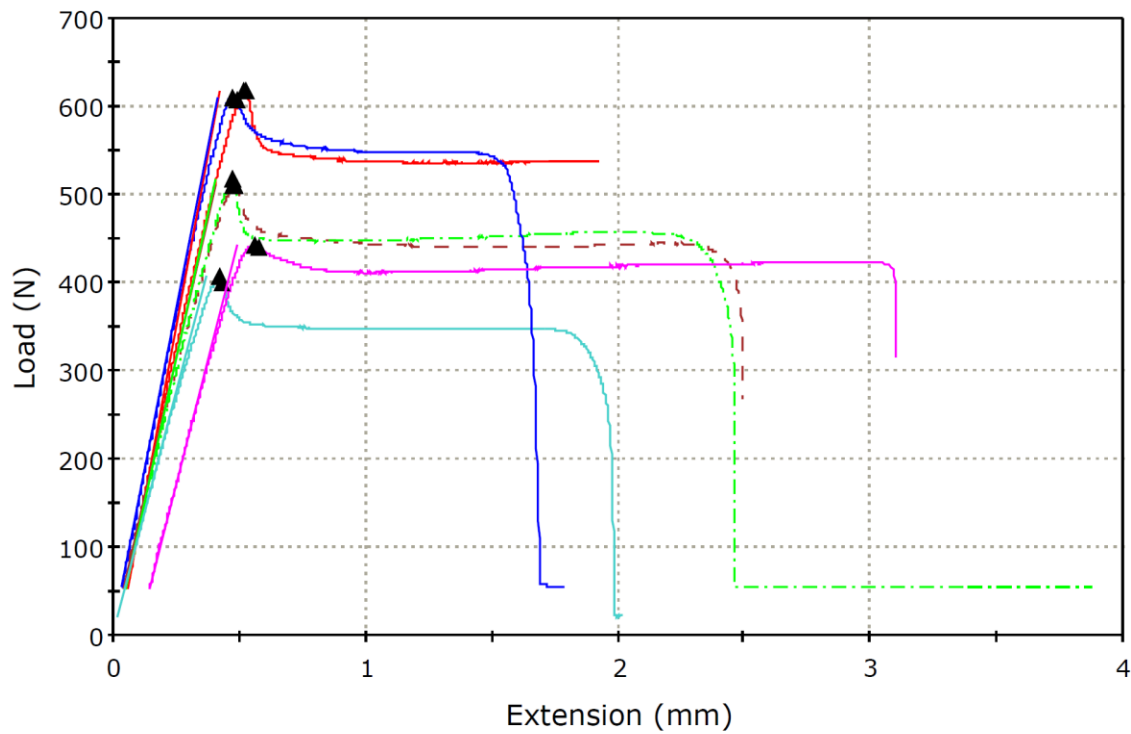
Figure S4.37 Load vs. extension curves for 3 mol% kDa PMMA in ABS in the longitudinal orientation (colors represent multiple test specimens of the same bimodal blend)
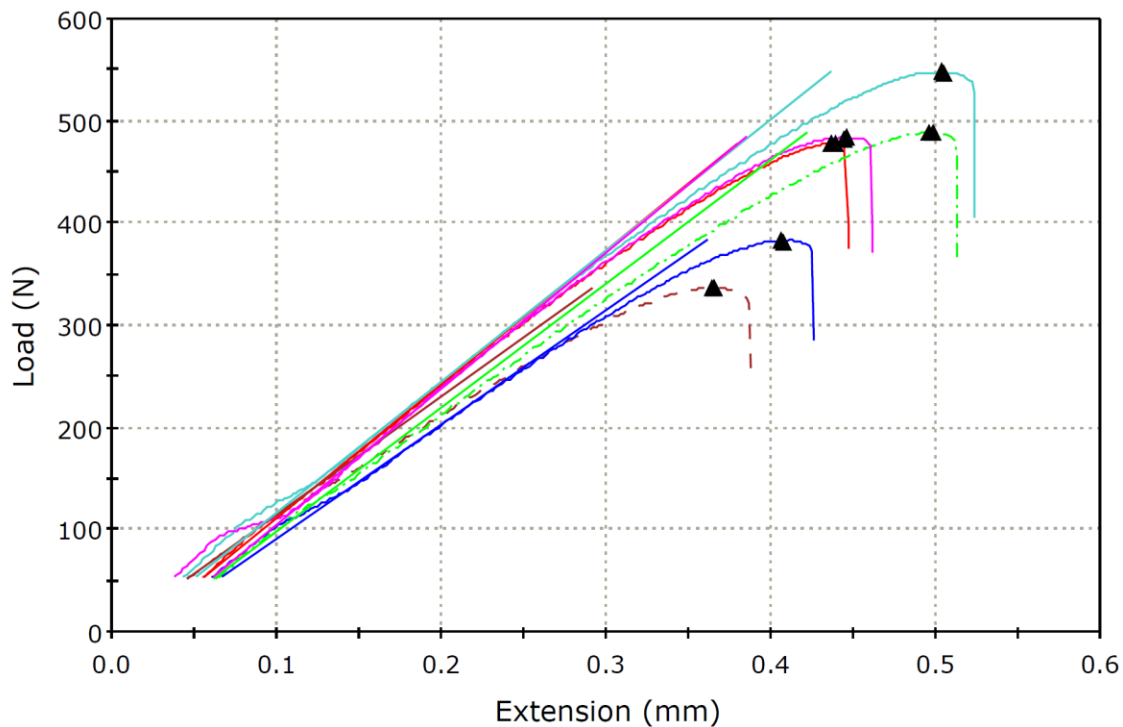
Figure S4.38 Load vs. extension curves for 3 mol% 33 kDa PMMA in ABS in the transverse orientation (colors represent multiple test specimens of the same bimodal blend)
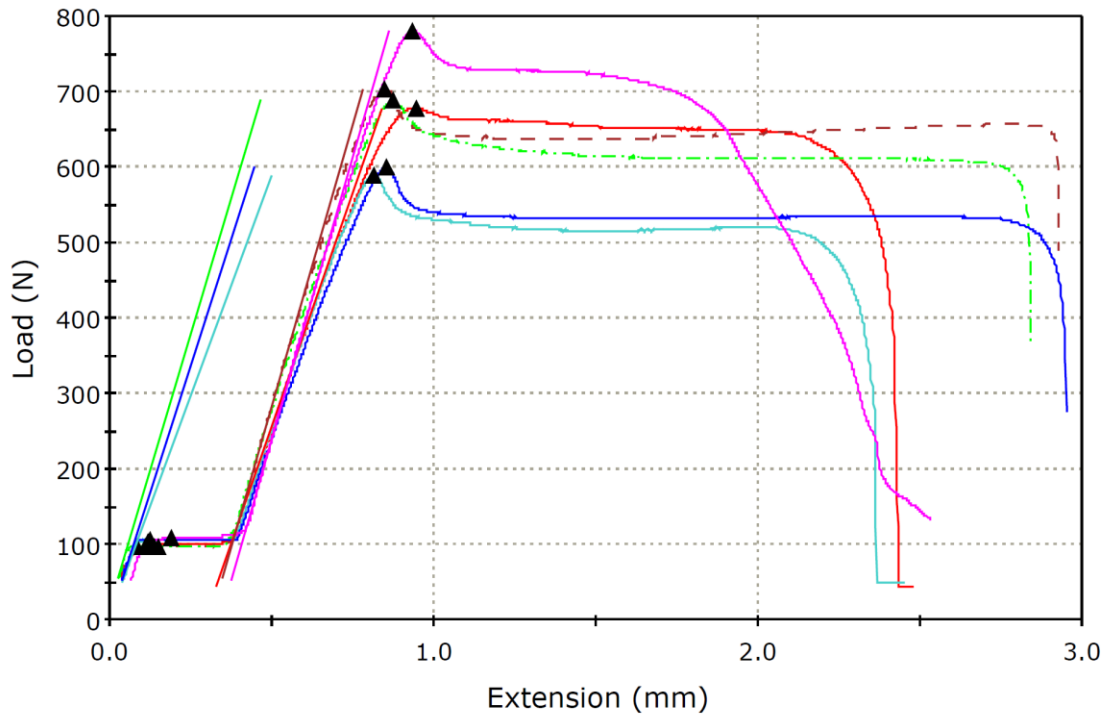
Figure S4.39 Load vs. extension curves for 3 mol% 67 kDa PMMA in ABS in the longitudinal orientation (colors represent multiple test specimens of the same bimodal blend)
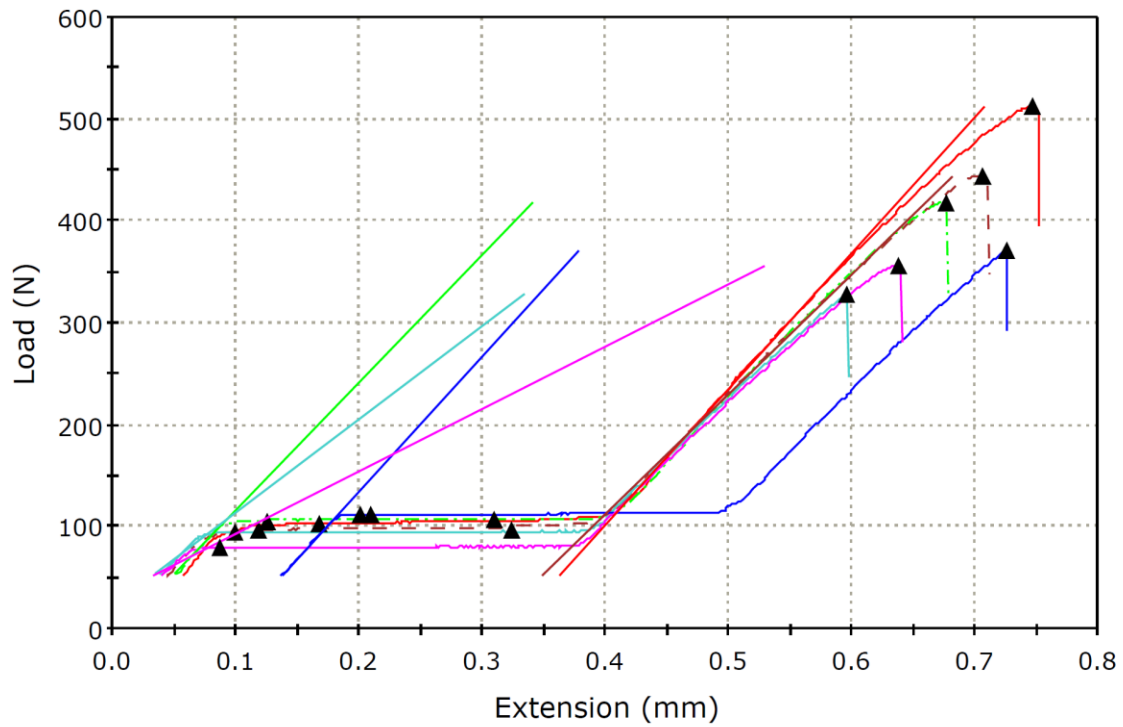
Figure S4.40 Load vs. extension curves for 3 mol% 67 kDa PMMA in ABS in the transverse orientation (colors represent multiple test specimens of the same bimodal blend)
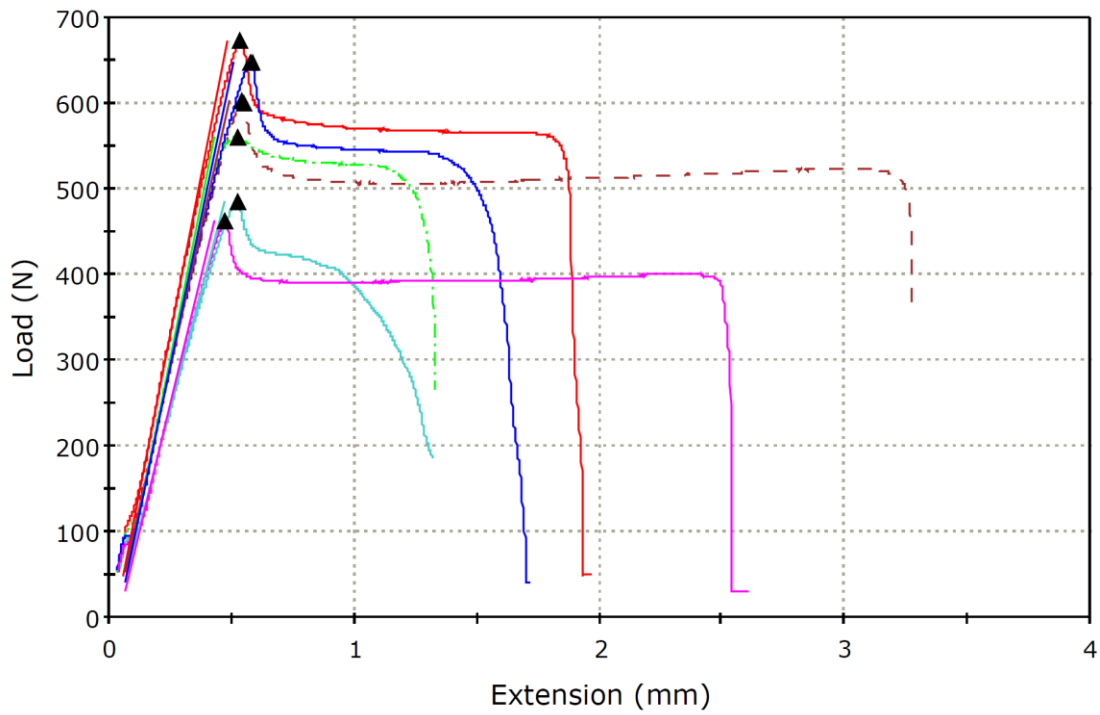
Figure S4.41 Load vs. extension curves for 3 mol% 100 kDa PMMA in ABS in the longitudinal orientation (colors represent multiple test specimens of the same bimodal blend)

Figure S4.42 Load vs. extension curves for 3 mol% 100 kDa PMMA in ABS in the transverse orientation (colors represent multiple test specimens of the same bimodal blend)

Figure S4.43 Load vs. extension curves for 3 mol% 3-arm 33 kDa PLA in ABS in the longitudinal orientation (colors represent multiple test specimens of the same bimodal blend)

Figure S4.44 Load vs. extension curves for 3 mol% 3-arm 33 kDa PLA in ABS in the transverse orientation (colors represent multiple test specimens of the same bimodal blend)

Figure S4.45 Load vs. extension curves for 3 mol% 220 kDa PLA in ABS in the longitudinal orientation (colors represent multiple test specimens of the same bimodal blend)

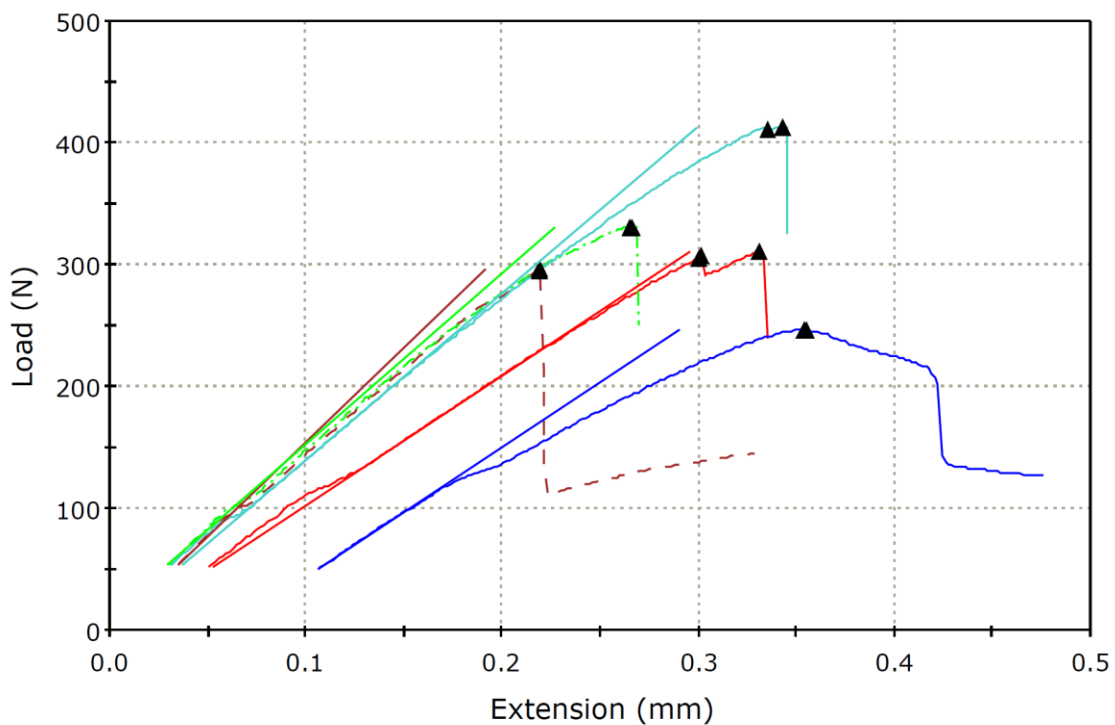**Figure S4.46 Load vs. extension curves for 3 mol% 220 kDa PLA in ABS in the transverse orientation (colors represent multiple test specimens of the same bimodal blend)**
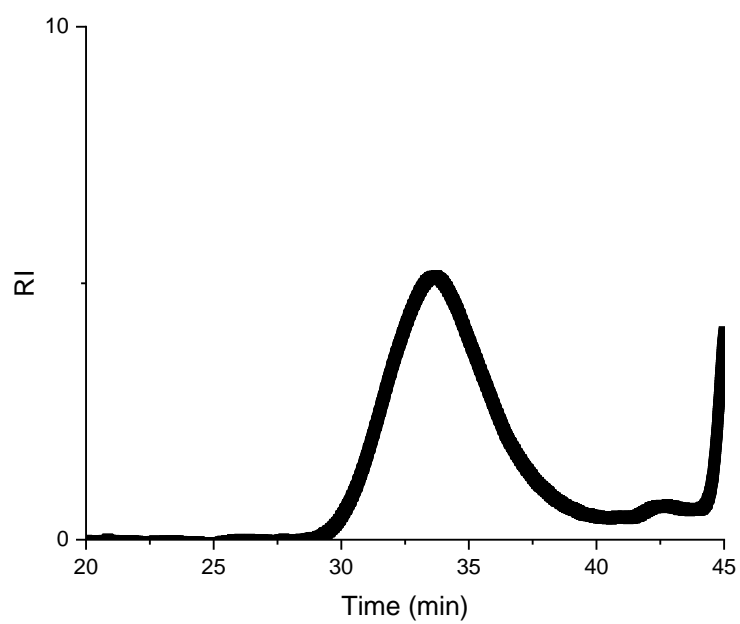
Figure S5.1 GPC trace of dimethacrylated PLA (PLADM)
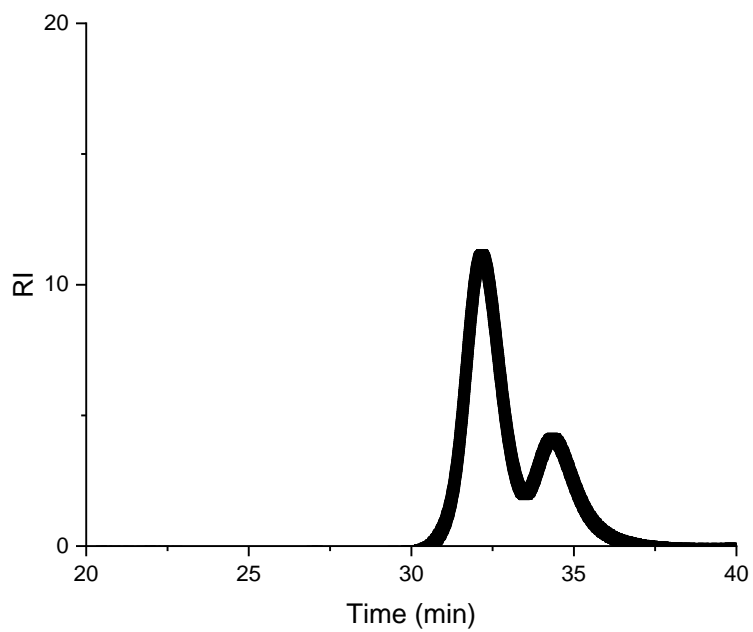
Figure S5.2 GPC trace of trimethacrylated PLA (PLATM)
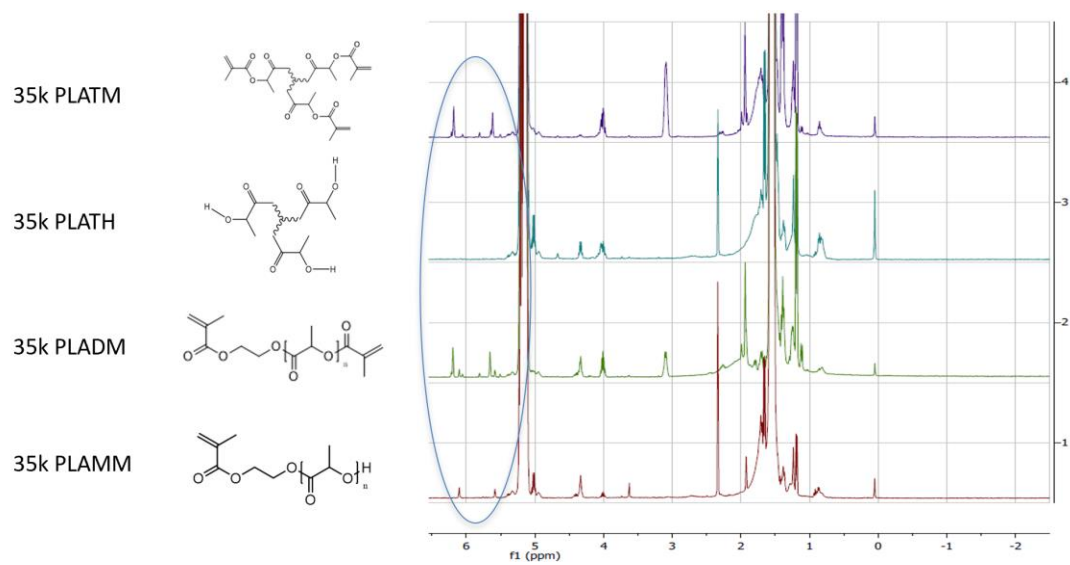
Figure S5.3 H-NMR showing successful addition of methacrylate end-groups
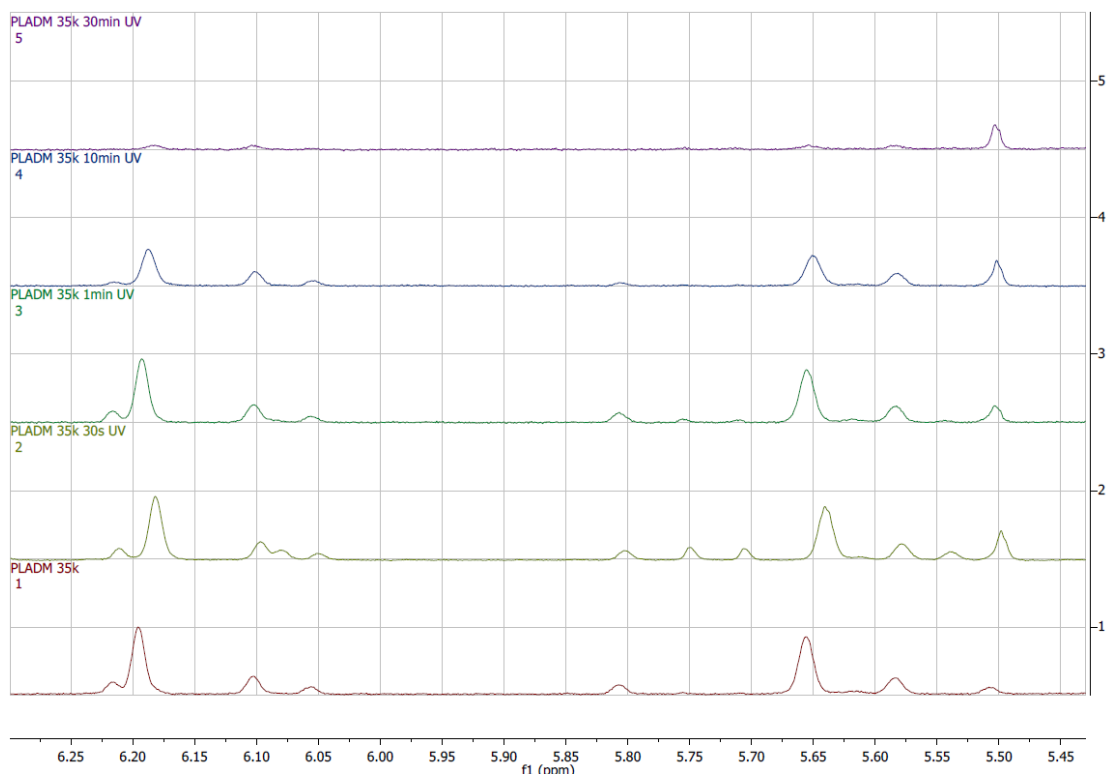
Figure S5.4 H-NMR showing disappearance of methacrylate end groups upon exposure to UV (365 nm) light in PLADM additive at 50°C
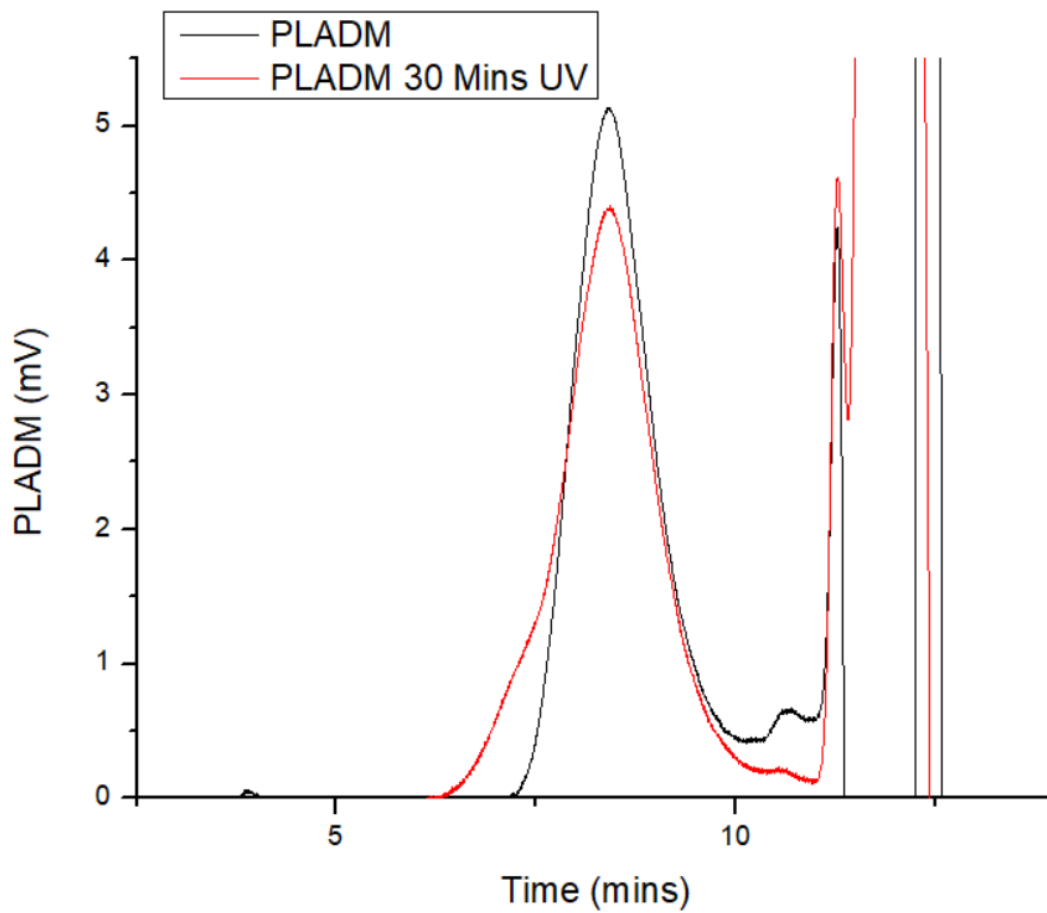
Figure S5.5 GPC trace showing increase in MW with UV irradiation of PLADM additive at 50°C
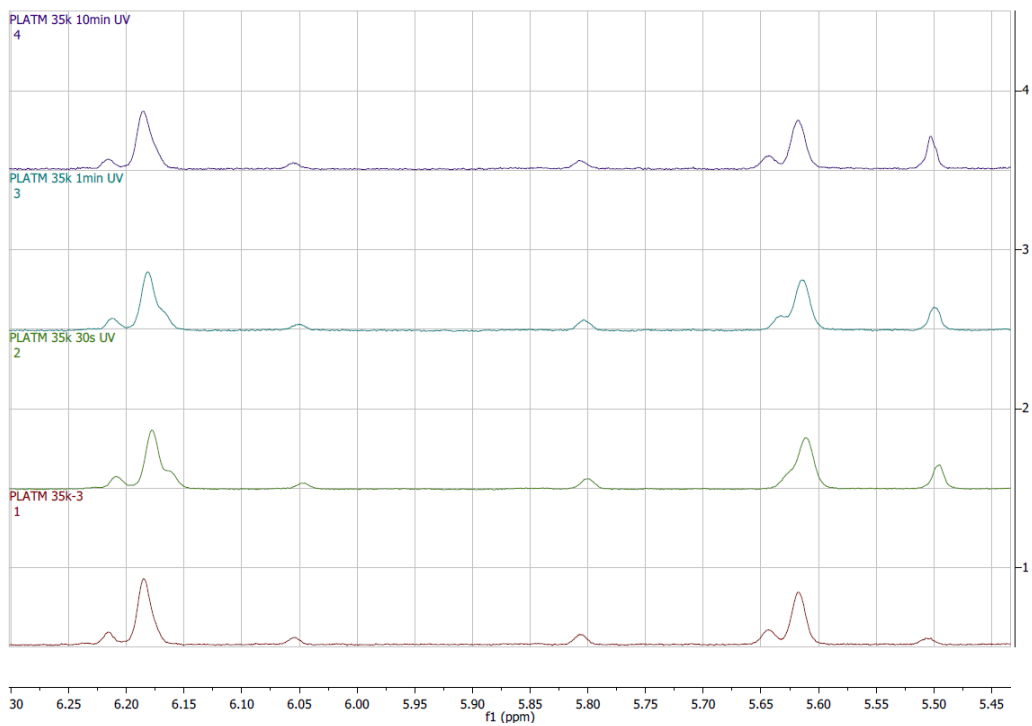
Figure S5.6 H-NMR showing change in methacrylate end-groups with exposure to UV (365 nm) light for the PLATM additive at 50°C
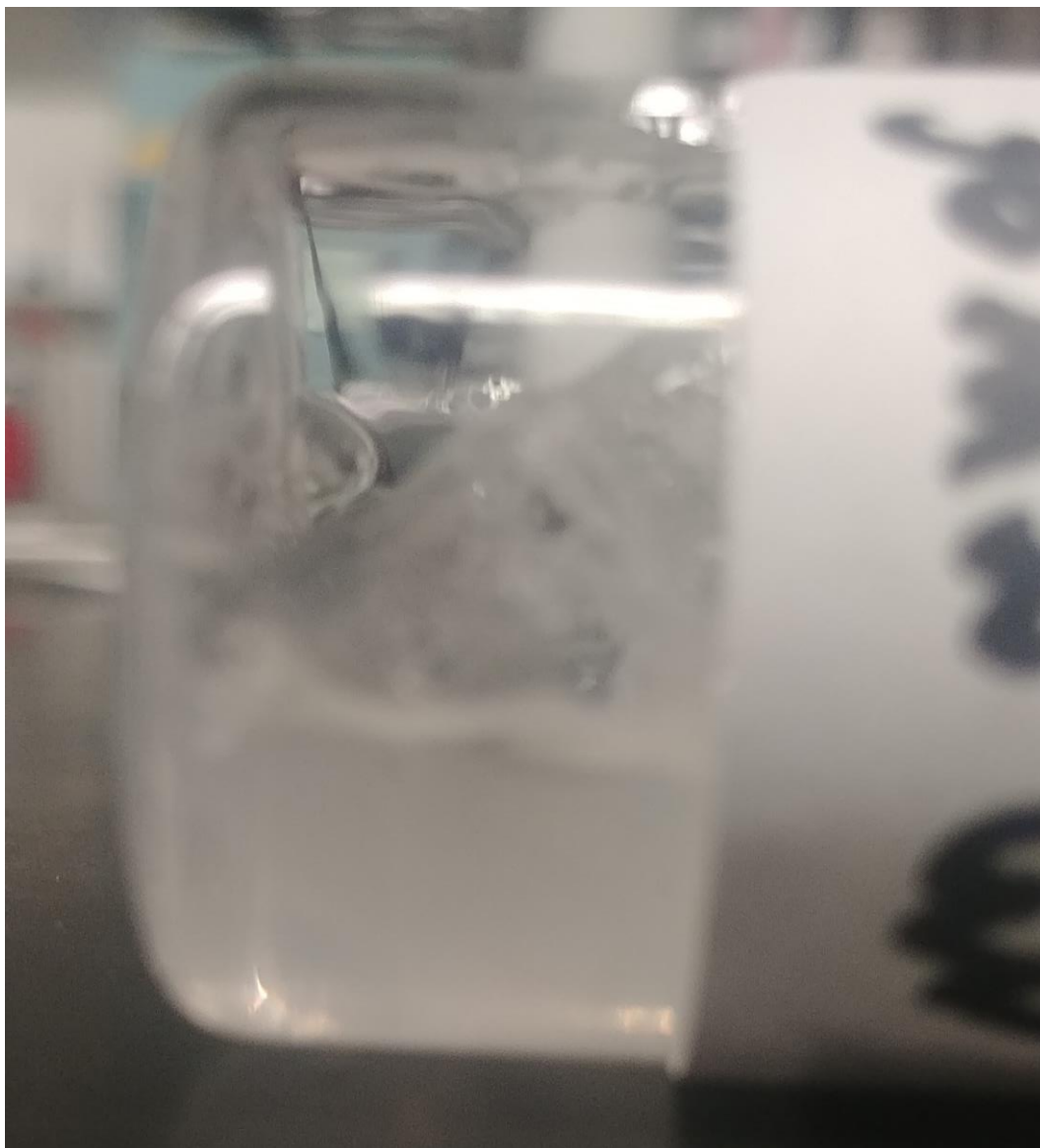
Figure S5.7 gelation of PLATM additive after 30 mins of exposure to UV (365 nm) light at 50°C
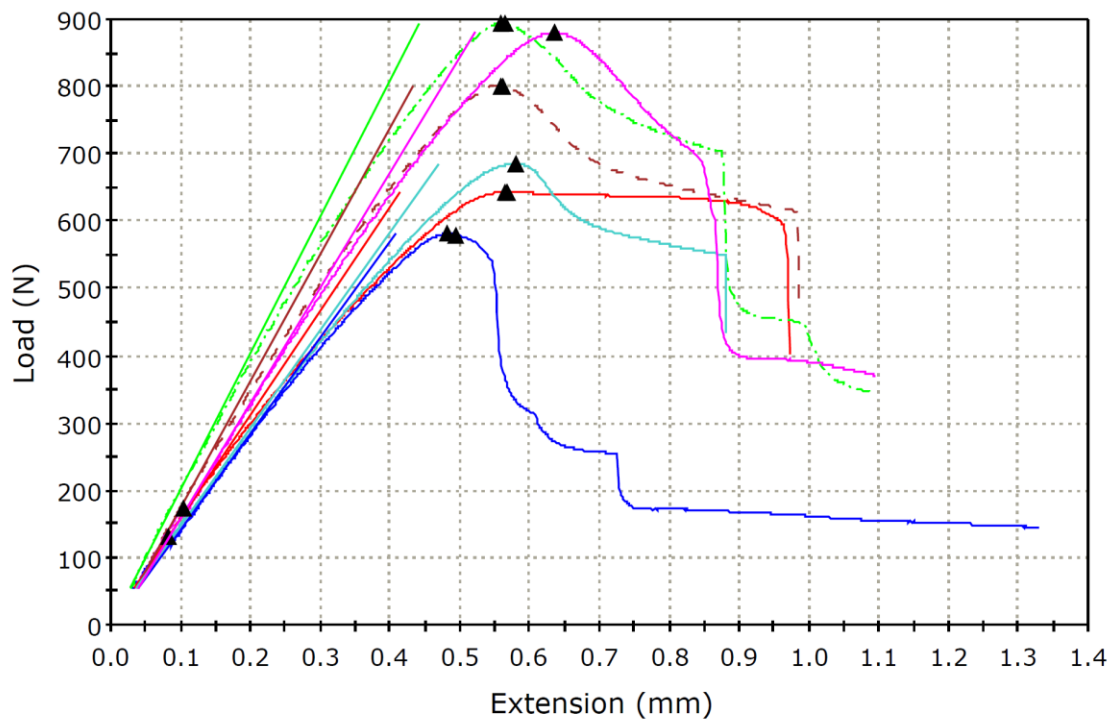
Figure S5.8 Load vs. extension curves for 220 kDa PLA (Neat) in the longitudinal orientation under UV (365 nm) light (colors represent multiple test specimens of the same bimodal blend)
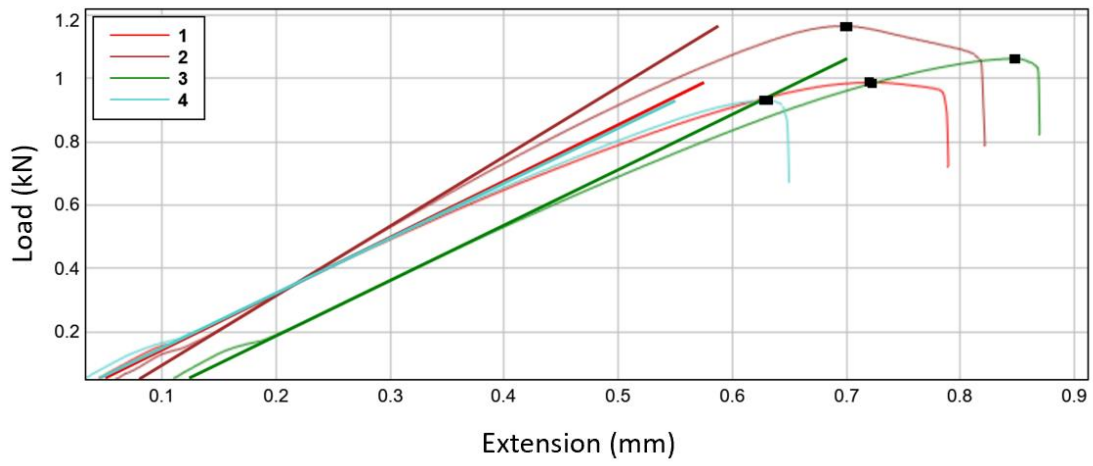
Figure S5.9 Load vs. extension curves for 220 kDa PLA (Neat) in the transverse orientation under UV (365 nm) light (colors represent multiple test specimens of the same bimodal blend)

Figure S5.10 Load vs. extension curves for 0.5 wt% DMPA in PLA in the longitudinal orientation under UV (365 nm) light (colors represent multiple test specimens of the same bimodal blend)
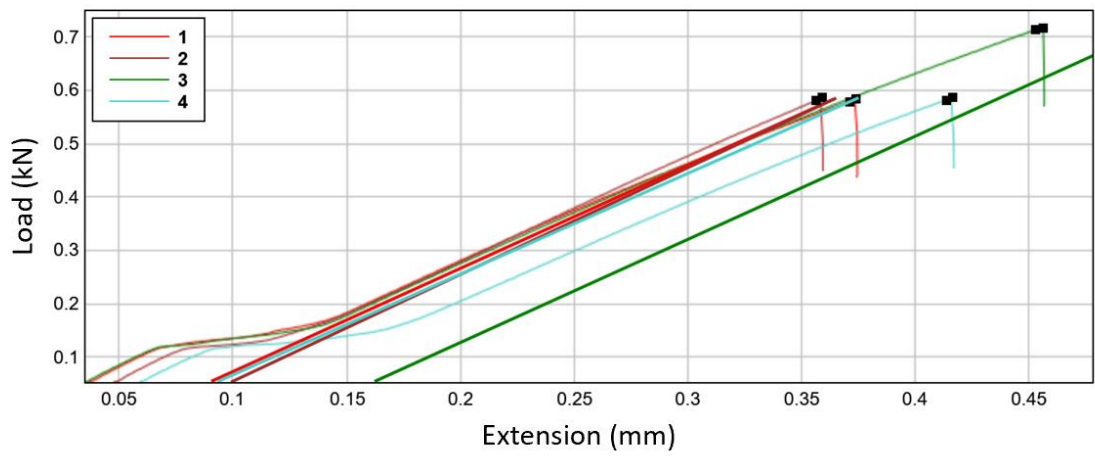
Figure S5.11 Load vs. extension curves for 0.5 wt% DMPA in PLA in the transverse orientation under UV (365 nm) light (colors represent multiple test specimens of the same bimodal blend)
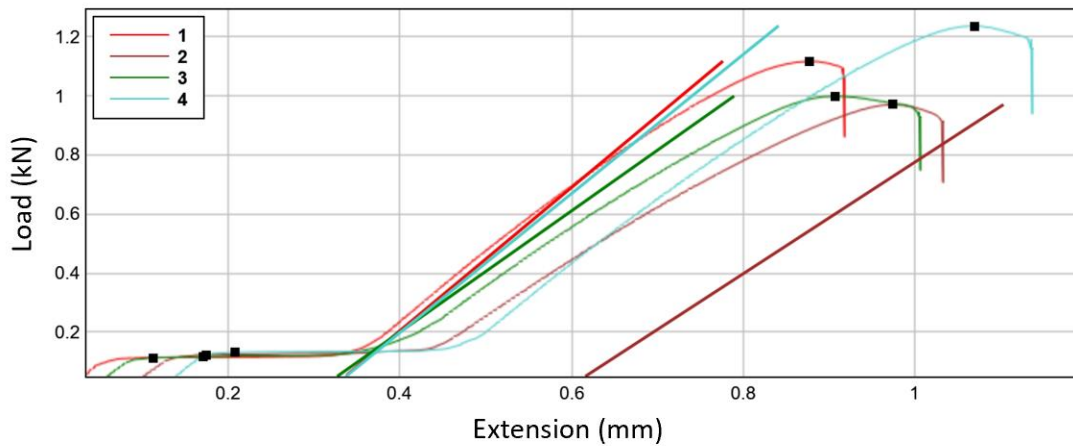
Figure S5.12 Load vs. extension curves for 3 mol% 35k kDa PLADM in PLA in the longitudinal orientation under UV (365 nm) light (colors represent multiple test specimens of the same bimodal blend)
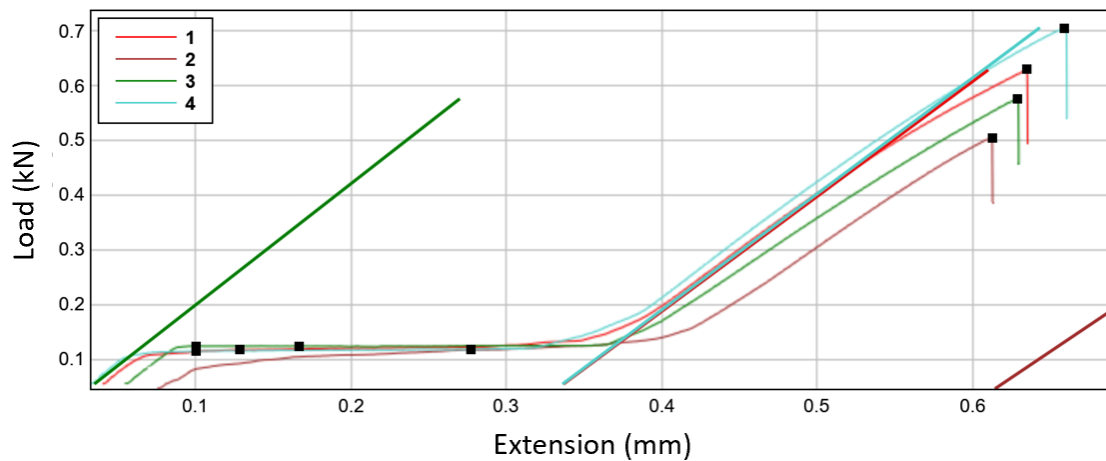
Figure S5.13 Load vs. extension curves for 3 mol% 35 kDa PLADM in PLA in the transverse orientation under UV (365 nm) light (colors represent multiple test specimens of the same bimodal blend)
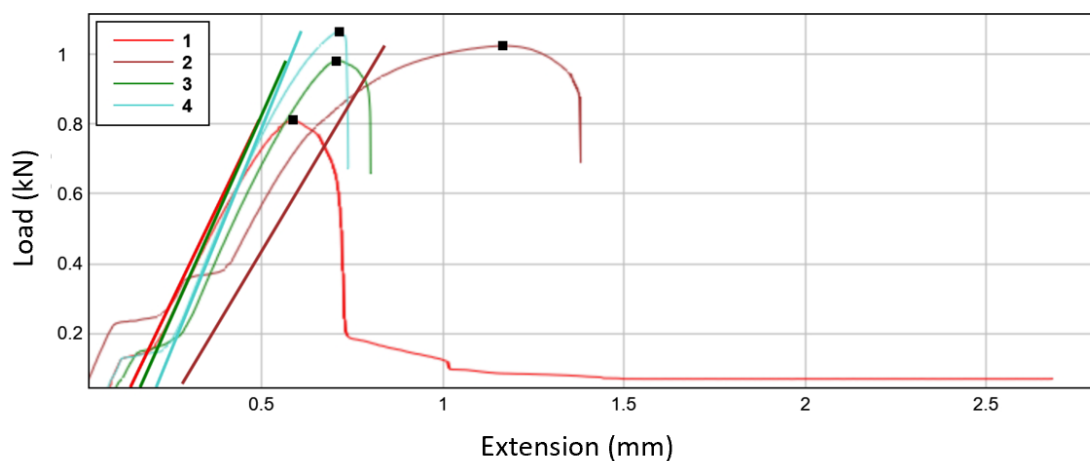
Figure S5.14 Load vs. extension curves for 3 mol% 3-arm 35 kDa PLATM in PLA in the longitudinal orientation under UV (365 nm) light (colors represent multiple test specimens of the same bimodal blend)
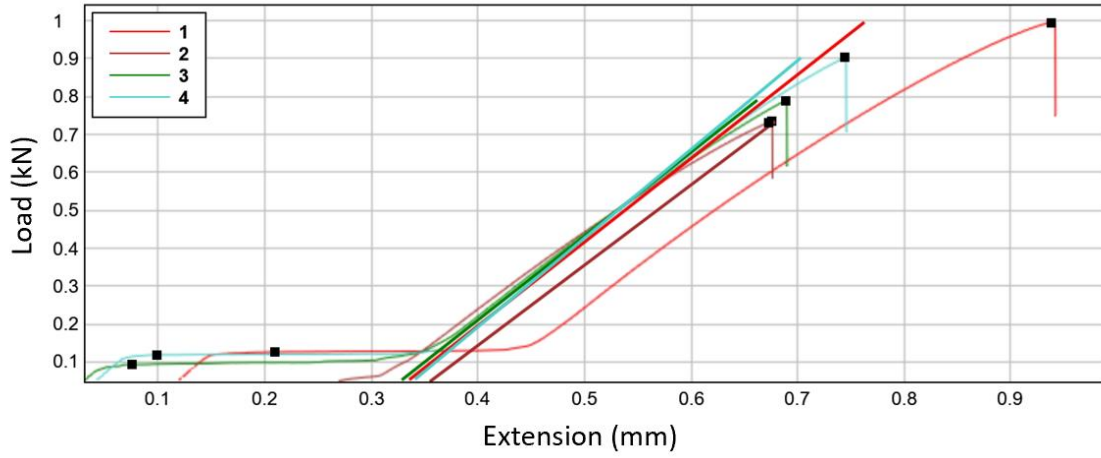
Figure S5.15 Load vs. extension curves for 3 mol%3-arm 35 kDa PLATM in PLA in the transverse orientation under UV (365 nm) light (colors represent multiple test specimens of the same bimodal blend)

VITA

Neiko Phillip Levenhagen graduated from the University of Wisconsin, Stevens Point with a B.S. in Polymer Chemistry in May 2014. His educational journey continued after joining the University of Tennessee, Knoxville in August 2014 to pursue his Ph.D. in Polymer Chemistry.